



**HAL**  
open science

# Remote sensing and numerical modeling of the oceanic mixed layer salinity in the Bay of Bengal

Akhil Valiya Parambil

► **To cite this version:**

Akhil Valiya Parambil. Remote sensing and numerical modeling of the oceanic mixed layer salinity in the Bay of Bengal. Earth and Planetary Astrophysics [astro-ph.EP]. Université Paul Sabatier - Toulouse III, 2015. English. NNT : 2015TOU30333 . tel-01430675

**HAL Id: tel-01430675**

**<https://theses.hal.science/tel-01430675>**

Submitted on 10 Jan 2017

**HAL** is a multi-disciplinary open access archive for the deposit and dissemination of scientific research documents, whether they are published or not. The documents may come from teaching and research institutions in France or abroad, or from public or private research centers.

L'archive ouverte pluridisciplinaire **HAL**, est destinée au dépôt et à la diffusion de documents scientifiques de niveau recherche, publiés ou non, émanant des établissements d'enseignement et de recherche français ou étrangers, des laboratoires publics ou privés.



Université  
de Toulouse

# THÈSE

En vue de l'obtention du

## DOCTORAT DE L'UNIVERSITÉ DE TOULOUSE

Délivré par : *l'Université Toulouse 3 Paul Sabatier (UT3 Paul Sabatier)*

---

---

Présentée et soutenue le *02/04/2015* par :

**AKHIL VALIYA PARAMBIL**

**Titre: Apport des données spatiales pour la modélisation numérique de la couche de mélange du Golfe du Bengale**

**Title: Remote sensing and numerical modeling of the oceanic mixed layer salinity in the Bay of Bengal**

---

---

### JURY

HALL NICK  
BLANKE BRUNO  
ECHEVIN VINCENT  
VIALARD JÉRÔME  
DURAND FABIEN  
LENGAIGNE MATTHIEU  
*de BOYER MONTÉGUT CLÉMENT*

Professeur d'Université  
LPO, Brest  
LOCEAN, Paris  
LOCEAN, Paris  
LEGOS, Toulouse  
LOCEAN, Paris  
LOS-IFREMER, Brest

Président du Jury  
Rapporteur  
Rapporteur  
Examinateur  
Directeur de thèse  
Co-Directeur de thèse  
Invité

---

### École doctorale et spécialité :

*SDU2E : Astrophysique, Sciences de l'Espace, Planétologie*

### Unité de Recherche :

*LEGOS, Toulouse*

### Directeur(s) de Thèse :

*DURAND Fabien et LENGAIGNE Matthieu*

### Rapporteurs :

*BLANKE Bruno et ECHEVIN Vincent*

## Acknowledgments

वक्रतुण्ड महाकाय कोटिसुर्य समप्रभा ।  
निर्विघ्नं कुरु मे देव सर्वकार्येषु सर्वदा ॥

First of all I express my sincerest thanks to my advisors ‘Dr. Fabien Durand’, ‘Dr. Matthieu Lengaigne’ and ‘Dr. Jerome Vialard’ for their careful guidance and for being with me throughout my PhD. Many thanks to ‘Dr. de Boyer Montegut’ and ‘Dr. P M Muraleedharan’ for paving the way to the French collaboration and also for the constant support. I use this opportunity to express my heartfelt thanks to ‘Rachid Benshilla’, ‘Julien Jouanno’ and ‘Guillaume Samson’ for being with me with valuable comments and advices, while I was struggling with my model.

I am indebted to CNES for the financial support for my PhD and Yaelle Silvera, CNES for helping me to complete all the formalities with CNES. I thank the Director of LEGOS ‘Yves Morel’ and Directors of NIO ‘S R Shetye (former)’, ‘SWA Naqvi (present)’ for allowing me to do the research and use the facilities at LEGOS and NIO. I also extend my sincere thanks to ‘Martine Mena, LEGOS’, ‘Brigitte Cournou, LEGOS’, ‘Nadine Lacroux, LEGOS’, ‘Mary Claude Cathala, Doctoral School’ and ‘T P Simon, NIO’ for all the help and facilities they offered. I thank ‘OLVAC’ my group at LEGOS for their constant support. I express my special thanks to ‘Thierry Delcroix’, ‘Fabrice Papa’, ‘Gael Alory’, ‘Lionel Gourdeau’, ‘Nick Hall’, ‘Rosemary Morrow’, ‘Gildas Cambon’, ‘Sylvan’ and ‘Elenna’ for making my first days in France smooth with their friendly approach.

I express my sincere thanks to ‘University Paul Sabatier (UPS)’ for accepting me as a PhD student and ‘CROUS’ for providing me accomodation throughout my stay. I am truly grateful to the members of the jury for accepting the invitation to review my thesis.

Finally, I express my thanks and love to my friends, ‘Hindumathi palanisamy’, ‘Awnesh Singh’, ‘Chandreshkar Deshmukh’, ‘Raphael Onguene’, ‘Dwi Yoga’, ‘Swen Julien’, ‘Cori Pegliasco’, ‘Eve’ and ‘Casimir’ for helping me to survive in France without knowing French. Special thanks to ‘Baby Aaradhya’, the little one at home who made my life joyful.

*Dedicated to my friend and wife, Keerthi*

## Résumé

*Le Golfe du Bengale (GdB), dans l'océan indien Nord, est sous l'influence d'intenses vents de mousson, qui se renversent saisonnièrement. Les fortes pluies et les apports fluviaux associés à la mousson de Sud-Ouest font du GdB l'une des régions les moins salées des océans tropicaux. La forte stratification haline proche de la surface qui en découle contribue à limiter le mélange vertical, ce qui maintient des températures de surface élevées et favorise la convection atmosphérique et les pluies. Cette stratification en sel a ainsi des implications profondes sur les échanges air-mer et sur le climat des pays riverains. L'objectif de ma thèse est d'améliorer la description de la variabilité de la salinité de surface (SSS) du GdB, et de comprendre ses mécanismes aux échelles de temps saisonnières à interannuelles.*

*Les climatologies existantes ont permis de mettre en évidence un cycle saisonnier marqué de la SSS, avec un dessalement intense de la partie Nord du bassin pendant l'automne, suivi par une expansion de ces eaux dessalées le long du bord Ouest du bassin. Cette langue dessalée s'érode finalement pendant l'hiver, pour revenir à son extension minimale au printemps. Cependant, la rareté des observations in-situ de SSS ne permet d'observer les fluctuations interannuelles autour de ce cycle saisonnier que de manière parcellaire dans le GdB. Le développement récent de la télédétection spatiale de la SSS (missions SMOS et AQUARIUS) a ouvert de nouvelles opportunités à cet égard. Cette technologie reste toutefois délicate dans le cas d'un bassin de petite taille tel que le GdB, du fait des contaminations éventuelles du signal de SSS par les interférences radio et par les sources d'origine continentale. Une validation systématique des produits satellites par comparaison à un jeu de données in-situ exhaustif montre qu'Aquarius capture de façon réaliste les évolutions saisonnières et interannuelles de la SSS partout dans le GdB. A l'inverse, SMOS ne parvient pas à restituer une salinité meilleure que les climatologies existantes. L'analyse des données Aquarius et de notre produit in-situ révèlent également que les plus fortes fluctuations saisonnières et interannuelles de SSS apparaissent dans le Nord du GdB, près de l'embouchure du Gange-Brahmapoutre et le long du bord Ouest, peu après la mousson d'été.*

*La durée limitée des données Aquarius et la rareté des observations in-situ empêchent une évaluation adéquate des mécanismes pilotant cette variabilité saisonnière et interannuelle à partir des observations. En conséquence, nous avons utilisé une simulation régionale d'un modèle de circulation océanique, forcé sur les vingt dernières années. Mes résultats montrent que les apports fluviaux du Gange-Brahmapoutre pilotent le fort dessalement saisonnier qui se produit peu après la mousson d'été dans le Nord du Golfe du Bengale. Les fluctuations interannuelles de ce dessalement sont pilotées par les variations interannuelles du débit du Gange-Brahmapoutre à l'issue de la mousson d'été, ainsi que par les fluctuations de la tension de vent en hiver et au printemps. L'advection horizontale induite par le courant de bord Ouest s'écoulant vers le Sud est responsable de l'extension de la langue d'eau dessalée depuis le Nord du GdB le long du bord Ouest. La variabilité interannuelle de la SSS dans cette région est forcée à distance par la variabilité du Dipôle de l'Océan Indien, qui déclenche des ondes de Kelvin côtières se propageant jusqu'à la côte est de l'Inde. Ces ondes y modulent l'intensité du courant de bord ouest et l'advection vers le Sud des eaux douces du Nord du GdB. Contrairement à ce qui était connu jusqu'alors, nous avons finalement montré que l'apport d'eau salée dans les couches superficielles du GdB (nécessaire pour l'équilibre à long terme de la SSS du bassin) se produit essentiellement via les échanges verticaux turbulents avec les eaux de subsurface salées, et non pas via les échanges horizontaux avec le reste de l'Océan Indien.*

## Abstract

*Located in the Northern Indian Ocean, the Bay of Bengal (BoB) is forced by intense seasonally reversing monsoon winds. Heavy rainfall and strong river runoffs associated with the southwest monsoon makes the bay one of the freshest regions in the tropical ocean. This surface fresh water flux induces strong near surface salinity stratification, which reduces vertical mixing and maintains high sea surface temperatures and deep atmospheric convection and rainfall. This intense near surface haline stratification has therefore profound implications on the air-sea exchanges, and on the climate of the neighboring countries. The goal of my thesis is to improve the description of the Sea surface salinity (SSS) variability in the BoB and to understand the oceanic and atmospheric processes driving this variability at seasonal and interannual timescales.*

*Existing climatologies reveal a marked seasonal cycle of SSS with an intense freshening of the northern part of the basin during fall that subsequently spreads along the western boundary. This fresh pool finally erodes during winter, to reach its minimal extent in spring. The paucity of in-situ SSS observations however prevented to monitor the interannual fluctuations around this seasonal picture with a good spatial coverage. The recent development of SSS remote-sensing capabilities (with SMOS and AQUARIUS satellites) may help with that regard. However this is particularly challenging for a small semi-enclosed basin such as the Bay of Bengal, because of the potential contamination of the SSS signal by radio frequency interferences and land effects in the near coastal environment. A thorough validation of these satellite products to an exhaustive gridded in-situ dataset shows that Aquarius reasonably captures the large-scale observed seasonal and interannual SSS evolution everywhere in the BoB while SMOS does not perform better than existing climatologies, advocating for improvements of its SSS retrieval algorithm there. Aquarius and in-situ data also reveal that the largest SSS fluctuations (at both seasonal and interannual timescales) occur near the Ganga-Brahmaputra river mouth and along the eastern coast of India shortly after the summer monsoon.*

*The short time span of the Aquarius and paucity of the in-situ data however prevented a proper assessment of the mechanisms driving these seasonal and*

*interannual SSS variability from observations. To reach that goal, I therefore used an ocean general circulation model regional simulation, forced with interannual altimeter-derived estimates of river runoffs and precipitations over the past twenty years. This model accurately simulates the seasonal and interannual SSS fluctuations of the in-situ data. My results show that the strong seasonal freshening that occurs shortly after the monsoon in the northern part of the Bay primarily results from the Ganges-Brahmaputra river discharge. Interannual fluctuations of this freshening are driven by interannual variations of the Ganga-Bramaputra river runoffs right after the monsoon and by wind stress fluctuations from winter to spring. Horizontal advection by the southward flowing coastal current is responsible for the seasonal southward expansion of fresh pool from the northern BoB to the east coast of India. The interannual SSS variability in this region is remotely controlled by the Indian Ocean Dipole variability, that drives coastal Kelvin waves propagating to the eastern coast of India. These waves modulate the intensity of the coastal current and the related advection of fresh water from the northern part of the Bay. Contrary to what was thought before, we showed that the salt influx into the upper BoB (necessary to maintain its long-term haline equilibrium) occurs primarily through turbulent vertical exchanges with the underlying saltier waters, rather than by horizontal exchanges with the rest of the Indian ocean.*

# *Table of Contents*

---

Acknowledgments	
Résumé	1
Abstract	3
<b>CHAPTER 1 - INTRODUCTION</b>	
<b>1.1. GENERAL INTRODUCTION</b>	<b>11</b>
1.1.1. Particularities of the Indian Ocean climate	11
1.1.2. A brief historical overview of Indian Ocean circulation knowledge	12
1.1.3. The Bay of Bengal haline structure and its climatic consequences	14
<b>1.2. THE BAY OF BENGAL CLIMATE VARIABILITY</b>	<b>17</b>
1.2.1. Geography of the Bay of Bengal	17
1.2.2. Seasonal timescales	18
1.2.2.1. Atmospheric variability	18
1.2.2.2. Oceanic Response	23
1.2.3. Interannual timescales	26
1.2.3.1. Relevant interannual climate modes	26
1.2.3.2. Interannual variability of freshwater fluxes	30
<b>1.3. THE BAY OF BENGAL SALINITY</b>	<b>31</b>
1.3.1. Salinity observations	31
1.3.1.1. <i>In-situ</i> SSS observations and related climatologies	31
1.3.1.2. Remote sensing initiatives	33
1.3.2. Seasonal SSS variations and related mechanism	35
1.3.3. Interannual SSS variations and related mechanisms	37
<b>1.4. SCIENTIFIC QUESTIONS</b>	<b>39</b>
<b>1.5. ORGANIZATION OF THESIS</b>	<b>42</b>
<b>CHAPTER 2 - DATA AND METHODOLOGY</b>	
<b>2.1. GENERAL INTRODUCTION</b>	<b>43</b>
<b>2.2. OBSERVATION DATA</b>	<b>43</b>
2.2.1. <i>In-situ</i> SSS dataset	43
2.2.2. SSS Climatology	49
2.2.3. Satellite SSS	49
<b>2.3. MODEL CONFIGURATION</b>	<b>54</b>
2.3.1. Model setup	54
2.3.2. Forcing datasets	58
2.3.3. Reference and sensitivity experiments	64
2.3.4. Model mixed layer salinity budget	64

## **CHAPTER 3 - ASSESSMENT OF SMOS AND AQUARIUS SURFACE SALINITY RETRIEVAL IN THE BAY OF BENGAL**

Foreword	66
Abstract	68
<b>3.1. INTRODUCTION</b>	<b>69</b>
<b>3.2. DATASETS AND METHODS</b>	<b>72</b>
3.2.1. SMOS level-3 data	72
3.2.2. Aquarius level 3 data	73
3.2.3. Validation datasets	74
3.2.4. Colocation method	75
<b>3.3. GENERAL EVALUATION OF THE REMOTELY SENSED SSS PRODUCTS</b>	<b>77</b>
<b>3.4. SEASONAL EVALUATION OF REMOTELY SENSED PRODUCTS</b>	<b>80</b>
<b>3.5. INTERANNUAL EVALUATION OF REMOTELY-SENSED PRODUCTS</b>	<b>84</b>
<b>3.6. SUMMARY AND DISCUSSION</b>	<b>88</b>
3.6.1. Summary	88
3.6.2. Discussion	90
3.6.3. Perspectives	91

## **CHAPTER 4 – A MODELLING STUDY OF THE PROCESSES GOVERNING THE SURFACE SALINITY SEASONAL CYCLE IN THE BAY OF BENGAL**

Foreword	94
Abstract	96
<b>4.1. INTRODUCTION</b>	<b>97</b>
<b>4.2. DATA AND METHODS</b>	<b>103</b>
4.2.1. Model description and setup	103
4.2.2. The salt budget in the model	105
4.2.3. Validation datasets	106
<b>4.3. VALIDATION</b>	<b>107</b>
<b>4.4. PROCESSES OF THE SSS SEASONAL CYCLE ALONG THE INDIAN COASTLINE</b>	<b>110</b>
4.4.1. Overall picture	110
4.4.2. Northern Bay of Bengal	114
4.4.3. The Western BoB and the Southern Tip of India	119
<b>4.5. SUMMARY AND DISCUSSION</b>	<b>122</b>
4.5.1. Summary	122
4.5.2. Discussion	123
Appendix. Energy required for increasing surface salinity by vertical mixing	127

## **CHAPTER 5 - INTERANNUAL VARIABILITY OF BAY OF BENGAL SEA SURFACE SALINITY: A MODELLING APPROACH**

Foreword	130
<b>5.1. INTRODUCTION</b>	<b>132</b>
<b>5.2. DATA AND METHODS</b>	<b>137</b>
5.2.1. Model configuration and forcing	137
5.2.2. Reference and sensitivity experiments	138
5.2.3. SSS validation datasets	142
<b>5.3. VALIDATION OF MODELLED INTERANNUAL SSS VARIATIONS</b>	<b>142</b>
<b>5.4. PROCESSES DRIVING SSS INTERANNUAL VARIABILITY</b>	<b>148</b>
5.4.1. Main patterns of SSS variability	148
5.4.2. Relative importance of each forcing	154
<b>5.5. SUMMARY AND DISCUSSION</b>	<b>160</b>
5.5.1. Summary	160
5.5.2. Discussion	162
<b>CHAPTER 6 - SUMMARY AND PERSPECTIVE</b>	
<b>6.1. SUMMARY</b>	<b>166</b>
<b>6.2. PERSPECTIVES</b>	<b>170</b>
<b>REFERENCES</b>	<b>174</b>

## ACRONYMS

ARGO	Array for Real-time Geostrophic Oceanography
AS	Arabian Sea
ASIRI	Air-Sea Interaction Research Initiative
BLT	Barrier Layer Thickness
BoB	Bay of Bengal
BOBPS	Bay of Bengal Process Study
BOMBEX	Bay of Bengal Monsoon Experiment
CAP	Combined Active-Passive
CV	Cauvery
CATDS	Centre Aval de Traitement des Données SMOS
CLIVAR	Climate Variability and Predictability
CMAP	CPC Merged Analysis of Precipitation
CNES	Centre National d'Etudes Spatiales
CONAE	Comisión Nacional de Actividades Espaciales
CORE	Coupled Ocean-Atmosphere Response Experiment
CPC	Climate Prediction Center
CTCZ	Continental Tropical Convergence Zone
CT	Conductivity-Temperature
CTD	Conductivity-Temperature-Depth
DFS	Drakkar Forcing Set
DMI	Dipole Mode index
EBOB	Effects of Bay of Bengal Freshwater Flux
ECMWF	European Center for Medium range Weather Forecast
EICC	East Indian Coastal Current
ENSO	El-Niño Southern Oscillation
ENVISAT	Environmental Satellite
EOF	Empirical Orthogonal Function
ERA I	ERA Interim Reanalysis
ERS	European Remote Sensing (satellites)
ESA	European Space Agency
GB	Ganges-Brahmaputra

GD	Godavari
GDAC	Global Data Acquisition centers
GEKCO	Geostrophic and Ekman Current Observatory
GEOSAT	GEOdetic SATellite
GPCP	Global Precipitation Climatology Project
IIOE	International Indian Ocean Expedition
IR	Irawaddy
INCOIS	Indian National Centre for Ocean Information Systems
INDEX	Indian Ocean expedition
IndOOS	Indian Ocean Observing System
IO	Indian Ocean
IOD	Indian Ocean Dipole
NIOP	Netherlands Indian Ocean Program International Maritime
INMARSAT	Satellite Organization
ISCCP	International Satellite Cloud Climatology Project
ITCZ	Inter Tropical Convergence Zone
JGOFS	Joint Global Ocean Flux Study
KR	krishna
MH	Mahanadi
MIRAS	Microwave Imaging Radiometer using Aperture Synthesis
MLD	Mixed Layer Depth
MONTBLEX	Monsoon Trough Boundary Layer Experiment
NASA	National Aeronautics and Space Administration
NEMO	Nucleus for European Modelling of the Ocean
NIOA	North Indian Ocean Atlas climatology
ODIS	Ocean Data Information Systems
OGCM	Ocean general circulation model
OMM	Ocean Mixing and Monsoon
OMNI	Ocean Moored buoy Network for Northern Indian Ocean
OPA	Océan Parallélisé
PC	Principal Component
PO.DAAC	NASA's Physical Oceanography Distributed Active Archive Center

RAMA	Research Moored Array for African-Asian-Australian Monsoon Analysis and Prediction
RFI	Radio frequency interference
RMSD	Root Mean Square Difference
SLA	Sea level Anomaly
SMAP	Soil Moisture Active and Passive
SMOS	Soil Moisture and Ocean Salinity
SSH	Sea Surface Height
SSM/I/S	Special Sensor Microwave/Imager
SSS	Sea Surface Salinity
SST	Sea Surface Temperature
STD	Standard deviation
TAO	Tropical Atmosphere Ocean
TCs	Tropical Cyclones
TOGA	Tropical Ocean Global Atmosphere
TOPEX	Ocean Topography Experiment
TRITON	TRIangle Trans-Ocean buoy Network
TRMM	Tropical Rainfall Measuring Mission
TSG	Thermosalinograph
TVD	Total Variance Diminishing
WOA	World Ocean Atlas 2009
WOCE	World Ocean Circulation Experiment
WOD	World Ocean Database 2009
XBT	eXpendable BathyThermograph
XCTD	eXpendable Conductivity-Temperature-Depth

# Chapter 1

## Introduction

---

### 1.1. General Introduction

#### 1.1.1. Particularities of the Indian Ocean climate

The Indian Ocean (IO) has a unique geographical setting, being the only tropical basin to be bounded by a continental landmass to the north. The Eurasian land mass offers a striking contrast to the IO further south, much of it being extremely arid and exhibiting a very steep orography. The differential heating between the Eurasian land mass and the ocean to the south results in a strong monsoonal wind forcing that reverses seasonally in the northern IO, i.e. the southwest monsoon that blows from the southwest towards the northeast in boreal summer and the northeast monsoon that blows in the opposite direction in boreal winter (Figure 1.1). The anchoring of the rising branch of the Walker circulation over the maritime continent also prevents the formation of steady equatorial easterlies. As opposed to the Atlantic or Pacific oceans, there is therefore no permanent upwelling in the eastern part of the basin. In contrast, upwelling occurs in the northwestern part of the basin, along the coasts of Oman and Somalia in response to the wind monsoonal forcing (Figure 1.1). This absence of climatological upwelling in the eastern IO explains why a large part of this basin displays Sea Surface Temperatures (SST) exceeding 28°C (Figure 1.1), the threshold for deep atmospheric convection [Graham and Barnett, 1987]. This tropical basin therefore accounts for a non-negligible part of the Indo-Pacific warm pool extension and is prone to very active air-sea interactions across a variety of time scales.

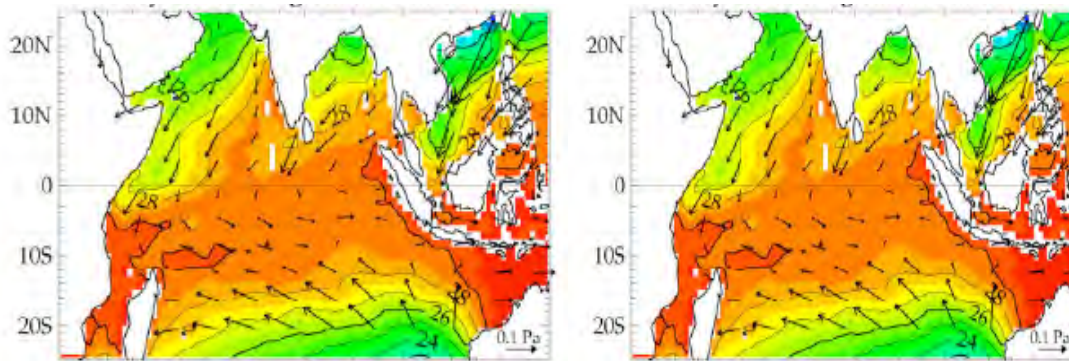


**Figure 1.1.** Maps of Quickscat windstress and TMI SST during (**top**) January and (**bottom**) July. [Taken from Vialard, *Habilitation à Diriger les Recherches*, 2009]

The IO is also the only ocean with a low-latitude opening at its eastern boundary i.e. low-latitude exchange of water between the Indian and Pacific oceans through the Indonesian archipelago. It gains additional heat from the tropical Pacific via the Indonesian throughflow, but has to evacuate the heat gained from both the atmosphere and Indonesian throughflow towards the south. The IO is also biogeochemically unique, having one of the three major open ocean oxygen minimum zones in the eastern Arabian Sea (AS) and Bay of Bengal (BoB) [Morrison *et al.*, 1999]. Upwelling of this oxygen-depleted water leads to the formation of the world's largest natural low-oxygen zone over the continental shelf off the Indian west coast. This oxygen deficiency has intensified in recent years and strongly impacted biology and living resources, including a sharp decline in demersal fish catch, more frequent episodes of fish mortality and a shorter fishing season.

### **1.1.2. A brief historical overview of IO circulation knowledge**

The IO was the least known among the world ocean prior to 1960's because of the lack of in-situ observations. The International Indian Ocean Expedition (IIOE; 1960-1965) led to an unprecedented amount of data collection in this region. This basin wide survey resulted in a comprehensive atlas [Wyrtki, 1971, reprinted in 1988], which forms a major reference for the IO research, and revealed several important features like the SST cooling in the western AS and the appearance of a strong current boundary current offshore the Somalia coast in response to the summer monsoon forcing [Swallow and Bruce, 1966]. The next intensive expedition took place a decade

later (INDEX, 1976-1979) and allowed to assess the physical response of the Somali current to the summer monsoon [e.g. Swallow et al., 1983] and provided a first description of the associated biogeochemical response [Smith and Codispoti, 1980]. In the following decade, many regional studies were conducted on boundary currents, focusing on the Somali current [e.g. Swallow et al., 1988; Swallow et al., 1991; Schott et al., 1988] or the west Australian boundary circulations [e.g. Smith et al., 1991]. At the same time, considerable additional data were collected, including XBT from volunteer observing ships, GEOSAT satellite altimetry [e.g. Perigaud and Delecluse, 1992], and surface drifter studies [Molinari et al., 1990]. The next cycle of investigations began with the Netherlands Indian Ocean Program (NIOP, 1992-1993), as part of the international Joint Global Ocean Flux Study (JGOFS), which focused on the western AS and Oman upwelling [e.g. Weller et al., 1998; Lee et al., 2000; Flagg and Kim, 1998; Shi et al., 2000]. The World Ocean Circulation Experiment (WOCE), implemented at about the same time, had a much wider geographical coverage in the IO and allowed to considerably increase the number of high quality IO observations.

These early programs largely focused on the AS, paying less attention to the BoB hydrography. The first notable coordinated efforts to monitor the BoB is the Bay of Bengal Monsoon Experiment (BOBMEX-99), followed by the Bay of Bengal Process Study (BOBPS, 2000-2006), which may be viewed as a follow-up to the JGOFS AS efforts. These programs focused on the BoB provided valuable insights on the coupled ocean-atmospheric processes associated with the intraseasonal modes and on the influence of the riverine inputs on the upper-ocean characteristics in the Bay. The discovery of an intrinsic mode of variability in the IO in the late 90's, the Indian Ocean Dipole, also fosters the design of a plan for the IO Observing System (IndOOS), which eventually led to the Research Moored Array for African-Asian-Australian Monsoon Analysis and Prediction (RAMA) [McPhaden et al., 2009], a system of moored observation buoys in the IO that collects meteorological and oceanographic data, similar to the basin-wide observing systems developed two decades earlier in the Pacific and Atlantic Oceans. Along with this array, the success of the Argo program [Roemmich et al., 1999], the network of Moored Buoy Network in Northern Indian Ocean (OMNI), frequently repeated ship based observations, satellites data and regional programs in the IO considerably increased the number of process studies in this basin in the last decade. The oceanographic research in the BoB

is now truly exploding, with programs such as the Continental Tropical Convergence Zone (CTCZ), the Air-Sea Interactions in Northern Indian Ocean/Ocean Mixing and Monsoon (ASIRI-OMM) and Effects of Bay of Bengal Freshwater Flux on Indian Ocean Monsoons (ASIRI-EBOB) programs that aimed at understanding the atmospheric convection and its interactions with the upper ocean characteristics in the BoB.

### 1.1.3. The BoB haline structure and its climatic consequences

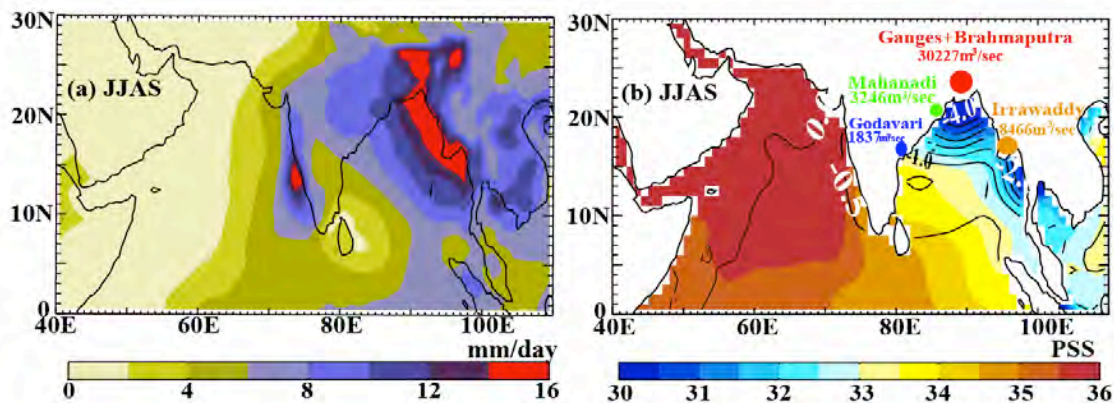


**Figure 1.2.** Summer (June–September) climatology of (a) GPCP [Huffman *et al.*, 1997] rainfall (b) North Indian Ocean Atlas climatology [Chatterjee, *et al.*, 2012] Sea Surface Salinity (SSS, shaded), SSS minus salinity at 50 m depth (contours). The dots indicate the locations of major river mouths; the radius of each is proportional to the magnitude of mean fresh water outflow ( $\text{m}^3/\text{s}$ ). The annual mean outflow is indicated, for each river.

The Indian peninsula divides the northern IO into two adjacent seas, the AS and BoB (Figure 1.2a). Compared to other low-latitude seas, the AS and BoB are very peculiar basins because they are surrounded by landmasses and hence under a marked continental influence. Despite their similar geographical setting and latitude range (i.e. similar incoming solar radiation at the top of the troposphere), those two basins exhibit contrasted ocean physical characteristics. The AS is a concentration basin (i.e. evaporation exceeds precipitation) and receives high saline water from the Red Sea and from the Persian Gulf, making the salinity of the upper layer rather high (Figure 1.2b). In contrast, heavy precipitation (Figure 1.2a) and large river runoffs lead to a fresher upper layer over the BoB (Figure 1.2b). The low salinity surface waters lay above much saltier water (33–34.5 units, depending on the location) below 50 m, resulting in sharp near-surface haline stratification there (Figure 1.2b).

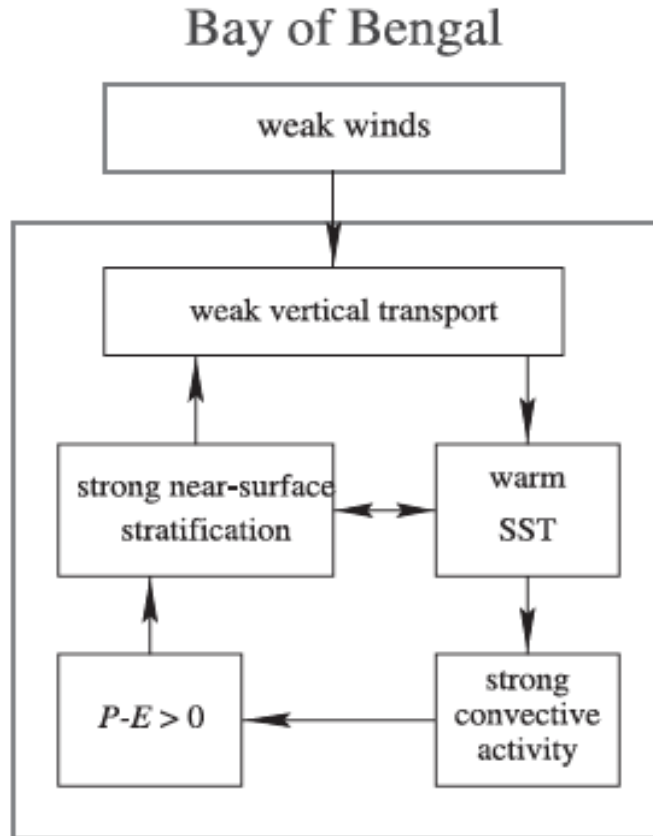


**Figure 1.3.** A schematic of the feedback cycles that lead to the BoB being warmer and sustaining organized convection in the atmosphere, leading to the large number of low-pressure systems that form in the northern bay. [Taken from *Shenoi et al., 2002*]

This very strong near-surface halocline in the BoB potentially plays a strong role in the Northern IO climate [*Shenoi et al., 2002*]. It strengthens the density stratification and usually results in a shallow mixed layer [*Mignot et al., 2007; Thadathil et al., 2007; Girishkumar et al., 2013*]. Combined with a homogeneous thermal stratification, this often results in the formation of a barrier layer, the layer between the base of the mixed layer and the top of the thermocline [*Lukas and Lindstrom, 1991*]. This BL prevents the vertical exchanges of momentum and heat between the upper mixed layer and the thermocline, thus inhibiting entrainment cooling of the mixed layer. This results in high SST throughout the basin [*Shenoi et al., 2002; de Boyer Montégut et al., 2007*], which almost permanently remains above the 28°C threshold for deep atmospheric convection [*Gadgil et al., 1984*]. The schematic provided on Figure 1.3 illustrates the positive feedback cycle that leads to warm SST and sustaining organized atmospheric convection in the BoB: the haline structure favours high SST, and hence deep atmospheric convection and rain that reinforce the haline stratification.

The salinity stratification may also impact the intensity of tropical cyclones (TCs) that develop over the BoB [Sengupta *et al.*, 2008; Neetu *et al.*, 2012]. The BoB is indeed home to 5% of the total annual number of cyclones worldwide [Alam *et al.*, 2003]. Because of the high population density along coastal areas and the poor disaster management, most of the TCs have catastrophic impacts. TCs cool the ocean surface under their tracks, which reduces the enthalpy flux to the atmosphere and hence tends to inhibit further TCs intensification [Cione and Uhlhorn, 2003]. Neetu *et al.* [2012] further demonstrated that surface cooling induced by cyclones is about three times larger during pre-monsoon season than during post-monsoon season in the BoB because the post-monsoon season exhibits a deeper thermal stratification combined with a considerable upper-ocean freshening that strongly inhibits surface cooling induced by vertical mixing underneath cyclones. They further showed that the haline stratification explains a large part of the cooling inhibition offshore of northern rim of the Bay, where salinity seasonal changes are the strongest. Freshwater from monsoon rain and river runoff may influence the intensity of the strongest cyclones in the BoB through their influence on the amplitude of cyclone-induced cooling. Finally, this salinity stratification may also influence the amplitude of intraseasonal variability of the SST [Vinayachandran *et al.*, 2012] and biological productivity regimes [Prasanna Kumar *et al.*, 2002].

These potentially strong impacts of haline stratification in the BoB on the mean climate of the region or on air-sea interactions below TCs call for a precise description and understanding of the sea surface salinity (SSS) spatial structure and temporal variability within the Bay. **This thesis aims at studying the variability of near-surface salinity in the BoB and its driving processes, making use of several data sources, i.e. *in-situ* observations, remote sensing data and an ocean model.** In the following, we will hence focus on the BoB, describe how it is forced by the atmosphere and what is known about its oceanic variability.

## 1.2. The BoB climate variability

### 1.2.1. Geography of the BoB

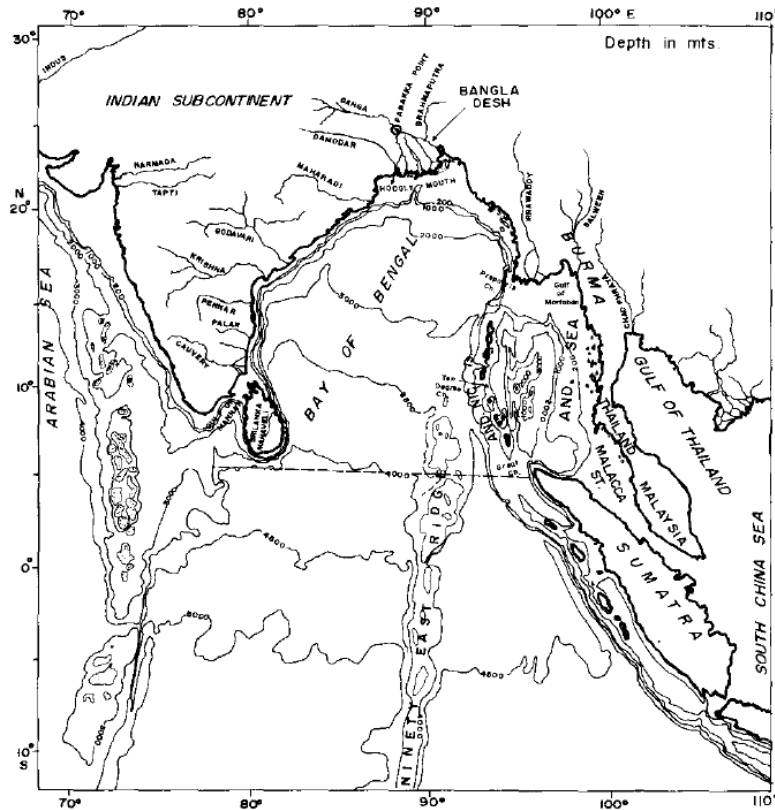


**Figure 1.4.** Map of BoB and surrounding oceanic and land areas. [Taken from Varkey *et al.*, 1996]

The BoB is the northeastern arm of the IO, located between 6°N and 23°N and 80°E and 100°E. It occupies about  $2.2 \times 10^{12} \text{ m}^2$  with an average depth of 2600 m. It is bounded to the west by the east coasts of Sri Lanka and India, on the north by the deltaic region of the Ganges-Brahmaputra river system, and on the east by the Myanmar peninsula. The southern boundary opens towards the IO (Figure 1.4) and lays at 6°N based on the geostrophic current structure [Varkey, 1986]. The topography is conical in shape with its wider (~2000 km) and deeper (~4000 m) end towards south and narrower and shallower end towards north. A thick uniform abyssal plain occupies almost the entire BoB gently sloping southward, which are dissected at many places by the underwater valleys. A chain of Islands, the Andaman and Nicobar Islands with complex bottom topography enriches the southeastern side of the Bay. This separates the rest of the BoB from a semi-enclosed sub-basin, the Andaman Sea. The BoB is also fed by a the freshwater influx from a number of large rivers – the Ganges and its distributaries such as Padma and Hooghly, the Brahmaputra and its distributaries such

as Yamuna and Meghna, other rivers such as the Irrawaddy, Godavari, Mahanadi, Krishna and Cauveri. The continental shelves along the east coast of India are very narrow (< 45 km), but along the mouths of the Ganges and Irrawaddy are very wide (> 200 km).

### **1.2.2. Seasonal timescales**

The northern IO climate is well known for its large seasonal cycle, associated with reversing monsoonal circulations [e.g. *Schott et al.*, 2002]. The northern IO climate is usually divided into four seasons: the summer monsoon, the winter monsoon, and two inter-monsoon seasons in fall and spring. The seasonal variability of air-sea fluxes and of the upper ocean responses are respectively discussed in Sections 1.2.2.1 and 1.2.2.2.

#### **1.2.2.1. Atmospheric variability**

##### **(a) Wind**

The BoB is forced locally by seasonally reversing monsoon winds and remotely by the winds in the equatorial IO [*McCreary et al.*, 1993]: we will hence not only focus on the BoB when describing wind forcing but discuss it for the entire northern IO. The northeast (i.e. Winter) monsoon drives the climate of the northern IO during the northern hemisphere winter (December - March). It is characterized by high pressure over the Asian land mass. Consequently, the monsoon winds are directed away from the Asian continent, causing northeasterly wind stresses over the AS and BoB (Figure 1.5a). The northeast monsoon winds are strong, with a speed exceeding 4 m/s in the western AS and in the central BoB. The winds are more northerly in head of the AS and BoB, and more easterly in the Andaman Sea (Figure 1.5a). The northeast monsoon advects dry continental air over the ocean, and is the dry season for most of southern Asia.

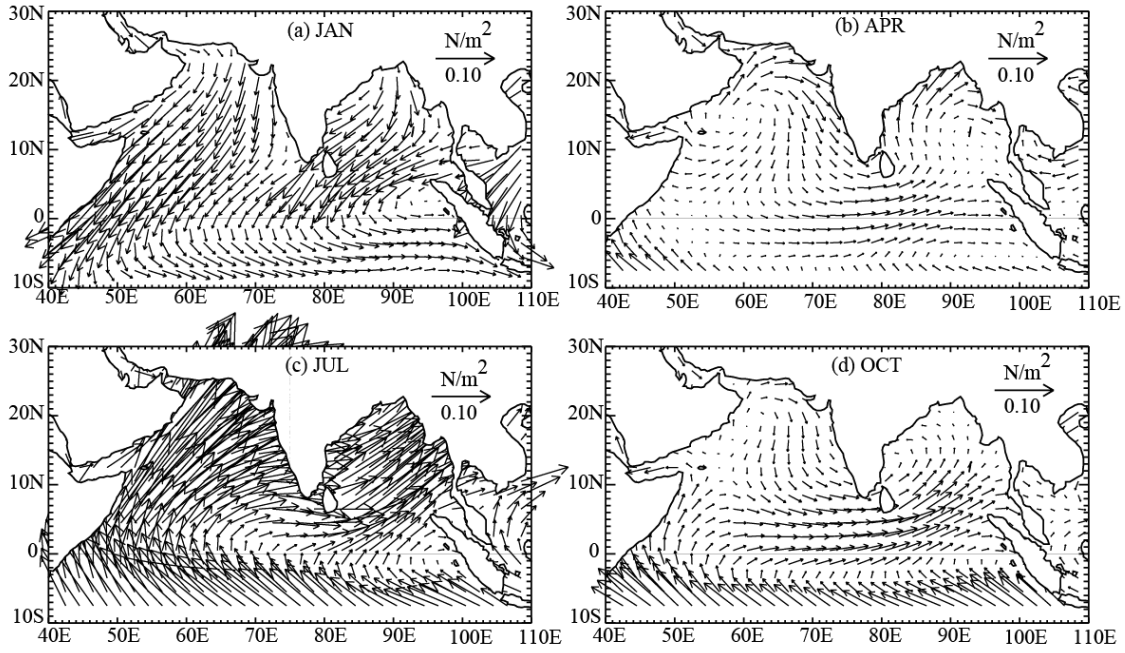


**Figure 1.5.** Monsoon wind stress fields from the Tropflux [Praveen Kumar *et al.*, 2012] climatology for (a) January, (b) April, (c) July, (d) November.

The surface wind field reverses (Figure 1.5c) and strengthens with wind speed exceeding 6 m/s during the height of summer monsoon (June/July/August). This wind reversal is due to large-scale northward migration of the inter-tropical convergence zone (ITCZ) in response to differential heating between land and sea. The southwest or summer monsoon drives the climate of the northern IO during the northern hemisphere summer (June - September). During the summer season, there is a continuation of the southern hemisphere trade winds into the AS in the form of a narrow atmospheric jet, the Findlater Jet [Findlater, 1971]. During the summer monsoon the wind over the western AS is twice as strong as over the BoB. The summer monsoon winds are much stronger than the winter monsoon winds and hence the annual mean winds over the northern IO are southwesterly [Shenoi *et al.*, 2002].

The periods between the two monsoons are the transition phases, characterised by weak winds (Figure 1.5b, d). During the transition phases, winds are mainly anticlockwise in the BoB.

### (b) Heat flux

The net heat flux through the ocean surface ( $Q_{sf}$ ) can be written as

$$Q_{sf} = R_s + R_l + Q_l + Q_s$$

Where  $R_s$  is the net shortwave radiation,  $R_l$  is the net longwave radiation,  $Q_l$  the

latent heat flux, and  $Q_s$  the sensible heat flux through the surface. The climatological evolution of surface fluxes over the BoB is shown on Figure 1.6.  $R_s$  and  $Q_l$  display a bimodal distribution.  $R_s$  is minimum during the summer monsoon (owing to clouds) and during winter (when maximum shortwave flux at the top of the atmosphere has moved to the southern hemisphere).  $Q_l$  is maximum during the onset of the summer monsoon in June, when the winds strengthen and humidity increases rapidly in the lower troposphere, and during winter, when the winds are weaker but near-surface humidity is low. Due to the low-latitude position of the BoB, the net surface heat gain  $Q_{sf}$  is generally positive, except during December–January, when it is negligible. The heat flux distribution displays a semi-annual cycle largely set by  $Q_{sf}$  and  $Q_l$  seasonal evolution, with monthly averages ranging from 0 to  $120 \text{ W/m}^2$  [Rao and Sivakumar, 2000; Shenoi et al., 2002; de Boyer Montégut et al., 2007]. The minimum ocean heat gain therefore occurs during the peaks of winter (under the influence of dry and cold northeasterly winds) and summer monsoon (due to strong wind and high nebulosity) seasons. As a result of light wind and clear sky, the maximum ocean heat gain occurs during the monsoon transition periods.  $R_l$  displays weaker seasonal variation, with a minimum during the summer monsoon due to the greenhouse effect induced by increased humidity and cloudiness.

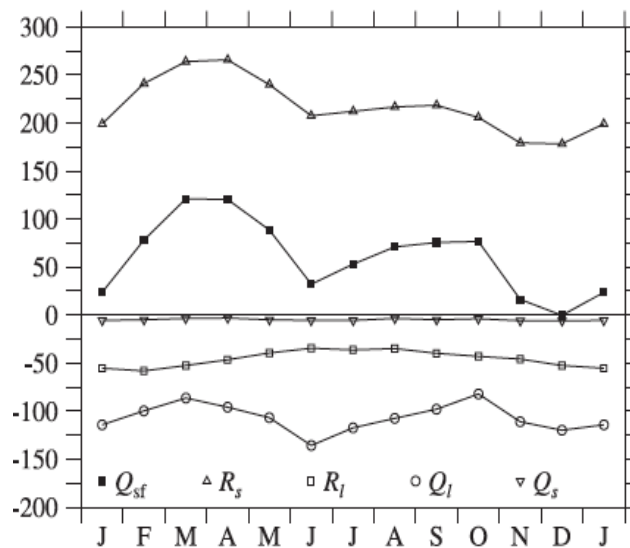
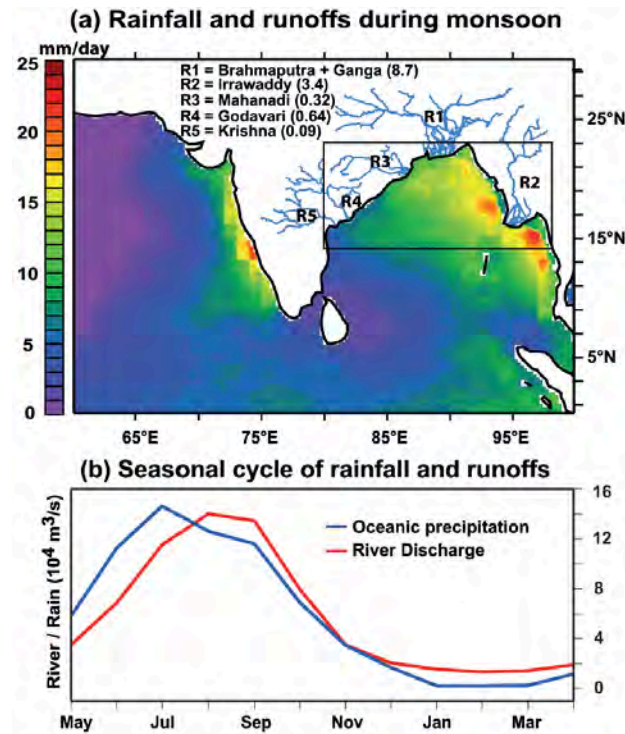


Figure 1.6. The heat budget of the upper ocean in the BoB. [Taken from Shenoi et al., 2002]

### (c) Fresh water Flux (precipitation, runoff)

The BoB is a dilution basin, due to large seasonal fresh water fluxes from rivers [Subramanian, 1993] as well as excess precipitation over evaporation [Prasad,

1997]. The cross-equatorial low-level winds over the western IO/east African highland and a westerly flow extending from the AS to the south China Sea result in a strong moisture flux toward the Asian landmass, initiating precipitation there (Figure 1.7a). The orographic structure of the Asian landmass provides anchor points where the maximum monsoon rainfall is concentrated, especially along the Western Ghats and the Burmese coast (Figure 1.7a).



**Figure 1.7.** (a) Average climatological rainfall from July to September ( $\text{mm day}^{-1}$ ) from Tropical Rainfall Measuring Mission (TRMM) 3B42 data. The major rivers in the northern BoB are drawn on the map and their average river discharge during July to September ( $10^4 \text{ m}^3 \text{ s}^{-1}$ ) is indicated. (b) Average freshwater flux into the BoB ( $10^4 \text{ m}^3 \text{ s}^{-1}$ ) north of  $14^\circ\text{N}$  from rainfall over the ocean (blue curve) and the major rivers (red curve) indicated in (a). [Taken from Chaitanya et al., 2014a]

As a consequence of the continental precipitation during the southwest monsoon, a large fraction of the runoff to the ocean occurs during or shortly after the summer season, and contributes to the freshwater flux into the northern BoB in roughly equal proportion with rainfall over the ocean (Figure 1.7b). All the major rivers flowing into the Bay exhibits their maximum discharge from July to September (Figure 1.8). The largest rivers that flow into the BoB are the Ganges-Brahmaputra and the Irrawaddy (Figure 1.7a), which mean discharge at the river mouths amounts respectively to  $\sim 8.7 \times 10^4 \text{ m}^3 \text{ s}^{-1}$  and  $\sim 3.4 \times 10^4 \text{ m}^3 \text{ s}^{-1}$  during July-September (Figure 1.8a) [Papa et al., 2012; Dai and Trenberth, 2002]. Three other smaller rivers on the

East Indian coast (Mahanadi, Godavari and Krishna) together contribute to  $\sim 10^4 \text{ m}^3 \text{ s}^{-1}$  (Figure 1.8b). As a result, these five river systems bring on average a total of  $\sim 1100 \text{ km}^3$  of continental freshwater into the BoB between July and September.

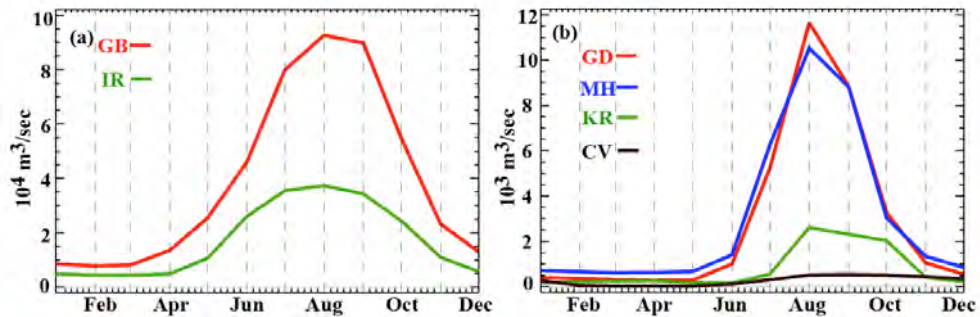


**Figure 1.8.** Seasonal cycle of the (a) Ganga-Brahmaputra (GB) and Irrawady (IR) (b) Godavari (GD), Mahanadi (MH), Krishna (KR) and Cauvery (CV). [Papa *et al.*, 2012; <http://www.india-wris.nrsc.gov.in/>]

The yearly freshwater flux received by the BoB largely exceeds the freshwater flux evaporated back to the atmosphere [Shenoi *et al.*, 2002; Sengupta *et al.*, 2006]. Just like Precipitation (**P**) and river runoff (**R**), evaporation (**E**) exhibits a very well defined seasonal variability [Rao and Sivakumar, 2003], displaying a semi-annual cycle with maxima during summer monsoon (strong winds) and winter monsoon (strong winds and dry air) seasons (cf Section 1.2.2.1b). On the other hand, both **P** and **R** display single seasonal peaks during July and August respectively. The residual of  $\mathbf{P+R-E}$  is positive (Figure 1.9) almost throughout the year, maximum during the peak of the summer monsoon.

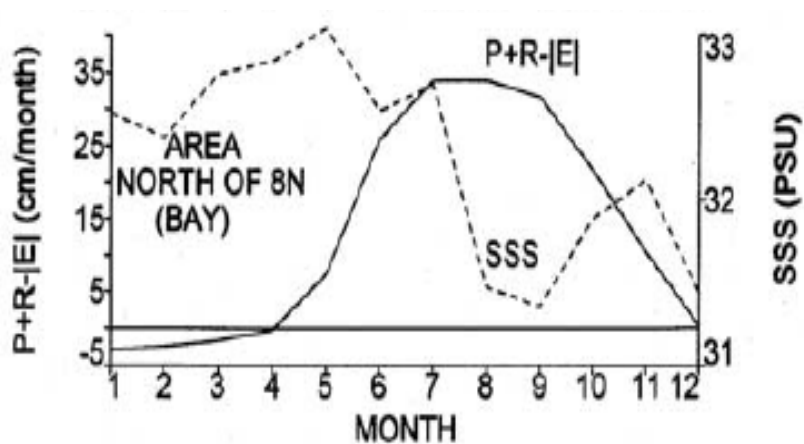


**Figure 1.9.**  $\mathbf{P+R-E}$  and SSS for the entire BoB, North of 8N. [Taken from Rao and Sivakumar, 2003]

### 1.2.2.2. Oceanic Response

Annually reversing wind and remote forcing from the equator modifies the basin scale sea level signals in the BoB [e.g. *McCreary et al.*, 1993]. In the equatorial IO, two upwelling and downwelling Kelvin waves propagate eastward each year. These pairs of Kelvin waves reflect at the eastern boundary and propagate along the coastal waveguide of BoB as coastal Kelvin waves [*McCreary et al.*, 1993]. These Kelvin waves also trigger westward propagating Rossby waves into the interior BoB [*McCreary et al.*, 1996]. The downwelling observed at the southern tip of India in winter (Figure 1.10) is the result of remote forcing from the BoB, that has propagated counter clockwise along the coasts as a coastal Kelvin wave [*McCreary et al.*, 1993; *Samson et al.*, 2014]. The pronounced downwelling is opposed to the local alongshore wind. As stated above, the shallow thermocline along the eastern and northern rim of BoB (Figure 1.10) is the signature of a coastal Kelvin wave that emanates from an equatorial Kelvin waves forced by equatorial winds a couple of months before [*Samson et al.*, 2014]. This pronounced coastal upwelling starts three months before the local along shore winds start becoming upwelling favourable [*McCreary et al.*, 1996; *Shankar et al.*, 1996]. Sea level patterns in summer are usually opposite to those found during the winter season (not shown).

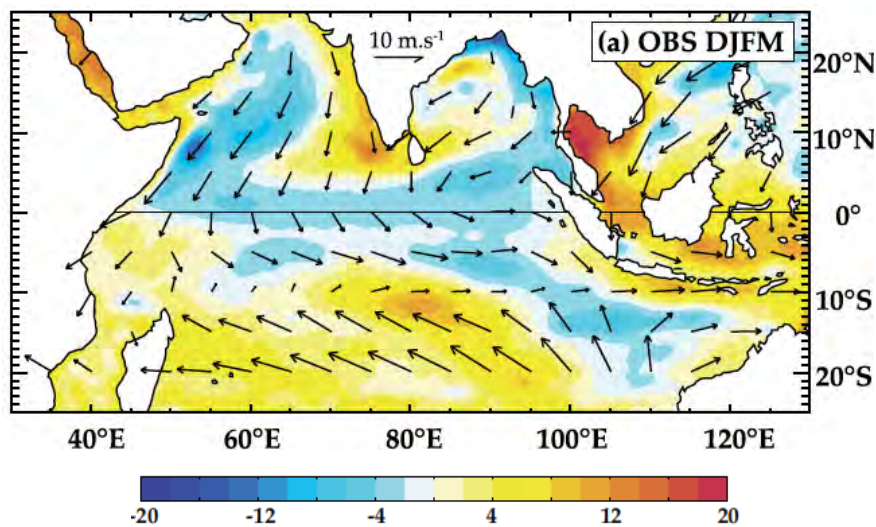


**Figure 1.10.** Winter (DJFM) climatology of sea level anomalies (color, in cm) and 10 m wind (vector). [Taken from *Samson et al.*, 2014]

The seasonal reversal of the wind also drives a reversal of most upper ocean currents north of 10°S, a unique feature among the three tropical oceans (Figure 1.11).

The monsoon currents include a large anticyclonic gyre in the BoB surface waters during the northern hemisphere winter. This gyre decays into intense eddies in spring [Chelton *et al.*, 2011] and then transitions into a weaker, cyclonic gyre by late summer. The western recirculation region of this flow is an intensified western boundary current, the East Indian Coastal Current (EICC). This is a major oceanic current in the BoB, as it is responsible for most of the surface and thermocline water transport in this basin [Schott and McCreary, 2001; Shankar *et al.*, 2002] and plays a key role in connecting the BoB with equatorial IO and AS [Shankar *et al.*, 2002; Durand *et al.*, 2009; Shenoi, 2010]. The EICC reverses seasonally, flowing northward before and during summer monsoon (Figures 1.11a and 1.11b and southward after summer monsoon (Figures 1.11 c and 1.11 d). Only during November–December and March–April the EICC forms a continuous flow between the northern BoB and the southeastern coast of Sri Lanka. Due to the remote forcing from the Equatorial IO and BoB interior, the EICC reverses several months before the wind reversal [Yu *et al.*, 1991; McCreary *et al.*, 1993, 1996; Shankar *et al.*, 1996]. The remote forcing together with local wind forcing and intrinsic oceanic instabilities modulate the spatio-temporal variability of the EICC [Durand *et al.*, 2009; Chen *et al.*, 2012; Cheng *et al.*, 2013].

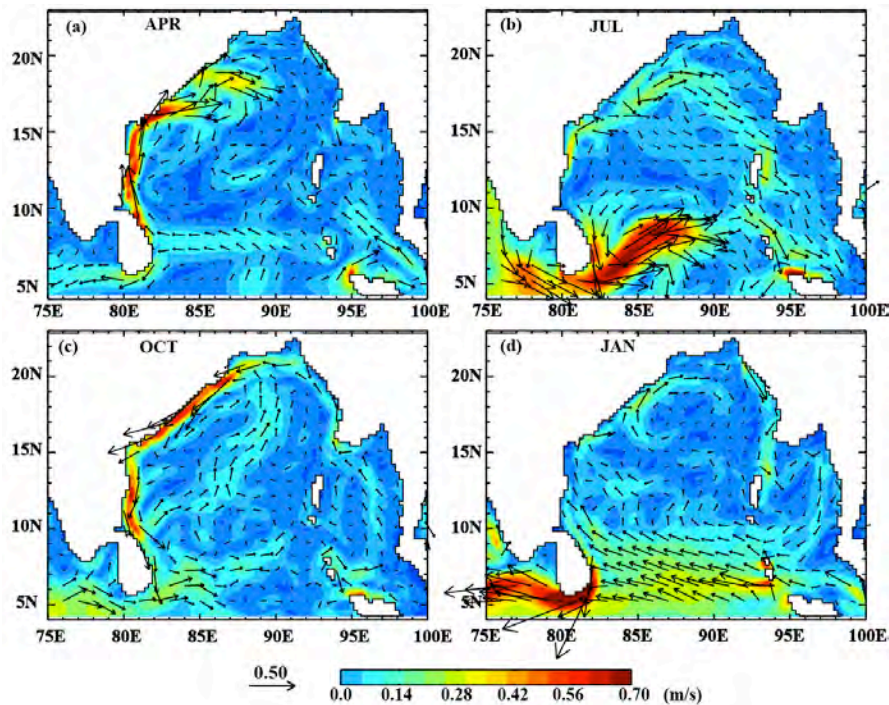


**Figure 1.11.** Climatological surface current vectors from GEKCO current [Sudre *et al.*, 2013] over the 2002-2007 period.

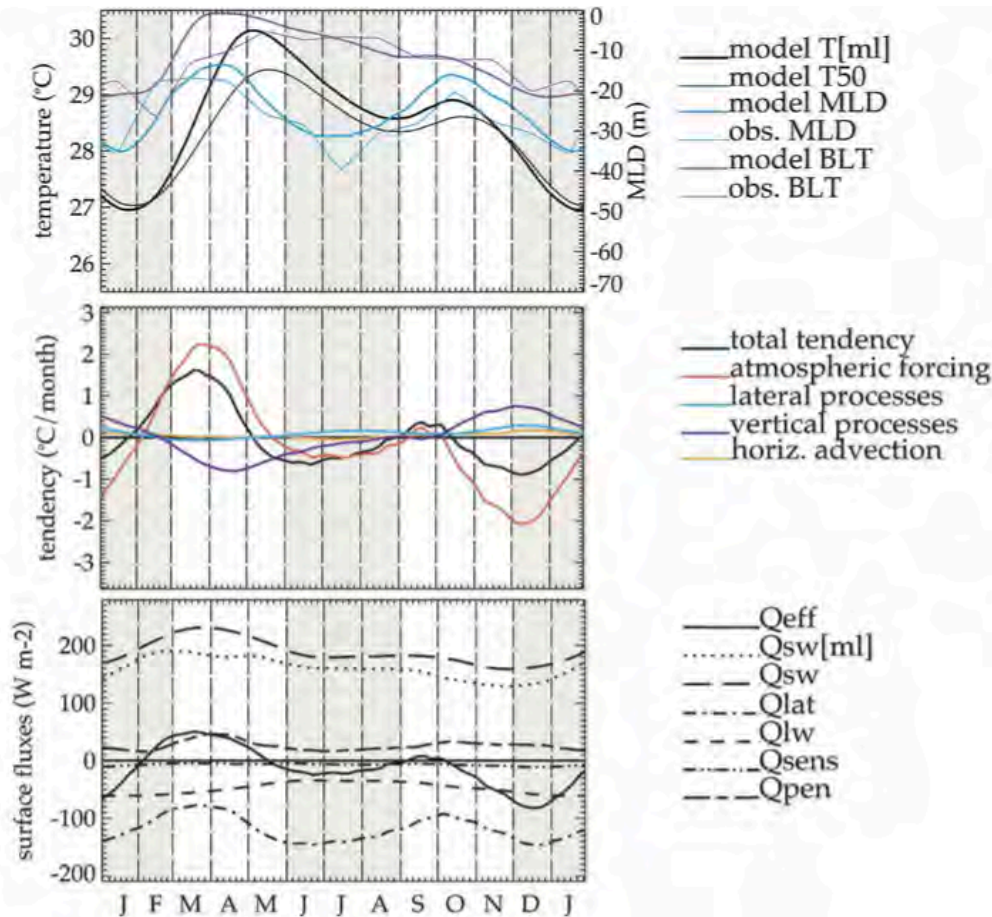


**Figure 1.12.** (Top) Mixed layer depth (MLD), mixed layer temperature ( $T_{ml}$ , a proxy for SST), temperature integrated over 0–50 m ( $T_{50}$ ), and barrier layer thickness (BLT) computed from ocean model simulation and MLD and BLT from observations [de Boyer Montégut et al., 2004]; (middle) SST seasonal tendencies in the mixed layer; and (bottom) surface heat fluxes (positive into the ocean), effective net heat flux in the mixed layer ( $Q_{eff} = Q_{net} - Q_{pen}$ ), net shortwave radiation flux in the mixed layer [ $Q_{sw}(ml)$ ], net shortwave radiation flux at the surface ( $Q_{sw}$ ), latent heat flux ( $Q_{lat}$ ), net longwave radiation flux ( $Q_{lw}$ ), sensible heat flux ( $Q_{sens}$ ), and penetrative solar heat flux [ $Q_{pen} = Q_{sw} - Q_{sw}(ml)$ ], in the BoB. [Taken from de Boyer Montégut et al., 2007]

Regarding the SST, the BoB displays a semi-annual cycle, with SST warming during intermonsoon and cooling during monsoon [Shenoi et al., 2002]. In the BoB, the SST seasonal cycle is essentially driven by atmospheric heat fluxes, with oceanic processes playing a secondary role (Figure 1.12). The net heat flux seasonal cycle is largely controlled by latent heat flux variations since the seasonally varying solar flux effect is damped by the effects of light penetration (incoming solar heat flux is weaker during the monsoon because of clouds, but the deeper mixed layer absorbs a larger fraction of the incoming flux). The transmitted solar heat flux indeed represents an average of  $28 \text{ W.m}^{-2}$  heat loss beneath the mixed layer over the year. In winter the cold, dry air advected southward from the continent drives strong latent heat losses,

resulting in a SST cooling in the northern BoB during this season. This buoyancy forcing results in convective mixing and the mixed layer deepens and entrain the warm subsurface water from the barrier layer (with a mixed-layer warming contribution of 2.1°C in the BoB when integrated over winter) [*de Boyer Montégut et al., 2007*]. Hence the SST in winter remains relatively high (above 27°C; Figure 1.12). During the spring intermonsoon, SST rises gradually as the sun moves poleward over the Northern Hemisphere and light winds result in weak evaporative cooling. As a result, the BoB becomes the warmest area among the world oceans [*Joseph, 1990*], with SST exceeding 30°C by May. The mixed layer shallows and penetrative solar radiation increases and reaches its maximum and heats subsurface water. With the onset of summer monsoon in June, SST decreases in the BoB as the result of strong winds (i.e. strong evaporative cooling, latent heat loss). Decrease of solar heat flux due to high cloud cover also decreases the SST. Freshening due to precipitation and runoff leads to surface salinity stratification and barrier layer development [*Thadathil et al., 2007*]. After the summer monsoon, i.e. in fall, the mixed layer shoals and BoB warms again due to weaker evaporative cooling. The barrier layer continues to strengthen [*de Boyer Montégut et al., 2007*]

### **1.2.3. Interannual timescales**

#### **1.2.3.1. Relevant interannual climate modes affecting the BoB**

The IO has long been viewed as largely passive, with interannual variations arising from remote forcing of El Niño - Southern Oscillation (ENSO). This vision has changed at the turn of the XXIst century with the discovery of a specific mode of climate variability in the IO referred to as the Indian Ocean Dipole (IOD) mode [e.g. *Saji et al., 1999; Webster et al., 1999*]. The interannual variability in the northern IO is therefore mainly driven by these two modes: ENSO through its remote signature over the IO and the direct impact of the IOD.

ENSO is the strongest mode of interannual climatic variability on Earth [e.g. *Wang and Picaut, 2004; McPhaden, 2004*]. It originates in the tropical Pacific and consists of two opposite phases, the warming phase called ‘El Niño’ and the cooling phase called ‘La Niña’, recurring approximately every 2-7 years. Its positive phase (El Niño) is characterized by warm SST anomalies in the central and eastern tropical

Pacific associated with enhanced deep atmospheric convection in the western and central Pacific. These SSTA usually appear in spring and amplify under the effect of the Bjerknes feedback [Bjerknes, 1969], a positive air–sea feedback loop in the tropical Pacific. ENSO usually lasts about one year (from late spring to late winter) and peaks toward the end of the year. ENSO is often described by the Niño3 or Niño3.4 indices, calculated as the averaged SST anomalies over the Niño3 (150°W–90°W, 5°N–5°S) or Niño3.4 region (170°W–120°W, 5°N–5°S).

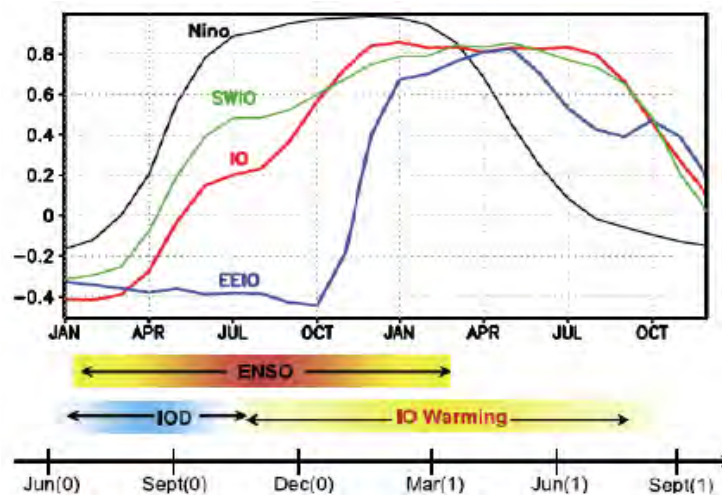


**Figure 1.13. (Top)** Correlation of November–January Niño3 index with SSTA averaged over the eastern equatorial Pacific (160–120°W, 5°S–5°N; black), the tropical IO (40–100°E, 20°S–20°N; red), the southwest IO (50–70°E, 15–5°S; green), and the eastern equatorial IO (90–110°E, 10°S–equator; blue). **(Bottom)** Seasonality of the major interannual IO climate modes, IOD and ENSO. [Taken from Schott *et al.*, 2009]

These ENSO-induced changes in deep atmospheric convection in the central Pacific have worldwide climatic impacts through atmospheric teleconnections [e.g. Trenberth *et al.*, 1998]. Within the tropics, most of the ENSO remote impacts occur through shifts of the Walker circulation. For example, the eastward shift of the Walker circulation during an El Niño induces anomalous subsidence, increased surface solar heat flux and reduced surface wind over the IO. As a result, the entire IO basin warms during an El Niño [Figure 1.13; Klein *et al.*, 1999; Ohba and Ueda, 2005; Xie *et al.*, 2009]. This warming peaks in winter and spring, and can last until early summer, two seasons after the peak of ENSO, possibly maintained by local air–sea interactions over the IO [Xie *et al.*, 2009; Du *et al.*, 2009]. The effect of ENSO on the Indian summer monsoon has also been noted [e.g. Walker, 1924; Gershunov *et al.*, 2001; Fasullo, 2004; Xavier *et al.*, 2007].

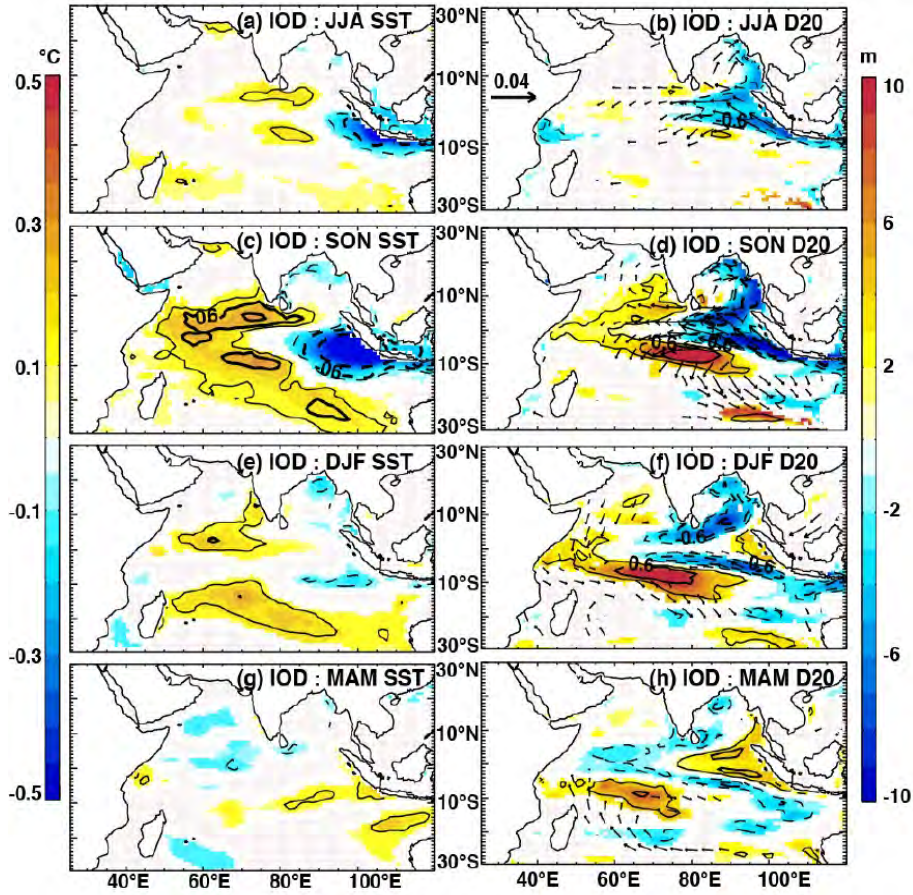


**Figure 1.14.** Partial regression coefficients of de-seasoned anomalies of SST (**left panels**), D20 (**colour; right panels**) and wind stress (**arrows; right panels**) as regressed onto the IOD index, with the influence of ENSO removed. Regression coefficients are computed for the 1961- 2001 period and are shown when beyond a 90% significance level. Thin, normal and thick contours indicate correlation coefficients of 0.4, 0.6 and 0.8 respectively. [Taken from *Currie et al.*, 2013]

The IOD is an independent mode of interannual variability that often co-occurs with ENSO. A positive IOD event is associated with cold SST anomalies off the coasts of Java and warm SST anomalies in the western IO, accompanied by anomalous easterlies in the central IO [Figure 1.14; e.g. *Saji et al.*, 1999; *Webster et al.*, 1999; *Murtugudde et al.*, 2000]. These wind and SST anomalies grow together in a positive feedback loop [*Reverdin et al.*, 1986; *Webster et al.*, 1999] similar to the Bjerknes feedback involved in ENSO development [*Bjerknes*, 1969]. Like ENSO, the IOD is phase-locked to the seasonal cycle. It develops during boreal summer, culminates in fall, and decays by the end of the year (Figure 1.14). The IOD is usually described by the Dipole Mode Index (DMI), i.e. the difference in SST anomalies between western tropical IO (50-70°E, 10°S-10°N) and southeastern tropical IO (90-100°E, 10°S-0°N). The wind signals associated with the IOD modulate the thermocline depth in most of

the tropical IO: the anomalous easterly winds raise the thermocline in the eastern part of the basin (Figure 1.14) and, together with off-equatorial Rossby wave responses, deepen the thermocline and warm the SST in the western IO, resulting in characteristic zonal anomaly patterns in sea level height, as well as surface and subsurface temperature structures (Figure 1.14) [e.g. *Feng and Meyers, 2003; Murtugudde et al., 2004; Rao et al., 2002*]. Thermocline anomalies typically initiate earlier and persist longer than the surface temperature signals [*Horii et al., 2008*]. Negative IOD events feature opposite anomalies over similar regions [*Meyers et al., 2007; Vinayachandran et al., 2002a*].

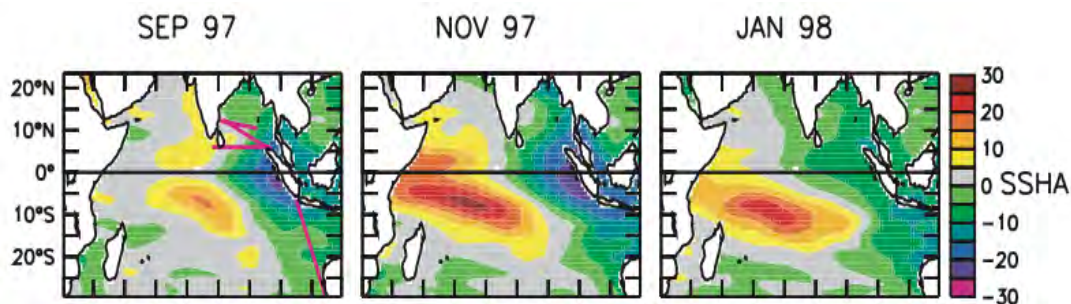


**Figure 1.15.** Evolution of Topex/Poseidon sea surface height anomalies (cm) during September 1997 (**first column**), November 1997 (**middle column**) and January 1998 (**right column**) [Taken from *Rao et al., 2002*]

These two interannual modes of variability (ENSO and IOD) not only influence the Equatorial IO but also strongly affect the hydrography of the BoB. *Shankar [1998]* first reported large negative sea level anomalies (SLAs) off the Indian east coast during 1961, one of the strongest positive IOD events on record. *Rao et al. [2002]* further demonstrated that the positive IOD in fall 1997 induced a negative SLA along the eastern rim of the Bay associated with an anomalous anticyclonic circulation in the BoB (Figure 1.15). Negative (resp. positive) SLAs have also been reported off the east coast during El Niño (resp. La Niña) events [*Han and Webster, 2002; Srinivas et al., 2005; Singh, 2002*]. However, due to the co-occurrence of ENSO with IOD events, these studies did not clearly distinguish the respective impact of these two modes on SLA in the BoB. The study of *Aparna et al. [2012]* addressed this issue and showed that these two modes have distinct SLA signatures, with IODs associated with a single SLA peak in fall along the rim of the Bay while ENSO exhibits weaker but multiple SLA peaks (April–December and November–July), with a relaxation between the two peaks. The northern IO response to IOD largely dominates the one to ENSO in terms of SLA [*Currie et al., 2013*] and mixed layer depth [*Keerthi et al., 2013*].

### 1.2.3.2. Interannual variability of freshwater fluxes

The patterns of precipitation over the BoB and adjoining continents [e.g. *Gadgil, 2003*] as well as the riverine freshwater supply to the BoB [*Papa et al., 2012*] vary significantly from year to year. The standard deviation of interannual variability of the summer monsoon rainfall amounts to approximately 10% of the long-term mean summer rainfall [*Gadgil, 2003*]. Precipitation in two regions, the “Western Ghats” and “Ganges-Mahanadi Basin”, accounts between 80-90% of the interannual variability of Indian continental summer rainfall [*Vecchi and Harrison, 2004*]. The year-to-year variability of the summer monsoon rainfall (Figure 1.16) is sufficient to trigger drought and flood conditions, with major agricultural, economic and social impacts [e.g. *Gadgil and Kumar, 2006*]. Many factors influence the variations of the summer monsoon precipitation on interannual timescales, including ENSO [e.g. *Pant and Parthasarathy, 1981; Rasmusson and Carpenter, 1982; Meehl, 1987; Webster and Yang, 1992*], the IOD [e.g. *Cherchi and Navarra, 2012*] and the snow cover on the Tibetan plateau and in Eurasia [e.g. *Blanford, 1884; Hahn and Shukla, 1976; Meehl, 1994; Shuen et al., 1998; Wu and Kirtman, 2003*]. Of these factors, the strongest association has been found with ENSO, although the relationship appears to have weakened in recent decades [*Kumar et al., 1999*].

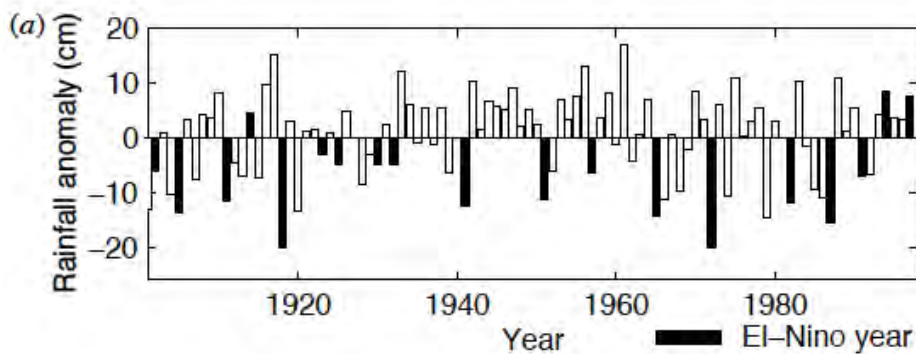


**Figure 1.16.** Interannual variation of the all-India summer monsoon rainfall during 1901–1998; the El Nino years are shaded. [Taken from *Gadgil, 2003*]

As we said already, the continental river discharges accounts for about half of the total freshwater received by the BoB [*Sengupta et al., 2006*]. Even though the spatiotemporal distribution of precipitation over the BoB is well documented [*Xie and Arkin, 1997; Adler et al., 2003; Hoyos and Webster, 2007; Rahman et al., 2009*], much less was known about the contribution of continental runoff. Recently, combining the

*in-situ* discharge datasets and the high-resolution satellite altimetry over rivers, *Papa et al.* [2010, 2012] produced interannual time series of total discharge of major rivers in the BoB over the 1993-2012 period. This river discharge dataset displays strong interannual variations of the Ganga-Brahmaputra river runoff (Figure 1.17), with a standard deviation of  $12500\text{m}^3/\text{s}$  [*Papa et al.*, 2010].

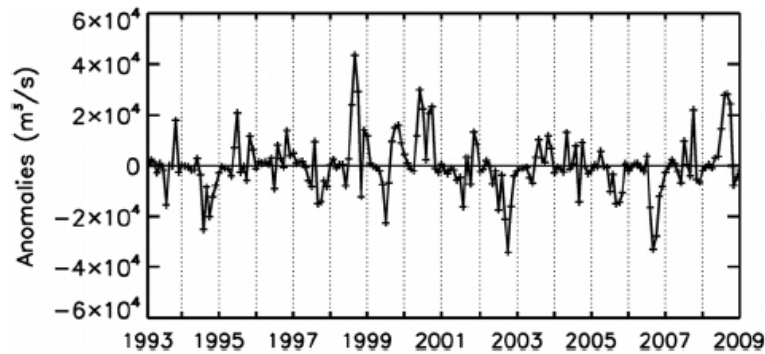


**Figure 1.17.** Deseasonalized anomalies (obtained by subtracting the 16 year mean monthly value from individual months) of the Ganga- Brahmaputra monthly river discharge at the river mouth for 1993–2008. [Taken from *Papa et al.*, 2010]

### 1.3. The BoB salinity

#### 1.3.1. Salinity observations

Over the recent years, the salinity observing network in the BoB has tremendously improved due to the advent of the Array for Real-Time Geostrophic Oceanography (Argo) [*Roemmich et al.*, 2009] program and the launch of satellite missions dedicated to the monitoring of SSS salinity. As this thesis makes an extensive use of these data, the salient features of the salinity observing network in the BoB is summarized below but will be described in more details in the next chapter.

##### 1.3.1.1. *In-situ* SSS observations and related climatologies

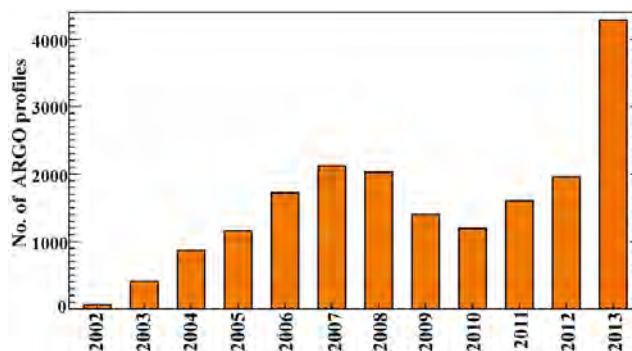


**Figure 1.18.** Evolution of yearly number of individual Argo profiles (<ftp.ifremer.fr/ifremer/argo>) from 2002 to 2013 over the BoB.

Historically, the BoB is a poorly sampled basin (except maybe during the first Indian Ocean International Expedition). From 2002 onwards, with the advent of Argo, the number of individual profiling floats has tremendously increased (Figure 1.18), improving the observational spatial coverage compared to the historical period. The *in-situ* observation dataset used in this thesis (Figure 1.19a) comprises all the available *in-situ* SSS measurements available over the BoB during the 2006-2014 periods and will be more extensively described in chapter 2. Its coverage remains however sparse along the coast and in the Andaman Sea (Figure 1.19). This is mainly because Argo profilers with a parking depth of 1000 m, cannot access the continent shelf, which is typically shallower than 200 m. Most of the data very close to the Indian coast consist of oceanographic cruises data.

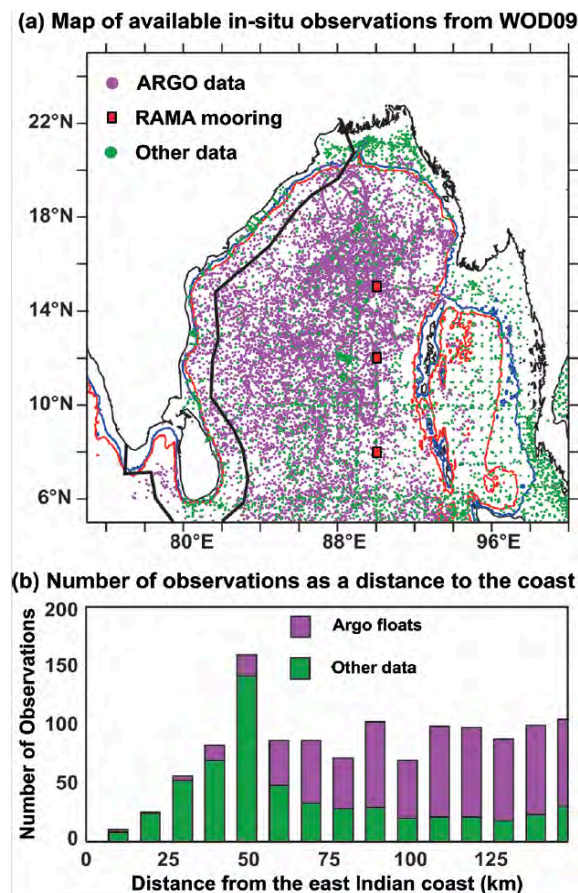


**Figure 1.19.** (a) Map of available SSS observations in the WOD09 [Boyer *et al.*, 2009] from Argo profilers (pink), RAMA moorings (red squares), and other datasets (green). The blue and red contours indicate ocean depths of 200 and 1000 m, respectively. The black contour delineates the area for which statistics are computed from (b) the number of observations in the western BoB as a function of the distance to the coast (in 10-km bins). Argo data are shown in pink and other datasets are shown in green. [Taken from Chaitanya *et al.*, 2014a]

The most accurate SSS climatology in the BoB is certainly the recent North Indian Ocean Atlas climatology (NIOA) [Chatterjee *et al.*, 2012], which is an improved version of World Ocean Atlas 2009 (WOA09) Climatology [Locarnini *et al.*, 2010; Antonov *et al.*, 2010]. This recent climatology includes all the data from the World Ocean Database 2009 (WOD09), complemented with Conductivity-Temperature-Depth (CTD) stations from Indian oceanographic cruises. An objective analysis gridding procedure (similar to that of WOA09), allows to fill the spatial data gaps and to smooth out the space scales shorter than 4°. The inclusion of the Indian oceanographic cruises database in NIOA considerably improves the data coverage in the periphery of the BoB compared with WOA09, especially along its western boundary [Chatterjee *et al.*, 2012].

### 1.3.1.2. Remote sensing initiatives

These *in-situ* measurements of salinity have recently been complemented by the development of remote-sensing capabilities of ocean surface salinity (Figure 1.20). The Soil Moisture and Ocean Salinity (SMOS) European mission [Mecklenburg *et al.*, 2008] launched in November 2009 and the Argentina/US Aquarius mission [Lagerloef *et al.*, 2008] operating since June 2011 both provide global SSS estimates. These satellites measure microwave radiations emitted from the earth surface, at wavelengths where surface emissivity is most sensitive to ocean surface salinity. If corrected accurately from the other effects that modulate this emissivity (sea surface temperature, atmospheric composition, sea state, etc.), this allows estimating the surface ocean salinity. These new spaceborne SSS measurements are routinely validated, with global root-mean-square errors around 0.3-0.4 pss for monthly Aquarius SSS fields on a ~150 km global grid [Lagerloef *et al.*, 2013] and for 10-days SMOS averages on a ~100 km grid in the tropical regions [Boutin *et al.*, 2012]. Recent research has demonstrated the value of these satellite missions in capturing open-ocean signals related to large-scale climate modes such as La Niña signature in the tropical Pacific [Hasson *et al.*, 2014], the IOD signature in the eastern part of this basin [Durand *et al.*, 2013] or planetary waves signature in the southern IO [Menezes *et al.*, 2014]. SMOS and Aquarius surface salinity products are still very new, and have not yet been thoroughly evaluated in many regions of the world. It therefore remains

unclear as to whether these satellite data can accurately capture SSS variations in relatively small basins surrounded by continental masses. The BoB, a semi-enclosed basin with a typical width of ~1000-2000 km, is indeed very challenging for satellite retrieval algorithms as the potential contamination of the SSS signal near land, such as radio frequency interference (RFI) linked to artificial sources (e.g. radars that emit in the frequency band of the instruments) and “land-induced” contamination on antenna side lobes [Reul *et al.*, 2012; Subrahmanyam *et al.*, 2013], could obscure climatically relevant signals there. The satellite remote sensing provides a unique opportunity to improve the monitoring of SSS variations. Hence, the arrival of these missions was a top ranking motivation for my PhD. One key advantage is their ability to sample regions that are devoid of observations.



**Figure 1.20.** Images of (Top) SMOS in orbit (from ESA), (Bottom) Aquarius in orbit (from NASA)

### 1.3.2. Seasonal SSS variations and related mechanism

Previous studies have investigated the seasonal variations of SSS in the BoB using both observations and models [Rao and Sivakumar, 2003; Shetye et al., 1991a, 1991b, 1993, 1996; Han et al., 2001; Vinayachandran et al., 2002b; Sengupta et al., 2006; Vinayachandran and Kurian, 2007; Benschila et al., 2014; Chaitanya et al., 2014a, 2014b]. Many of the above mentioned observational studies were based on hydrographic measurements along specific shipping lanes and dedicated cruises, or historical climatologies from before the Argo era, limiting the spatial and temporal coverage of salinity profiles available in BoB.

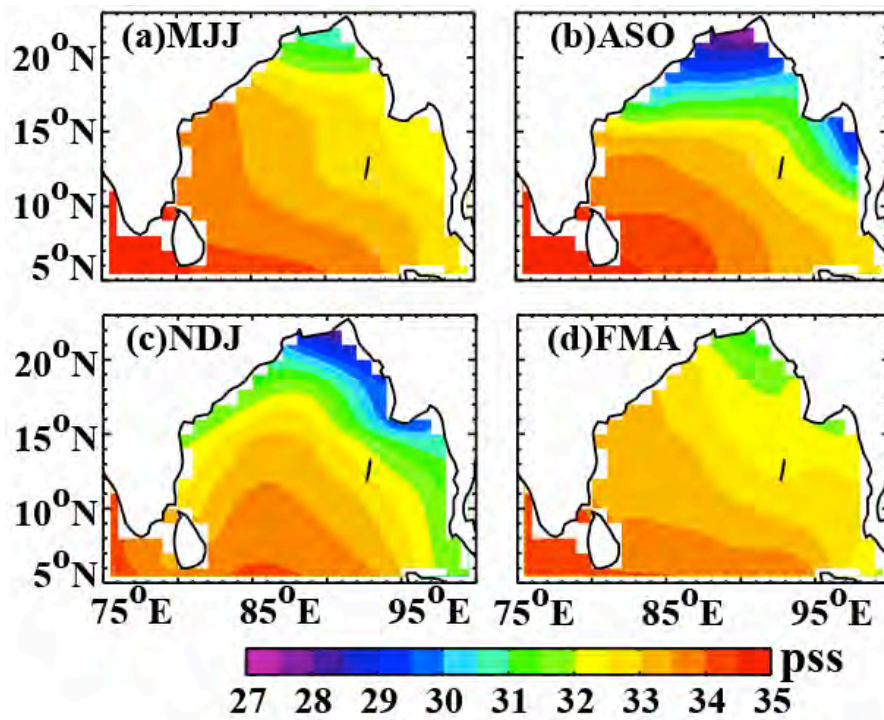


**Figure 1.21.** Climatological SSS from NIOA [Chatterjee et al., 2012] for (a) summer (MJJ), (b) autumn (ASO), (c) winter (NDJ), (d) spring (FMA).

The seasonal cycle of BoB salinity estimated by the NIOA climatology is displayed on Figure 1.21. The observed SSS field displays a contrasted pattern, with fresh waters in the northeastern BoB, and saltier waters in the central and southern basin. This large-scale gradient exists all year, but is seasonally modulated. During the pre-summer monsoon season (May–June–July), surface waters with salinity below 31 are restricted to the far northeastern BoB (Figure 1.21 a). During summer monsoon, the huge river runoff and excess precipitation lead to low-salinity water in the vicinity

of river mouths in the northern BoB [*Rao and Sivakumar, 2003*]. As discussed in Section 1.2.2.1(c), the freshwater supply varies strongly at seasonal timescale, with about 70% of the annual inflow (from precipitation and runoff) occurring during the summer monsoon north of 15°N. The observed freshening of the northern BoB in late summer clearly follows the seasonal maximum of precipitation in June and of river discharge in August. The role of freshwater forcing in the seasonal evolution of surface salinity has already been highlighted by several studies [e.g. *Shetye et al., 1996; Han et al., 2001; Sengupta et al., 2006*]. With the progression of summer monsoon, the surface waters freshen the northern part of the BoB, and the freshening expands southward (Figure 1.21b). This southward expansion is especially noticeable along the eastern and western boundaries of the BoB, with clear signatures along the East coast of India at 16N and in the southeastern BoB [*Rao and Sivakumar, 2003; Vinayachandran et al., 2005; Sengupta et al., 2006; Benschila et al., 2014*]. The southward flowing western boundary current (EICC) play a key role in the southward export of the fresh waters during this season [*Benschila et al., 2014; Chaitanya et al., 2014a*]. These fresh waters start retreating back northwards in the winter, to reach their minimal extent in the spring.

Several modelling studies provided some understanding of the impacts of the freshwater forcing on the upper BoB [*Howden and Murtuggude, 2001; Han and McCreary, 2001; Han et al., 2001; Yu and McCreary, 2004*]. They concluded that river runoff is the dominant factor in freshening the northern part of the bay during the southwest monsoon and that lateral advection is largely responsible for the spreading of this fresh water along the east coast of India and into the AS. Most previous numerical modeling studies discussing the mechanisms of BoB SSS variability however used a relaxation toward the observed surface salinity climatology. While this strategy allows keeping the surface salinity realistic [e.g. *Diansky et al., 2006; Wu et al., 2007; Sharma et al., 2010; Nyadjro et al., 2011*], the relaxation term act to artificially compensate any error in the forcing or in the model physics. The relaxation term is sometimes strong in some locations of the BoB, so that it may be hazardous to infer robust conclusions about the mechanisms of SSS variability [*de Boyer Montegut et al., 2005*]. The aforementioned modelling studies were also suffering from a lack of realistic fresh water flux, and scarcity of validation data set.

### 1.3.3. Interannual SSS variations and related mechanisms

The scarcity of available SSS *in-situ* observations and the lack of reliable continental freshwater forcing prevented for long investigating the interannual SSS variations within the Bay. The recent improvement of the SSS observing system and the availability of interannually-varying river runoff estimates [Jian *et al.*, 2009; Furuichi *et al.*, 2009; Papa *et al.*, 2010, 2012] recently allowed Chaitanya *et al.* [2014b] to provide a preliminary description of the year-to-year SSS variability over the recent period in the northern BoB. They revealed that the year-to-year variability of SSS is particularly strong in the northeastern part of the BoB during the past few years (Figure 1.22), with anomalous spells of about one pss amplitude. Based on a simple mixed layer salinity budget, they suggested that interannual variability of SSS is mainly driven by fresh water fluxes, with the variability of oceanic surface circulation associated with IOD events also potentially playing some role.

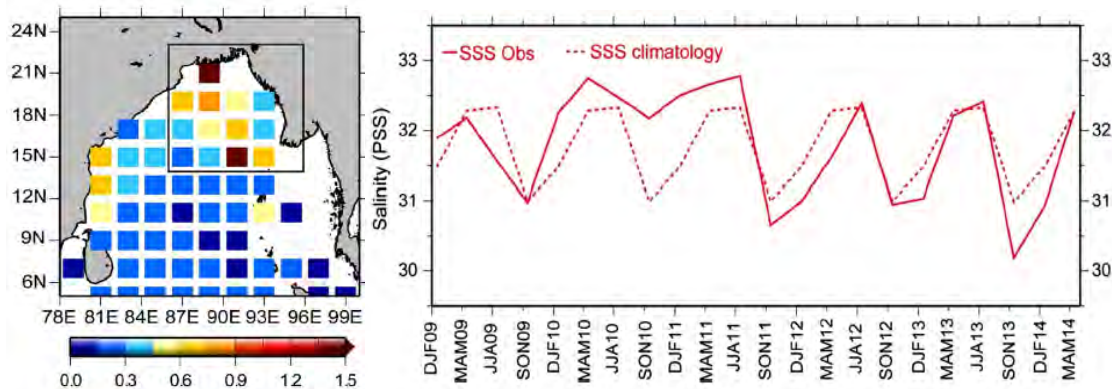


**Figure 1.22.** (Left) Standard deviation of SSS interannual variability over 2009–2014 in from observations (in practical salinity scale). (Right) Trimonthly evolution of SSS averaged over the NEB box, from observation (solid red) and NIOA climatology (red dashes), from December 2009 to May 2014. The black frame on the left panel features the limits of the north-eastern bay (NEB) box. [Taken from Chaitanya *et al.*, 2014b]

Aside *in-situ* measurements, remotely sensed surface salinity data from Aquarius and SMOS provide an interesting alternative to assess this year-to-year SSS variability. Using SMOS data, Durand *et al.* [2013] demonstrated that the positive 2011 IOD event (negative 2010 IOD event) was associated with fresh (salty) anomalies in the central IO south of the equator and salty (fresh) anomalies just north of the equator, and attributed these SSS variations to variations in horizontal advection process associated with IOD-related surface currents changes.

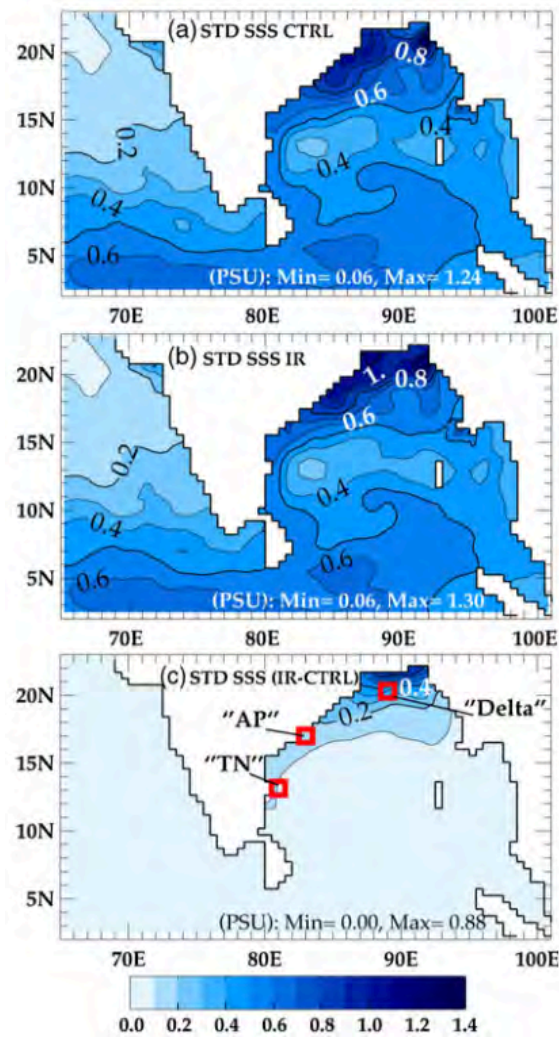


**Figure 1.23.** (a) Standard deviation of interannual SSS variations in an ocean simulation with climatological runoffs forcing of the Ganga-Brahmaputra. (b) Same as (a) but with interannual climatological runoffs forcing of the Ganga-Brahmaputra. (c) Standard Deviation of the SSS difference between these two simulations. Isocontours are every 0.1. Indicated on each plot are the extreme values. [Taken from *Durand et al.*, 2011]

On the modelling front, there were only a handful of studies that discussed the SSS interannual variability in the BoB. In line with *Durand et al.* [2013], forced ocean model analysis have illustrated that low surface salinity waters are advected from the eastern part of the Bay southwestward into the equatorial IO during positive IODs [*Thompson et al.*, 2006; *Grunseich et al.*, 2011]. Using coupled model outputs, *Vinayachandran and Nanjundiah* [2009] further suggested that, along with the equatorial IO, the northern BoB also exhibits the large SSS interannual variability in summer, largely driven by year-to-year monsoonal fresh water flux variations. The unrealistic runoff and oceanic precipitation forcing generated by their coupled model however considerably hampered the robustness of their conclusions. Forcing an ocean

model with interannually varying discharges of major river runoff data set, *Durand et al.* [2011] demonstrated that the impact of these rivers on the interannual SSS variability in BoB is strong in the northern part (north of 15°N) (Figure 1.23). The above studies therefore suggest that the interannual SSS variability in the BoB is rather large, with a considerable influence of Ganga-Brahmaputra river runoff and precipitations at the head of the Bay. However, an exhaustive study describing the main interannual SSS patterns in the Bay, their main driving processes and the climate modes they are associated with is still lacking.

#### 1.4. Scientific questions

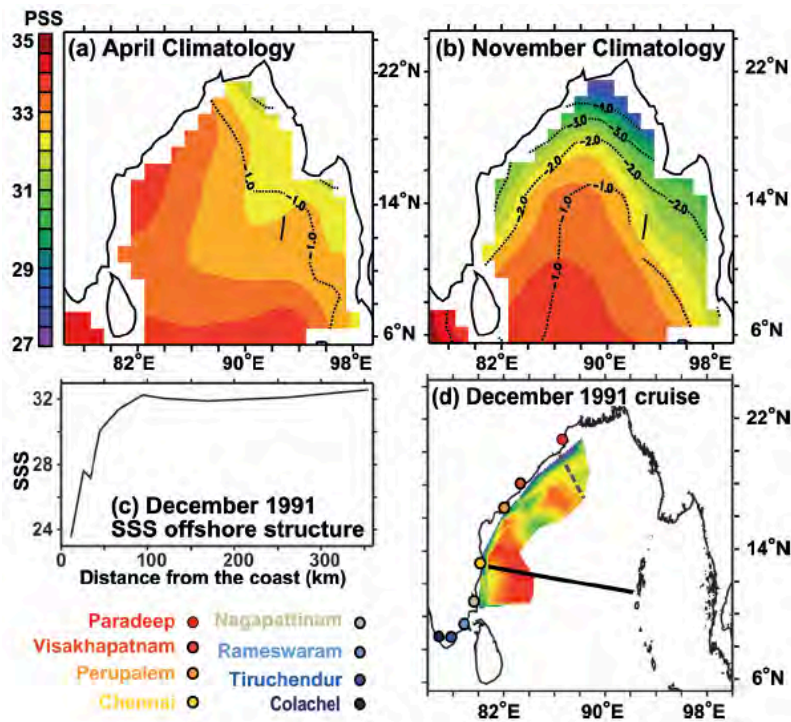


**Figure 1.24.** Climatological map of SSS from *Chatterjee et al.* [2012] in (a) April and (b) November (the contours show the surface salinity minus the salinity at 50-m depth). (c) SSS measured during the Dec 1991 cruise described in *Shetye et al.* [1996] along the transect indicated by the black dashed line offshore of Paradeep displayed in (d). (d) Map of SSS in Dec 1991 derived from *in-situ* measurements performed during an oceanic cruise [taken from *Shetye et al.*, 1996]. The colored circles in (d) indicate the location of the eight salinity coastal measurements stations used in that study (i.e., Paradeep, Visakhapatnam, Perupalem, Chennai, Nagapattinam, Rameshwaram, Tiruchandur, and Colachel) when following the coast from the northern BoB toward the western coast of India. The Chennai–Port Blair transect is indicated by the black continuous line, while the transect in (c) is indicated by the black dashed line. [Taken from *Chaitanya et al.*, 2014b]

The Argo program has considerably increased the number of temperature and salinity profiles in the central part of the BoB since 2002. The *in-situ* data coverage

used in the existing SSS climatologies is now sufficient to capture the main large-scale SSS seasonal features in the Bay [Chatterjee *et al.*, 2012]. There is still however a sparse coverage in the coastal regions. Using coastal SSS measurements, in combination with high-resolution data along an offshore transect, Chaitanya *et al.* [2014a] demonstrated that there is a very intense freshening (up to 10 units in the northern Bay) in a narrow (~50 to 100 km) coastal strip, flowing like a ‘river in the sea’ that quickly expands southward along the east Indian coast after the monsoon (Figure 1.24). This narrow freshening is not well captured by climatologies [e.g. Chatterjee *et al.*, 2012] due to both a poor data sampling in the coastal region and the 4° horizontal smoothing used in those climatologies [Figure 1.24]. The monitoring of SSS interannual variability is even more challenging due to the insufficient spatio-temporal sampling of the *in-situ* network [Vinayachandran and Nanjundiah, 2009; Chaitanya *et al.*, 2014b]. The advent of satellite salinity measurements provides a unique opportunity to improve the monitoring of SSS variations in this climatic relevant region. The recent improvements in the SSS retrieval algorithms and the reasonable temporal coverage of both satellite missions (~3 years) now allows a qualitative assessment of the ability of these satellites to capture the SSS in this region.

**(1) The first objective of this PhD is to assess the ability of SMOS and Aquarius to retrieve the SSS seasonal cycle and interannual variability in the BoB. Do SMOS and Aquarius bring more information than existing climatologies? To what extent the land effects in this semi-enclosed basin impair the remotely sensed signal?**

While the improved *in-situ* salinity-observing network allows describing the SSS seasonal evolution within the bay, it is however not yet sufficient to quantitatively assess the processes that govern the SSS evolution. Observational results from Chaitanya *et al.* [2014a] however suggest that the EICC plays a key role in the southward expansion of this narrow coastal freshwater strip after the monsoon but cannot explain its demise during the following months. Using an ocean model simulation without any SSS relaxation and a proper river runoffs forcing may allow to infer the processes governing the SSS seasonal evolution in the BoB, in particular those contributing to the southward expansion and retreat of the “river in the sea” along the east coast of India during the post-monsoon.

- (2) The second objective of this PhD is therefore to use a modelling configuration without any relaxation to SSS climatology, able to reproduce the post-monsoon “river in the sea”, and to provide a quantitative analysis of the processes that contribute to the SSS seasonal cycle in the BoB. In particular, what are the processes that cause the southward expansion and subsequent retreat of the “river in the sea” along the east coast of India during the post-monsoon season?**

Finally, very little is known about the interannual SSS variations and their driving processes in the BoB. The few modelling studies that have tackled this issue [Durand *et al.*, 2011; Vinayachandran and Nanjundiah, 2009] suggest that the interannual SSS variability in the BoB is rather large, with a considerable influence of Ganga-Brahmaputra river runoff and precipitations at the head of the Bay. However, an exhaustive study describing the main interannual SSS patterns in the Bay, the climate modes to which they may be related and their main driving processes is still lacking.

- (3) The last objective of this PhD is hence to investigate the interannual variability of BoB salinity using a modelling approach. In particular: is our model able to reproduce observed SSS interannual anomalies in the BoB? Is the interannual variability of SSS in the BoB linked to a particular climate mode such as ENSO, the IOD or the interannual variations of the monsoon? What are the main processes that contribute to SSS interannual variations, in particular in high variability regions such as the northern BoB or the east coast of India? Is the SSS variability rather driven by freshwater fluxes (rainfall, river runoff) or by other processes?**

## 1.5. Organization of Thesis

This thesis manuscript is organized and presented as follows:

- **Chapter 2** gives a detailed description of the various observational and model datasets used for this study and the methodology employed to analyse these datasets.
- **Chapter 3** provides an in-depth assessment and comparison of the ability of SMOS and Aquarius satellites to monitor the seasonal and interannual SSS signals in the BoB. The article will be submitted to International Journal of Remote Sensing before the PhD defense.
- **Chapter 4** estimates the contributions of the processes that govern the SSS seasonal evolution in the BoB, based on our numerical model. It consists of a paper published in JGR-Oceans [*Akhil et al.*, 2014].
- **Chapter 5** describes the SSS interannual variability in the BoB, relates it to the main climate modes over the IO and understand the main mechanisms controlling its variations, again based on our numerical model. The contents of this chapter will serve as the basis for an article to be submitted in the following months.
- **Chapter 6** reviews the main results of this thesis. In addition, some challenges and perspectives for future work are discussed.

## Chapter 2

### Data and Methodology

---

#### 2.1. General Introduction

Historically, salinity spatio-temporal variability in the BoB has been poorly explored due to the lack of observations. Over the past few years, the SSS observing system in the BoB has greatly improved. The launch of the Argo program allowed to considerably increase the number of temperature and salinity profiles in the central part of Bay. Together with Argo, RAMA moorings, OMNI moorings, ship-of-opportunity thermosalinograph transects, dedicated hydrographic cruises and coastal observations now provide a much-improved salinity spatial and temporal sampling. The recent development of SSS remote-sensing capabilities (SMOS and Aquarius) now provide a new opportunity to monitor SSS variations, but face particular challenges in the land-surrounded BoB. Despite the recent improvement in salinity observations in the BoB, the detailed mechanisms of SSS interannual variability are still difficult to tackle from observations, and we had to resort to numerical modelling. The lack of reliable estimates of river runoffs into the BoB were, up to recently, a major limitation for correctly representing salinity and its variability in ocean models. The recent release of satellite-derived runoffs for major rivers into the BoB has now lifted this barrier. The analyses presented in this thesis are thus based on : a) an exhaustive compilation of all available *in-situ* SSS observations, b) SMOS and Aquarius retrieved SSS, and c) an eddy-permitting ocean general circulation model regional simulation forced with realistic river runoffs and precipitation fluxes. This chapter describes the observation datasets and modelling strategy I used in this PhD.

#### 2.2. Observational Data

##### 2.2.1. *In-situ* SSS dataset

Systematic *in-situ* oceanographic measurements are important for establishing « ground » truth and validating satellite measurements and numerical models. The *in-*

*situ* SSS data used in this thesis consist of the gridded product of *Chaitanya et al.*, [2014b], which compiles all *in-situ* SSS measurements available over the BoB during the 2006-2014 period. It is based on various types of data: Argo profilers, ship-of-opportunity eXpendable Conductivity-Temperature-Depth (XCTD) profiles and bucket measurements, RAMA moorings [McPhaden *et al.*, 2009], OMNI moorings [Venkatesan *et al.*, 2013], ship-of-opportunity thermosalinograph (TSG) transects and dedicated hydrographic cruises. A brief description of each of these datasets and the methodology used is given below.

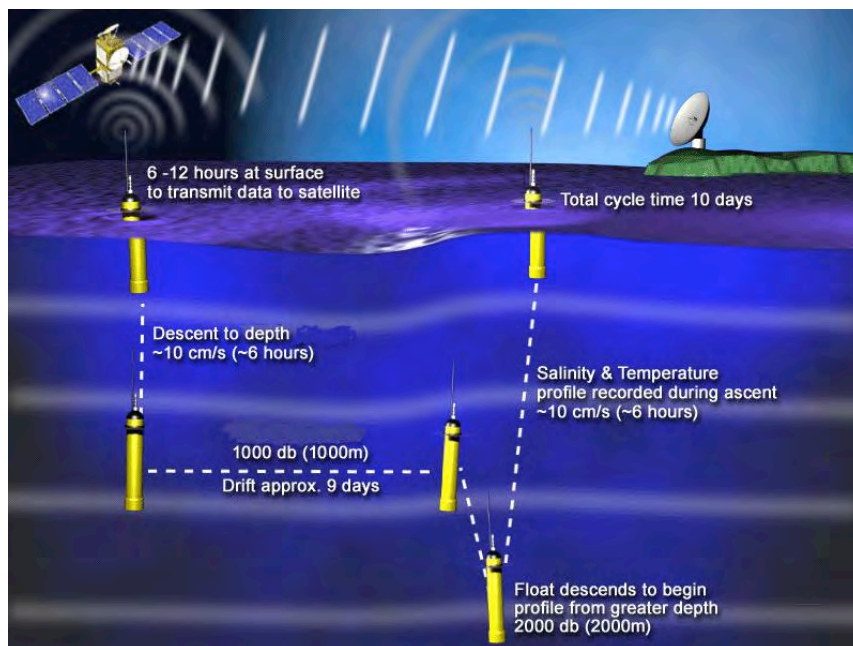


**Figure 2.1.** Argo profiler cycle (adapted from <http://www.argo.ucsd.edu/>)

**ARGO:** Argo profilers are free drifting profiling floats that measure the temperature and salinity. Argo profilers usually drift at a depth of 1000 m (see Figure 2.1). Every 10 days they descend to a depth of 2000 m and then ascend to the sea surface measuring the temperature and salinity with a vertical resolution of 5 to 10 m. After reaching the surface, the temperature and salinity data are transmitted via Argos or Iridium satellite systems to Global Data Acquisition centers (GDAC), from where the data is delivered worldwide as real time observations. The data centres subsequently operate calibration and validation of the real time profiles to issue the so-called delayed mode data, which are quality controlled and qualified via a quality flag. The main contributor to our SSS dataset is the ARGO database available from IFREMER Data Center (<ftp.ifremer.fr/ifremer/argo>). The uppermost valid

measurement depth (i.e. with « good » or « probably good » quality flag; see Argo quality control manual, [www.argodatamgt.org/content/download/341/2650/file/argo-quality-control-manualV2.7.pdf](http://www.argodatamgt.org/content/download/341/2650/file/argo-quality-control-manualV2.7.pdf)) is extracted from each salinity profiles, typically at about 8 m depth.

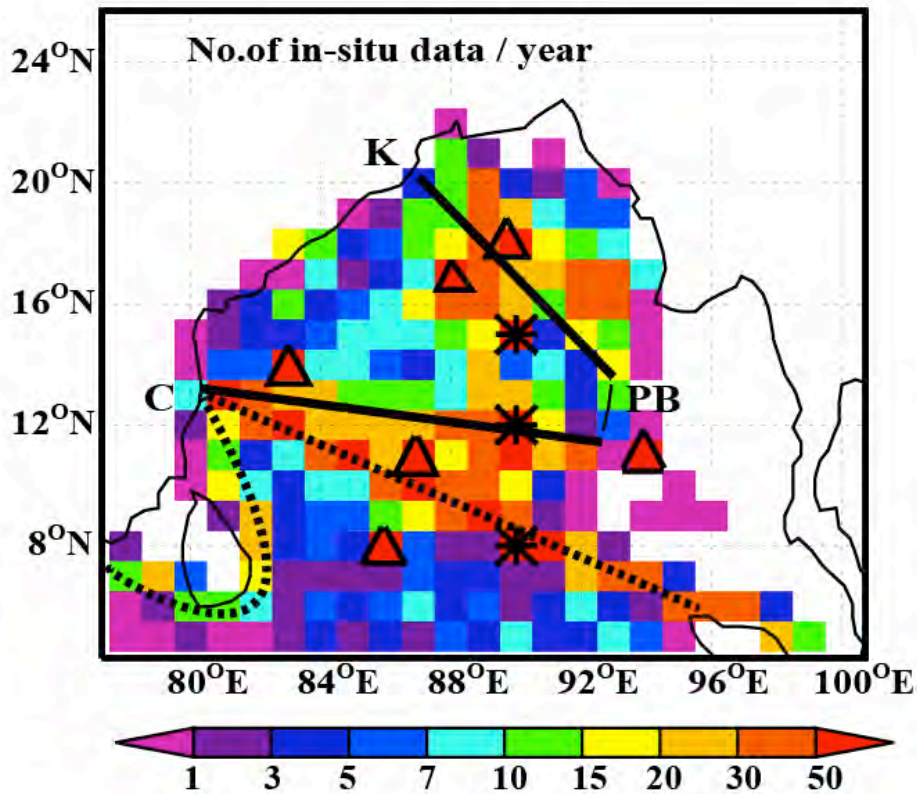


**Figure 2.2.** Total number of *in-situ* salinity profiles per  $1^{\circ} \times 1^{\circ}$  box and per year from 2006-2014. Stars indicate RAMA moorings and black triangles OMNI moorings. The thick black lines indicate frequently repeated salinity measurements along two ship-of-opportunity lines (Chennai - Port Blair or C - PB and Kolkata - Port Blair or K - PB) while the black dashed line indicates the track of the TSG-equipped M/S Lavender merchant ship.

**XCTD and bucket measurements:** The XCTD Profiling System is an accurate and cost-effective means to collect underway salinity profiles from a ship. Our *in-situ* dataset includes all valid measurements from bucket samples and XCTD salinity measurements collected along two repeated merchant ship tracks between Chennai (label « C » in Figure 2.2) and Port Blair (label « PB »), and between Kolkata (label « K ») and Port Blair. The bucket samples are analyzed using a Guild Line 8400 Autosol salinometer following standard international procedures. This ensures typical accuracy of salinity of about  $10^{-3}$ . XCTD salinity records over the upper 4 m were discarded and the 5-m records were considered as SSS.

**RAMA Mooring:** RAMA [McPhaden *et al.*, 2009] is a moorings network that monitors surface meteorology and subsurface ocean parameters in the IO (Figure 2.3). It is an element of IndoOOS, an international program for observing the IO. RAMA consists of both surface and subsurface moorings. Surface mooring data are telemetered to shore in real time via the Argos satellite relay system, and transmitted to the operational weather, climate and ocean forecasting centers across the world. Three RAMA buoys (stars on Figure 2.2) have been deployed in the BoB, at 90°E–8°N, 90°E–12°N and 90°E–15°N. Data return rates vary between 50% at 8°N and 12°N and 75% at 15°N. The 5-day averaged salinity data obtained from the RAMA website (<http://www.pmel.noaa.gov/tao/disdeld/disdeld-rama.html>) are used.

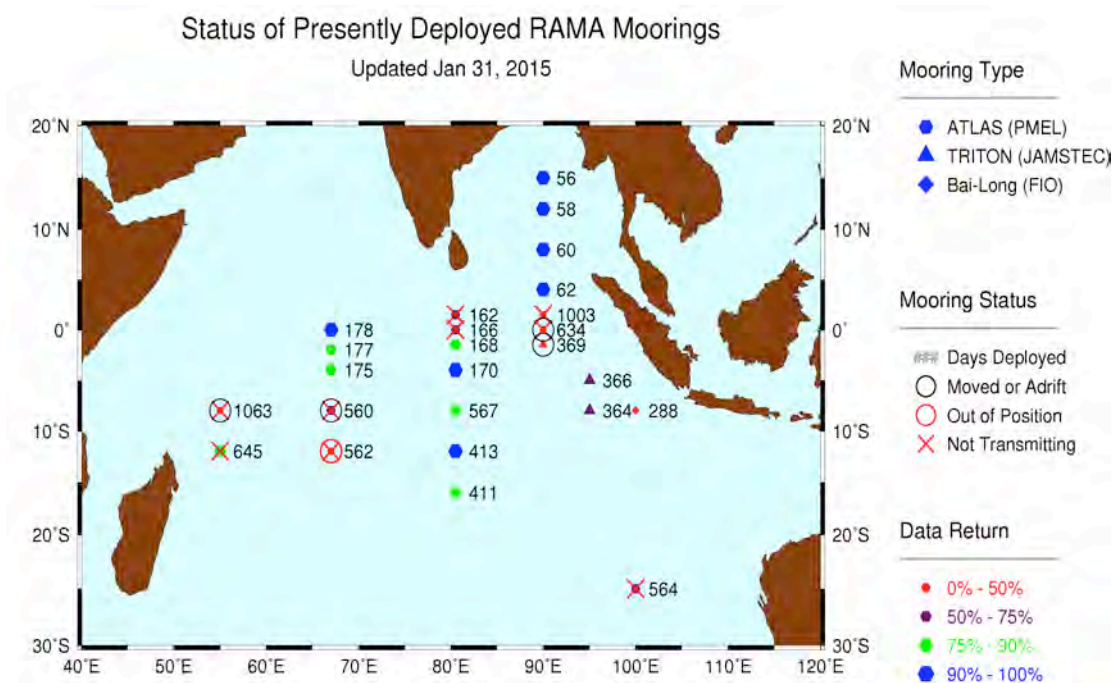


**Figure 2.3.** Present status of the RAMA moorings network. (Taken from <http://www.pmel.noaa.gov/>)

**OMNI Mooring:** OMNI is an Indian program of deep-ocean moorings deployed since 2011 in the BoB. The OMNI network consists of six moored buoy systems located at 11°N–86.5°E, 8°N–85.5°E, 14°N–83°E, 16.5°N–88°E, 10.5°N–94°E, 18.2°N–89.7°E (triangles on Figure 2.2). Similarly to RAMA moorings, they are equipped with surface and subsurface sensors to measure oceanographic and meteorological parameters in real time. The conductivity temperature (CT) sensors are fitted at 5, 10, 15, 20, 30, 50, 75, 100, 200 and 500-m depth along the mooring line (Figure 2.4). Data from all sensors are collected during the last 10 min of every hour

and transmitted every 3 hours to the shore station using INMARSAT geostationary satellite [Venkatesan *et al.*, 2013]. After standard quality control procedures, all data are archived at the Indian National Centre for Ocean Information Systems (INCOIS) and delivered to users through the Ocean Data Information Systems (ODIS) [Shesu *et al.*, 2013]. Salinity data at 5-m depth from the six moorings from mid-2011 are used.

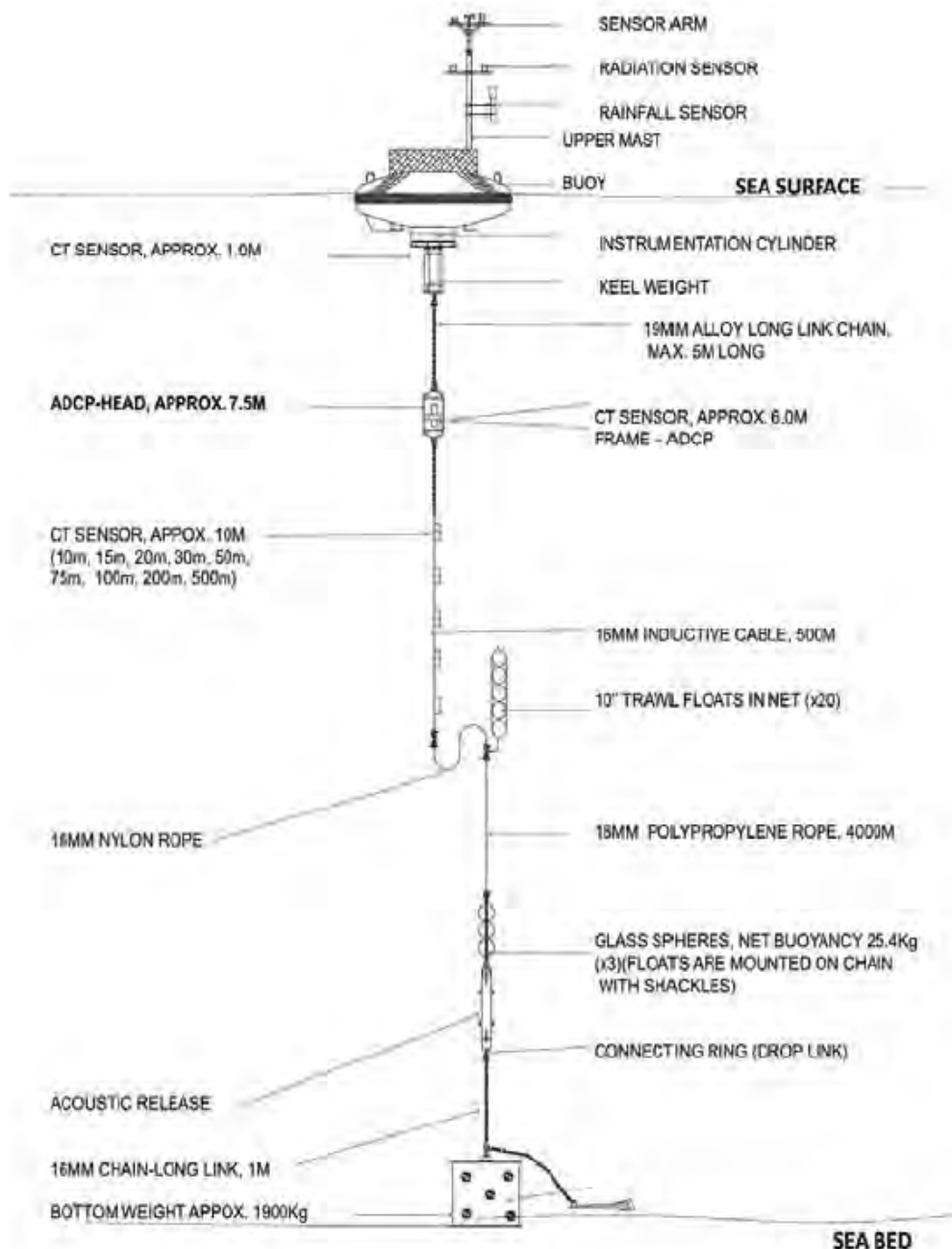


**Figure 2.4.** Mooring configuration of OMNI buoy. [Taken from Venkatesan *et al.*, 2013]

**Thermosalinograph:** SSS is commonly measured on ships using TSGs, which measures the properties (temperature, salinity) of water collected through a special inlet located on the ship's hull. As part of the French Service d'Observation "SO-SSS", a merchant ship (M/S Lavender) equipped with a TSG has been crossing the southern BoB (black dashed line on Figure 2.2) ten times from 2009 to September 2013 (typically once every five months). Due to ships' average draught and speed, it is difficult to assign a specific depth to the thermosalinograph measurements. The data is considered to be representative of the 0-10 m upper ocean layer [Delcroix *et al.*, 2005], with an average 3 km resolution along track. The TSG data went through a delayed-mode quality control including comparison with climatology and correction with external water samples.

**Hydrographic cruises:** A few near-surface measurements from shipborne CTD (Conductivity, Temperature, and Depth) were made available by the National Institute of Oceanography Data Centre (India). CTD is the primary tool for determining essential physical properties of seawater such as temperature and salinity. Most of the observations were collected in the coastal western Bay, between 0 and 10 m depth, during 2009-2011.

**Data reduction and gridding:** The above-mentioned datasets are heterogeneous in space and time. These datasets originate from different depths within the upper 10 m of the ocean (Argo at 8 to 9 m, RAMA at 10 m, XCTD at 5 m, etc...). Chaitanya *et al.* [2014b] demonstrated that the heterogeneity of the spatio-temporal sampling achieved by these various datasets is unlikely to affect the estimate of the SSS. The estimated error arising from the different vertical sampling depth is indeed typically much smaller than the magnitude of the SSS variations reported in their analysis. Details about the steps for combining SSS data originating from different sources can be found in Chaitanya *et al.* [2014b]. In line with de Boyer Montegut *et al.* [2004], Chaitanya *et al.* [2014b] merged these data sources into a single dataset by computing the median of all available individual measurements (irrespective of their nature: autonomous profiler, mooring record, underway datum) onto a  $2^{\circ} \times 2^{\circ}$  trimonthly grid. This grid cell size gives the best compromise between the resolved scales and actual data coverage. To validate the satellite derived SSS, I regridded this data onto the SMOS and Aquarius native  $1^{\circ} \times 1^{\circ}$  monthly grids (the two grids are offset

by 0.5 in latitude and longitude). In order to avoid introducing any spurious signal in the merged product, the data gaps were not filled. The resulting gridded dataset is rather heterogenous, with a good coverage along the central BoB and sparse coverage along the near coastal regions (Figure 2.2).

### **2.2.2. SSS Climatology (NIOA)**

The recent NIOA SSS climatology produced by *Chatterjee et al.* [2012] is used to validate the SSS seasonal cycle from the satellite data and model outputs. This  $1^{\circ} \times 1^{\circ}$  monthly climatology includes all the data from the WOD09 [*Locarnini et al.*, 2010; *Antonov et al.*, 2010], complemented with CTD stations from Indian oceanographic cruises. The significance of NIOA climatology is that it presents a more reliable estimate for salinity fields.

### **2.2.3. Satellite SSS**

The advent of satellite salinity measurements provides a unique opportunity to improve the monitoring of SSS variations. The SMOS European mission [*Mecklenburg et al.*, 2008] launched in November 2009 and the Argentina/US Aquarius mission [*Lagerloef et al.*, 2008] operating since June 2011 both provide global SSS estimates at monthly resolution. A more detailed description of each of these missions is given below.

#### **(a) SMOS**

SMOS has been designed to observe soil moisture over land and salinity over the oceans [*Mecklenburg et al.*, 2008]. The SMOS satellite was launched in November 2009, on a sun-synchronous circular orbit at an altitude of 760 km with a three day repeat cycle. It carries an interferometric radiometer, the Microwave Imaging Radiometer using Aperture Synthesis (MIRAS), with a fixed two-dimensional interferometric antenna. The SMOS MIRAS is an L-band (1.4 GHz) radiometer with 69 mini antennas mounted in a precisely defined Y-shaped array on three deployed arms (Figure 2.5). The arms do not rotate but are fixed to the satellite. Using the interferometric radiometer, SMOS measures the microwave radiation emitted from the Earth surface. Moisture and salinity modify the emissivity of soil and seawater

respectively, and thereby affect microwave radiation emitted from the surface of the Earth. The SMOS radiometer exploits the interferometry principle: the 69 small receivers measure the phase difference of the incident radiation. The technique is based on cross-correlation of observations from all possible combinations of receiver pairs. A two-dimensional 'measurement image' is taken every 1.2 seconds. As the satellite moves along its orbital path each observed area is seen under various viewing angles. Polarized signals collected by the radiometers are cross-correlated to construct maps of brightness temperatures over a 100-km-wide swath. The swath is divided into pixels with a spatial resolution of 35 km at nadir. MIRAS calibration is very challenging and requires sophisticated corrections as well as pre- and post-processing algorithms. Since mid-july 2010, SMOS has been delivering the images of 'brightness temperature' that are used to produce global maps of ocean salinity averaged over 30 days. In August 2010, French Space Agency (CNES) was able to provide the first global map of SSS with SMOS data.



**Figure 2.5.** An image of SMOS (Taken from European Space Agency (ESA))

Data products that are generated sequentially from downloaded SMOS data by software processors (adapted from <http://www.argans.co.uk/smos/pages/overview.html>) consist of:

- Level 0 (L0) products are SMOS payload data with added Earth Explorer product headers.

- Level 1a (L1a) products are SMOS reformatted and calibrated observations, the so-called 'Calibrated Visibilities'.
- Level 1b (L1b) products are the output of the image reconstruction of SMOS observation measurements
- Level 1c (L1c) products are L1b geographically projected onto an ISEA 4H9 grid.
- Level 2 (L2) products are Ocean Salinity half-orbit swath-based maps on the ISEA 4H9 grid.
- Level 3 (L3) products are global maps of ocean salinity.

The official SMOS ESA mission team delivers data up to level 2. The spatio-temporal averaged and analyzed products (level 3) are generated and distributed by two dedicated processing centers : Centre Aval de Traitement des Données SMOS (CATDS, available at <http://www.catds.fr>) in France and CP3/4 in Spain.

The level 3 data consists of daily composites with  $0.25^\circ \times 0.25^\circ$  spatial resolution, and 10 day composite and monthly composites with spatial resolutions of  $0.25^\circ \times 0.25^\circ$ ,  $0.5^\circ \times 0.5^\circ$ ,  $1^\circ \times 1^\circ$ . Because of the interferometric principle of SMOS, local strong radio frequency interference (RFI) signals in the physical space, as well as land sources can contaminate large portion of the SMOS reconstructed brightness temperature images. The BoB is a semi-enclosed basin and is prone to strong RFIs and land contamination. Hence we use the latest  $1^\circ \times 1^\circ$  gridded monthly SSS composites from the V02 version of the SMOS Level-3 research product generated by the CATDS, France. This product has decreased noise level and is built from ESA level 1B products. It includes an improved RFI mitigation and a  $5^\circ \times 5^\circ$  adjustment with regards to the WOA SSS climatology [Antonov *et al.*, 2010] to remove residual temporal drifts and land contamination in SMOS brightness temperature level 1 products [Reul *et al.*, 2014]. This SSS bias mitigation and the improved RFI handling has been shown to improve the data quality close to the coasts compared to other level 3 products [Zhang *et al.*, 2013]. Data of the first four months of 2010 were not reprocessed because of reduced data quality during that period. The product we use in this thesis therefore covers the May 2010-December 2013 period.

## (b) Aquarius

Aquarius (Figure 2.6) is a NASA microwave radiometer designed to provide highly precise SSS data, launched on 10 June 2011, aboard the Argentina (CONAE) SAC-D satellite. The SAC-D satellite carries Aquarius set of three L-band radiometers along with a scatterometer, operating at 1.4 GHz and 1.2 GHz respectively. They are designed to provide global salinity maps on a monthly basis with a spatial resolution between 76 and 156 km, a swath width of 390 km, and an accuracy of 0.2 psu. The data collected by the radiometer are being used together with sea surface temperature collected from other platforms to derive salinity data. The radar scatterometer data is used to correct for the ocean surface roughness. The satellite crosses the equator at 6 am and 6 pm. The Aquarius instrument continuously points away from the sun to avoid glint. Aquarius achieves a global coverage every 7 days. The satellite provides two independent maps each week, one for ascending orbit and the other for descending orbit. These are averaged over a month to reduce the measurement noise and accuracy requirement.



**Figure 2.6.** An image of Aquarius (Taken from NASA)

PO.DAAC (NASA's Physical Oceanography Distributed Active Archive Center) provides Level 2 SSS data as well as gridded level 3 SSS products generated by the Aquarius Ground Segment at Goddard. Level 3 products are released with daily, 8 day, monthly, 3 months, and annual temporal resolutions.

We use the latest Aquarius level-3  $1^{\circ} \times 1^{\circ}$  monthly composites. This product combines the measurements from the three radiometers using the Combined Active-Passive (CAP) Algorithm applied to version 3.0 of the Aquarius/SAC-D data updated in July 2014. This algorithm simultaneously retrieves SSS, wind speed and wind direction by minimizing the sum of squared differences between a model and the observations, and includes a rain corrected salinity retrieval based on collocated SSMI/S SST and WindSAT wind data. This product covers the August 2011-June 2014 period.

### **(c) Intercomparison of SMOS and Aquarius**

SMOS and Aquarius are the first two satellite missions carrying L-band radiometers onboard. Even though both radiometers are measuring the brightness temperature, they have differences in their architecture and operation principles. The SMOS satellites measure the microwave radiation emitted from the earth's surface using an L-band (1.4 GHz) passive radiometer 'MIRAS'. The SMOS radiometer captures 'brightness temperature' images by combining the signals measured with 69 receivers arranged in Y-shape. Hence SMOS needs an accurate image reconstruction. Aquarius carries 3 passive radiometers, and 1 active scatterometer, operating at 1.4 GHz & 1.2 GHz respectively. The 3 radiometers measure the brightness temperature directly and the scatterometer measures the surface roughness. Surface roughness modifies the brightness temperature of the sea surface. For Aquarius, the surface roughness data collected by its own scatterometer simultaneously with brightness temperature is used to derive the surface salinity data. But SMOS have to depend on information from other sources, which will not be simultaneous with its measurements. SMOS swath is larger than 1000km and the field of view has a hexagon-like shape and 'measurement image' is taken every 1.2 seconds. The SMOS achieves global coverage (revisit time) in every 3 days. For Aquarius, the total swath is 390km and revisit time is 7 days [Aretxabaleta *et al.*, 2010; <http://www.esa.int/>; <http://podaac.jpl.nasa.gov/aquarius>].

A comparison on satellite specification is shown in the table 2.1 [taken from *Aretxabaleta et al., 2010*].

	<b>SMOS</b>	<b>Aquarius</b>
<b>Agency</b>	ESA	NASA/CONAE
<b>Launch</b>	02-Nov-2009	Expected 2011
<b>Satellite size</b>	Small-Medium 360Kg/400W	Large 1405Kg/1165W
<b>Radiometer</b>	Interferometric	Polarimetric
<b>Frequency</b>	1.4 GHz	1.413 GHz
<b>Antenna</b>	69 receivers in Y-shape	3 independent beams
<b>Data collection</b>	Cycles of H, V, co- & cross- polar data integrated over 1.2 seconds	Data averaged and retained every 1.44 seconds
<b>Brightness temperature</b>	Recovered through image reconstruction	Directly retrieved
<b>Surface roughness</b>	Estimated from auxiliary data (ECMWF)	L-Band 1.26 GHz Scatterometer using real aperture and 2.5- meter reflector antenna.
<b>Revisit time</b>	3 days	7 days
<b>Main errors</b>	Radiometric sensitivity, Faraday rotation, Sun contamination, Auxiliary SST & wind	Radiometric sensitivity, Faraday rotation, Sun contamination, measured wind
<b>Land contamination</b>	Large (up to 1000km)	Expected to be smaller (up to 400km)

**Table 2.1.** Aquarius and SMOS comparison [Taken from *Aretxabaleta et al., 2010*]

## 2.3 Model Configuration

In this thesis, we use an ocean general circulation model (OGCM) to simulate the salinity variability in the BoB. A description of the model setup, forcing datasets, reference simulation and sensitivity experiments is given below. We also detail the methodology for diagnosing the mixed layer salinity budget in the model.

### 2.3.1. Model setup

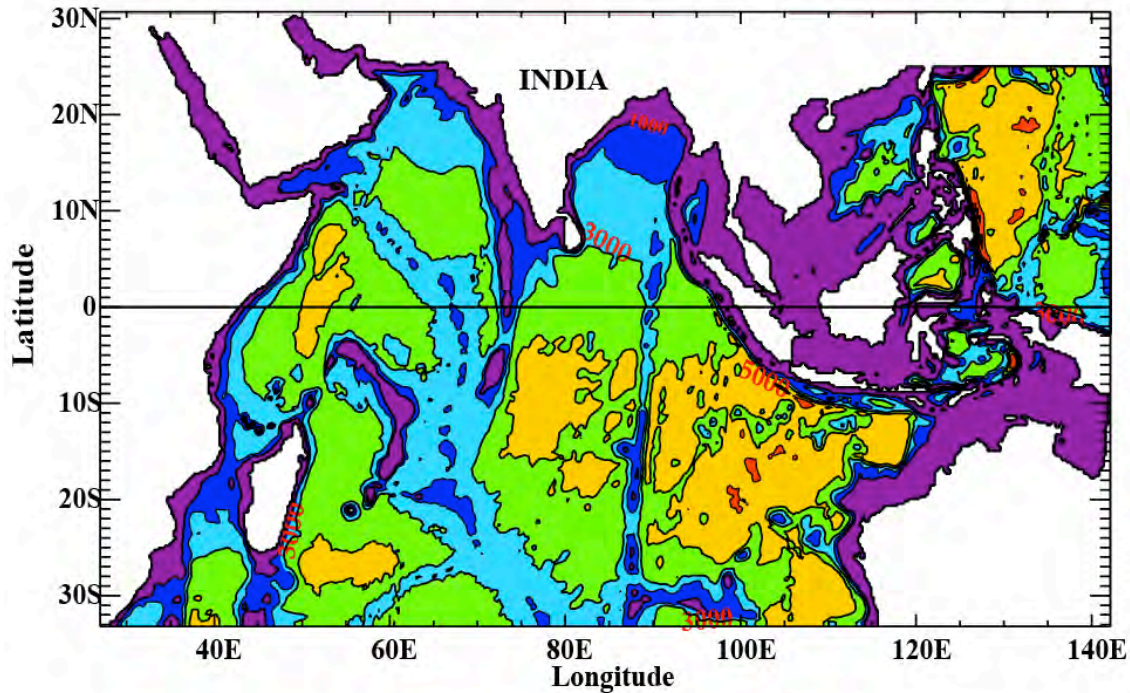


Figure 2.7. The Model Bathymetry. Isocontours are plotted every 1000 m.

The model configuration used in this study was developed as part of the DRAKKAR project [DRAKKAR Group, 2007], a European modelling project which provides the framework for joint and co-ordinated modelling studies between research groups in France, Germany, Russia and Finland. The model is based on the NEMO (formerly known as OPA, Océan Parallélisé) OGCM [Madec, 2008], and is a sub-domain from the global  $0.25^\circ$  resolution (i.e. cell size  $\sim 25$  km) ORCA025 coupled ocean/sea-ice model configuration described by Barnier *et al.* [2006]. This regional configuration extends from  $26.75^\circ$  E to  $142.25^\circ$  E and from  $33.2^\circ$  S to  $30.3^\circ$  N (Figure 2.7). The model is based on standard primitive equations. It assumes the Boussinesq (density variations are neglected except in their contribution to the buoyancy force) and hydrostatic (the vertical momentum equation is reduced to a balance between the vertical pressure gradient and the buoyancy force) approximations, the incompressibility hypothesis (the three dimensional divergence of the velocity vector is assumed to be zero), and uses a free-surface formulation [Roullet and Madec, 2000]. The density is computed from potential temperature, salinity, and pressure using the Jacket and McDougall [1995] equation of state.

The time stepping used in NEMO is a three level scheme represented as :

$$\mathbf{x}^{t+\Delta t} = \mathbf{x}^{t-\Delta t} + 2\Delta t \text{ RHS}_x^{t-\Delta t, t, t+\Delta t} \quad (2.1)$$

where  $\mathbf{x}$  stands for  $\mathbf{u}$ ,  $\mathbf{v}$ ,  $\mathbf{T}$  or  $\mathbf{S}$  ; RHS is the Right-Hand-Side of the corresponding time evolution equation ;  $\Delta t$  is the time step ; and the superscripts indicate the time at which a quantity is evaluated. The tendency terms of the equations are evaluated either centered in time, or forward, or backward depending of the nature of the term.

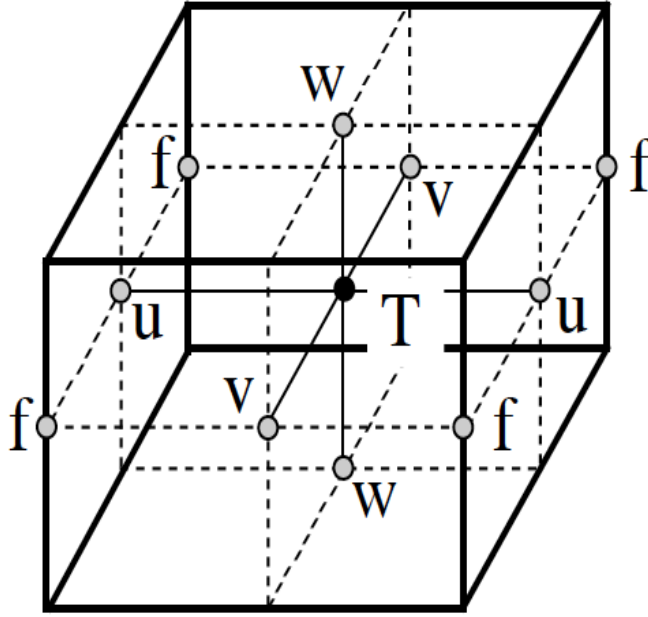


**Figure 2.8.** Arrangement of variables.  $T$  indicates scalar points where temperature, salinity, density, pressure and horizontal divergence are defined.  $(u, v, w)$  indicates vector points, and  $f$  indicates vorticity points where both relative and planetary vorticities are defined. [taken from Madec, 2012].

The model is discretised on a staggered Arakawa C grid [Mesinger and Arakawa, 1976] with masking of land areas. In an Arakawa C grid, the arrangement of variables is the same in all directions. It consists of cells centred on scalar points ( $\mathbf{T}$ ,  $\mathbf{S}$ ,  $\mathbf{P}$ ,  $\rho$ ) with vector points ( $\mathbf{u}$ ;  $\mathbf{v}$ ;  $\mathbf{w}$ ) defined in the centre of each face of the cells. The relative and planetary vorticity,  $\zeta$  and  $\mathbf{f}$ , are defined in the centre of each vertical edge and the barotropic stream function  $\psi$  is defined at horizontal points overlying the  $\zeta$  and  $\mathbf{f}$ -points (Figure 2.8).

The experiments in this study use an eddy-permitting resolution. The nominal horizontal resolution is  $0.25^\circ$  at the equator, leading to horizontal dimensions of  $463 \times 273$ . The vertical grid has 46 levels (with 7 levels in the upper 50 m), with 6 m

spacing at the surface increasing to 250 m in the deep ocean. The maximum depth in the model is 5844 m. The model uses a partial step representation of the bottom topography, i.e. making the depth of the bottom cell variable and adjustable to the real depth of the ocean for a better representation of topographic slopes [Barnier *et al.*, 2006]. The bathymetry is a smooth combination of US Department of Commerce, National Oceanic and Atmospheric Administration, National Geophysical Data Center 2-min Gridded Global Relief Data (ETOPO2v2) and General Bathymetric Chart of the Oceans data over shelves [Nisha *et al.*, 2013]. The Pamban pass (Indo-Sri Lanka pass) is closed, unlike in the original ORCA025 grid (figure 2.7). Keeping the Pamban pass open leads to significant transport of BOB water to the AS through this pass, making the model solution unrealistic [Durand *et al.*, 2007]. The African continent closes the western boundary of the domain. The oceanic portions of the eastern, northern and southern boundaries are handled using a radiation-relaxation approach [following Marchesiello *et al.*, 2001], where we use the radiation condition to determine whether a boundary is passive (outward propagation) or active (inward propagation). The boundaries are constrained with a 150-day time-scale relaxation to 5-day-average velocities, temperature and salinity from an interannual global  $0.25^\circ$  simulation [Dussin *et al.*, 2009].

As mentioned in the introductory section, all previous numerical modeling studies investigating the SSS variations in the BoB used a relaxation term toward the observed surface salinity climatology. This choice allows to keep the surface salinity realistic but also artificially compensates any error in the forcing or in the model physics. This strong impact of the relaxation term may therefore prevent to draw any robust conclusions about the mechanisms of SSS variability [de Boyer Montegut *et al.*, 2005]. As our modelling framework is mainly used to infer the mechanisms of SSS seasonal and interannual variability in the BoB, we did perform a simulation without any restoring towards the SSS climatology: this simulation did not exhibit any significant salinity drift and allow to accurately captures the main seasonal and interannual SSS variations in the BoB (see Chapter 4 and 5). These results strongly suggests that the model physics and surface forcing from our current regional configuration are now accurate enough to prevent the use of a SSS relaxation term. This choice therefore allowed us to confidently use the online salinity budget from the model presented in section 2.3.4 in order to assess the oceanic and atmospheric processes responsible for SSS variations in the BoB.

Other numerical choices worth noting are:

- a TVD (Total Variance Diminishing) advection scheme for tracers [*Levy et al.*, 2001] which, compared to the centred scheme, avoids the generation of overshoots in case of sharp gradients. In the TVD formulation, the tracer at velocity points is evaluated using a combination of an upstream and a centred scheme.
- Lateral mixing acts along isopycnal surfaces, with a Laplacian operator and a constant  $200 \text{ m}^2 \text{ s}^{-1}$  isopycnal diffusivity coefficient [*Lengaigne et al.*, 2003].
- a horizontal biharmonic viscosity for momentum (decreasing poleward as the cube of the grid size).
- Short-wave fluxes penetrate into the ocean based on a single exponential profile [*Paulson and Simpson*, 1977] corresponding to oligotrophic water (attenuation depth of 23 m).
- there is no exchange of heat or salt through the ocean bottom, i.e.: a no flux boundary condition is applied on active tracers at the bottom
- The vector invariant form of the momentum equations; Coriolis and momentum advection terms are evaluated using a leapfrog scheme, i.e. the velocity appearing in these expressions is centred in time.
- Vertical mixing is computed from a turbulence closure scheme based on a prognostic vertical turbulent kinetic equation, which performs well in the tropics [*Blanke and Delecluse*, 1993].
- The river discharges are introduced as precipitation on the pixels surrounding the river mouths, resulting in a runoff forcing applied to the first layer of the model only. However, in reality, the freshwater inflows from the rivers flowing along the rim of BoB are vertically distributed over the depth of the estuaries (~40 m for the case of the Bramaputra). Recent tests where river runoffs are applied over the depth of the estuary however demonstrate that vertically distributing or not the runoffs do not significantly impact the salinity distribution.

### 2.3.2. Forcing Datasets

The ocean needs six fields as surface boundary conditions (1) the two components of the surface ocean stress (2) the incoming solar and non-solar heat fluxes (3) the surface fresh water fluxes. Each of the terms are described below.

#### (i) Momentum and heat fluxes

The set of simulations analysed in this thesis uses similar model configuration and forcing strategy. The only differences are the model forcing datasets and the length of the experiments.

In Chapter 4 (analysing seasonal salinity variability), the model is initialized from rest with World Ocean Atlas 2009 climatological temperature and salinity in January 2001, and only the January 2002–December 2007 period is analyzed. The model is forced by interannually varying fluxes of momentum and heat from the Drakkar Forcing Set #4 (DFS4) described in *Brodeau et al.* [2010] over January 2001–December 2007. The starting point of DFS4 is the CORE data set developed by *Large and Yeager* [2004]. The CORE bulk formulae are used to compute latent and sensible heat fluxes, with surface atmospheric variables (air temperature, humidity, and winds at 10 m) from ERA40 reanalysis [*Uppala et al.*, 2005] from 2000 to 2002, and European Center for Medium range Weather Forecast (ECMWF) analysis after 2002. The main advantage of DFS4 is that corrections have been applied to ECMWF variables (used in the calculation of turbulent fluxes) to remove unrealistic time discontinuities and to correct for obvious global and regional biases in ERA40 fields. Winds have been rescaled so that the climatological mean matches that of the QuickScat winds. Air temperature and humidity have been corrected. Radiative fluxes are based on the International Satellite Cloud Climatology Project (ISCCP)-FD surface radiations [*Zhang et al.*, 2004], which have been shown to outperform all the other available products, including ECMWF products [*Praveen Kumar et al.*, 2012]. Following *Large and Danabasoglu* [2006] recommendations, turbulent fluxes are computed every 6 hours while radiative fluxes are applied on a daily basis, with a linear interpolation to the model time step.

In Chapter 5 (analysing interannual salinity variability), the model is forced by DFS5.2 for the period 1990-2012 and only the January 1996 –December 2012 period is analyzed in the present study. The DFS5.2 data set has taken advantage of ERA-interim, the most recent atmospheric reanalysis produced at ECMWF [Dee *et al.*, 2011]. ERA-interim provides the surface atmospheric variables every 3 hours on a regular grid of  $\sim 0.7^\circ$  resolution. Compared to previous reanalyses, it has the great advantage of an increased spatial resolution and denser time sampling that resolves the diurnal cycle. No scaling is applied to ERA-I winds. ERAinterim overestimates shortwave radiation and the daily  $1^\circ \times 1^\circ$  TropFlux product [Praveen Kumar *et al.*, 2012], derived from the International Satellite Cloud Climatology Project (ISCCP)-FD surface radiations [Zhang *et al.*, 2004] with ad-hoc corrections derived from the tropical moored buoy array (TAO-TRITON-RAMA), is hence used.

#### (ii) **Surface fresh water fluxes (precipitation)**

In Chapter 4 (describing seasonal salinity variability), precipitation are based on a blending of several satellite products including two of the most widely used data sets: Global Precipitation Climatology Project (GPCP) [Huffman *et al.*, 1997] and CPC Merged Analysis of Precipitation (CMAP) [Xie and Arkin, 1997]. The CMAP produces pentad and monthly analyses of global precipitation in which observations from rain gauges are merged with precipitation estimates from several satellite-based algorithms. The analyses are on a  $2.5^\circ \times 2.5^\circ$  grid and extend back to 1979. The GPCP is a mature global precipitation product that uses multiple sources of observations, including surface information and satellites. GPCP product is available on monthly ( $2.5^\circ \times 2.5^\circ$ ), pentad ( $2.5^\circ \times 2.5^\circ$ ) and daily estimates (starting from 1996,  $1^\circ \times 1^\circ$ ). In Chapter 5 (describing interannual salinity variability), the model is forced with interannually varying precipitations from the GPCP (1990-1996 pentad estimates, 1996-2012 daily estimates).

#### (iii) **Surface fresh water fluxes (River runoff)**

For the seasonal analysis (Chapter 4), we use the monthly climatology of continental runoffs from Dai and Trenberth [2002], except for the Ganges-Brahmaputra river system for which we use altimetric-derived monthly interannual

estimates [Papa *et al.*, 2010]. The Ganga-Brahmaputra is the largest river outflow into the BoB with an annual mean outflow of  $30227\text{m}^3/\text{s}$  ( $\sim 8.7 \times 10^4 \text{ m}^3\text{s}^{-1}$  during monsoon) (Figure 2.9).

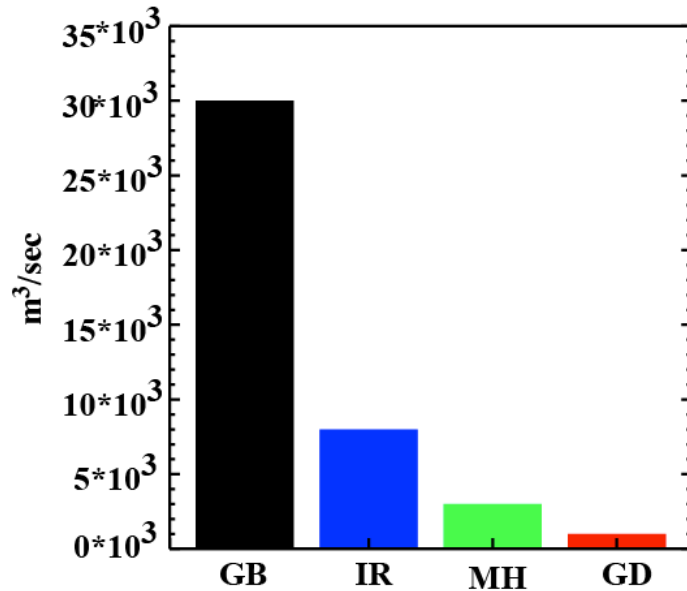


**Figure 2.9 :** The annual mean outflow of the major rivers, Ganga-Brahmaputra (GB), Irawady (IR), Mahanadi (MH), Godavari (GD).

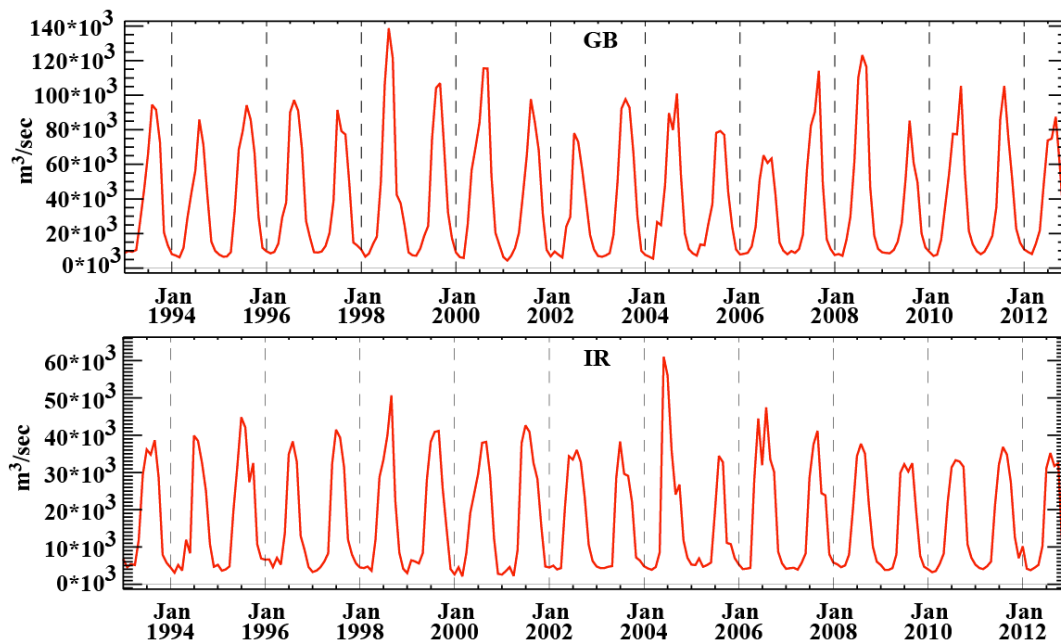


**Figure 2.10 :** Time series of upscaled satellite altimeter derived river discharges (**top**) GB, (**bottom**) IR.

For the interannual analysis (Chapter 5), we use interannually varying river runoff from altimetry-derived estimates for the major rivers (Ganga-Brahmaputra

(GB), Irrawaddy (IR)) and *in-situ* gauge discharge data for the smaller peninsular rivers (Mahanadi (MH), Godavari (GD), Krishna (KR) and Cauvery (CV)). For the GB river system, the monthly estimate of continental freshwater flux (Figure 2.10) is provided by *Papa et al.* [2012]. It is basically an update of the product of *Papa et al.* [2010]. This time-series is derived from a combination of *in-situ* level discharge relationships (the so-called rating curve, [*Papa et al.*, 2010]) with river water level retrieved from multiple altimetry satellites (TOPEX/Poseidon, ERS-2, ENVISAT and Jason-2). For the IR River, *in-situ* discharge time series are unfortunately not available over the recent period. *Furuichi et al.* [2009] published monthly estimates derived from *in-situ* observations over the 1966-1996 period. A rating curve is established using these monthly *in-situ* discharge estimates together with TOPEX/Poseidon river level time series over their common period of availability (1993-1996). *Papa et al.* [2012] used this rating curve to derive a continuous, monthly estimate of the IR river discharge (Figure 2.10) at the river mouths for 1993-2012 using TOPEX/Poseidon (1993-2002), ENVISAT (2002-2008) and Jason-2 (2008 onwards). During the recent period (2009 onwards), the estimates of river discharge rely on Jason-2 observations. No runoff data are available after December 2012.

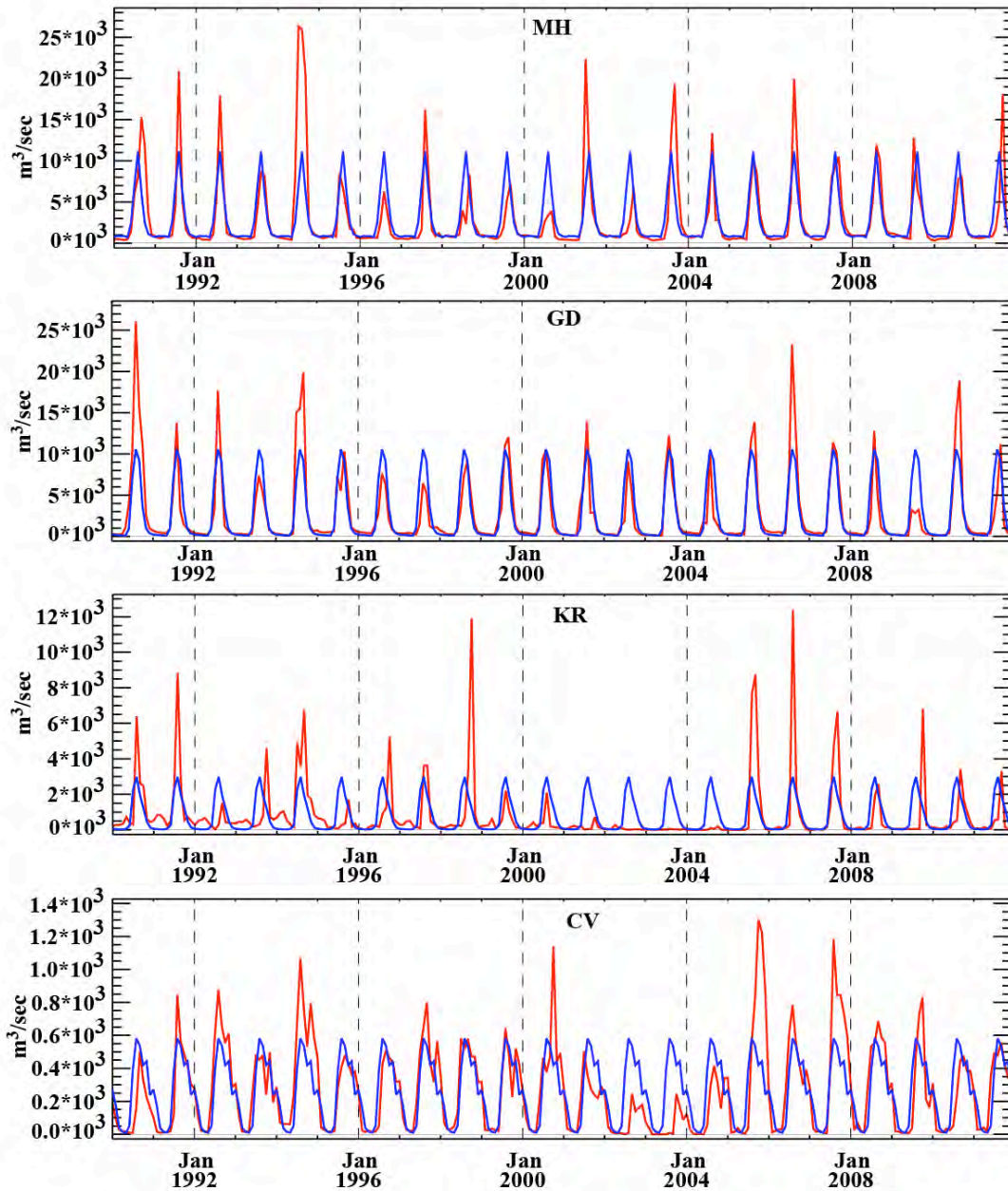


**Figure 2.11.** Time series of interannual river runoff (red) and Dai and Trenberth climatological runoff (blue) for peninsular rivers, Mahanadi(MH), Godavari(GD), Krishna (KR), Cauvery (CV).

For the peninsular rivers, we used interannual gauge discharge data (<http://www.india-wris.nrsc.gov.in/>). The river gauges are typically located quite far upstream of the river mouths. In order to adjust the river gauge data to the flow at the river mouth (which is the flow actually transferred to the ocean), we have to operate an upscaling. To do so, the gauge data are scaled by a constant coefficient to constrain the long-term mean discharge to be identical to that of the runoff climatology of *Dai and Trenberth* [2002]. The upscaling value we obtained for each of the peninsular rivers is: MH(1.89418), GD (1.04641), KR (1.47769), CV (1.08344). Figure 2.11 shows the

interannual runoff (after applying this upscaling) coefficient and the corresponding climatological runoff of the peninsular rivers flowing into the BoB. All these rivers show large interannual variations.

### 2.3.3. Reference and sensitivity experiments

The reference experiment (REF) is the model simulation using the forcing described above. In Chapter 5, we also performed sensitivity experiments to evaluate the importance of each of the forcing fluxes (viz. precipitation flux, runoff freshwater flux, momentum) on SSS interannual variability in the BoB (see Table 2.1). To illustrate the influence of each of the above forcing terms, we introduced the interannually-varying fluxes sequentially one by one, while keeping the other fluxes as seasonal climatologies. Table 2.1 summarizes the experiments used in this study. The  $\text{Tau}_{\text{int}}$  experiment retains the interannual wind forcing flux while all fresh water fluxes are introduced as seasonal climatologies. The  $\text{P}_{\text{int}}$  experiment has interannual precipitation and climatological wind speed and river run off. The  $\text{R}_{\text{int}}$  experiment keeps runoff as interannual and precipitation and wind as climatology.

<b>Name</b>	<b>Description</b>
<b>REF</b>	Full forcing interannual
<b>Tau<sub>int</sub></b>	Interannual <b>Tau</b> and all other forcing are climatology
<b>P<sub>int</sub></b>	Interannual <b>P</b> and all other forcing are climatology
<b>R<sub>int</sub></b>	Interannual <b>R</b> and all other forcing are climatology

**Table 2.1:** List of experiments used in this study

### 2.3.4. Model mixed layer salinity budget

One of the main goals of this work is to understand how oceanic processes act to balance the atmospheric forcing and regulate SSS in the BoB. The mixed layer salinity (or temperature) budget method [e.g. *Vialard et al.*, 2002] allows to compute the salinity tendency terms vertically averaged within the time-varying mixed layer depth (MLD). This methodology has been extensively used, for example for studying the salinity balance in the Pacific [*Vialard et al.*, 2002] or the processes driving SST in the northern IO [*de boyer Montégut*, 2005]. The model MLD is defined as the depth where density is  $0.01 \text{ kg}\cdot\text{m}^{-3}$  higher than surface density. Such a small criterion allows the vertically averaged mixed layer salinity to be a good proxy of SSS [*de Boyer*

Montégut *et al.*, 2007]. In order to compute the ocean mixed layer (ML) salinity budget, the various terms contributing to salinity evolution are averaged over the ML online, stored as 5 day averages, and grouped as follows:

$$\begin{aligned} \partial_t \langle S \rangle = & - \underbrace{\langle u \partial_x S + v \partial_y S \rangle}_a - \underbrace{\langle w \partial_z S \rangle}_b - \underbrace{\frac{1}{h} \frac{\partial h}{\partial t} (\langle S \rangle - S(z = h))}_c \\ & + \underbrace{\frac{(k \partial_z S)(z = h)}{h}}_d + \underbrace{\frac{(E - P - R)S}{h}}_e + \underbrace{\langle D_l(S) \rangle}_f \end{aligned} \quad \text{----- (2.2)}$$

Where brackets denote the vertical average over the time-varying mixed layer depth  $\mathbf{h}$ ,  $\mathbf{S}$  is the model salinity,  $(\mathbf{u}, \mathbf{v}, \mathbf{w})$  are the components of ocean currents,  $\mathbf{D}_l(\mathbf{S})$  the lateral diffusion operator,  $\mathbf{k}$  the vertical diffusion coefficient,  $\mathbf{E}$  is the evaporation,  $\mathbf{P}$  the precipitation, and  $\mathbf{R}$  the river runoff. The term (a) represents the horizontal advection, (b) the vertical advection, (c) is the entrainment, (d) the vertical diffusion through the mixed layer base, (e) is freshwater flux forcing of the mixed layer, and (f) is lateral diffusion. I will use this salinity budget calculation to infer the respective contributions of these processes to the seasonal SSS evolution in the BoB. Terms b, c and d are grouped to collectively represent the effect of exchanges between the mixed layer and interior ocean (may they be due to upwelling or mixing). The term f was usually negligible in the situations we examined. This method has never been used in a model of the BoB without SSS relaxation, which is one of the novel points of my PhD.

## Chapter 3

# Assessment of SMOS and Aquarius surface salinity retrieval in the Bay of Bengal

---

### Foreword

As presented in the introduction chapter, the BoB is a semi-enclosed basin with strong meridional and vertical salinity gradients. This intense haline stratification has a strong impact on the regional climate. An improved description and understanding of its variability is hence essential. Despite a recently much improved *in-situ* salinity observational network (in particular since the advent of Argo), the spatio-temporal sampling of *in-situ* observations is yet insufficient to provide a complete description of the SSS variations. There is in particular still a dearth of *in-situ* SSS observations in coastal regions, which practically prevent from correctly estimating even the mean seasonal cycle there. There are additionally completely data-void regions such as the Andaman Sea. Finally, the current *in-situ* data only offer a very partial view of the basin-scale SSS interannual anomalies. The recent development of SSS remote-sensing capabilities (SMOS and AQUARIUS satellites) offers an interesting opportunity to obtain a higher spatial resolution and more complete spatial sampling, as well as a better temporal sampling of SSS at basin scale in the BoB, even in areas that are completely devoid of *in-situ* observations such as the Andaman Sea. However, the BoB is a particularly challenging region for the application of satellite-derived SSS measurements, mainly because of the potential contamination of the signal by radio-frequency interferences (RFI) and by land sources. Hence the objective of this chapter is to provide an in-depth assessment of the ability of most recent SSS products from both satellites to monitor the seasonal and interannual SSS signals in the BoB over a ~3-4 years period. This is done by comparing their retrieved SSS to co-located data from the exhaustive *in-situ* SSS dataset described in Chapter 2. The SMOS dataset does not seem to offer much added value compared to existing climatologies, possibly because it is more heavily influenced by RFI and land-contamination due to the larger footprint inherent to its measurement technique, a major caveat for a small, semi-

enclosed basin like the BoB. On the other hand, the Aquarius dataset seems to reasonably capture large-scale SSS patterns over the BoB, both at seasonal and interannual timescales, making it a promising new tool to investigate SSS variability in this basin.

Previous preliminary studies of Aquarius and SMOS performance in the BoB, using older versions of the products and considering a much shorter period, concluded about severe problems for SMOS and Aquarius. Our study considers a much more complete *in-situ* database for validation and demonstrates that, despite noisy fields at small scale, Aquarius does a good job of capturing large-scale SSS seasonal cycle and interannual anomalies.

**The contents of this chapter are based on the following submitted article:**

VP Akhil, M Lengaigne, F Durand, J Vialard, MG Keerthi, VV Gopalakrishna, VS Chaitanya, J Boutin, C de Boyer Montégut (2015) **An assessment of the ability of SMOS and Aquarius missions to retrieve seasonal and interannual surface salinity signals in the Bay of Bengal**, to be submitted to International Journal of Remote Sensing.

## Abstract

The BoB exhibits a wide range of SSS, with very fresh water induced by heavy monsoonal precipitation and river runoffs to the north, and saltier water to the south. This semi-enclosed basin surrounded by land is a particularly challenging region for the application of satellite-derived SSS measurements because of the potential contamination of the SSS signal in this near-coastal environment by RFI and land sources. The present study thus validates and compares the latest level-3 monthly gridded ( $1^\circ \times 1^\circ$ ) SSS products from SMOS and Aquarius missions against an exhaustive *in-situ* SSS product in the Bay. Our results reveal that SMOS SSS does not perform better than existing climatologies in this region. This is in stark contrast with Aquarius that outperforms both SMOS and existing SSS climatologies everywhere in the Bay. While SMOS only captures the SSS seasonal evolution in the northern part of the Bay, Aquarius accurately captures the seasonal signal everywhere in this basin. In contrast with SMOS, the Aquarius product is also able to capture SSS non-seasonal anomalies, with a  $\sim 0.75$  correlation with box-averaged *in-situ* data in the northern, central and western part of the Bay. While this study demonstrates that Aquarius can be confidently used to monitor interannual SSS variations in this climatically important region, the serious issues encountered by SMOS advocate for improvements of its SSS retrieval algorithm for this region.

### 3.1. Introduction

The BoB stands out as a very peculiar region for salinity distribution in the tropical belt. The strong oceanic rainfall and continental runoffs during summer monsoon into this relatively small and semi-enclosed basin results in an intense dilution of the seawater in northern part of the Bay, therefore inducing some of the lowest SSS in the tropical belt (Figure 3.1). The resulting very sharp near-surface salinity vertical stratification is believed to play a key role in the regional climate. Indeed, the enhancement of near-surface ocean stability by salinity stratification reduces vertical mixing. As a result, SST remains above 28.5°C, a necessary condition to maintain deep atmospheric convection and rainfall, hence providing a positive feedback loop between high SST, strong rainfall and strong vertical salinity stratification [Shenoi *et al.*, 2002]. The BoB salinity stratification may also influence the intensity of the devastating tropical cyclones that form over the Bay. The sharp vertical salinity stratification after the monsoon indeed inhibits vertical mixing and surface cooling below cyclones, hence promoting an intense evaporation at the ocean surface that feeds the cyclone “heat engine” and favours its intensification [Neetu *et al.*, 2012 and reference therein]. Last but not least, salinity could also act as a marker of changes in the water cycle associated with anthropogenic forcing [e.g. Terray *et al.*, 2012].

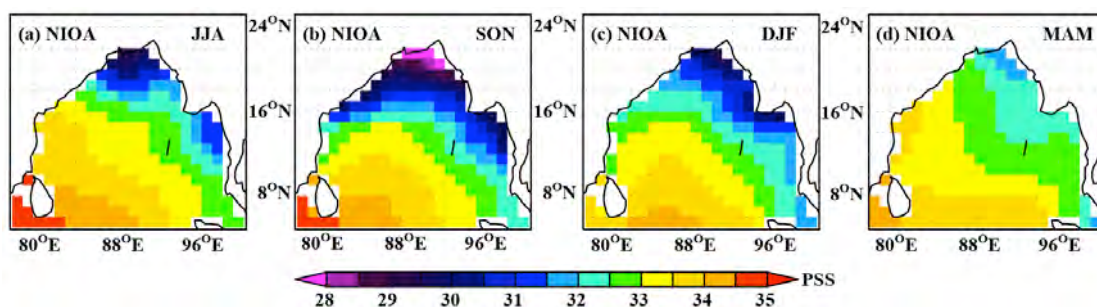


**Figure 3.1.** Climatological SSS in the BoB from NIOA [Chatterjee *et al.*, 2012] for (a) JJA, (b) SON, (c) DJF, (d) MAM.

Despite the potentially important role of salinity in the climate dynamics of this region, the salinity distribution in the BoB has not yet been fully described. Existing salinity climatologies derived from available hydrographic data [Chatterjee *et al.*, 2012; Zweng *et al.*, 2013] reveal a strong freshening in the northeastern part of the Bay during summer in response to the huge freshwater flux driven by monsoonal

rainfall and GB river discharge (Figure 3.1a). This freshwater pool further strengthens and expands southward along the eastern and western boundaries of the Bay in fall (Figure 3.1b). It then weakens during winter (Figure 3.1c) and retreats back to the very northeastern part of the Bay during spring (Figure 3.1d). While these climatologies are not able to capture the fine spatial scale of this coastal freshening [Chaitanya *et al.*, 2014a], the *in-situ* data coverage used in these products is sufficient to capture the main large-scale SSS seasonal features in the Bay [Chatterjee *et al.*, 2012]. The monitoring of SSS interannual variability is however generally far more challenging due to the insufficient spatio-temporal sampling of the *in-situ* network [Vinayachandran and Nanjundiah, 2009; Chaitanya *et al.*, 2014b].

The advent of satellite salinity measurements provides a unique opportunity to improve the monitoring of SSS variations in this climatically important region. The SMOS European mission [Mecklenburg *et al.*, 2008] launched in November 2009 and the Argentina/US Aquarius mission [Lagerloef *et al.*, 2008] operating since June 2011 both provide global SSS estimates at monthly resolution. These new spaceborne SSS measurements are routinely validated, with global root-mean-square errors around 0.3-0.4 pss for monthly Aquarius SSS fields on a ~150 km global grid [Lagerloef *et al.*, 2013] and for 10-days SMOS averages on a ~100 km grid in the tropical regions [Boutin *et al.*, 2012]. Recent research has demonstrated the value of these satellite missions in capturing open-ocean signals related to large-scale climate modes such as La Niña signature in the tropical Pacific [Hasson *et al.*, 2014], the IOD signature in the eastern part of this basin [Durand *et al.*, 2013] or planetary waves signature in the southern IO [Menezes *et al.*, 2014]. Whether these satellite data can accurately capture SSS variations in relatively small basins surrounded by continental masses however remains unclear. Near-coastal environments are indeed particularly challenging for the application of satellite-derived SSS measurements because RFI linked to artificial sources (e.g. radars that emit in the frequency band of the instruments) and “land-induced” contamination on antenna side lobes [Reul *et al.*, 2012; Subrahmanyam *et al.*, 2013], can obscure relevant signals there. A recent study [Gierach *et al.*, 2013] however successfully demonstrated the ability of both Aquarius and SMOS to monitor the SSS variation in the Gulf of Mexico, offering promises for monitoring SSS evolution in a near-coastal environment.

The BoB, a ~1000-2000 km wide semi-enclosed basin similar to the Gulf of Mexico, is also very challenging for satellite retrieval algorithms. A thorough validation of the SSS remotely-sensed products is therefore a pre-requisite before using these data to describe and understand the SSS evolution in this region. Preliminary analyses reported major issues in the satellites ability to retrieve SSS there. *Subrahmanyam et al.*, [2013] and *Ratheesh et al.*, [2013] indeed reported an erratic behaviour of the level-3 SMOS dataset in this region for the year 2010, with weak and insignificant spatial correlations, and attributed this behaviour to RFIs and land contamination. Similarly, analyses performed by *Ratheesh et al.* [2014] for level-3 Aquarius dataset over the entire IO region from August 2011 to December 2012 reported a 0.5 pss overestimation and a poor agreement with observations for SSS values lower than 32 pss, which are typical of the northern part of the Bay.

While these preliminary studies are not encouraging, improvements such as a rain-corrected salinity retrieval for Aquarius [*Yueh et al.*, 2014] and an improve handling of RFI contamination for SMOS [*Reul et al.*, 2014] are now available for the most recent SSS products derived from the microwave instruments on board these satellites. In addition, both missions have now accumulated about three years of data, allowing a qualitative assessment of the ability of each satellite to capture the SSS seasonal and interannual evolution in this region. The goal of the present study is therefore to provide an in-depth, up-to-date assessment of the ability of both satellites to monitor the seasonal and interannual SSS signals in the BoB. This will be done by splitting the basin into various sub-regions and by comparing remotely-sensed SSS to a comprehensive dataset compiling all *in-situ* observations available during the recent period [*Chaitanya et al.*, 2014b]. This paper will focus on the validation of the most recent versions of monthly  $1^\circ \times 1^\circ$  level-3 products for both missions. Due to the larger number of measurements used to compute the SSS pixel-average, these coarse resolution products are indeed expected to exhibit a better accuracy compared to higher resolution products [*Hernandez et al.*, 2014]. Our manuscript is organized as follows. Section 3.2 presents the satellite products and *in-situ* SSS datasets, as well as our validation method. Section 3.3 provides an overview of the quality of the remotely-sensed SSS. The ability of the satellite products to retrieve the SSS seasonal cycle and the departure from this seasonal cycle is discussed in Section 3.4 and 3.5 respectively. Section 3.6 finally concludes our study and discusses its main outcome.

## 3.2. Datasets and methods

This section describes the two satellite SSS products (Sections 3.2.1 and 3.2.2), the *in-situ* dataset (Sections 3.2.3) used in the present study and discusses the collocation method used to compare *in-situ* and remotely sensed data (Section 3. 2.4).

### 3.2.1. SMOS level-3 data

SMOS is a polar orbiting satellite with a passive microwave sensor operating within the L-Band (at 1.404-1.423 GHz), operated as part of ESA's Living Planet Programme [McMullan *et al.*, 2008; Mecklenburg *et al.*, 2012]. SMOS was launched on 2<sup>nd</sup> November 2009, making it the first satellite to provide continuous multi-angular L-band radiometric measurements over the globe. It is based on 69 individual radiometers that are used to retrieve the SSS field through polarimetric interferometry (see Kerr *et al.* [2010]; Reul *et al.* [2012, 2013], and references therein for further details on the measurement technique). Due to the interferometry principle and the antenna shape, the field of view is about 1000 km wide and a global coverage is achieved within three days.

Instantaneous SSS retrievals under the satellite swath, corresponding to ESA level-2 SSS products, have a spatial resolution of 43 km but exhibit a rather low accuracy of 0.6 to 1.7 pss [Reul *et al.*, 2012; Boutin *et al.*, 2012]. To decrease the noise level in the retrievals, we use the latest 1°×1° gridded monthly SSS composites from the V02 version of the SMOS level-3 research product generated by the CATDS, France. This product is built from ESA level 1B products. It includes an improved RFI mitigation and a 5°×5° adjustment to the World Ocean SSS climatology of Antonov *et al.* [2010] to remove residual temporal drifts and land contamination in SMOS brightness temperature level 1 products [Reul *et al.*, 2014]. This SSS bias mitigation and the better handling of RFIs improves the data quality close to the coast compared to other level-3 products [Zhang *et al.*, 2013].

Data of the first four months of 2010 were not reprocessed because of a reduced data quality during that period. This product therefore covers the May 2010-December 2013 period. As shown on Figure 3.2a, this product has very little missing values throughout the central and southern Bay. The percentage of valid data however drops considerably in the northeastern part of the basin near the GB river mouth, with hardly any SSS retrieval north of 20°N. This drop largely results from brightness temperatures flagged as outliers (not shown).

### **3.2.2. Aquarius level 3 data**

Aquarius is NASA's new Earth orbiting mission launched on 10<sup>th</sup> June 2011. The Aquarius instrument measures the brightness temperature of the sea surface within the L-band (1.400-1.427 GHz) with three separate radiometers. These data, in combination with concurrent SST, scatterometer measurements, and other auxiliary data, are used to estimate SSS. The resolution of individual SSS measurements is about 100 km and a global coverage of the ocean is obtained after about 7 days.

This study uses the latest Aquarius level-3 1°×1° monthly composites. This product combines the measurements from the three radiometers using the Combined Active-Passive Algorithm applied to version 3.0 of the Aquarius/SAC-D data updated in July 2014 (available at <ftp://podaac-ftp.jpl.nasa.gov/allData/aquarius/L3/mapped/CAPv3>). This algorithm simultaneously retrieves SSS, wind speed and wind direction by minimizing the sum of squared differences between model and observations and includes a rain-corrected salinity retrieval based on collocated SSMI/S and WindSAT data.

This product covers the August 2011 - June 2014 period. Like SMOS (Figure 3.2a), Aquarius exhibits very few missing data south of 15°N (Figure 3.2b). However, Aquarius offers a better spatial coverage in the northernmost part of the basin as compared to SMOS, because there is no far-reaching RFI issue for Aquarius whose antenna lobes are much narrower than for SMOS, due to the interferometry technique used for the SMOS instrument.

### 3.2.3. Validation datasets

The recent NIOA SSS climatology issued by *Chatterjee et al.* [2012] and shown in Figure 3.1 is used to qualitatively validate the SSS seasonal cycle from the satellite data. This  $1^{\circ} \times 1^{\circ}$  monthly climatology includes all the data from the WOD09 [*Locarnini et al.*, 2010; *Antonov et al.*, 2010], complemented with CTD stations from Indian oceanographic cruises. The inclusion of the Indian oceanographic cruises database in NIOA considerably improves the data coverage in the periphery of the BoB compared with WOD09, especially along its western boundary [*Chatterjee et al.*, 2012]. Interannual SSS anomalies from both satellite datasets and *in-situ* products detailed below are calculated by subtracting this NIOA climatology from their raw values.

Comparisons with a recent *in-situ* dataset directly derived from the one presented in *Chaitanya et al.* [2014b] will allow a quantitative validation of the satellites retrieval. This dataset compiles all the available *in-situ* SSS measurements available over the BoB from December 2008 to June 2014. It gathers six different salinity data sources: Argo profilers [*Roemmich et al.*, 2009], ship-of-opportunity XCTD profiles and bucket measurements [*Chaitanya et al.*, 2014b], RAMA moorings [*McPhaden et al.*, 2009], OMNI moorings [*Venkatesan et al.*, 2013], ship-of-opportunity thermosalinograph transects [*Alory et al.*, 2015] and dedicated hydrographic cruises. Argo profiles are the main contributor to this SSS product. Considering the uppermost valid measurements within the 5 m to 15 m layer results in more than 10000 valid salinity measurements over the 2009-2014 period, which are typically located at around 8 m depth. This *in-situ* dataset also includes 1200 valid measurements at about 1 m depth from bucket samples and at 5 m depth from XCTD salinity measurements collected on an approximately monthly basis along two repeated merchant ship tracks between Chennai (label « C » in Figure 3.2c, d) and Port Blair (label « PB »), and between Kolkata (label « K ») and Port Blair. In addition, our dataset comprises pointwise salinity measurements at 1 m depth over the 2009-2014 period from three RAMA moorings ( $90^{\circ}\text{E}-8^{\circ}\text{N}$ ;  $90^{\circ}\text{E}-12^{\circ}\text{N}$  and  $90^{\circ}\text{E}-15^{\circ}\text{N}$ ; circles on Figure 3.2c, d) and at 5 m depth from six OMNI moorings ( $11^{\circ}\text{N}-86.5^{\circ}\text{E}$ ,  $8^{\circ}\text{N}-85.5^{\circ}\text{E}$ ,  $14^{\circ}\text{N}-83^{\circ}\text{E}$ ,  $16.5^{\circ}\text{N}-88^{\circ}\text{E}$ ,  $10.5^{\circ}\text{N}-94^{\circ}\text{E}$ ,  $18.2^{\circ}\text{N}-89.7^{\circ}\text{E}$ ; triangles on Figure 3.2c, d). Finally, this dataset also includes salinity measurements representative of the 0-10 m

upper ocean layer derived from a thermosalinograph on-board a merchant ship (M/S Lavender) crossing the southern Bay every 3-4 months during the October 2008 to October 2012 period (dotted line in Figure 3.2c, d) and a few 0-10 m depth measurements from ship borne CTD casts performed by the National Institute of Oceanography Data Centre (India) in the coastal western Bay. More details on this dataset can be found in *Chaitanya et al.* [2014b], who demonstrated that the error arising from the diverse sampling depths of these measurements within 0-10 m is typically much smaller than the magnitude of the SSS variations reported in their analysis. Using this dataset, *Chaitanya et al.* [2014b] further demonstrated that the northern part of the Bay exhibits strong interannual SSS variations (more than 1pss), largely driven by freshwater flux variability.

#### **3.2.4. Colocation method**

In a similar way to *Chaitanya et al.* [2014b], these six data sources were merged into a single dataset by computing the median of all available individual measurements (irrespective of their nature: autonomous profiler, mooring, underway ship measurements), at the spatial and temporal resolution of the satellite products ( $1^{\circ} \times 1^{\circ} \times 1$  month). The gridding is performed on both the SMOS and AQUARIUS native  $1^{\circ} \times 1^{\circ}$  grids (as the two grids are offset by  $0.5^{\circ}$ , both in latitude and in longitude), resulting in two versions of our gridded product. The main difference with the original *in-situ* product presented in *Chaitanya et al.* [2014b] is the temporal resolution: while *Chaitanya et al.* [2014b] presented a three monthly product, the present study uses a monthly resolution to allow a validation of the two satellite level-3 products at their native temporal resolution.

Figures 3.2c, d illustrate the data density of the *in-situ* data, collocated with each of the remotely sensed SSS products. The *in-situ* validation data density is rather heterogeneous, with a reasonably good sampling over most of the central part of the Bay but sparser data in near-coastal regions. This analysis also reveals that the Andaman Sea (east of  $93^{\circ}\text{E}$  and south of  $15^{\circ}\text{N}$ ) is practically devoid of *in-situ* observations, preventing an assessment of the remotely sensed SSS products there.

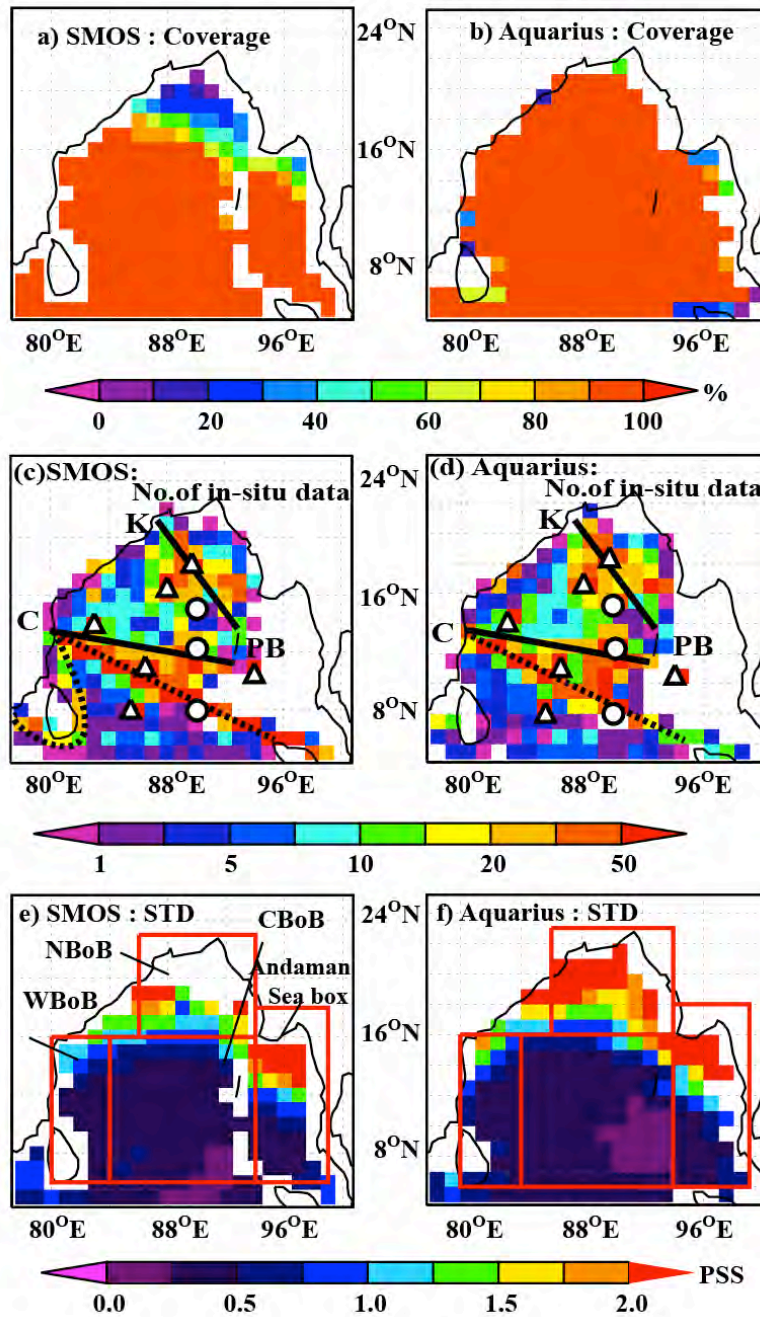


**Figure 3.2.** Percentage of valid monthly SSS retrievals in the BoB for (a) SMOS and (b) Aquarius. Total number of *in-situ* observations profiles per  $1^\circ \times 1^\circ$  box and per year collocated with (c) SMOS and (d) Aquarius. Circles on panels c and d indicates RAMA mooring location, while triangles indicate OMNI moorings. The two continuous lines on panels c, d indicate the track of merchant ships between Port Blair (PB) and Chennai (C) / Kolkata (K), along which  $\sim 1200$  XCTD and bucket measurements were collected. The dotted line indicates the track of the merchant ship along which thermosalinograph measurements are performed. (e) SMOS and (f) Aquarius SSS standard deviation. The standard deviation on panels e, f is only shown for pixels with more than 11 months of data. The red boxes on panels (e) and (f) indicate the limits of the regions discussed in Sections 3.3 and 3.4: NBoB ( $86^\circ\text{E}$ - $94^\circ\text{E}$ ;  $16^\circ\text{N}$ - $23^\circ\text{N}$ ), WBoB ( $80^\circ\text{E}$ - $84^\circ\text{E}$ ;  $6^\circ\text{N}$ - $16^\circ\text{N}$ ), CBoB ( $84^\circ\text{E}$ - $94^\circ\text{E}$ ;  $6^\circ\text{N}$ - $16^\circ\text{N}$ ) and Andaman Sea box ( $94^\circ\text{E}$ - $99^\circ\text{E}$ ;  $6^\circ\text{N}$ - $18^\circ\text{N}$ ).

In the following, a detailed description of the SSS variability in the BoB will be inferred by dividing the domain into four coherent sub-regions outlined on Figure 3.2e, f. The first sub-region covers the northern part of the basin (NBoB, 86°E-94°E; 16°N-23°N) where the largest SSS fluctuations are found (Figure 3.2e, f), due to the proximity of the GB river mouths and monsoonal precipitation [Rao and Sivakumar, 2003; Akhil *et al.*, 2014]. The second sub-region is located in the western part of the Bay (WBoB, 80°E-84°E; 6°N-16°N) and encompasses the coastal region through which the NBoB freshening is transported southward during winter as a fresh tongue that hugs the eastern Indian coastline [Chaitanya *et al.*, 2014a]. A third sub-region is located in the central BoB (CBoB, 84°E-94°E; 6°N-16°N), where the SSS variability is known to be weaker. Finally, a fourth sub-domain is considered in the Andaman Sea (94°E-99°E; 6°N-18°N), where the variability derived from satellite products is about as strong as in the northern part of the basin (Figure 3.2e, f) but cannot be validated due to the lack of *in-situ* observations (Figure 3.2c, d). We will compare the remotely-sensed SSS to *in-situ* data on the 1° x 1° x monthly grid, but also from averages over the boxes above. This spatial averaging has the advantage of smoothing out representation error of the *in-situ* data, as well as potential noise in the satellite retrievals, and to focus the comparison with *in-situ* data on large-scale features.

### 3.3. General evaluation of the remotely-sensed SSS products

Figure 3.3a, b provides a synthetic view of the consistency between the 1°×1° monthly remotely-sensed SSS estimates and the *in-situ* reference product. These panels illustrate that the agreement with *in-situ* dataset is generally better for Aquarius (0.82 correlation) as compared to SMOS dataset (0.69 correlation). In addition, Aquarius does not exhibit any significant basin-scale SSS bias (0.01 pss), while SMOS generally underestimates the SSS in the BoB (-0.22 pss). Rather surprisingly, Aquarius however exhibits the same RMSD as SMOS (~0.88). Those statistics are however computed over different samples, due to the different periods, grids and missing data of the two satellite products. Computing the above statistics for the same sample (i.e. common pixels for the SMOS, Aquarius and reference *in-situ* product; numbers in brackets on Figure 3.3a, b) to allow a fair comparison between the two satellite products reveals that Aquarius outperforms SMOS retrieval for all considered

statistics. The Aquarius RMSD, in particular, is 0.68 and smaller than SMOS (0.89) when considering the sample common to the three products.

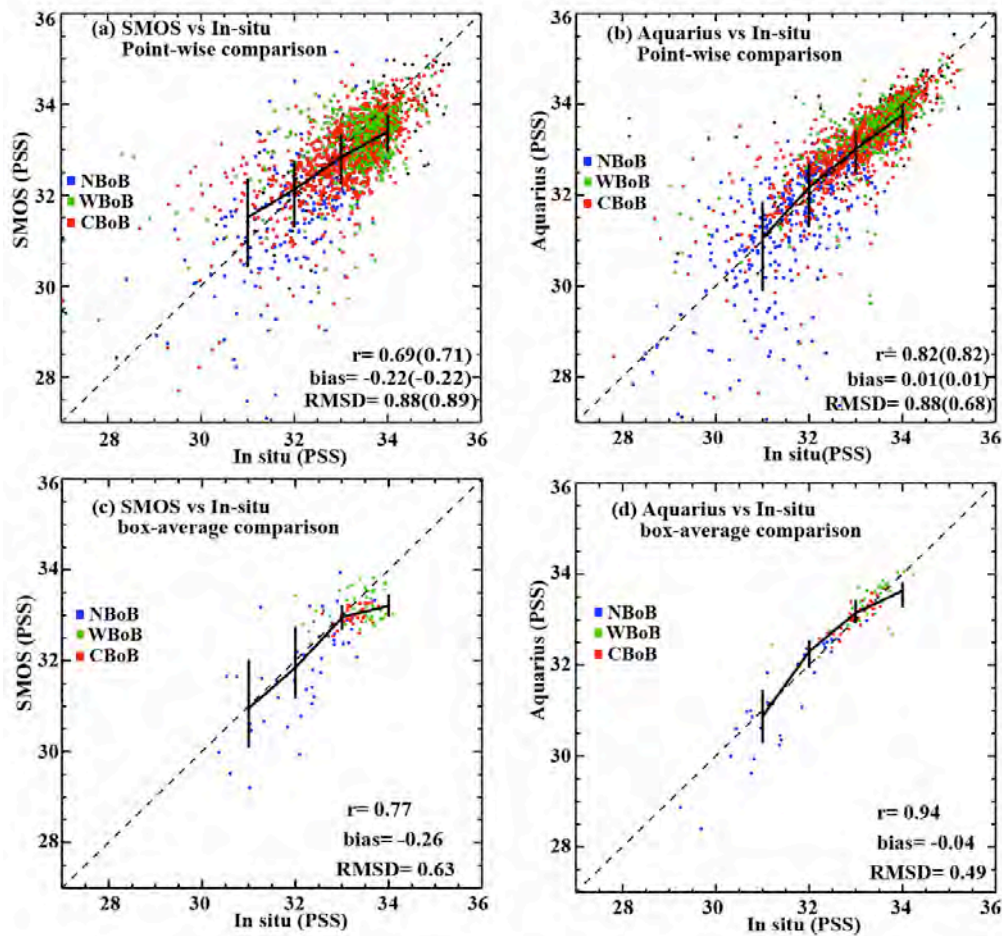


**Figure 3.3.** Scatter plot of (a) SMOS and (b) Aquarius monthly SSS retrievals against collocated estimates from the gridded *in-situ* dataset. The statistics are computed from May 2010 to December 2013 for SMOS and from August 2011 to June 2014 for Aquarius. The corresponding correlation ( $r$ ), root-mean square difference (RMSD) and bias are provided on the lower right of each panel. Values in brackets correspond to collocated SMOS, Aquarius and *in-situ* data (i.e. the same spatio-temporal sampling is used for both datasets, and the statistics for the two satellites are hence strictly comparable). (c) and (d) are similar to (a) and (b), but for averaged monthly SSS values over the boxes displayed on Figure 3.2e, f. Blue dots indicate collocated data located in NBoB, green in WBoB and red in CBoB, while black dots indicate collocated data outside these boxes. The black line indicates median value of each 1ps *in-situ* SSS bin while vertical bars indicate the upper and lower quartiles of the distribution.

This sensitivity of Aquarius RMSD to the collocation method (0.68 for the common sample and 0.88 for the *in-situ* – Aquarius collocated data) arises from the extended Aquarius spatial coverage that allows retrieving SSS in the very northern part of Bay, which is not the case for the SMOS product (Figure 3.2a, b). In this region, the SSS variability is known to be larger than in the other regions, resulting in larger SSS error compared to other regions of the BoB (illustrated by the larger scatter

between Aquarius and *in-situ* data for low SSS values, Figure 3.3b). A closer look at Figure 3.3a, b also reveals that the satellites performance strongly varies depending on the SSS value. While Aquarius does not show any significant bias for SSS ranging from 34 to 31 pss, SMOS is generally fresher than the reference product for SSS higher than 33 and saltier for SSS lower than 33. The scatter of both satellites around the reference value is also particularly large for the NBoB box (blue dots on Fig 3.3ab) compared to the other regions.

Aside from an inaccurate SSS retrieval, small spatial scale and high frequency SSS features sampled by *in-situ* observations but not by the satellite products may account for some of the inconsistencies between *in-situ* and satellite measurements. Comparing spatial averages of these three datasets over the large boxes presented in Section 3.2.4 allows to smooth out a large part of small scale SSS variations in the *in-situ* datasets as well as noise in the satellite data retrieval and therefore to assess the impact of small spatial scale and high frequency features on our SSS validation. The results are presented on Figure 3.3c, d. Both SMOS and Aquarius correlations increase by  $\sim 0.1$  when computing box-averaged values rather than pixel-wise. The RMSD reduction is however larger for Aquarius (from 0.88 to 0.49) than for SMOS (from 0.88 to 0.63). This larger error reduction in Aquarius suggests that part of the mismatch between Aquarius and *in-situ* data is attributable to small-scale spatial noise smoothed out when averaging over a large box (typically 1000 km wide) while a larger part of the SMOS retrieval error has probably a broader spatial scale, and hence cannot be reduced by spatial averaging.

Figure 3.4 further provides a synthetic assessment of the ability of both satellites to retrieve the SSS in the NBoB, WBoB and CBoB sub-regions. It features the bias, correlation and RMSD between box-averaged satellite and *in-situ* values. As far as the mean state is concerned, SMOS retrievals exhibit a systematic fresh bias everywhere in the Bay (Figure 3.4a), ranging from -0.19 pss in WBoB to -0.35 pss in NBoB. This result is opposite to *Reul et al.* [2012] and *Ratheesh et al.* [2012] who both reported a salty bias of SMOS retrievals over the Bay over the year 2010, in earlier versions of SMOS products. In contrast, Aquarius exhibits a bias weaker than 0.1 pss in CBoB and WBoB and a fresh bias of -0.26 pss in NBoB (Figure 3.4a). The phase agreement is also considerably better for Aquarius than for SMOS in all sub-

regions: Aquarius correlations range from 0.79 in WBoB to 0.94 in NBoB while SMOS correlations are considerably weaker, ranging from 0.24 in WBoB to 0.69 in NBoB (Figure 3.4b). Aquarius also outperforms SMOS in all BoB sub-regions when considering the RMSD statistics (Figure 3.4c).

The above analyses show that Aquarius outperforms SMOS for all statistics and all sub-regions of the BoB. SMOS appears to be particularly poor in retrieving the SSS variability in the central and western part of the BoB while Aquarius performs accurately over the entire BoB. The SSS variability in each sub-region can either arise from seasonal variations or from departures from the mean seasonal cycle. The next two sections provide a validation of both satellites at these two timescales.

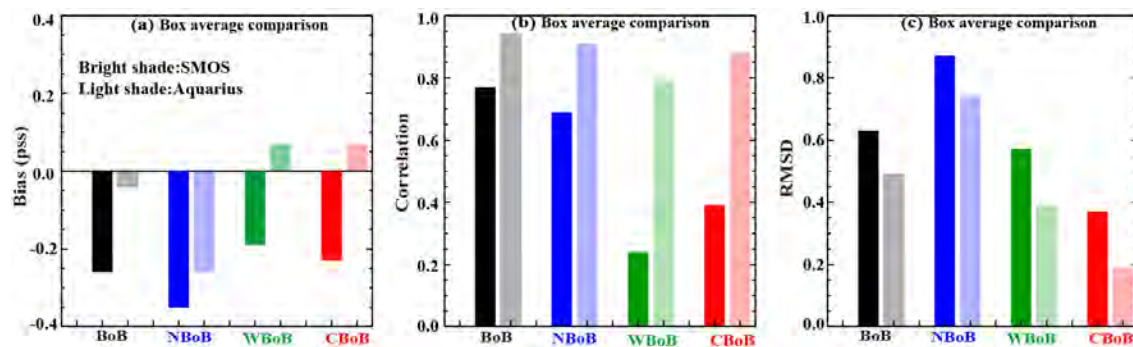


**Figure 3.4.** (a) Systematic bias, (b) correlation and (c) RMSD of box averaged satellite SSS retrievals (SMOS in Bright shade and Aquarius in Light shade) against box averaged gridded *in-situ* SSS dataset over each sub-region of the BoB.

### 3.4. Seasonal evaluation of the remotely-sensed products

Figure 3.5 displays the NIOA quarterly climatology, along with the corresponding climatology derived from SMOS and Aquarius. Of course, the three products are not expected to be strictly comparable, because SMOS and Aquarius measurements cover a much shorter period than those gathered in the NIOA. This figure hence only provides a qualitative assessment of the remotely-sensed SSS spatial distribution. A more quantitative validation of the seasonal SSS evolution of satellite data against *in-situ* measurements will be presented in Figure 3.6.

As already mentioned in the introduction, there is a strong contrast between fresh waters to the northeast and saltier waters in the southwestern part during the

monsoon (Figure 3.5a). Highest SSS values ( $>34$  pss) are found near the southern tip of Sri Lanka while freshest waters ( $<31$  pss) hug the vicinity of the GB estuaries. Following the summer monsoon withdrawal (Figure 3.5b), these northernmost waters further freshen below 30 pss and expand along both western and eastern boundaries. Finally, the eastern and western freshwater tongues gradually erode during winter and spring (Figure 3.5c, d). SMOS and Aquarius data qualitatively capture this basin-scale seasonal evolution (Figure 3.5e to 3.5l). Some differences between satellite and *in-situ* climatologies can however already be noticed: SMOS SSS are fresher than NIOA in the WBoB in summer (Figure 3.5a, e) and Aquarius SSS are fresher than NIOA in the NBoB in fall (Figure 3.5b, j). Large differences can also be found for both satellites in the Andaman Sea but the quality of NIOA climatology there is likely to be strongly hampered by the lack of *in-situ* observations in this region.

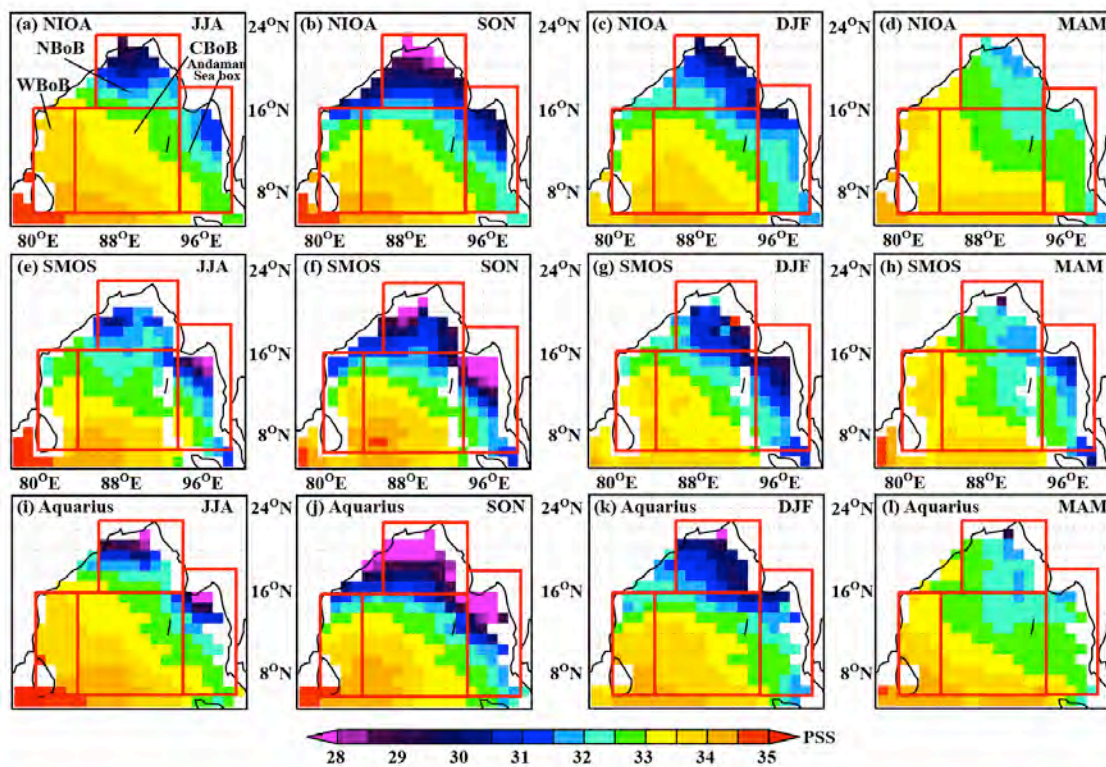


**Figure 3.5. (Upper panels)** Climatological SSS in the BoB for (a) JJA, (b) SON, (c) DJF, (d) MAM from NIOA climatology. **(Middle panels)** Same for SMOS climatology computed over May 2010 - December 2013 period. **(Bottom panels)** Same for Aquarius climatology computed over August 2011- June 2014 period. Salinity is given in pss (practical salinity scale, in  $\text{g kg}^{-1}$ ).

Figure 3.6 further provides a quantitative assessment of the SSS seasonal cycle from the satellites retrieval in the three sub-regions considered (NBoB, CBoB and WBoB) by comparing them to their collocated *in-situ* dataset. First of all, the seasonal

evolution of SSS in the three selected boxes from the collocated *in-situ* datasets (black lines on Figure 3.6) agrees reasonably well with the one derived from the NIOA box average (blue lines on Figure 3.6), with correlation larger than 0.8. This suggests that the *in-situ* dataset somewhat captures the observed seasonal variations in the BoB, despite the limited number of years (around three) used to build the seasonal cycle and the rather heterogeneous spatial coverage of this *in-situ* dataset (Figure 3.2c, d).

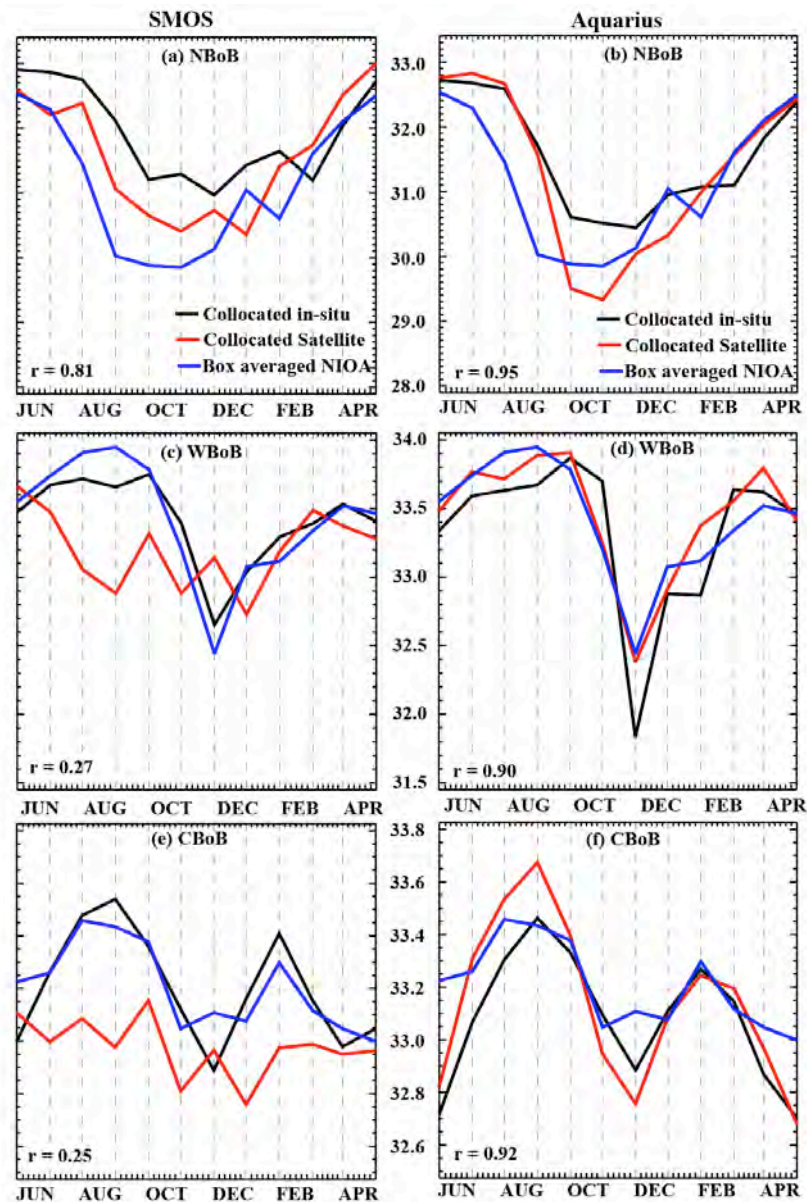


**Figure 3.6.** Time series of the seasonal SSS evolution in (a) NBoB, (c) WBoB and (e) CBoB (outlined on Figure 3.2e, f) from the gridded *in-situ* product (black line), collocated SMOS retrieval (red line), and box-averaged NIOA climatology (blue line). (b,d,f) Same as (a,c,e) but for Aquarius retrieval. Correlation of *in-situ* vs satellite is given in each panel.

In the northern part of the Bay, a 1.5 pss freshening is observed between July and October (black line on Figure 3.6a, b) in response to the huge fresh water flux from monsoonal rainfall and GB river discharge. This freshening is followed by a gradual saltening from November onward. The observed freshening is larger for the *in-situ* dataset collocated with Aquarius (Figure 3.6b) than for the one of SMOS (Figure 3.6a) due to the extended Aquarius data coverage in the northeastern most part of the Bay (Figure 3.2a, b) where the lowest salinities are found. Both satellite retrievals are able to capture this strong seasonal freshening reasonably well but overestimate the freshening signal during the post-monsoon season (red and black lines on Figure 3.6a, b). The phase agreement of Aquarius with the *in-situ* dataset is however better than the one derived from SMOS, with correlations of 0.95 and 0.81 respectively.

The WBoB SSS also displays a seasonal freshening similar to that of NBoB but occurring with a two month delay (Figure 3.6c, d), corresponding to the time it takes for the fresh waters in the northern Bay to be advected southward by the EICC along the western boundary [Chaitanya *et al.*, 2014a; Benshila *et al.*, 2014; Akhil *et al.*, 2014]. The observed freshening in WBoB is also larger for the *in-situ* dataset collocated with Aquarius (Figure 3.6d) than for the one of SMOS (Figure 3.6c). While Aquarius accurately reproduces the seasonal timing of this coastal freshening very accurately (0.9 correlation), SMOS displays a too early seasonal freshening starting in June, with several spurious peaks, resulting in a poor phasing with *in-situ* observations (0.27 correlation).

Finally, the SSS seasonal cycle in CBoB exhibits a semi-annual signal with two salinity minima occurring during fall and spring (Figure 3.6e, f). As for WBoB, Aquarius captures very accurately these seasonal variations (0.92 correlation; Figure 3.6f) while SMOS displays an erratic behaviour and is unable to retrieve this seasonal evolution (0.25 correlation; Figure 3.6e).

This validation shows that Aquarius adequately reproduces the observed SSS seasonal cycle in both near-coastal and open-ocean regions. In contrast, SMOS is unable to capture the seasonal variability south of 16°N, neither in the coastal region along the west coast of India nor in the central part of the Bay.

### 3.5. Interannual evaluation of remotely-sensed products

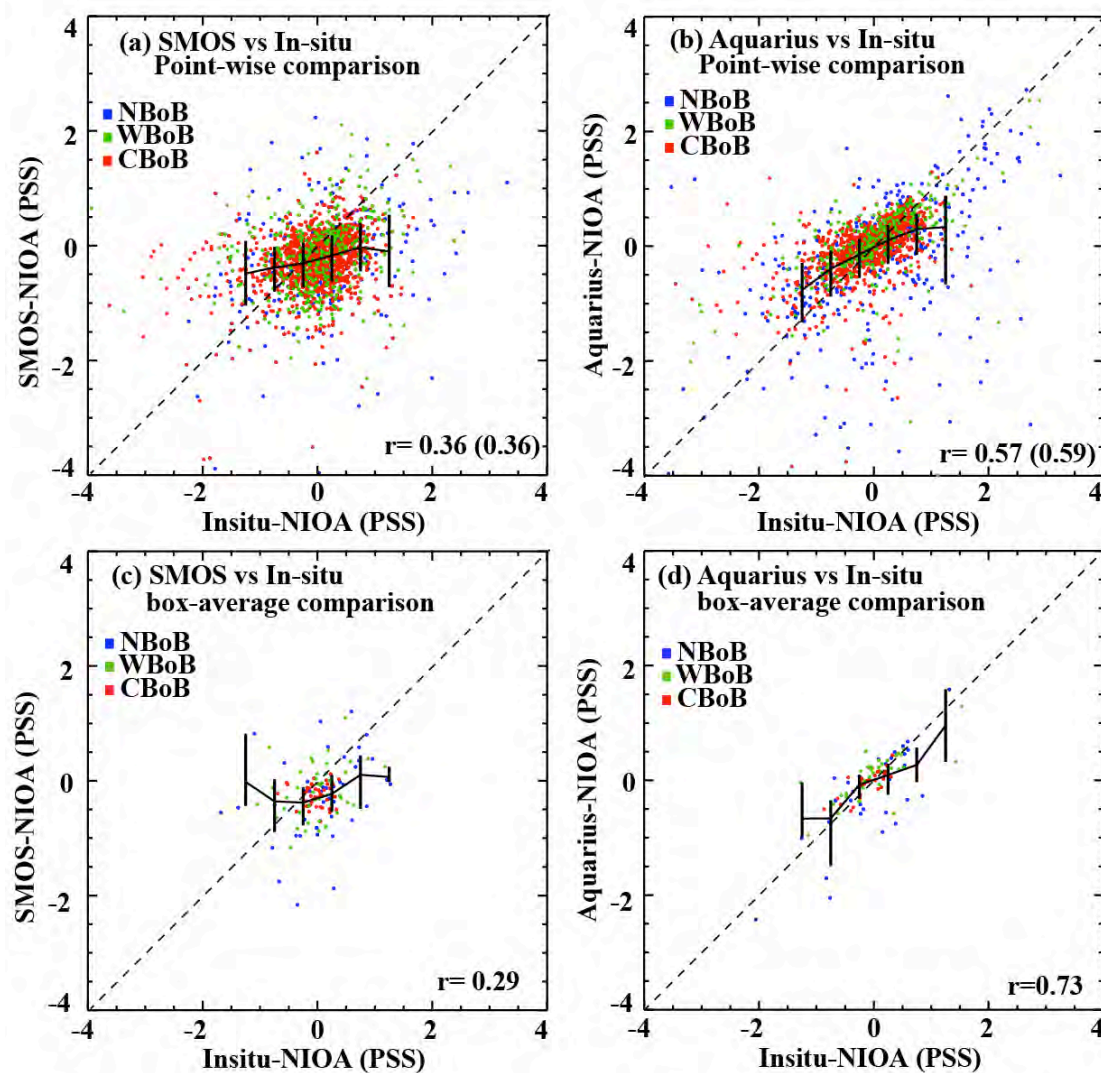


**Figure 3.7.** As Figure 3.3 but for SSS departures to the seasonal cycle calculated with respect to the NIOA climatology.

As existing *in-situ* climatologies such as NIOA already provide a reasonable description of SSS seasonal variations, a considerable added value of satellite products is their potential to describe SSS departures from the mean seasonal cycle. In order to qualitatively assess the satellites skill in capturing SSS non-seasonal anomalies, Figure 3.7 displays a scatterplot of each of the satellite SSS estimates deviations from the NIOA climatology against those from the *in-situ* reference product. A good agreement between satellites and *in-situ* data seasonal anomalies would result in a cloud of points aligned along the  $x = y$  axis while a strong underestimation of the non-seasonal

variability of the satellite SSS estimates would result in a cloud of points aligned along the  $y = 0$  axis. Figure 3.7a and 3.7c reveals that SMOS retrieval considerably underestimates the observed non-seasonal variations and exhibits a poor phase agreement with *in-situ* observations for both point-wise and box averaged comparisons (0.36 and 0.29 correlation, respectively). In stark contrast with SMOS, Aquarius reasonably captures the amplitude and phase of the observed SSS seasonal anomalies (0.57 and 0.73 correlation for point-wise and box averaged comparison respectively, Figure 3.7b, d) and may therefore provide additional valuable information with respect to the information already contained in the existing climatologies.

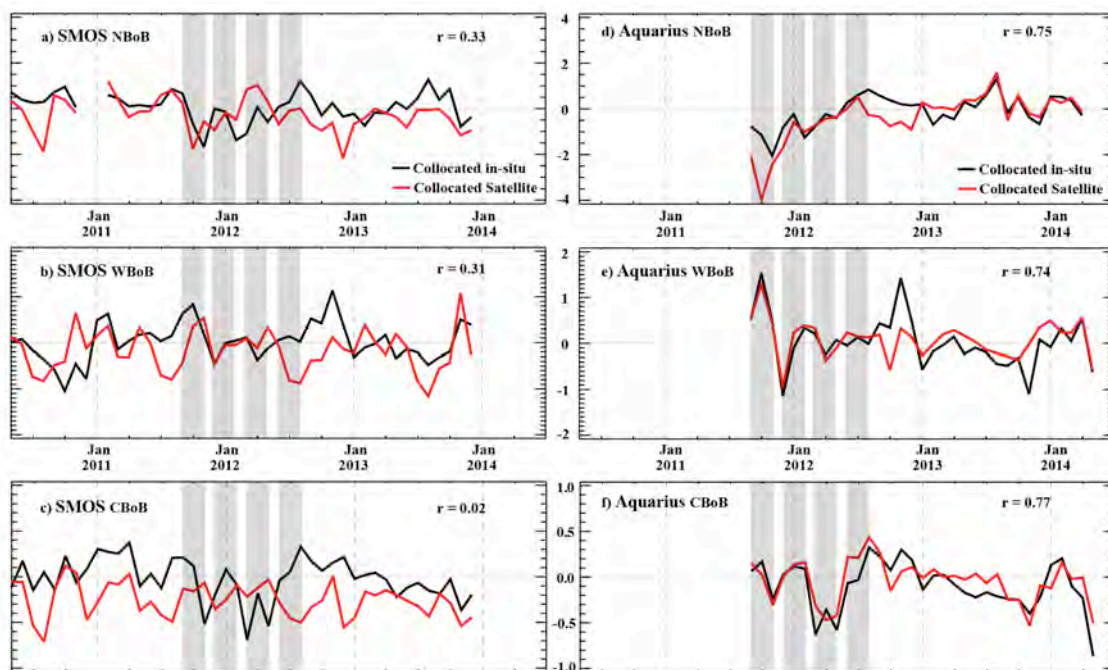


**Figure 3.8.** Time series of box-averaged monthly SSS interannual anomalies over (a) NBoB, (b) WBoB and (c) CBoB (outlined on Figure 3.2e, f) from the gridded *in-situ* product (black line) and SMOS retrieval (red lines) on SMOS grid. (d, e, f) Same as (a, b, c) but for Aquarius on Aquarius grid. The thick red curve shows the satellite SSS averaged over all collocated data with the *in-situ* dataset in the box. The grey shading indicates the seasons for which the maps of Figure 3.9 are plotted.

A more detailed analysis on the ability of the satellites retrieval to capture the temporal evolution in the three boxes where *in-situ* data are available (NBoB, WBoB, CBoB) is further provided on Figure 3.8. The largest departures from the seasonal climatology occur in the NBoB box, with *in-situ* anomalies ranging between -1.5 and 1.5 pss (Figure 3.8a, d). The *in-situ* dataset indicates a freshening anomaly following the 2011 monsoon that lasts until spring 2012, followed by a salty anomaly in the 2012 post-monsoon, a fresh anomaly in early 2013 and a salty anomaly during the 2013

monsoon. Aquarius displays a reasonably good phase agreement with the *in-situ* anomalies in this region (0.75 correlation; Figure 3.8d). In particular, it captures the timing of the anomalous freshening from late 2011 to mid-2012 accurately, although its amplitude is twice larger than in observations in late 2011. Aquarius also captures the anomalous saltening observed during the 2013 monsoon. In contrast, SMOS exhibits a poor phase agreement with *in-situ* anomalies there (0.33 correlation; Figure 3.8a), being unable to capture neither the early 2012 anomalous freshening nor the mid-2013 saltening.

The WBoB SSS also displays large departures from its climatology, ranging from -1 to 1 pss. For instance, the freshening along the east Indian coastline following the monsoon is stronger than normal in 2010 and weaker than normal in 2011 and 2012 (Figure 3.8b, e). Once again, SMOS behaves poorly in this region (0.31 correlation; Figure 3.8b): it does not reproduce well the fresh event in late 2011 and salty events in late 2012 and 2013, only performing well in late 2013. In contrast, Aquarius SSS estimates display a good phase agreement with the *in-situ* dataset over most of the period (0.74 correlation): it is able to capture the abrupt change from salty to fresh anomalies in late 2011, freshening over 2013 and salty anomalies in early 2014. It however misses completely the strong saltening signal evident in the *in-situ* dataset in late 2012.

In CBoB, the departures from the seasonal cycle are weaker than in the NBoB and WBoB boxes, with anomalies that do not exceed 0.5 pss. The *in-situ* SSS display fresher than normal conditions in early 2012 and most of 2013 and saltier than normal conditions in late 2012. As for the two other boxes, Aquarius accurately captures these departures from the seasonal cycle (0.77 correlation) while SMOS completely fails (0.02 correlation).

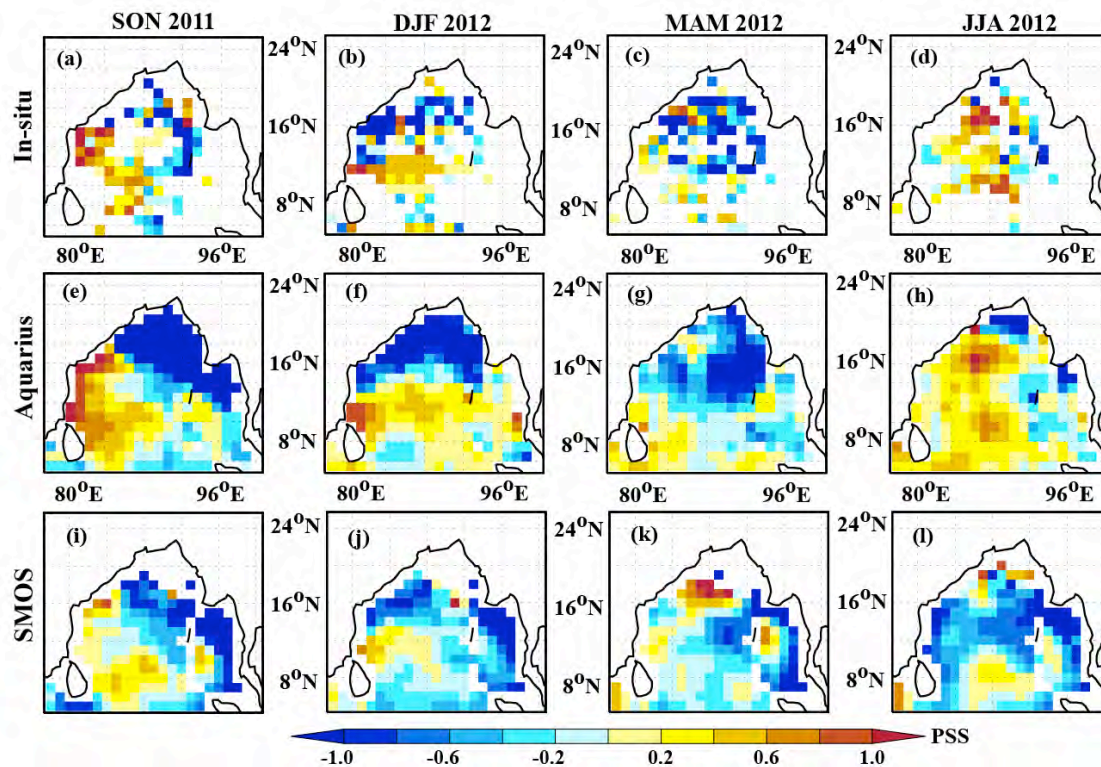


**Figure 3.9.** Monthly mean SSS interannual anomalies for **(first column)** SON 2011, **(second column)** DJF 2011-12, **(third column)** MAM 2012, **(fourth column)** and JJA 2012 from **(first row)** the gridded *in-situ* dataset, **(second row)** Aquarius and **(third row)** SMOS.

As discussed in the previous section, strong departures from the seasonal climatology occur in late 2011 and early 2012 in each of the sub-regions: an anomalous freshening in NBOB from fall 2011 to summer 2012, an anomalous salting in fall 2011 in WBoB, and an anomalous freshening in spring 2012 followed by a salting signal in summer 2012 in CBoB. The performance of the two satellites in reproducing the spatial patterns related to these seasonal departures from the climatology is illustrated on Figure 3.9.

The *in-situ* product indeed indicates that the northeastern BoB is fresher than normal in fall 2011, while salty anomalies are observed to the south of 16°N along the east coast of India (Figure 3.9a). The freshening in NBoB expands southward along the east coast of India in winter 2012 (Figure 3.9b) and in the central part of the Bay around (15°N; 90°E) in spring 2012 (Figure 3.9c). These anomalies in CBoB reverse sign in summer 2012 (Figure 3.9d), with two cores of salty anomaly observed around (16°N; 86°E) and (10°N; 88°E). Aquarius is able to capture the broad spatial structure of the anomalies depicted by the *in-situ* dataset (Figure 3.9e, h). In contrast, although SMOS captures the NBoB freshening in fall 2011 and winter 2012 (Figure 3.9i, j), it is

unable to capture either the saltening along the eastern coast of India in fall 2011, nor the amplitude and spatial extent of the freshening in the CBoB in spring 2012 (Figure 3.9k) nor the salty anomalies in summer 2012 (Figure 3.9l). This example thus illustrates the ability of Aquarius to retrieve regional features in the salinity field within the BoB and the caveats related to SMOS retrieval.

## **3.6. Summary and discussion**

### **3.6.1. Summary**

The BoB is a challenging but very important region for satellite-derived SSS measurements. The BoB stands out as a very peculiar region for salinity structure in the tropical belt, displaying a contrasted SSS distribution, with very fresh water to the north induced by heavy monsoonal precipitation and river runoffs, and saltier water to the south. The resulting near-surface salinity vertical stratification in the northern Bay has been suggested to play a key role in the regional climate and on tropical cyclones intensification there. These climatic implications call for an improved description of the BoB salinity spatial distribution and temporal variability and satellite SSS measurements may help in that regard. Although existing salinity climatologies derived from available hydrographic data describe adequately the large-scale SSS seasonal cycle in the Bay, the monitoring of SSS interannual variability is far more challenging due to the insufficient spatial sampling of the *in-situ* network. The recent development of SSS remote sensing capabilities may therefore provide valuable information on the departures from the seasonal cycle in this region. However, the BoB is a semi-enclosed basin with a typical width of ~1000-2000 km, where satellite SSS measurements are likely to be contaminated by radio frequency interferences and land signals. The goal of this study is therefore to perform a validation of the most recent SMOS V02 level-3  $1^\circ \times 1^\circ$  and Aquarius V03 level-3  $1^\circ \times 1^\circ$  gridded monthly salinity retrievals against a comprehensive gridded *in-situ* SSS product in the BoB to infer whether these satellite datasets can confidently be used to describe SSS variations in this climatically important region.

Our results reveal large differences in the ability of these two satellite products to retrieve SSS variability. The spatial coverage of the SMOS product is poorer compared to Aquarius, especially in the northern portion of the BoB. SMOS exhibits a systematic fresh bias everywhere in the Bay (-0.19/-0.35 depending on the region). In contrast, the mean SSS field retrieved from Aquarius is accurate, except in the northern part of the Bay where it exhibits a -0.26 fresh bias. The seasonal variability depicted by Aquarius retrievals is also accurate in the northern, central and western part of the basin with correlation to the reference *in-situ* dataset exceeding 0.9. In contrast, SMOS retrievals fail to represent the SSS seasonal cycle in the western and central part of the basin. Aquarius retrievals are also able to capture departures from the mean seasonal cycle, with ~0.75 correlation with large-scale SSS interannual variations from the *in-situ* dataset in all regions. Aquarius for instance successfully captures the main spatio-temporal features of the anomalous freshening event that occurred in the northern and central part of the BoB in late 2011 and early 2012. In contrast, SMOS estimate generally fails to capture the timing and spatial patterns of SSS departures from the seasonal cycle.

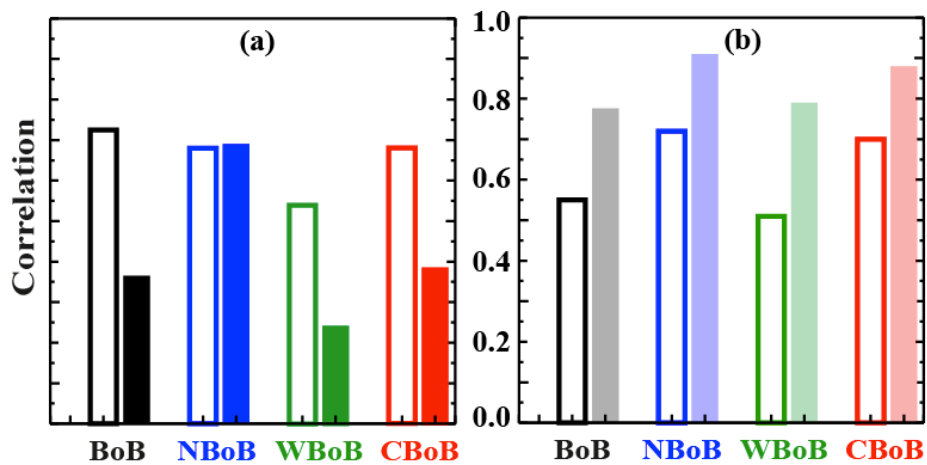


**Figure 3.10.** (a) Correlation of SMOS SSS retrieval (coloured bars) and NIOA climatology (coloured frames) against gridded *in-situ* SSS dataset over each sub-region of the BoB. (b) Same as (a) but for Aquarius.

Figure 3.10 provides a compelling summary of the added value provided by the two satellite retrievals compared to the existing climatologies. The SMOS retrieval indeed displays a poorer phase agreement with the *in-situ* reference dataset than the NIOA climatology over the WBoB and SBoB and a similar agreement over the NBoB (Figure 3.10a). In contrast, the situation is far more promising for Aquarius, which exhibits higher correlations with *in-situ* observations than SMOS and NIOA over all

the sub-regions (Figure 3.10b). This indicates that the current version of Aquarius retrievals provide additional information with respect to the existing SSS climatologies in the BoB, while SMOS does not.

### 3.6.2. Discussion

Preliminary assessments of one-year data from earlier versions of both level-3 SMOS [Reul *et al.*, 2012; Subrahmanyam *et al.*, 2012; Ratheesh *et al.*, 2013] and Aquarius datasets [Ratheesh *et al.*, 2014] over the BoB reported major issues in the satellites ability to retrieve SSS there. In this paper, we provide in-depth validations of the latest version of these level-3 products over a longer period (~3 years). Our results indicate that the latest version of the Aquarius retrieval performs considerably better than earlier versions, especially for low SSS values in the northern part of the Bay. This better performance could be related to the recent inclusion of a rain-corrected salinity retrieval in the latest Aquarius products [Yueh *et al.*, 2014]. In contrast, although the performance of the latest SMOS SSS product is slightly better than it was in the earlier (not shown), it still exhibits significant caveats at both seasonal and non-seasonal timescales, despite the inclusion of an improved handling of RFI contamination [Reul *et al.*, 2014].

*Subrahmanyam et al.* [2012] and *Durand et al.* [2013] reported errors of the order of 0.2 pss for SMOS level-3 data in the southern equatorial IO. This indicates that the bad performance of SMOS reported in that paper is specific to the BoB, and that SMOS performs much better in the open tropical IO. There can be several reasons behind the contrasted ability of SMOS and Aquarius to capture SSS in the BoB. First, the SMOS instrument has a much wider footprint (~1000 km) compared to Aquarius (~100 km). SMOS post-processing currently assumes that there are no large gradients within this footprint, which results in a larger pollution by RFI and land contamination [Reul *et al.*, 2012; Boutin *et al.*, 2013] than Aquarius. It is however surprising to note that SMOS behaves better in the northern part of the Bay than in its central part, which is located further away from land. In any case, the poor performance of the level-3 SMOS product pleads for improvements in its data processing chains, RFI sortings and bias corrections applied when producing level-1 data.

Another caveat of the current study concerns the very strong salinity horizontal gradients, sometimes over relatively small horizontal scales, which have been spotted in the past in the BoB [e.g. *Shetye et al.*, 1996; *Hareesh Kumar et al.*, 2013; *Chaitanya et al.*, 2014a]. Those small-scale SSS structures raise the question of the representation of individual *in-situ* measurements, against the retrieved SSS from satellite, that is representative of a larger spatial scale (typically  $1^\circ \times 1^\circ \times 1$  month). We however believe that re-gridding individual SSS data by taking their median value on a  $1^\circ \times 1^\circ \times 1$  month grid allows to limit somewhat this representation issue. We also did validate average time series over larger boxes in typical regions of variability (NBoB, WBoB, CBoB), which hopefully further reduces this representation issue. While the error statistics of individual satellite data on the  $1^\circ \times 1^\circ \times 1$  month grid should be taken cautiously (i.e. the RMSD is probably enhanced by the representation error), we believe that the statistics computed for the entire NBoB, WBoB and CBoB boxes (Figures 3.3c, d, 3.4, 3.6, 3.7c, d, 3.8 and 3.10) provide a more reasonable evaluation of the actual level of error of those satellite products. Another caveat is of course the length of the time series ( $\sim 3$  years). A more in-depth assessment of the capability of the satellites to estimate the seasonal cycle in the BoB will probably be needed a couple of years down the line, but we believe that the current analysis still clearly points out that, while the current Aquarius SSS retrieval can be used within the BoB, there is still some work to be done to improve existing SMOS retrievals.

### **3.6.3. Perspectives**

One key-advantage of spaceborne SSS products is their ability to sample regions that are completely devoid of *in-situ* observations. One such region is the Andaman Sea. This region exhibits a large SSS variability in the spaceborne measurements (Figure 3.2e, f) and model simulations [*Akhil et al.*, 2014]. Like the northern part of the Bay, the Andaman Sea is characterized by intense monsoonal rains [*Hoyos and Webster*, 2007] and continental runoff [*Furuichi et al.*, 2009]. Although no *in-situ* SSS observations are available in this region for the recent period, satellites reveal vigorous signals there (Figure 3.11). Both SMOS and Aquarius indicate a strong seasonal freshening of  $\sim 2$  pss during the monsoon and post-monsoon seasons, followed by a subsequent saltening in winter-spring. The magnitude of these SSS

changes is comparable to those observed in the northern or western part of the BoB (Figure 3.6). The Andaman Sea post-monsoon freshening depicted by the two satellites is larger than the one suggested by the NIOA climatology. Due to the very limited availability of salinity data in the Andaman sea [Antonov *et al.*, 2010; Chatterjee *et al.*, 2012], and relatively good performance of Aquarius in other regions, one is tempted to believe that it is the NIOA climatology that is erroneous there, and that Aquarius brings us an improved knowledge of the seasonal cycle of SSS in the Andaman Sea. Beyond this seasonal picture, both SMOS and Aquarius data suggest a larger seasonal fresh anomaly during and after the 2012 monsoon than during other years. It would be interesting to assess the quality of the spaceborne SSS products in the Andaman Sea, in order to judge if they can be used for monitoring SSS and understand mechanisms of SSS variability there.

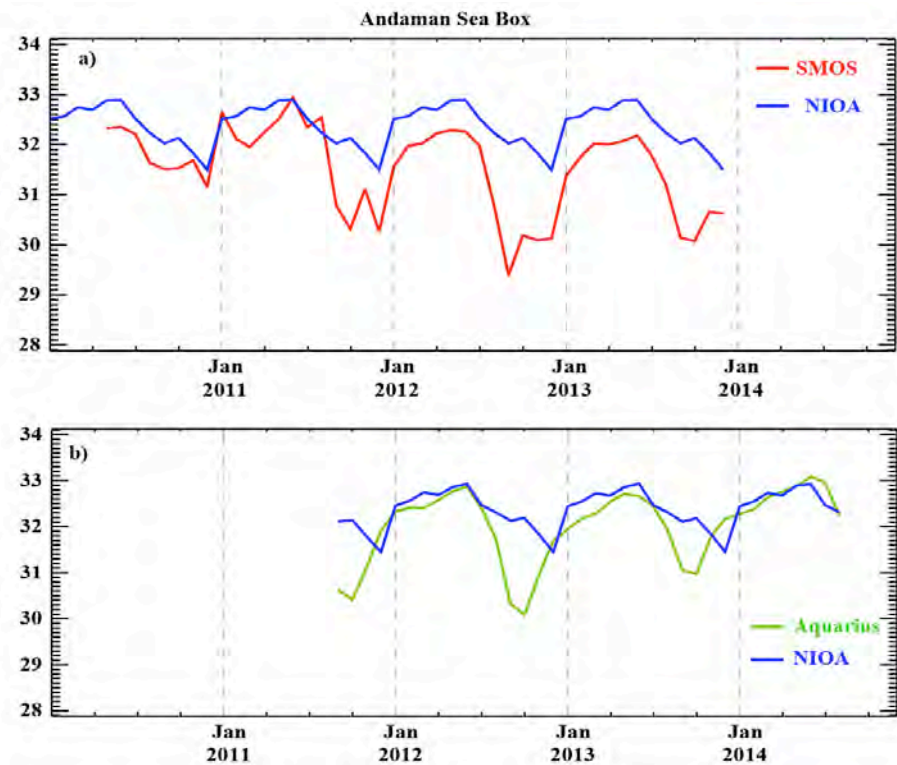


**Figure 3.11.** (a) Box-averaged monthly time series of SSS from SMOS (red) and NIOA climatology (blue) for the Andaman Sea box (framed on Figure 3.2e, f). (b) Same as (a) but for Aquarius (green).

It would also be very interesting to better understand the mechanisms driving the interannual SSS variability in the BoB. Using a similar *in-situ* SSS dataset to the one used in this study, combined with satellite estimates of rainfall and GB river runoffs, Chaitanya *et al.* [2014b] already suggested that interannual SSS variability in

the northeastern part of the Bay over the 2009-2012 period was primarily driven by freshwater flux variability, and in particular river runoffs. Given the ability of Aquarius to capture the interannual SSS variations in the BoB to some extent, it is very tempting to perform a similar salt budget to the one of *Chaitanya et al.* [2014b] but using the more spatially complete Aquarius SSS retrieval. Interannual river runoffs data derived from satellite measurements are however only currently available until the end of 2012 (i.e. only 15 months of common data with remotely-sensed SSS) [*Papa et al.*, 2012], so far precluding a meaningful investigation of the interannual mixed-layer salt budget in the BoB. Once interannual runoffs data from the main BoB rivers (i.e. GB and IR) become available for the recent years, a promising follow-up of this work would therefore be to use the Aquarius SSS dataset to assess the main processes that control the interannual SSS variations in the different regions of the BoB.

The present study is dedicated to SMOS and Aquarius salinity assessment. Beyond these two pioneering missions, some evolutions in the field of ocean salinity remote sensing are expected shortly. The next generation of spaceborne sensors usable for SSS monitoring, beginning with Soil Moisture Active Passive (SMAP) satellite (successfully launched on 29th January 2015, see [smap.jpl.nasa.gov](http://smap.jpl.nasa.gov)), promises significant progresses in our ability to retrieve valuable spaceborne estimates of SSS field in the global ocean. We believe our study, focused on one of the most challenging areas of the world ocean, paves the way for the future of spaceborne salinity science there.

## Chapter 4

### Processes governing sea surface salinity seasonal evolution in the BoB, based on our numerical model

---

#### Foreword

As seen in Chapters 1 and 3, the BoB SSS displays a marked seasonal variability. But the relative importance of the processes governing the seasonal SSS evolution is not yet known accurately. Previous (pre-Argo) salinity budget studies [e.g. Rao and Sivakumar, 2003] from available climatologies indeed suffered from insufficiencies in the observational network. In addition, as discussed in the introduction, some fine features such as the post-monsoon “river in the sea” (coastal freshwater plume) observed along the east coast of India are not resolved by those climatologies. In parallel, most of the previous modelling studies of the BoB SSS seasonal cycle were either suffering from unrealistic fresh water fluxes into the BoB [Vinayachandran and Nanjundiah, 2009; Seo et al., 2009] or using a relaxation toward the observed surface salinity climatology to avoid salinity drift [e.g. Diansky et al., 2006; Nyadjro et al., 2011]. This last technique results in artificially modifying the freshwater flux to keep SSS close to observations, and may hence result in an over-representation of the role of atmospheric forcing in salt budget studies. The recent availability of accurate monthly time series of river discharges for the Ganges and Brahmaputra estimated from satellite altimetry [Papa et al., 2010, 2012] represents an unprecedented quantification of the continental freshwater flux into the BoB. We used an eddy-permitting regional simulation forced by surface fluxes, including interannual river runoffs and precipitations and with no relaxation toward climatological observed SSS. Despite the absence of relaxation, the model SSS seasonal cycle agrees well with available observations. The model is even able to reproduce a sharp post-monsoon “river in the sea” along the east coast of India, in good agreement with available *in-situ* observations, but that is blurred by excessive spatial smoothing in available climatologies. Building on this good performance of the model, we provide a quantitative analysis of the processes that contribute to the SSS seasonal cycle in the BoB in this chapter. The model confirms the role of river runoffs for the Northern BoB

freshening during and just after the monsoon and the role of lateral advection for the southward expansion of the post-monsoon “river in the sea” along the east coast of India. Finally, our model is also the first one to explain that the gradual saltening of the western BoB after the monsoon arises from vertical mixing of surface fresh water with deeper, saltier water.

**The contents of this chapter are based on the following published article:**

Akhil VP, F Durand, M Lengaigne, J Vialard, MG Keerthi, VV Gopalakrishna, C Deltel, F Papa and C de Boyer Montegut (2014), **A modeling study of the processes of surface salinity seasonal cycle in the BoB**, Journal of Geophysical Research-Oceans, 119,3926-3947, doi: 10.1002/2013JC009632.

## Abstract

In response to the Indian Monsoon freshwater forcing, the BoB exhibits a very strong seasonal cycle in sea surface salinity (SSS), especially near the mouths of the GB and along the east coast of India. In this paper, we use an eddy-permitting (~25 km resolution) regional ocean general circulation model simulation to quantify the processes responsible for this SSS seasonal cycle. Despite the absence of relaxation towards observations, the model reproduces the main features of the observed SSS seasonal cycle, with freshest water in the northeastern Bay, particularly during and after the monsoon. The model also displays an intense and shallow freshening signal in a narrow (~100 km wide) strip that hugs the east coast of India, from September to January, in good agreement with high-resolution measurements along two ships of opportunity lines. The mixed layer salt budget confirms that the strong freshening in the northern Bay during the monsoon results from the GB river discharge and from precipitation over the ocean. From September onward, the East India Coastal Current transports this freshwater southward along the east coast of India, reaching the southern tip of India in November. The surface freshening results in an enhanced vertical salinity gradient that increases salinity of the surface layer by vertical processes. Our results reveal that the erosion of the freshwater tongue along the east coast of India is not driven by northward horizontal advection, but by vertical processes that eventually overcome the freshening by southward advection and restore SSS to its pre-monsoon values. The salinity-stratified barrier layer hence only acts as a “barrier” for vertical heat fluxes, but is associated with intense vertical salt fluxes in the BoB.

## 4.1. Introduction

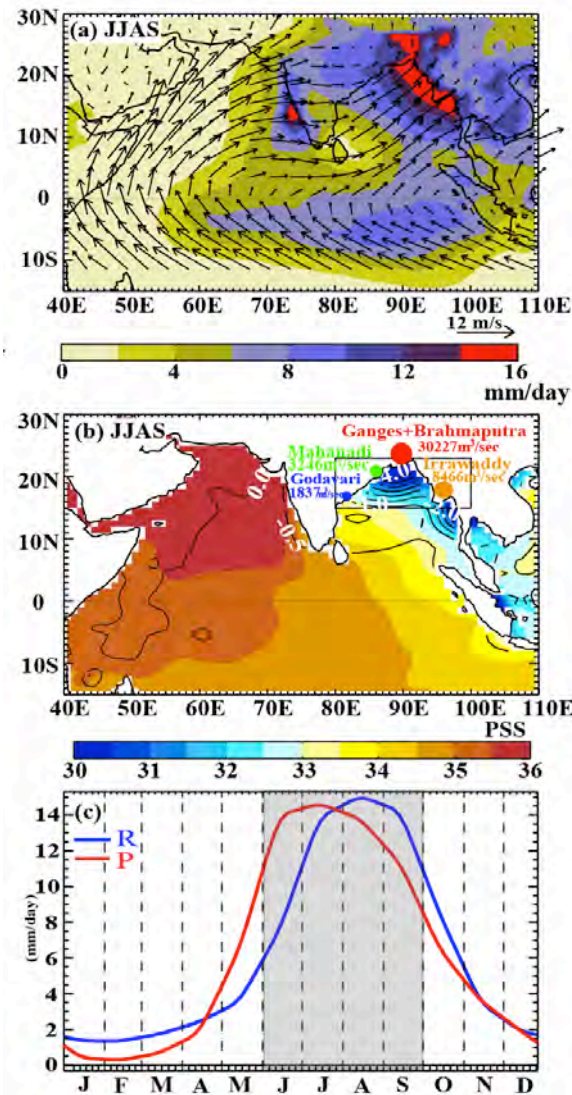


**Figure 4.1.** Summer (June to September) climatology of (a) GPCP rainfall (shaded) and 10 m QuikSCAT wind (vectors), (b) NIOA SSS (shaded), SSS minus salinity at 50 m depth (contours). The dots indicate the locations of major river mouths, the radius of each is proportional to the magnitude of mean fresh water outflow ( $\text{m}^3/\text{sec}$ ). The annual mean outflow is indicated, for each river. (c) Seasonal evolution of DFS4 rainfall in the BoB northward of  $15^\circ\text{N}$  (integrated over the ocean only) and of runoff from major rivers (GB, IR, MH and GD).

The Indian peninsula splits the northern IO into two semi-enclosed basins: the AS to the west and the BoB to the east (Figure 4.1). The northern IO is forced by annually reversing winds that blow from the southwest during the summer monsoon (May to September; Figure 4.1a) and from the northeast during the winter monsoon (November to March). This drives a seasonal reversal of most of the upper ocean currents north of  $10^\circ\text{S}$ , a unique feature among the three tropical oceans. The EICC flows along the western boundary of the BoB (Figure 4.2a-d). This is a major oceanic

current in the BoB, as it is responsible for most of the surface and thermocline water transport in this basin [Schott and McCreary, 2001; Shankar et al., 2002] and plays a key role in connecting the BoB with equatorial IO and AS [Shankar et al., 2002; Durand et al., 2009; Shenoi et al., 2010]. The EICC reverses seasonally, flowing northward before and during summer monsoon (Figure 4.2d and 4.2a) and southward after summer monsoon (Figure 4.2b and 4.2c). Only during November-December and March-April does the EICC form a continuous flow between the Northern BoB and the South-eastern coast of Sri Lanka. The EICC reversal precedes wind reversal by several months. This is due to the remote wind forcing from the equatorial IO and eastern rim of the BoB, which propagates to the east coast of India in the form of coastal Kelvin waves [Yu et al., 1991; McCreary et al., 1993, 1996; Shankar et al., 1996]. This remote forcing, in conjunction with local wind forcing and intrinsic hydrodynamic instabilities, yields a rich spatio-temporal variability of the EICC [Durand et al., 2009; Chen et al., 2012; Cheng et al., 2013].

Although the BoB and AS are located in the same latitudinal belt and are both influenced by monsoons, the upper haline structure of these two basins differs markedly, with considerably fresher surface waters and more intense haline stratification in BoB (Figure 4.1b). The stronger humidity horizontal convergence results in much more intense rainfall over the BoB and surrounding continent (Figure 4.1a) than over the AS. Oceanic rainfall and continental runoffs (dominated by a handful of powerful rivers, *i.e.* Ganges, Brahmaputra, IR, MH and GD) contribute roughly equally to the total freshwater received by the BoB, north of 15°N (Figure 4.1c). These freshwater sources are located in the northern BoB (Figure 4.1a, b), resulting in lowest SSS there (less than 33 units, in practical salinity scale). The low salinity surface waters lay above much saltier water (33 to 34.5 units, depending on the location) below 50 m, resulting in a sharp near-surface haline stratification (Figure 4.1b).

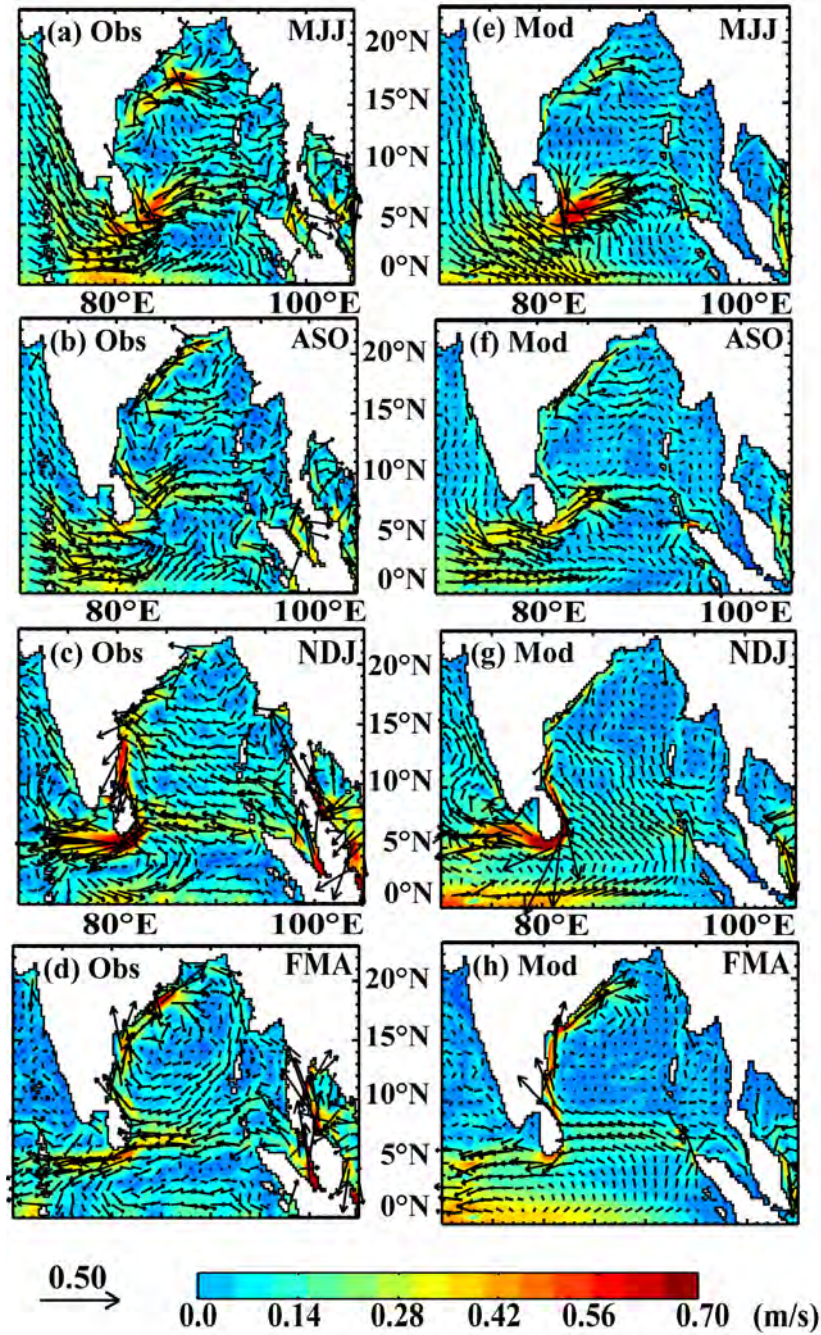


**Figure 4.2.** (left) Climatological surface current speed (color,  $\text{m}\cdot\text{s}^{-1}$ ) and direction (vectors) in the BoB for (a) summer (MJJ), (b) autumn (ASO), (c) winter (NDJ), (d) spring (FMA) from GEKCO product. The climatology is computed over the 2002-2007 period. (right) Same for the model.

This very strong near-surface halocline potentially plays a strong role in maintaining the Northern IO climate [Shenoi *et al.*, 2002]. It indeed strengthens the density stratification and usually results in a shallow mixed layer [Mignot *et al.*, 2007; Thadathil *et al.*, 2007; Girishkumar *et al.*, 2013]. Combined with a homogeneous thermal stratification, this often results in the formation of a barrier layer, the layer between the base of the mixed layer and the top of the thermocline [Lukas and

*Lindstrom*, 1991]. This barrier layer prevents the vertical exchanges of momentum and heat between the upper mixed layer and the thermocline. This barrier layer is held responsible for the high SST throughout the basin [*Shenoi et al.*, 2002; *de Boyer Montégut et al.*, 2007], which almost permanently remains above the 28°C threshold for deep atmospheric convection [*Gadgil et al.*, 1984]. The salinity stratification also reduces the effects of storm-induced surface cooling in the BoB, which may in turn favour the intensification of tropical cyclones [*Sengupta et al.*, 2008; *Neetu et al.*, 2012; *Vincent et al.*, 2012]. It has also the potential to influence the amplitude of intra-seasonal variability of the SST [*Vinayachandran et al.*, 2012] and biological productivity regimes [*Prasanna Kumar et al.*, 2002]. These strong impacts of haline stratification in the BoB call for a precise description and understanding of the SSS spatial structure and temporal variability within the bay.

Observational studies describing the SSS within the BoB are mostly based on hydrographic measurements along dedicated cruises tracks and specific shipping lanes [*Shetye et al.*, 1991; *Murty et al.*, 1992; *Shetye*, 1993; *Shetye et al.*, 1996; *Webster et al.*, 2002; *Babu et al.*, 2003; *Rao and Sivakumar*, 2003, *Vinayachandran et al.*, 2007] as well as on ARGO profilers data [e.g. *Vinayachandran et al.*, 2013, *Parampil et al.*, 2010]. *Rao and Sivakumar* [2003] reported a marked seasonal cycle of SSS, illustrated in Figure 4.3. During August-September-October, a tongue of low salinity (inferior to 30, in the practical salinity scale) water forms in the north-eastern BoB (Figure 4.3b). This fresh pool spreads along both eastern and western boundaries of the basin in fall and early winter (Figure 4.3c). Subsequently, during late winter, the freshwater tongue weakens and retreats back to the North-eastern Bay (Figure 4.3d). The freshwater supply varies strongly at seasonal timescale (Figure 4.1c), with about 70% of the annual inflow (from precipitation and runoff) occurring during the summer monsoon north of 15°N. The observed freshening of the northern BoB in late summer (Figure 4.3b) clearly follows the seasonal maximum of precipitation in June and of river discharge in August (Figure 4.1c). While this role of freshwater forcing in the seasonal evolution of surface salinity has already been highlighted by several studies [e.g. *Shetye et al.*, 1996, *Han et al.*, 2001; *Sengupta et al.*, 2006], the potential role of other processes (advection and vertical mixing in particular) is more difficult to evaluate from observations only. Earlier studies however proposed that the southward flowing EICC in November-December-January (Figure 4.2c) could play a role in conveying

the freshwater plume southward along the western coast of India [Shetye *et al.*, 1996; Jensen, 2001; Rao and Sivakumar, 2003].

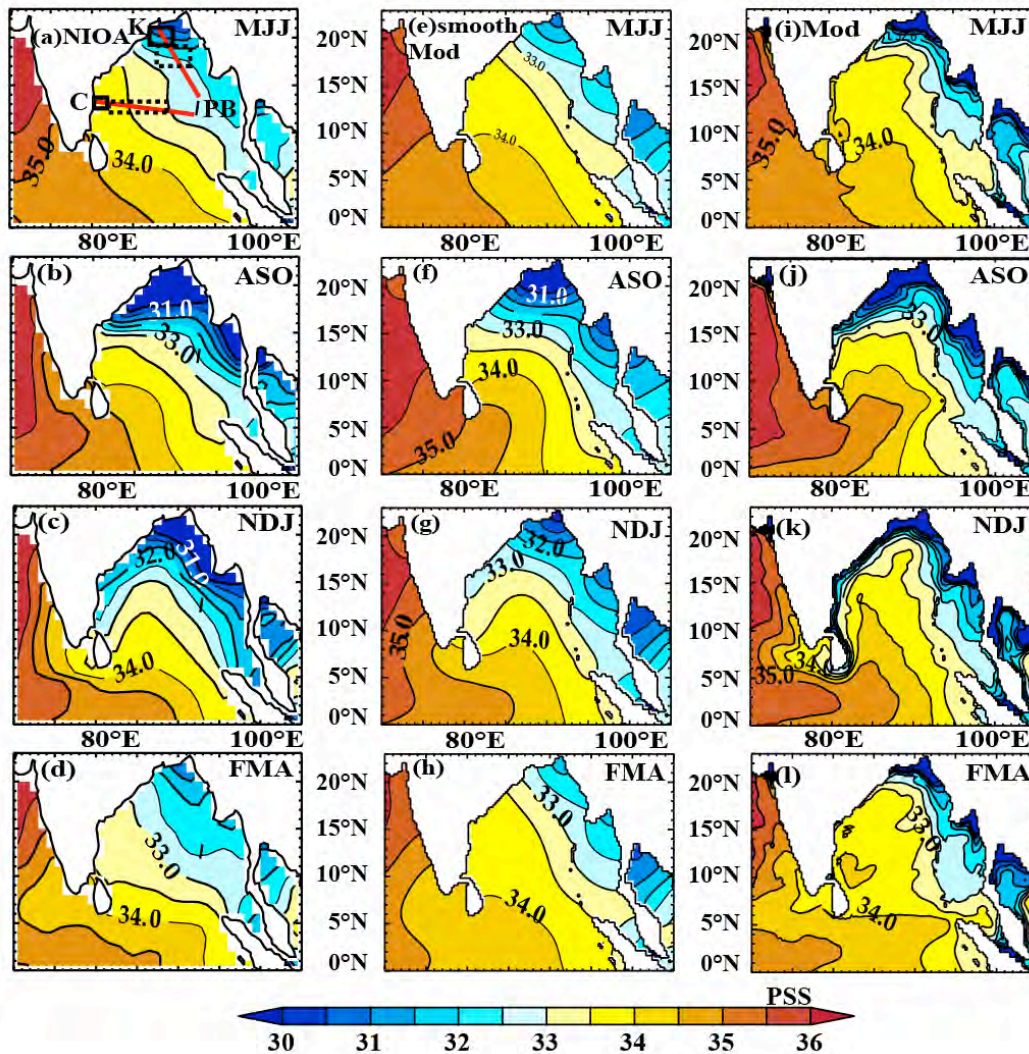


**Figure 4.3.** (left) Climatological SSS from NIOA [Chatterjee *et al.*, 2012] for (a) summer (MJJ), (b) autumn (ASO), (c) winter (NDJ), (d) spring (FMA). (Middle) Same for the model climatology computed over the 2002-2007 period, in which a 444 km Gaussian smoothing has been applied, as in NIOA. (Right) Model climatology again, but without smoothing. Salinity is given in practical salinity scale. The red lines on (a) indicate the tracks of frequently repeated salinity measurements along two ship-of-opportunity lines: Chennai - Port Blair in the western Bay (C-PB) and Kolkata - Port Blair in the Northern Bay (K - PB). The box average of those data in the coastal (solid black) and offshore (black dashes) regions are compared with model values in Figure 4.4.

Ship-based salinity observations are sparse in the IO. While the ARGO program has considerably increased the number of temperature and salinity profiles in the central part of BoB since 2002, there is still a sparse coverage of the coastal regions. This led the National Institute of Oceanography in Goa, India to develop a coastal salinity monitoring program at eight stations along the Indian coastline. Using this

data, in combination with high-resolution data along an offshore transect, *Chaitanya et al.* [2014] demonstrated that there is a very intense freshening (up to 10 units in the northern Bay) in a narrow (~50 to 100 km) coastal strip that quickly expands southward along the east Indian coast after the monsoon. This narrow freshening is not well captured by climatologies [e.g. *Chatterjee et al.*, 2012] due to both a poor data sampling in the coastal region and the 4° horizontal smoothing used in those climatologies. While it is difficult to derive a full salinity budget from observations, *Chaitanya et al.* [2014a] analyses also suggest that the EICC plays a key role in the southward expansion of this narrow coastal freshwater strip after the monsoon, while other processes than advection are necessary to explain its decay during the following months.

While the improved *in-situ* salinity observing network provides a better description of the SSS seasonal evolution within the bay, it is however not yet sufficient to quantitatively assess all the processes that govern the seasonal SSS evolution. Numerical ocean circulation models have the distinct advantage of generating long time series of salinity at regular spatial and temporal intervals. With increasing accuracy of the forcing data, models are now able to simulate seasonal salinity variations with some realism. Several modeling studies provided some understanding of the impacts of the freshwater forcing (precipitation, evaporation and runoff) on the upper BoB stratification and dynamics through sensitivity experiments [*Howden and Murtuggude*, 2001; *Han and McCreary*, 2001; *Han et al.*, 2001; *Yu and McCreary*, 2004]. The common conclusion of these modeling studies is that river runoff, and not precipitation, is the dominant factor in freshening the northern part of the bay during the southwest monsoon. *Han and McCreary* [2001], *Jensen* [2001], *Rao and Sivakumar* [2003] and *Nyadjro et al.* [2011] also identified lateral advection of low salinity waters from the northern BoB as the main driver of fresh water expansion along the east coast of India and into the AS during the monsoon. On the other hand, the eastern rim of the Bay appears to be a major export pathway of BoB freshwater toward the equator all year long [*Han and McCreary*, 2001; *Jensen* 2001, 2003].

Most previous numerical modeling studies of the mechanisms of BoB SSS variability used a relaxation toward the observed surface salinity climatology. While

this strategy allows keeping the surface salinity realistic [e.g. *Diansky et al.*, 2006; *Wu et al.*, 2007; *Sharma et al.*, 2010; *Nyadjro et al.*, 2011], the relaxation term will act to artificially compensate any error in the forcing or in the model physics. The relaxation term is sometimes strong in some locations of the BoB, so that it may be hazardous to infer robust conclusions about the mechanisms of SSS variability [*de Boyer Montégut*, 2005]. Some recent studies used coupled ocean-atmosphere models [*Vinayachandran and Nanjundiah*, 2009; *Seo et al.*, 2009] with no relaxation, but precipitation in the atmospheric component of these coupled models is still insufficiently realistic to result in a satisfactory representation of BoB SSS variability.

The main objective of this study is to estimate the contributions of the processes that govern the SSS seasonal evolution in the BoB. To that end, we use an eddy-permitting regional ocean model with no relaxation to SSS observations that includes an online calculation of the terms contributing to the mixed layer salinity evolution. The rest of the paper is organized as follows. Section 4.2 briefly describes the modelling strategy and validation data. Section 4.3 validates the model to available observations. Section 4.4 discusses the processes that govern the SSS seasonal evolution, with a particular focus on the Northern and Western rim of the BoB where SSS variability is strongest. A discussion of our results is provided in Section 4.5.

## **4.2. Data and methods**

### **4.2.1. Model description and setup**

The model configuration used in this study is based on the NEMO ocean general circulation modeling system [*Madec*, 2008], implemented in a regional IO configuration (27°E to 142°E, 33°S to 30°N) described in *Vialard et al.* [2013]. It solves the primitive equations on a  $\frac{1}{4}^\circ$  horizontal grid with 46 vertical levels (vertical resolution ranging from 6 m at the surface to 250 m at the bottom, with 7 levels in the upper 50 m). Vertical mixing is modeled using a turbulent closure model that resolves a prognostic equation for the turbulent kinetic energy [*Blanke and Delecluse*, 1993]. The open boundaries are handled using a radiation-relaxation approach (following *Marchesiello et al.* [2001]), where we use the radiation condition to determine whether

a boundary is passive (outward propagation) or active (inward propagation). The boundaries are constrained with a 150-day time-scale relaxation to 5-day-average velocities, temperature and salinity from an interannual global  $\frac{1}{4}^\circ$  simulation that has been carried out as part of the Drakkar project [Drakkar Group, 2007]. This global simulation has been extensively validated over the tropical IO [Keerthi et al., 2013; Nidheesh et al., 2012].

The model is forced by interannually varying fluxes of momentum, heat, precipitation, evaporation and runoff over January 2001 to December 2007 from the DFS4 described in Brodeau et al. [2010]. The starting point of DFS4 is the CORE dataset developed by Large and Yeager [2004]. The CORE bulk formulae are used to compute latent and sensible heat fluxes, with surface atmospheric variables (air temperature, humidity and winds at 10 m) from ERA40 reanalysis [Uppala et al., 2005] from 2000 to 2002, and European Center for Medium range Weather Forecast (ECMWF) analysis after 2002. Radiative fluxes are based on corrected International Satellite Cloud Climatology Project (ISCCP)-FD surface radiations [Zhang et al., 2004] while precipitation data are based on a blending of several satellite products, including two of the most widely used datasets: Global Precipitation Climatology Project (GPCP) [Huffman et al., 1997] and CPC Merged Analysis of Precipitation (CMAP) [Xie and Arkin, 1997]. All atmospheric fields are corrected to avoid temporal discontinuities and remove known biases (see Brodeau et al. [2010] for details). Following Large et al. [2006] recommendations, turbulent fluxes are computed every 6 hours while radiative fluxes are applied on a daily basis, with a linear interpolation to the model time step. We use monthly climatology of continental runoffs from Dai and Trenberth [2002], except for the GB river system for which we use altimetric-derived monthly interannual estimates [Papa et al., 2010]; this product gives us good confidence in the realism of the continental freshwater forcing of the model. We apply no relaxation to an observed SSS climatology in that experiment. The model is initialized from rest with World Ocean Atlas 2009 climatological temperature and salinity in January 2001, and only the January 2002 - December 2007 period is analyzed in the present study.

Experiments using this model configuration and a similar forcing strategy (i.e. same as the above but with a climatological runoff everywhere and a relaxation to the

observed SSS climatology) successfully reproduce intraseasonal [Nisha *et al.*, 2013; Vialard *et al.*, 2013] and interannual [Praveen Kumar *et al.*, 2014] SST fluctuations in the IO.

#### 4.2.2. The salt budget in the model

The model mixed layer depth (MLD) is defined as the depth where density is  $0.01 \text{ kg.m}^{-3}$  higher than surface density. Such a small criterion allows the vertically averaged mixed layer salinity to be a good proxy of SSS [de Boyer Montegut *et al.*, 2007]. In order to compute the ocean mixed layer (ML) salinity budget, the various terms contributing to salinity evolution are averaged over the ML online, stored as 5-day averages, and grouped as follows:

$$\begin{aligned} \partial_t \langle S \rangle = & - \underbrace{\langle u \partial_x S + v \partial_y S \rangle}_a - \underbrace{\langle w \partial_z S \rangle}_b - \underbrace{\frac{1}{h} \frac{\partial h}{\partial t} (\langle S \rangle - S(z = h))}_c \\ & + \underbrace{\frac{(k \partial_z S)(z = h)}{h}}_d + \underbrace{\frac{(E - P - R)S}{h}}_e + \underbrace{\langle D_l(S) \rangle}_f \end{aligned} \quad \text{----- 4.1}$$

where brackets denote the vertical average over the time-varying mixed layer depth  $h$ ,  $S$  is the model salinity,  $(u, v, w)$  are the components of ocean currents,  $D_l(S)$  the lateral diffusion operator,  $k$  the vertical diffusion coefficient,  $E$  is the evaporation,  $P$  the precipitation and  $R$  the river runoff. The term  $(a)$  represents the horizontal advection,  $(b)$  the vertical advection,  $(c)$  is the entrainment,  $(d)$  the vertical diffusion through the mixed layer base,  $(e)$  is freshwater flux forcing of the mixed layer and  $(f)$  is lateral diffusion.

We will use this salinity budget calculation to infer the respective contributions of these processes to the seasonal SSS evolution in the BoB. The term  $(f)$  for lateral diffusion is negligible as shall be seen in the following. In our budget term calculation, vertical processes gather vertical diffusion  $(b)$ , entrainment  $(c)$  and vertical advection  $(d)$ . Amongst these three terms, vertical diffusion dominates entrainment of vertical advection by far. For conciseness, The terms  $(b)$ ,  $(c)$  and  $(d)$  are grouped together in a vertical processes term, keeping in mind that vertical processes largely reflect the vertical diffusion term. Our analyses will thus focus on identifying the relative influences of vertical processes  $(b+c+d)$ , surface freshwater forcing  $(e)$  and horizontal advection  $(a)$ .

### 4.2.3. Validation datasets

The model SSS is validated against the recent NIOA SSS climatology provided by *Chatterjee et al.* [2012]. This 1° by 1° monthly climatology includes all the data from the WOD09 [*Locarnini et al., 2010; Antonov et al., 2010*], complemented with Conductivity-Temperature-Depth (CTD) stations from Indian oceanographic cruises. An objective analysis gridding procedure (similar to that of WOA9), allows to fill the spatial data gaps and to smooth out the space scales shorter than 4°. The inclusion of the Indian oceanographic cruises database in NIOA considerably improves the data coverage in the periphery of the BoB compared with WOD09, especially along its western boundary [*Chatterjee et al., 2012*].

The scarcity of salinity data in the BoB and the smoothing applied to NIOA climatology prevents a proper resolution of the SSS climatological cycle in coastal regions. We therefore also use repeated bottle measurements performed by passenger ships that ply between India and Andaman Islands (between Chennai and Port Blair, as well as between Kolkata and Port Blair; see tracks on Figure 4.3a), and adequately sample India coastal margins. The data set spans the September 2006–May 2011 period, with typically a monthly to bimonthly frequency (6 to 13 cruises per year). During each cruise, an on-board scientific observer collects surface seawater samples (bucket samples) every 50 to 100 km. The samples are subsequently analyzed for SSS following standard international procedures, using a Guild Line 8400 Autosol salinometer. This ensures a typical accuracy of SSS data of about  $10^{-2}$  unit. This long-term observational program allows us to validate the details of the model behavior in the coastal region of the northern BoB.

We finally use the Geostrophic and Ekman Current Observatory (GEKCO) surface current product of *Sudre et al.* [2013] to assess the model circulation. In this product, surface current is estimated from a combination of the geostrophic flow (estimated from altimetry) and Ekman flow (estimated from scatterometer winds) at a spatial resolution of 0.25° from October 1992 to present. A complete validation against in situ Eulerian and Lagrangian current observations can be found in *Sudre et al.* [2013]. Comparison with currents estimates derived from surface displacements of Argo floats results in correlations between 0.6 to 0.8 in the Northern IO. The observed

climatology has been computed over the same period as the model simulation, i.e. the 2002-2007 period.

### 4.3. Validation

Figure 4.2 shows the GEKCO (left panel) and modeled (right panel) seasonal climatology of surface ocean currents. During the monsoon onset (May to July), the EICC flows poleward in its central section, and equatorward to the South of 8°N (Figure 4.2a) in both the model and GEKCO. During the decay of summer monsoon winds (August-September- October), the EICC reverses in both datasets in the north-western BoB and starts flowing equatorward there (Figure 4.2b). The EICC is strongest during November-December-January, and appears as a continuous equatorward flow all along the east coasts of India and Sri Lanka, with velocity above 0.6 m.s<sup>-1</sup> in its southern portion (Figure 4.2c). There, it bends around the tip of Sri Lanka and flows into the South Eastern AS. This continuous flow does not last long, and reverses in February-March-April north of 8°N, then forming the western arm of a basin-wide anticyclonic gyre (Figure 4.2d). Overall, the model surface circulation (Figure 4.2e-h) successfully reproduces the observed temporal evolution. The model satisfactorily reproduces the timing of EICC reversals, in line with earlier coarser versions of NEMO [e.g. *Durand et al.*, 2011]. It must however be noted that the modeled velocities are slightly too weak, in particular in the northwestern basin before summer monsoon (Figure 4.2e) and along the east coast of India between Sri Lanka and 15°N where they are underestimated by about 30% in November-January (Figure 4.2c and g).

The observed SSS field displays a contrasted pattern, with fresh waters in the northeastern BoB, and saltier waters in the central and southern basin (Figure 4.3). This large-scale gradient exists all year, but is seasonally modulated. During the pre-summer monsoon season (May-June-July), surface waters with salinity below 31 are restricted to the far northeastern BoB (Figure 4.3a). With the progression of summer monsoon (August-September-October), the surface waters freshen in the northern part of the BoB, and the freshening expands southward (Figure 4.3b). This southward expansion is especially noticeable along the eastern and western boundaries of the BoB, with clear signatures along the East coast of India at 16°N and in the South-

Eastern BoB. Further south, saltier water (in excess of 34) prevail in the South-Eastern AS and the South-Western BoB. In fall (November-December-January) the fresh waters expand further south along the east coast of India, down to the northern tip of Sri Lanka (Figure 4.3c). Wintertime (February-March-April) is characterized by a northward retreat of the fresh waters in the western half of the basin and a salinity increase in the north-eastern part of the basin (Figure 4.3d). The seasonal evolution seen in NIOA product is generally consistent with the past literature [e.g. *Rao and Sivakumar, 2003*].

As was previously mentioned, the NIOA climatology uses a  $4^\circ$  Gaussian smoothing in order to overcome the sparseness of in situ observations. *Chaitanya et al. [2014]* suggest that this horizontal smoothing may blur small scale structures such as the narrow post-monsoon freshwater strip they describe in their dataset. In order to provide a consistent comparison between the NIOA climatology and the model, we have also applied a  $4^\circ$  Gaussian smoothing to the model (Figure 4.3e-h). The unsmoothed model is shown in Figure 4.3i-l. Overall, the smoothed model reproduces the main patterns of the observed SSS climatology, and in particular the contrast between saltier water to the southwest and fresher water to the northeast. It also reproduces satisfactorily the main features of the SSS seasonal cycle, with a freshening in the Northern BOB in ASO (Figures 4.3b and 4.3f), an expansion of the freshwater along the east coast of India in NDJ (Figures 4.3c and 4.3g), and gradual increase of salinity during FMA (Figures 4.3d and 3h). The smoothed model is in very good agreement with the NIOA climatology in MJJ and FMA (less than 0.5 unit salt bias), but displays a salty bias of up to 1.5 unit in ASO and 2 units in NDJ in the coastal strip, north of  $15^\circ\text{N}$  (figure not shown). The unsmoothed model SSS climatology displays much more intense gradients between freshest coastal waters and offshore saltier waters (Figure 3i-l). In particular it displays a narrow freshwater tongue hugging the east coast of India in NDJ, similar to the one described from observations by *Chaitanya et al. [2014]*. The realism of this narrow coastal freshwater strip is difficult to assess from a comparison with the smooth NIOA climatology. One way to address this issue is to perform a comparison to the high-resolution SSS sections harvested in the coastal region along the two ship tracks shown on Figure 4.3a.

Figure 4.4 shows the seasonal evolution of SSS in the coastal region (plain lines) near Kolkata at 21°N, 87°E (Figure 4.4a) and near Chennai at 13°N, 81°E (Figure 4.4b), along with the corresponding evolution further offshore (dashed lines), for the ship-borne observations (red), for the model (black) and for the NIOA climatology (blue). The observations and NIOA climatology both display a freshening of the Northern coastal BoB during the summer monsoon, a persistence of the freshwaters until November, followed by a salinity increase during winter-spring (Figure 4.4a). The south-western coastal basin displays a similar evolution, but with a three months delay (Figure 4.4b). The model and NIOA climatology both reproduce the timing and amplitude of the coastal freshening near Kolkata (Figure 4.4a). Near Chennai, the high-resolution ship-borne data display a 5 units drop in coastal SSS from October to November (Figure 4.4b). The model and NIOA both reproduce the timing of this coastal freshening, but underestimate it (by 50% for NIOA and by 30% for the model). The fresh offset of the model compared to NIOA close to the coast is hence not due to model bias, but to the spatial smoothing in the NIOA climatology: the smoothed model is indeed ~0.5 to 1 pss saltier than the climatology near Chennai at this season: Figure 4.3c and 4.3g.

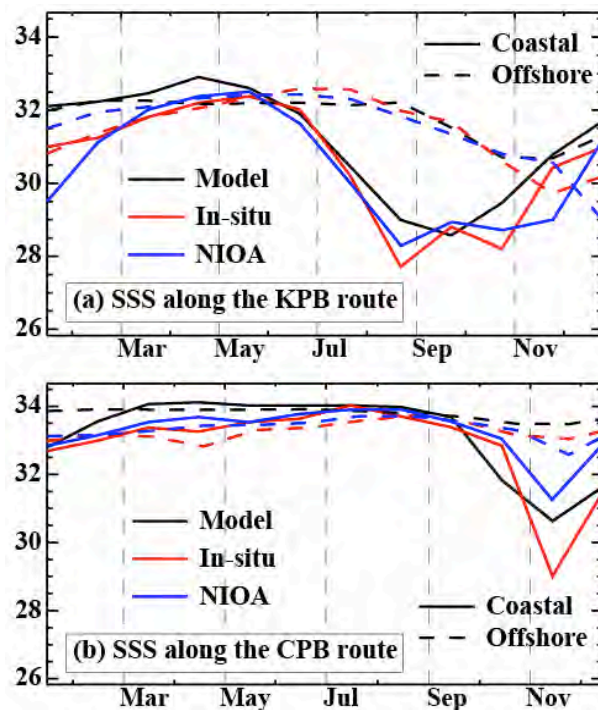
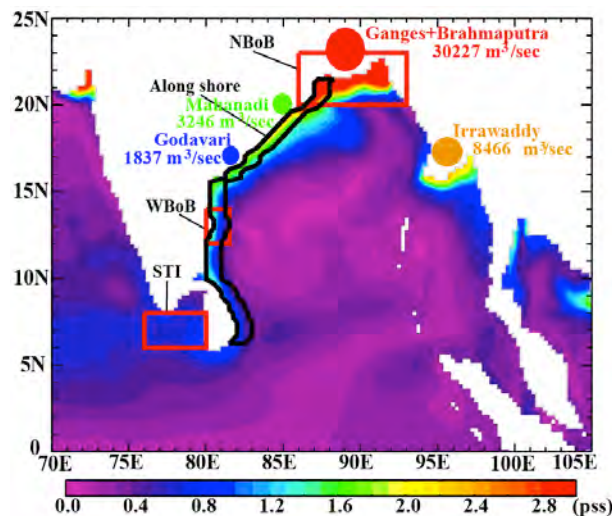


**Figure 4.4.** (a) Seasonal evolution of SSS from model (black), from ship-of-opportunity measurements (red) and from NIOA climatology (blue) along the K - PB route shown in Figure 4.3a. Solid lines are for the coastal box, dashes are for the offshore box. The boxes limits are shown on Figure 4.3a. (b) Same as (a), for the C - PB route.

The model displays a 1 unit salty bias of coastal SSS along the two ship tracks before monsoon season (April-May). Keeping in mind that the model SSS is not relaxed toward any observations, the reasonable agreement of the coastal SSS signal with the shipborne data is however quite remarkable. Overall, the comparison with the ship-of-opportunity data above suggests that, at least near Chennai and Kolkata, the model does not suffer from serious biases in the SSS and SSS gradient it simulates close to the coast. It also suggests that the model resolves the post-monsoon coastal freshening east of India slightly better than the NIOA climatology, in which spatial smoothing tends to damp this signal. We will discuss this issue further in the final section of the paper.

#### 4.4. Processes of the SSS seasonal cycle along the Indian coastline

##### 4.4.1 Overall picture



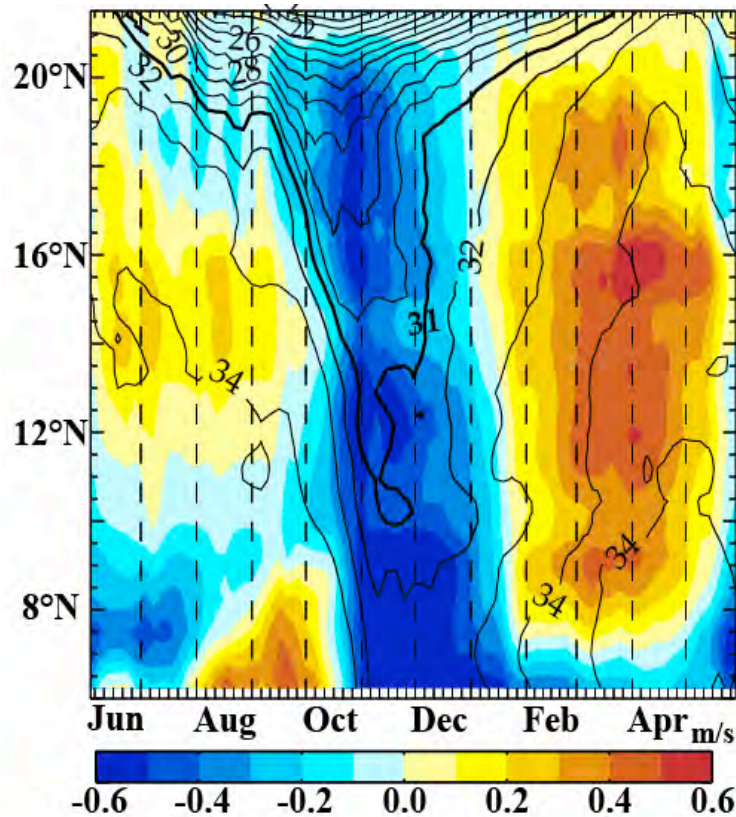
**Figure 4.5.** Standard deviation of the model's SSS monthly mean seasonal cycle. The red boxes feature the limits of the regions discussed in Section 4.4: NBoB (86°E-93°E; 20°N-23°N), WBoB (80°E-81.5°E; 12°N-14°N) and STI (76°E-80°E; 6°N-8°N); the black line delineates the coastal strip box (extending 1° eastward from the western boundary). The major rivers mouths shown in Figure 4.1 are repeated here, for convenience.

Figure 4.5 shows the standard deviation of the model SSS climatology, and highlights the regions of large seasonal SSS changes. As expected, the strongest SSS variability appears off the mouths of the major rivers (GB in the Northern BoB, and IR in the northern Andaman Sea), and - to a lesser degree - along the western boundary of

the basin. In order to quantify the processes controlling seasonal SSS variations in the model, the temporal evolution of the various tendency terms of Equation (4.1) are analyzed for a few areas, representative of the various regimes within the BoB. The geographical limits of the considered regions are highlighted in Figure 4.5. The Northern BoB (86°E-93°E; 20°N-23°N, hereafter NBoB) box is the region where most of the river freshwater enters the domain. The Western BoB (80°E-81.5°E; 12°N-14°N, hereafter WBoB) box is a region typical of the western coastal basin, with relatively high SSS variability. The Southern tip of India (76°E-80°E; 6°N-8°N, hereafter STI) box is adjacent to the southwestern end of BoB, at the southernmost extremity of the tongue of strong SSS variability. Finally we also define an along-shore strip (black boundaries in Figure 4.5) spanning the entire western boundary, from 21°N to 6°N. This strip corresponds to the tongue of maximum SSS variability, and will be used to display latitude-time sections of zonally-averaged variables. Since the mixed layer depth is a critical element in our SSS budget method, we provide here a brief validation of the model to the observed mixed layer depth climatology of *de Boyer Montégut et al.* [2004] (Table 4.1). Although the model systematically overestimates the mixed layer depth deduced from observations, the resulting mean biases and root-mean-square errors are relatively small (a few meters, corresponding approximately to one model vertical level thickness). We will first discuss the seasonal evolution of mixed layer salinity budget along this along-shore strip. We will then focus on the three boxes (NBoB, WBoB, STI) and investigate the mechanisms at stake for controlling SSS variability in each of those regions.

<b><u>Boxes</u></b>	<b><u>Bias</u></b>	<b><u>Rmsd</u></b>	<b><u>Mean OBS</u></b>	<b><u>Mean MOD</u></b>
<b><u>NBoB</u></b>	<b><u>-4.2</u></b>	<b><u>7.3</u></b>	<b><u>17.0</u></b>	<b><u>21.1</u></b>
<b><u>WBoB</u></b>	<b><u>-5.3</u></b>	<b><u>11.0</u></b>	<b><u>30.0</u></b>	<b><u>35.3</u></b>
<b><u>STI</u></b>	<b><u>-5.1</u></b>	<b><u>9.4</u></b>	<b><u>24.2</u></b>	<b><u>29.3</u></b>

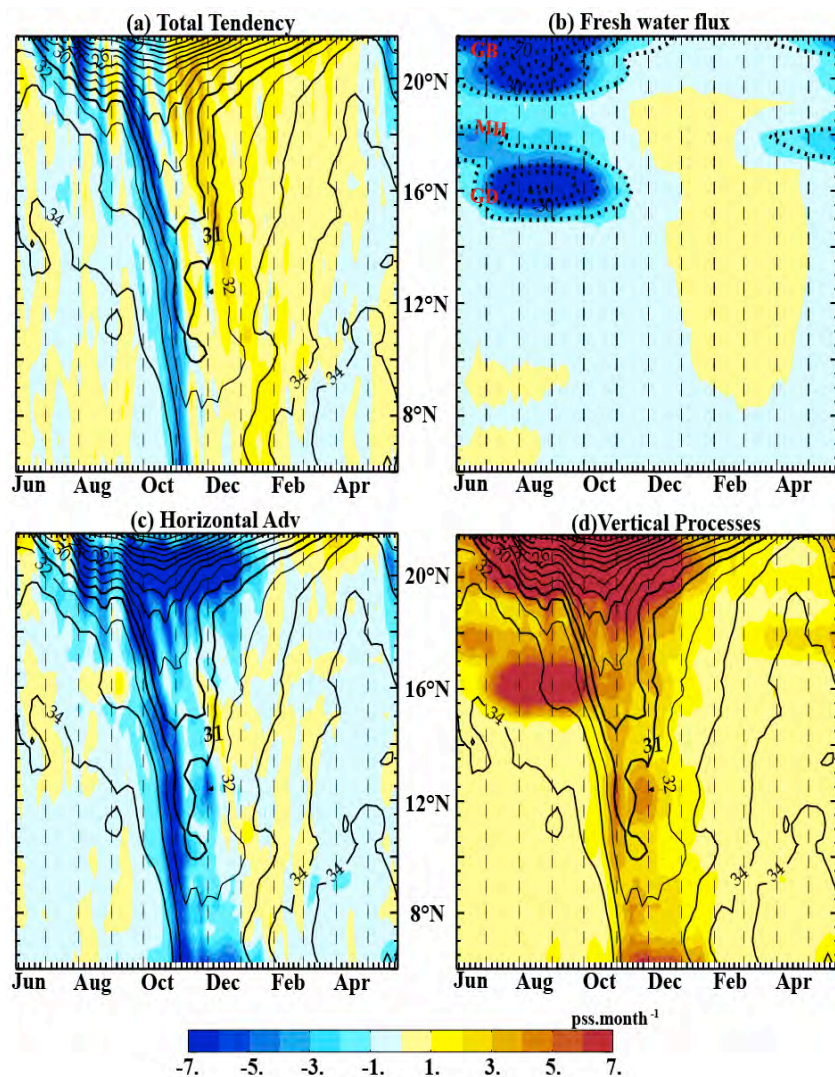
**Table 4.1** Statistics of Observed Climatological MLD (m) and Model MLD (m) in the Boxes Shown in Figure 4.5 : NBoB (86°E-93°E; 20°N-23°N), WBoB (80°E-81.5°E; 12°N-14°N) and STI (76°E-80°E; 6°N-8°N).



**Figure 4.6.** Latitude-time section of the model SSS (contours, pss) and along-shore current (shaded, negative values indicate southward current) seasonal cycle in the coastal strip box (limits defined by black lines on Figure 4.5) along east coast of Sri Lanka ( $6^{\circ}$ – $10^{\circ}$ N) and India ( $10^{\circ}$ – $21^{\circ}$ N).

Figure 4.6 displays a latitude-time evolution of the modeled seasonal SSS and alongshore surface currents within the strip off the East coast of India. From June, SSS starts decreasing in the northernmost part of the BoB, reaching values as low as 18 in October. This freshening quickly migrates southward in September-October. By November this fresh tongue reaches its southernmost limit, with salinity below 31 extending southward to  $10^{\circ}$ N. The three-month delay of the seasonal freshening off Kolkata relative to that off Chennai (Figure 4.4) is explained by the southward migration of the freshwater front, from  $20^{\circ}$ N to about  $10^{\circ}$ N, at a speed of about  $0.2 \text{ m.s}^{-1}$  (as inferred from the southward movement of the 31 isohaline). This fresh tongue considerably weakens in December-January, with a roughly simultaneously salinity increase in late November - early December throughout the  $10^{\circ}$ N– $19^{\circ}$ N portion of the coastal strip. Overlaying the time-latitude evolution of seasonal along-shore current (color) and SSS (contour) along the coastal strip (Figure 4.6) clearly illustrates that the southward migration of the freshwater front in September-October closely follows the current reversal (from poleward to equatorward) during this period. This suggests an active role of horizontal advection on the southward migration of the

SSS front. The retreat of the fresh tongue, on the contrary, occurs in December in the western BoB, about one month before the current reversal (from equatorward to poleward), suggesting that alongshore advection is not responsible for the northward retreat of the SSS front. Figure 4.6 also shows a gradual erosion of the SSS minimum as the freshwater tongue progresses southward, from values of less than 20 units at 21°N, to about 31 units at 10°N two months later. This erosion is suggestive of mixing processes, occurring along the path of the freshwater mass. A more quantitative analysis of the various terms contributing to the SSS seasonal variations along this coastal strip is further provided in the next paragraph.



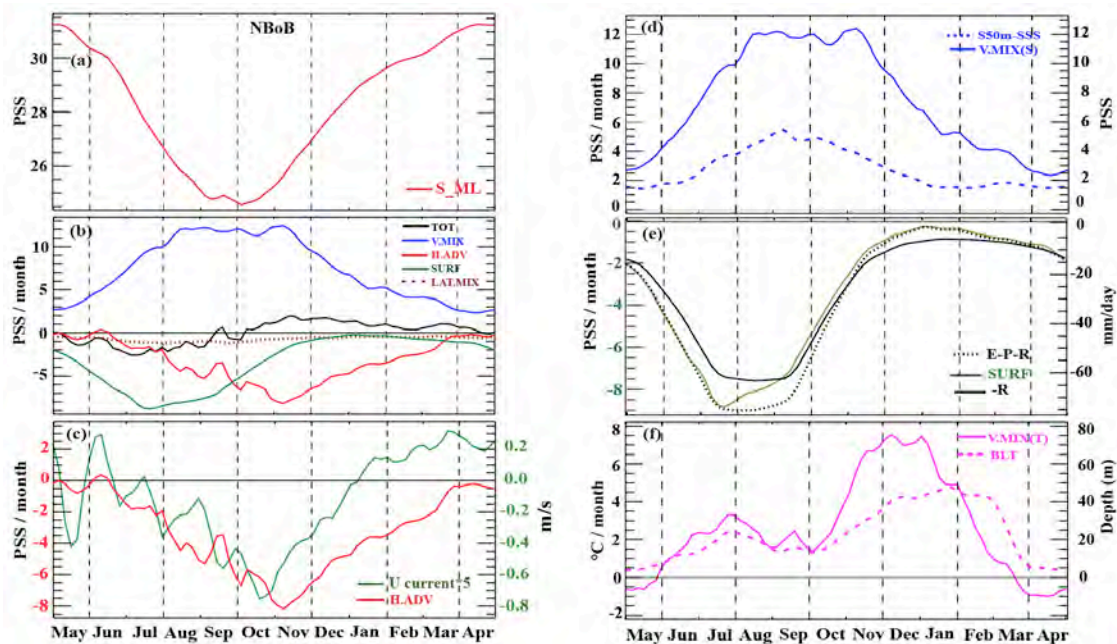
**Figure 4.7.** Latitude-time section of the model mixed layer salinity tendency terms ( $\text{pss.month}^{-1}$ ) mean seasonal cycle in the coastal strip box (limits shown on Figure 4.5) along east coast of Sri Lanka ( $6^{\circ}$ – $10^{\circ}\text{N}$ ) and India ( $10^{\circ}$ – $20^{\circ}\text{N}$ ): (a) total tendency, (b) freshwater forcing, (c) horizontal advection and (d) vertical processes. Surface salinity (pss) is shown in contours on panels (a), (c) and (d). River runoffs ( $\text{mm.day}^{-1}$ ) are displayed in contours on panel (b), with GB, MH and GD indicating respectively the mouths of Ganges Brahmaputra, MH and GD rivers. See equation (1) for the formula of the terms plotted above.

Figure 4.7a shows the latitude-time evolution of the total SSS tendency within the coastal strip. The most striking feature is the sharp freshening pattern, originating from the northern BoB in June-July, lasting until the end of September, and migrating southward from August to November. This freshening appears to be a subtle balance between three considerable larger terms: freshening by the atmospheric and continental freshwater flux (Figure 4.7b), freshening by the advection from horizontal circulation (Figure 4.7c) and salinity increase by vertical processes (Figure 4.7d). The freshening is initiated by continental runoff by major rivers (Ganges and Brahmaputra -henceforth GB- and GD mostly, with a lesser contribution of MH river) picking up in July, reaching their maximum in August, and decaying through October. Huge freshwater input occurs east of our coastal strip box limit as a combination of oceanic rainfall over the north-eastern BoB in summer (Figure 4.1) and part of the GB discharge. This freshwater is advected westward by the northern extent of the cyclonic gyre centered on (90°E, 19°N) from August to October; this is followed by a period of south-westward EICC throughout the northern part of the domain (November-December-January), which sustains the advection of the freshwater (Figure 4.2). This explains the strong freshening through horizontal advection seen during this period everywhere to the north of 18°N (Figure 4.7c). Figure 4.7c also confirms the key role of horizontal advection in driving the southward migration of the fresh tongue suggested in the previous paragraph. The vertical processes is defined as the sum of vertical diffusion, entrainment and vertical advection, and among these the vertical diffusion term dominates. Vertical processes consistently act to counteract the freshening driven by freshwater forcing and/or horizontal advection (Fig 4.7d). This is particularly visible from June to December north of 19°N, as well as near the GD river mouth centered on 16°N, from July to October, where vertical processes completely counteract the freshening induced by the GD runoff. The following gradual salinity increase of this fresh tongue (reflected as the moderately positive total tendency term from November to January in Figure 4.7a) is then mostly explained by vertical processes, which remain strongly positive all along the pathway of the SSS minimum tongue.

#### **4.4.2 Northern BoB**

The seasonal SSS evolution in the northernmost part of the domain (NBoB box) and its controlling processes are detailed in Figure 4.8. Consistent with what was

seen in the northernmost part of the coastal strip (Figure 4.7), the total tendency term evolution results from a subtle balance between three considerably larger terms: a systematic mixed layer freshening through freshwater forcing flux and horizontal advection, and a systematic salinity increase through vertical processes (Figure 4.8b). The freshening tendency during the first half of the monsoon is dominated by the freshwater input, almost completely driven by G-B discharge (Figure 4.8e), with a maximum freshening in July. From August to October, the salt input into the mixed layer resulting from mixing surface fresh water with underlying saltier water is maximum (Figure 4.8d) and acts to counteract the freshening through freshwater input. From September onward, vertical processes overwhelm the combined freshening effect of freshwater forcing and horizontal advection terms and are responsible for the gradual SSS increase. The freshening effect of horizontal advection broadly mirrors the evolution of the zonal current (Figure 4.8c), with a largest SSS decrease induced in October-November when the zonal current carries the freshwaters westward from the mouths of G-B and from the area of strongest precipitation in the North-Eastern BoB.



**Figure 4.8.** (a) Seasonal evolution of the average model mixed layer salinity over the NBoB box (limits shown in Figure 4.5) (b) Mixed layer salinity tendency terms ( $\text{pss month}^{-1}$ , horizontal advection in red, vertical processes in blue, surface freshwater forcing in green, lateral mixing in brown dashed line and total tendency in black). (c) Horizontal advection term (red,  $\text{pss.month}^{-1}$ ) and zonal current (green,  $\text{m.s}^{-1}$ ). (d) Vertical mixing term (blue,  $\text{pss month}^{-1}$ ) and salinity at 50 m depth minus SSS (blue dashed line,  $\text{pss}$ ). (e) freshwater forcing term (green,  $\text{pss.month}^{-1}$ ), freshwater flux E-P-R (black dashed line,  $\text{mm.day}^{-1}$ ) and river runoff (black line,  $\text{mm.day}^{-1}$ ). (f) Mixed layer temperature vertical mixing term (purple,  $^{\circ}\text{C.month}^{-1}$ ) and barrier layer thickness (dashed purple, m).

While the timing of the horizontal advection and surface forcing is easy to understand from the seasonal cycle of rain, runoff and currents, the timing of the vertical mixing term (that evolves in phase opposition with surface salinity, Figures 4.8a and 4.8b) deserves some explanation. As pointed out earlier, vertical mixing in the BoB mixes surface freshwater with underlying saltier water (i.e. it brings saltier water into the mixed layer). The effect of vertical mixing of subsurface water into the mixed layer is usually parameterized as  $w_e (\langle S \rangle - S_{-h})$ , where  $w_e$  is an entrainment speed (the result of vertical mixing by turbulence),  $\langle S \rangle$  is the mixed layer average salinity and  $S_{-h}$  is the salinity just below the mixed layer [e.g. *Niiler and Kraus, 1977*]. The vertical mixing term will thus increase as the salinity difference between the mixed layer and subsurface salinity increases. Figure 4.8d shows that the  $\langle S \rangle - S_{-h}$  difference is dominated by changes in SSS (i.e. the subsurface salinity  $S_{-h}$  varies much less than the surface salinity  $\langle S \rangle$ ). The vertical salinity gradient is hence large during the summer monsoon, when surface salinity is fresh, resulting in a stronger saltening under the effect of vertical mixing with underlying water.

The explanation above however neglects one factor,  $w_e$  (i.e. vertical mixing or turbulence at the bottom of the mixed layer) that is also affected by salinity stratification. The sharp vertical density stratification generated by massive monsoonal surface freshwater inflow is indeed usually believed to limit vertical exchanges between the surface layer and the deeper layers [e.g. *Shenoi et al., 2002; Agarwal et al., 2012; Thadathil et al., 2007*]. In other words, salinity stratification  $\langle S \rangle - S_{-h}$  has two opposite effects on the salinity vertical mixing term: on one hand an increase of the salt flux into the mixed layer due to the entrainment of relatively saltier water, but on the other hand a decrease due to an inhibition of turbulence and hence of  $w_e$ . Figure 4.8d indicates that the first effect dominates, and Figure 4.9 allows understanding why. Figure 4.9 provides the average temperature, salinity and density profiles for the NBoB domain, during August-September-October (when vertical processes are maximum) and during February-March-April (when they are weaker). Vertical mixing is the result of transformation of turbulent kinetic energy into potential energy. Assuming heat and salt conservation and a perfectly homogeneous mixed layer (as in *Jourdain et al. [2013]*), we computed the energy required to increase surface salinity by 0.5 unit by vertical mixing of the mixed layer with underlying saltier water (see

Appendix for details). The 0.5 unit value corresponds to the typical salinity increase observed in the NBoB box over a week or so, over the October-April period (similar qualitative results are obtained for SSS increase ranging from 0.2 to 2). During August-October, it is only necessary to mix down to 13 m depth to yield a 0.5 surface salinity increase, because the upper ocean stratification is strong and shallow in that season. In contrast, it is necessary to mix the ocean down to 25 m depth in spring in order to obtain a similar salinity increase because of the weaker upper haline stratification in that season. The associated necessary energy to produce this mixing increases by a factor of 4 between the two seasons, from  $133 \text{ J.m}^{-2}$  in summer to  $572 \text{ J.m}^{-2}$  in spring. The idealized computation in the Appendix also indicates that, for a given salinity change, the requested energy decreases when the salinity stratification increases. This confirms that the inhibiting effect of salinity on turbulence is overwhelmed by the effect of the vertical salinity gradient on the salinity flux at the bottom of the mixed layer. A larger salinity stratification at the bottom of the mixed layer hence favors larger salinity increase by vertical mixing, consistent with what is seen in Figure 4.8d.

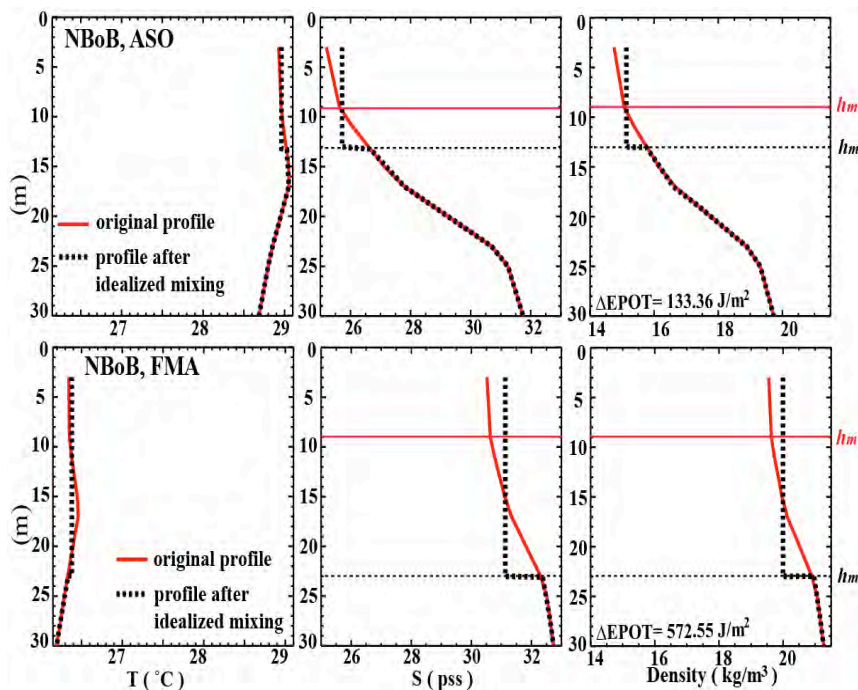


**Figure 4.9.** (top) Vertical profiles of model temperature, salinity and density averaged over NBoB box (limits shown on Figure 4.5) during August-September-October (red line). Black dashed lines show idealized profiles that would yield a SSS rise of 0.5 unit under the effect of vertical mixing, assuming the conservation of salt and heat (see Appendix for details). The difference in potential energy ( $\Delta\text{EPOT}$ ) of the water column before and after this mixing is indicated. Mixed layer depth ( $h_m$ ) before mixing (in red) and after mixing (in black) is also indicated. (bottom) same as top, for the February-March-April period.

While vertical salinity stratification favors a stronger vertical salinity mixing, the effect is quite different on temperature. Because of the barrier layer, there is indeed a weak temperature gradient (or even a temperature inversion) between the BoB mixed layer and top of the thermocline, hence preventing mixing to cool the surface layer. This can be verified in our model by examining the vertical mixing term for temperature (equivalent of Equation (1) for temperature, as was for example done in *de Boyer Montégut et al.* [2007] in the BoB, based on a similar model as ours). Figure 4.8f presents the modeled time series of the barrier layer thickness together with the vertical processes term of the mixed-layer temperature budget. This term displays a completely different evolution from the salinity vertical processes term, and remains positive most of the year. Because of the barrier layer effect (Figure 4.8f) and associated temperature inversion [*Thadathil et al.*, 2002, 2007], mixing indeed systematically acts to warm the surface, except for a very brief two months period in April-May when the salinity stratification is weak. There is also a very clear modulation of the magnitude of the temperature vertical mixing term by the thickness of the barrier layer: thick barrier layers result in a larger warming of the surface, while thin barrier layer are associated with a weaker amplitude effect of vertical mixing. This contrasted impact of vertical mixing on mixed-layer temperature and salinity may be summarized as follows: the barrier layer of the northern BoB enhances the mixed layer salinity increase by vertical processes, whereas it inhibits the mixed-layer cooling. As the vertical gradient of salinity at the bottom of the mixed layer is largely controlled by the mixed layer salinity (since subsurface variability of salinity is weaker than SSS variability), mixed layer salinity increase by vertical processes varies in phase with SSS.

In summary, freshwater forcing decreases mixed-layer salinity in the NBoB during the summer monsoon. By September, the bulk of the freshwater has entered the ocean and advection picks up and spreads those low salinity water over the entire Northern BoB. As salinity decreases, the vertical salinity gradient increases, and so does the surface salinity increase through vertical processes. In early October, surface salinity increase through vertical mixing overcomes the combined freshening through freshwater forcing flux and horizontal advection, and salinity starts increasing again. This surface salinity increases by vertical mixing lasts until the following monsoon onset (May).

### 4.4.3 The Western BoB and the Southern Tip of India

The WBoB box is located along the western boundary of the BoB, roughly halfway between the Northern source of freshwater and the southern limit of the basin (Figure 4.5). SSS decreases abruptly from  $\sim 34$  in late September to 31.3 in early November (Figure 4.10a). This abrupt drop of 2.7 units is about twice smaller than the salinity decrease in the NBoB box between May and October (6.7 units). From early December, salinity starts increasing quickly, and recovers its initial 34.0 value in late February.

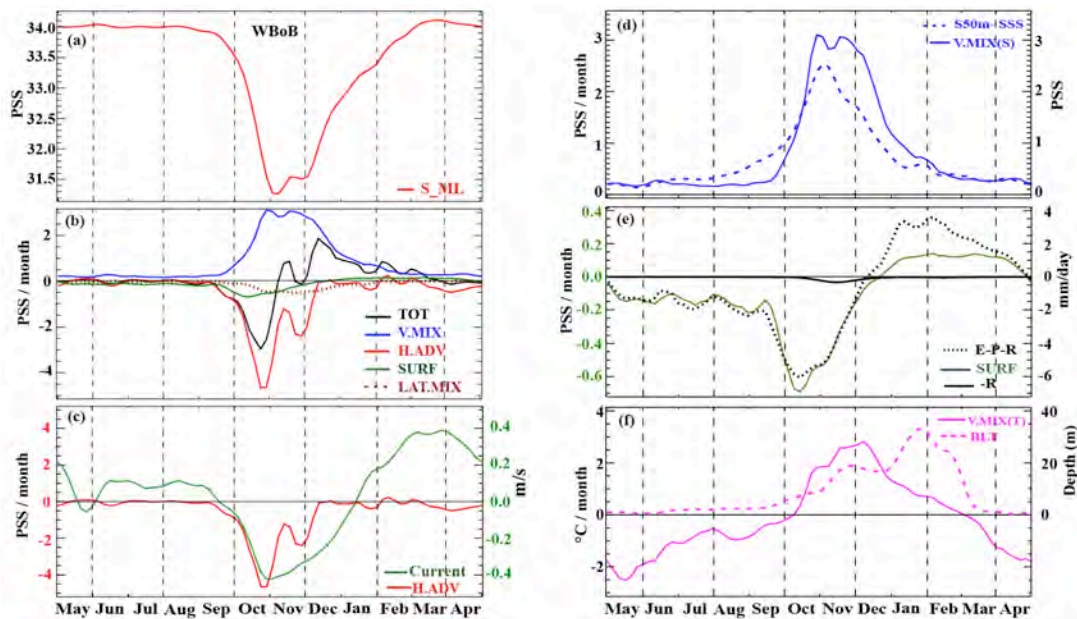


**Figure 4.10.** Same as Figure 4.8, for WBoB box (limits shown on Figure 4.5), except that the current (in green on panel c) is here the along-shore current.

The basic equilibrium driving this seasonal evolution is somewhat simpler than for NBoB box, as it only involves two processes: horizontal advection that drives the freshening phase and vertical processes that induce the subsequent surface salinity increase (Figure 4.10b). The atmospheric forcing term is rather weak in the WBoB box (Figure 4.10b), and almost entirely driven by atmospheric fluxes (Figure 4.10e), with a freshening effect in October November during the northeast monsoon, and evaporation from January to April. In contrast with the NBoB region, the total tendency term is of same order as the main individual terms. The horizontal advection is solely responsible for the September-October drop of SSS, as both the atmospheric freshwater flux and the horizontal diffusion remain weak (Figure 4.10b). The

horizontal advection terms pick up as soon as the southward-flowing EICC enters the domain (Figure 4.10c). The two quantities evolve in concert up to December, with a weaker freshening effect as the southward-flowing EICC decays in November-early December. Vertical processes start increasing in conjunction with the freshening onset in late September and then peak in November simultaneously with the maximum freshening (Figure 4.10b). The surface salinity increase simulated from early December onwards is not driven by the advective term as the EICC is still flowing southward at that time but by vertical processes that overcome the advective freshening from early December onward. Moreover, advective processes never act to increase the SSS subsequently, because the coastal tongue of low salinity is already strongly eroded (Figure 4.6) by the time the EICC turns northward again from mid-January onward. Just like in the NBoB box, the seasonal evolution of vertical processes term is the mirror of the vertical gradient of salinity in the upper layers (Figure 4.10d). Given that subsurface salinity varies much less than SSS at seasonal timescales, the evolution of SSS appears here again as a good proxy of the evolution of the vertical processes term (with low SSS favoring a stronger salt flux into the mixed layer through vertical processes, and vice-versa). As in the NBoB box, the vertical mixing of temperature behaves quite differently than the vertical mixing of salinity, with a cooling (warming) term in the absence (presence) of barrier layer (Figure 4.10f). To summarize, SSS along the west coast of India drops abruptly in fall when the southward-flowing EICC brings freshwater from the Northern BoB; the large salinity gradient between the surface and subsurface results in an enhanced surface salinity increase by vertical mixing, which then progressively erodes this freshening, and eventually restores the salinity to the pre-monsoon values.

The STI box, although not strictly located within the BoB, displays a similar behavior to the WBoB box: salinity drops suddenly in the post-monsoon season (from early November), and then increases gradually from January to August) (Figure 4.11a). Like in the WBoB box, the freshening phase is driven by horizontal advection, while vertical processes drive the subsequent surface salinity increase (Figure 4.11b). The atmospheric forcing term is also weaker than the other terms, and mostly associated with the northeast monsoon rains (Figure 11e). The magnitude of the seasonal SSS drop does not exceed 2 units, significantly less than in the WBoB box. The quasi-zonal Summer Monsoon Current (Figure 4.11c) flows westward from

November to March, and carries freshwaters from the BoB into the South-Eastern AS [Shenoi *et al.*, 1999; Durand *et al.*, 2007], through the STI region; this explains the evolution of horizontal advection in that box. Just like in the WBoB box, surface salinity increase by vertical processes counterbalances the freshening by horizontal advection. The evolution of the magnitude of vertical processes closely mirrors the evolution of vertical gradient of salinity in the upper layers, which evolves like SSS here as well (Figure 4.11d). On the other hand, the vertical mixing of temperature is rather related to the barrier layer thickness (Figure 4.11f), as in the WBoB box. One specific aspect of STI box, however, lies in the saltening effect of zonal advection at the beginning of summer monsoon (May and June; Figure 4.11d). At this time, the West India Coastal Current carries salty Arabian Sea water southward along the west coast of India, and feeds the eastward-flowing Summer Monsoon Current [Shankar *et al.*, 2002]. The cumulated effect of this saltening advection throughout the spring and summer seasons is however much weaker than the saltening due to vertical mixing in the STI box (Figure 4.11c).

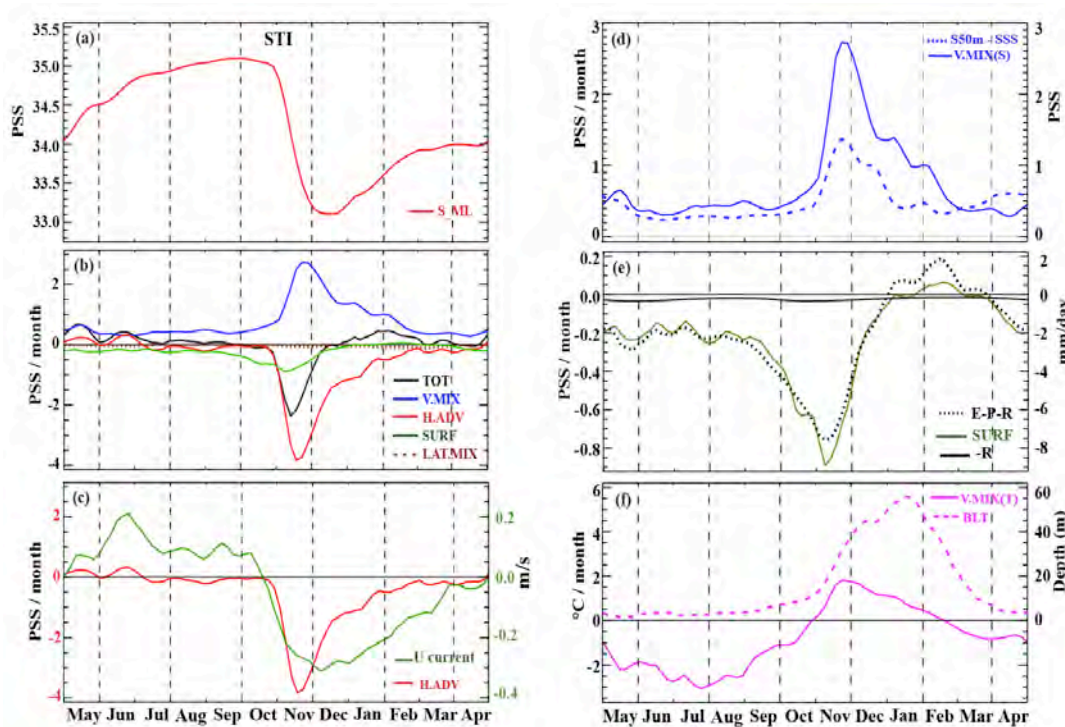


**Figure 4.11.** Same as Figure 4.8, for STI box (limits shown on Figure 4.5).

The contrasted impact of vertical processes on mixed-layer salinity and temperature, observed in NBoB box and discussed in the previous section, is also seen in WBoB and STI boxes (Figure 4.10d and 4.11d). In October-February, the barrier layer is thick in the two boxes (Figure 4.10d and 4.11d). The barrier layer effect

implies that this season when vertical processes act to increase mixed layer salinity is also the period when the vertical processes do not cool (and even warm) the mixed layer.

Overall, the NBoB, WBoB and STI regions are quite homogeneous in their SSS variability mechanisms, with an inflow of freshwater in the Northern BoB, and a subsequent horizontal transport along the western boundary of the BOB by the southward-flowing EICC after the monsoon. This input of surface freshwater by EICC transport results in a larger vertical salinity stratification, which results in an increased surface saltening by vertical processes, which eventually restores mixed layer salinity to its pre-monsoon values.

## **4.5. Summary and discussion**

### **4.5.1 Summary**

The objective of our study is to quantify the mechanisms that contribute to the SSS seasonal cycle in the BoB. To that end, we use an eddy-permitting ( $1/4^\circ$ ) regional simulation forced with altimeter-derived estimates of the river runoff for the Ganges and Brahmaputra (the two most important rivers), and no relaxation toward climatological observed SSS. Despite this absence of relaxation, our model adequately reproduces the main features of the observed SSS field, with freshest waters in the northeastern BoB, especially during and after the summer monsoon. Our eddy-permitting model produces a narrow ( $\sim 100$  km wide) coastal strip of freshwater along the coast of India after the southwest monsoon, which is not well resolved by existing observational SSS climatologies. This narrow coastal freshening is confirmed by relatively high-resolution ( $\sim 50$  km and two month) salinity sections observed along two shipping lines between the east coast of India and central BoB. The relatively good agreement between the model and those observations encouraged us to use the model to quantify the dominant mechanisms of the SSS seasonal cycle. The BoB receives a large amount of freshwater from the Ganges and Brahmaputra and from oceanic precipitation during the summer monsoon, that is the main cause for a large drop in SSS in the northernmost part of the BoB. From late September onwards, this freshwater is advected southward by the EICC, as a thin tongue hugging the western

boundary and that reaches the South-Eastern AS in early December. The salt influx into the BoB mixed layer (necessary to the long-term surface salinity equilibrium in this dilution basin) occurs prominently through vertical exchanges at the bottom of the mixed layer, during the monsoon and post-monsoon seasons. The magnitude of these vertical exchanges varies in space and time: strongest surface salinity increase tendencies occur when/where salinity stratification is strong. This is explained by the amplifying effect of salinity stratification on the vertical salt flux at the bottom of the mixed layer, that overwhelms the stabilizing effect of salinity. Strong salinity stratification has hence a very contrasted effect on temperature and salinity fluxes at the bottom of the mixed layer: on one hand, it favors the presence of barrier layer and shuts down entrainment cooling, but on the other hand it promotes surface salinity increase by vertical exchanges. Barrier layer hence only acts as a barrier for vertical heat fluxes, but allows considerable vertical freshwater/salinity fluxes.

#### 4.5.2 Discussion

The most obvious limit of the current study is the observational coverage. The eastern half of the bay is in particular under-sampled compared to the western half [Chatterjee *et al.*, 2012], making it hard to study SSS variations there. For example, our model displays a remarkable region of high SSS variability off the mouths of the IR river (Figure 4.5). The SSS budget analysis in this area highlights mechanisms that are essentially similar to those in the NBoB region: surface freshwater (mostly from the river) is the dominant freshwater source; ocean circulation acts to spread it horizontally while vertical processes tend to increase the SSS. We did not display this analysis in the present paper, as the Andaman basin is completely devoid of SSS observations [Chatterjee *et al.*, 2012] and we are hence not in a position to ascertain the validity of the model simulation there.

Our study agrees with previous modeling studies [Howden and Murtugudde, 2001; Han and McCreary, 2001; Han *et al.*, 2001; Yu and McCreary, 2004] in designing river runoff, and not precipitation, as the dominant factor in freshening the northernmost part of the Bay during the southwest monsoon. Han and McCreary [2001], Jensen [2001], Rao and Sivakumar [2003] and Nyadjro *et al.* [2011] previously identified lateral advection of low salinity waters from the northern BoB as

the main driver of fresh water expansion along the east coast of India after the monsoon. Our study agrees with these previous studies, but additionally provides a description of the trapping of the freshening close to the coast. This very narrow coastal freshening seen in the model is supported by ship-of-opportunity data. These data suggest that, at least at 21°N and 13°N, the model does not suffer from serious biases in the SSS and cross-shore SSS gradient it simulates close to the coast. The much broader coastal freshening seen in NIOA is most likely due to the scarcity of salinity data in the BoB and/or to the 4° smoothing applied during the objective analysis of *Chatterjee et al.* [2012]. Both salinity and current observations close to the coast are needed to better understand the magnitude, trapping scale and timing of this freshening.

Contrary to what was suggested by *Shetye* [1996] and *Vinayachandran and Nanjundiah* [2009], we find that the salt influx into the BoB mixed layer is not the result of horizontal advection from AS waters into the South-Western BoB. The salt influx into the BoB mixed layer (necessary to the long-term surface salinity equilibrium in this dilution basin) occurs prominently through vertical exchanges at the bottom of the mixed layer, during the monsoon and post-monsoon season, as initially suggested by *Shetye* [1993]. The magnitude of these vertical exchanges varies in space and time: strongest surface salinity increase by vertical processes occur when/where salinity stratification is strong. *Vinayachandran and Nanjundiah* [2009] reported a relatively moderate magnitude of the vertical processes in their SSS budget during the post-monsoon season. Their budget however neglected the vertical diffusion term (term (d) in Equation (4.1)), which actually dominates the vertical processes in our model.

Although we identified vertical exchanges of salt as a key ingredient of the SSS budget, we are not in a position to quantitatively compare the balance from equation (1) in the model to an observed counterpart. Of course the relative realism of the model salinity and currents imply that the balance estimated from the model is valid at the first order. Our conclusions concerning the importance of vertical mixing for the long term upper ocean salinity balance in the BoB call for dedicated measurements of mixed layer processes, with microstructure measurements in order to estimate the vertical diffusivity in the upper oceanic layers, as in *Cuypers et al.* [2013]

and *Moum et al.* [2013]. In addition, it may also be relevant to assess the robustness of our quantitative SSS budget in other OGCMs, using different parameterizations of the vertical physics, horizontal resolution and/or forcing datasets.

The western rim of the BoB is an area of intense eddy activity [*Durand et al.* 2009]. A recent observational study indicates that those eddies may efficiently mix the coastal freshwater with offshore saltier water after the monsoon [*Hareesh Kumar et al.* 2013]. The ~25 km resolution of our model is eddy-permitting, but not really eddy-resolving, and does not permit assessing the effect of the oceanic mesoscale circulation on the coastal freshwater strip. Refining the model resolution may also be a way to further improve the realism of our simulation. Our rather coarse  $\frac{1}{4}^\circ$  model indeed underestimates the EEIC by ~30% on the south-eastern coast of India in winter (Figure 4.2c and 4.2g), with a possible impact on the timing of the simulated coastal freshening. Using a higher  $\sim 1/12^\circ$  horizontal resolution would improve the simulated EICC, as discussed in *Benshila et al.* [2014]. Finally, increasing the vertical resolution in the upper layers (from 6 m to 1 m) may improve the representation of the very steep near-surface salinity stratification that is occasionally observed in the BoB [*Vinayachandran and Kurian, 2007*] and would allow to test the impact of the diurnal cycle of the buoyancy forcing fluxes on the salinity stratification. The modeling of the BoB (and in particular of its salinity structure) will undoubtedly benefit from higher resolution simulations in the future.

There are two interesting perspectives for our work. First, we found that the surface layer freshwater flux is balanced by a downward freshwater flux to the ocean's subsurface at the seasonal scale. Since the BoB is a semi-enclosed basin, this downward freshwater flux has to be evacuated by the oceanic subsurface circulation, *i.e.* on average, the subsurface horizontal flow into the bay has to be saltier than the exit flow, in order to maintain the long-term balance. It will be interesting to study these subsurface freshwater fluxes in the future.

Due to the lack of data, very little is known about the interannual variation of SSS in BoB. The availability of remotely sensed surface salinity data from SMOS [*Mecklenburg et al., 2012*] and Aquarius [*Lagerloef et al., 2008*] satellites provides an interesting option for qualifying this interannual variability better. On the modeling

front, the major limitation for representing interannual salinity variability by models was the lack of reliable continental freshwater forcing [Vinayachandran and Nanjundiah, 2009; Durand *et al.*, 2011]. Now reliable interannual runoff estimates are available, at least for the dominant rivers of the BoB. This opens the way to study the mechanisms of SSS interannual variations of the BoB.

## **Appendix. Energy required for increasing surface salinity by vertical mixing**

Vertical mixing is the result of turbulent kinetic energy conversion into potential energy. In this appendix, we first summarize the approach of *Jourdain et al.* [2013], which allows computing the potential energy increase (*i.e.* required energy) to raise surface salinity by 0.5 units under the effect of vertical mixing. We then provide an analytical derivation of this necessary energy, in the idealized case of uniform salinity stratification, and no temperature stratification.

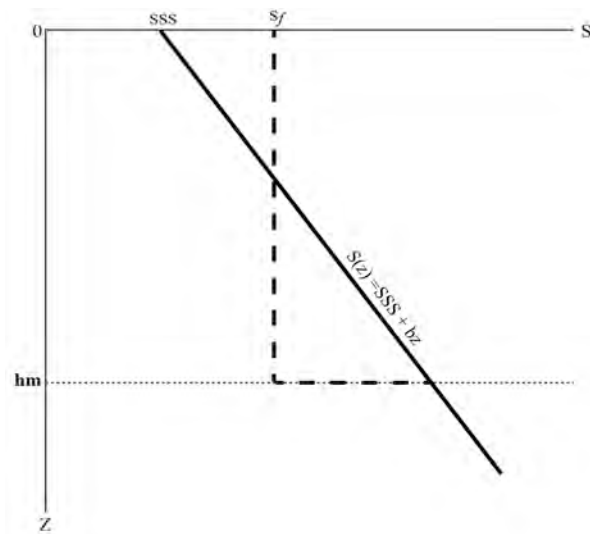


**Figure 4A1.** Idealized salinity profile used for the analytical computations. The thick black line corresponds to the idealized profile before mixing; the dashed line corresponds to the idealized profile after mixing.

### ***1) Diagnostic of necessary mixing energy from model profiles***

Given a model temperature, salinity and density ( $r_i$ ) profile (like the red profiles in Figure 4.9), we want to compute how much energy is necessary to increase salinity by 0.5 units by vertical mixing. We will assume that the mixed layer is perfectly homogeneous after mixing, and heat and salt conservation.

An idealized “profile after mixing” is constructed (dotted profiles on Figure 4.9), assuming a homogeneous temperature and salinity down to a depth  $h_i$  (the homogeneous temperature and salinity in this profile are obtained by assuming heat and salt conservation over the depth  $h_i$ ).  $h_i$  is increased iteratively until the difference in surface salinity between the original profile and idealized profile is 0.5 units. Once this “mixing depth”  $h_m$  has been obtained, the final profile density  $r_f$  is computed using the *Jacket and McDougall* [1995] equation of state. The necessary energy per unit area

that was needed for that mixing is computed from the potential energy change between the initial (red curves on Figure 4.9) and final (dotted curves on Figure 4.9) profiles using:

$$\Delta E = \int_{hm}^0 ((\rho_f - \rho_i)gz) dz$$

## 2) Analytical derivation in the case of uniform salinity stratification

In this section, we derive an analytical solution to the numerical calculation presented above for the simple case of an uniform salinity stratification, and negligible temperature effects (see figure 4A1) :

$$S(z) = SSS + bz, \text{ where } z \text{ is downward and } b \text{ and } SSS \text{ are constants.}$$

We assume that density  $\rho(z)$  is dominated by salinity changes, as is usually the case in the near-surface layer of the BoB [e.g. *Shenoi et al.*, 2002]:

$$\rho(z) = \rho_0[1 + \beta S(z)], \text{ where } \beta > 0$$

Salt conservation gives:

$$\begin{aligned} \int_{hm}^0 (SSS + bz) dz &= \int_{hm}^0 S_f dz \\ SSS h_m + \frac{bh_m^2}{2} &= S_f h_m \\ \frac{bh_m^2}{2} &= h_m (S_f - SSS), \quad \text{where } (S_f - SSS) = \Delta S \\ \Delta S &= \frac{bh_m}{2} \end{aligned}$$

The potential energy of the water column before mixing ( $E_B$ ) is:

$$\begin{aligned} E_B &= \int_{hm}^0 (\rho g z) dz \\ &= \int_{hm}^0 (\rho_0 [1 + \beta (SSS + bz)] g z) dz \\ &= g \rho_0 \int_{hm}^0 \left( (1 + \beta SSS) z + \beta b z^2 \right) dz \\ &= -g \rho_0 \left[ (1 + \beta SSS) \frac{h_m^2}{2} + \beta b \frac{h_m^3}{3} \right] \\ &= -\rho_0 g (1 + \beta SSS) \frac{h_m^2}{2} - \rho_0 g \beta b \frac{h_m^3}{3} \end{aligned}$$

The potential energy of the water column after mixing ( $E_A$ ) is:

$$\begin{aligned} E_A &= \int_{h_m}^0 (\rho g z) dz = \int_{h_m}^0 (\rho_0 g (1 + \beta S_f) g z) dz \\ &= -\rho_0 g (1 + \beta S_f) \frac{h_m^2}{2} \end{aligned}$$

The required energy  $\Delta E = E_A - E_B$  for increasing salinity by  $\Delta S$  under the effect of mixing is:

$$\begin{aligned} \Delta E &= -\rho_0 g \beta S_f \frac{h_m^2}{2} + \rho_0 g \beta S S_f \frac{h_m^2}{2} + \rho_0 g \beta b \frac{h_m^3}{3} \\ &= \rho_0 g \beta \Delta S \frac{h_m^2}{2} + \rho_0 g \beta b \frac{h_m^3}{3} \end{aligned}$$

and since  $\Delta S = \frac{b h_m}{2}$

$$\Delta E = \frac{\rho_0 g \beta b h_m^3}{12} = \frac{2}{3} \rho_0 g \beta \frac{\Delta S^3}{b^2}$$

$$\Delta S = \sqrt[3]{\frac{3}{2} \frac{\Delta E}{\rho_0 \beta g}} b^2$$

In this idealized case,  $\Delta S$  is proportional to  $b^{2/3}$ , i.e. for a given energy input  $\Delta E$ , the amplitude of the salinity change induced by mixing increases with the salinity stratification. Salinity stratification has two effects on the surface salinity change. On one hand, a strong salinity stratification increases the salt flux into the mixed layer for a given mixed layer depth deepening. On the other hand, salinity stratification increases the static stability of the water column, and tends to resist mixed layer deepening. The simple analytical calculation above suggests that the first effect dominates the second (i.e. larger vertical salinity stratification tends to favour large surface salinity changes through vertical mixing).

## Chapter 5

### Interannual variability of Bay of Bengal sea surface salinity: a modelling approach

---

#### Foreword

The IO is under the influence of two interannual climate modes: ENSO and the IOD. Whereas ENSO center of action is situated in the Pacific Ocean, its influence on the Walker Circulation remotely drives anomalies in the IO, such as an overall warming after an El Niño, or monsoonal rainfall anomalies over the Indian subcontinent. The IOD emerges from local air-sea interactions in the equatorial IO, and is also associated with clear climate anomalies peaking in boreal fall. Finally, the Indian summer monsoon also experiences variability that is independent from either the IOD or ENSO (e.g. internal variability) and that affects rainfall patterns over the northern IO and hence also the runoffs of major rivers into the BoB. While the SSS seasonal cycle has been studied to some extent, studies of the BoB SSS interannual variability are pretty rare. This is both due to the insufficient spatio-temporal sampling of the *in-situ* network and also the lack of reliable interannually varying continental freshwater forcing. As described in previous chapters, the recent availability of altimeter-derived discharges of major rivers into the BoB now provides an opportunity to better quantify the continental freshwater forcing flux into the general circulation models. In addition, the recent improvements in SSS *in-situ* observing system now provide some estimate of the SSS interannual variability in the BoB, too patchy for an exhaustive budget study, but dense enough to validate an ocean circulation model. Finally, as seen in Chapter 3, Aquarius provides an independent estimate of SSS interannual anomalies that can also be used to validate the model. In this chapter, I use the regional eddy permitting ocean general circulation model configuration presented in Chapter 4, but with a surface forcing that allows a simulation over an extended period (1990-2012). I describe the SSS interannual variability in the BoB in this model and compare it to available observations, relate it to the main climate modes in the IO and describe the main mechanisms controlling SSS interannual variations.

Due our limited background knowledge on this topic, the results in this chapter are almost entirely original. We first demonstrate that the model compares well with estimates of SSS interannual patterns from both *in-situ* data and Aquarius. Maxima of SSS interannual variations are found in boreal fall in three regions: the largest maximum is in the northern BoB, followed by the coastal region off east India and by the Andaman Sea. SSS interannual variations in the northern BoB are mostly driven by GB runoff interannual variations, which are themselves linked to ENSO (0.4 correlation) due to its impact on rainfall on the Indo-Gangetic plain. SSS variability along the east coast of India is linked to the circulation anomalies associated with IOD events, which induce either enhanced or reduced southward advection of northern BoB freshwater by the EICC. Finally, the model variability in the Andaman Sea region cannot be validated due to the lack of *in-situ* observations. This variability is not clearly associated to a climate mode and is the result of a mixture of effects from interannual wind stress, rainfall and river runoff variations.

**The contents of this chapter will serve as the basis for an article, describing the processes responsible for SSS interannual anomalies in the BoB.**

## 5.1. Introduction

The BoB is a semi-enclosed tropical basin, landlocked to the north by the Asian continent. This basin is forced by annually reversing monsoonal winds that blow from the during the summer monsoon (May–September) and from the northeast during the winter monsoon (November–March). Those alternating winds drive the EICC, a well-defined, seasonally reversing western boundary current in the BoB. The EICC flows northward before the summer monsoon and southward right after [Shankar *et al.*, 1996; McCreary *et al.*, 1996]. This is the major current system in the BoB, and it is largely responsible for the exchange of water masses between the BoB and AS [Shetye *et al.*, 1996; Durand *et al.*, 2007 and references therein]. The BoB is also characterized by a large seasonal freshwater influx from rivers as well as excess precipitation over evaporation [Shenoi *et al.*, 2002]. A large fraction of this net freshwater flux to the ocean occurs during or shortly after the monsoon, with a similar contribution from continental runoffs and monsoonal oceanic rainfall over the northern half of the BoB [e.g. Chaitanya *et al.*, 2014b]. The largest rivers that flow into the BoB are the GB in the northern end of the BoB and the Irrawaddy along the eastern side, with an average discharge of  $\sim 8.7 \times 10^4 \text{ m}^3 \text{ s}^{-1}$  and  $\sim 3.4 \times 10^4 \text{ m}^3 \text{ s}^{-1}$  respectively during July-September [Papa *et al.*, 2012; Dai and Trenberth, 2002]. Three other smaller rivers on the East Indian coast (Mahanadi, Godavari and Krishna) contribute to  $\sim 10^4 \text{ m}^3 \text{ s}^{-1}$  together. As a result, the BoB stands out as a very peculiar region for salinity distribution in the tropical belt, with SSS as low as 28 in the northern part of the Bay. These low salinity surface waters lay above much saltier subsurface waters, resulting in a sharp near-surface haline stratification [Shetye *et al.*, 1993; Vinayachandran *et al.*, 2013].

This intense near-surface haline stratification has profound implications on the air-sea exchanges, and thus on the climate of the neighbouring countries. The near surface low saline water increases vertical stability of the upper surface layer, strengthens the density stratification and maintains a thin mixed layer [Mignot *et al.*, 2007; Thadathil *et al.*, 2007; Girishkumar *et al.*, 2013]. Combined with a homogeneous thermal stratification, this often results in the formation of a barrier layer [Lukas and Lindstrom, 1991], an isothermal and salinity-stratified layer below

the surface mixed layer. This barrier layer prevents turbulent entrainment of cooler thermocline water into the mixed layer [*de Boyer Montégut et al.*, 2007] and consequently maintains SST often above 28°C, a threshold for deep atmospheric convection [*Gadgil et al.*, 1984]. *Shenoi et al.* [2002] suggested that this promotes a positive feedback between low SSS, high SST and atmospheric convective rainfall in the BoB, that anchors intense rainfall there. The salinity stratification also prevents the oceanic cooling effect during the development of atmospheric cyclones [e.g. *Neetu et al.*, 2012], hence potentially favouring intense cyclones [*Sengupta et al.*, 2008]. It has also the potential to influence the amplitude of intraseasonal variability of the SST [*Vinayachandran et al.*, 2012] and biological productivity regimes [*Prasanna Kumar et al.*, 2002]. These strong impacts of haline stratification in the BoB call for a better description and understanding of the SSS spatial structure and temporal variability within the Bay.

Several studies have already investigated seasonal SSS variations in the BoB, using both observations [*Rao and Sivakumar*, 2003; *Shetye et al.*, 1991, 1993, 1996; *Vinayachandran et al.*, 2002b; *Vinayachandran and Kurian*, 2007; *Chaitanya et al.*, 2014b] and models [*Jensen*, 2001; *Benshila et al.*, 2014; *Akhil et al.*, 2014]. They all reported a marked seasonal cycle of SSS, especially in the northern part of the basin. From summer to fall, the freshest surface waters expand from the northernmost part of the basin (to the north of 18°N) to the entire northeastern BoB. This fresh pool then spreads southward along both eastern and western boundaries of the basin in fall and early winter. These fresh waters start retreating back northward in winter, to reach their minimal extent in spring. Previous studies [*Shetye et al.*, 1996; *Han et al.*, 2001; *Sengupta et al.*, 2006; *Akhil et al.*, 2014] showed that the strong freshening during the monsoon mostly results from the GB river discharge. *Shetye et al.* [1996] suggested that the southward expansion of fresh water after the monsoon was the result of southward advection by the EICC. *Chaitanya et al.* [2014a] demonstrated from *in-situ* data that this freshening is actually concentrated in a narrow (~50 km to 100 km-wide) strip hugging the coast of India. *Akhil et al.* [2014] showed that this narrow freshwater strip along the east coast of India was reproduced in their modelling study. Their results also demonstrate that horizontal advection by the southward-flowing EICC is responsible for the southward expansion of the fresh pool in the northern BoB along the east coast of India, reaching the southern tip of India in November, consistent with

previous results by *Benshila et al.* [2014]. Northward horizontal advection by the reversing EICC is however not responsible for the erosion of this freshwater tongue, but occurs prominently through vertical exchanges at the bottom of the mixed layer that restore SSS to its pre-monsoon values [*Akhil et al.*, 2014].

Although the seasonal cycle is by far the most energetic timescale of upper BoB variability, the BoB climate also exhibits clear interannual variations. The patterns of precipitation over the BoB and adjoining continents [e.g. *Gadgil*, 2003] as well as the riverine freshwater supply to the BoB [*Papa et al.*, 2012] indeed vary significantly from year to year. Three climatic modes influence the interannual variability of wind and precipitation over the tropical IO: the ENSO, IOD, and the interannual fluctuations of the summer monsoon. ENSO originates in the tropical Pacific but remotely impacts the IO by inducing anomalous subsidence over the IO, resulting in a general warming of the basin [e.g. *Klein et al.*, 1999; *Xie et al.*, 2009]. The IO is also home to an indigenous mode of interannual variability, the IOD that often (but not always) co-occurs with ENSO. Peaking in boreal fall, it has a shorter lifetime than ENSO events, about 6 months. It is associated with a well-defined cold anomaly along the coast of Java and Sumatra, and more variable warming of the western IO [*Saji et al.*, 1999; *Webster et al.*, 1999]. The cooling off Java and Sumatra is associated with a local suppression of convection there, which is associated with anomalous easterlies over the central IO. Finally, interannual fluctuations of the Indian summer monsoon drive strong interannual wind, precipitation and runoffs anomalies over the northern IO [*Gadgil*, 2003]. ENSO has also been shown to partly drive these interannual fluctuations of the summer monsoon through atmospheric teleconnections [*Mujumdar et al.*, 2012].

These interannual variations strongly affect the hydrography of the Bay. *Shankar* [1998] reported large negative SLAs off the Indian east coast during 1961, one of the strongest positive IOD events on record. *Rao et al.* [2002] further demonstrated that a positive (resp. negative) IOD induces an anomalous cyclonic (resp. anticyclonic) circulation in the BoB in fall and results in fresh (resp. salty) anomalies in the eastern part of the Bay. Negative (resp. positive) SLAs have also been reported off the east coast during El Niño (resp. La Niña) events [*Han and Webster*, 2002; *Srinivas et al.*, 2005; *Singh*, 2002]. However, due to the co-occurrence of ENSO

with IOD events, these studies did not clearly distinguish the respective impact of these two modes on SLA in the BoB. The study of *Aparna et al.* [2012] addressed this issue and showed that these two modes have distinct SLA signatures, with IODs associated with a single SLA peak in fall along the rim of the Bay while ENSO exhibits weaker but multiple SLA peaks (April–December and November–July), with a relaxation between the two peaks.

The scarcity of available SSS *in-situ* observations and the lack of reliable continental freshwater forcing did for long prevent investigating the BoB interannual SSS variations. The recent improvement of the SSS observing system through the advent of the Argo program and the new dataset of satellite altimeter-derived discharges of major rivers (Ganges and Brahmaputra) that flow into the Bay [*Papa et al.*, 2012] recently allowed to provide a qualitative description of the year-to-year SSS variability over the 2009-2014 period in the northern part of the BoB, where the interannual SSS variability is particularly strong [*Chaitanya et al.*, 2014b]. Based on a simple mixed-layer model salt budget, these authors concluded that SSS interannual variability is mainly driven by fresh water fluxes in this region. They however underlined that the oceanic variability associated with the IOD may also contribute to SSS anomalies through lateral advection. Remotely-sensed surface salinity from Aquarius [*Lagerloef et al.*, 2008] and SMOS [*Reul et al.*, 2013] satellites may also provide an interesting alternative to assess year-to-year SSS variability. Using SMOS data, *Durand et al.* [2013] demonstrated that the positive 2011 IOD event (negative 2010 IOD event) was associated with fresh (salty) anomalies in the central IO south of the equator and salty (fresh) anomalies just north of the equator. They attributed these SSS variations to variations in horizontal advection process associated with IOD-related surface currents changes. However, the limited temporal coverage of this remotely-sensed datasets (3 to 5 years) and their problems in retrieving SSS signals in the Bay due to contaminations by land mass and radio-frequency interferences precludes an exhaustive description SSS interannual variations from these products, at present.

On the modelling front, there are only a handful of studies that discussed SSS interannual variability in the BoB. Forced ocean models have been used to illustrate that low surface salinity waters are advected from the eastern part of the BoB into the

equatorial IO during positive IODs [Thompson *et al.*, 2006; Grunseich *et al.*, 2011]. Using coupled model outputs, Vinayachandran and Nanjundiah [2009] further suggested that, along with the equatorial IO, the northern BoB in summer exhibits the largest SSS interannual variability in this basin, and that this variability is largely driven by year-to-year variations in the monsoonal fresh water flux. The unrealistic runoff and oceanic precipitation forcing generated by the coupled model however considerably hampered the robustness of the results of this coupled study. Forcing an ocean model with interannually varying discharges of the GB river system, Durand *et al.* [2011] demonstrated that the impact of these rivers on the interannual SSS variability in BoB is strong north of 15°N. The above studies therefore suggested that the interannual SSS variability in the BoB is rather large, with a considerable influence of GB river runoff and precipitations at the head of the Bay. However, an exhaustive study describing the main interannual SSS patterns in the Bay and their main driving processes is still lacking. No modelling study did for example provide a quantitative estimate of interannual wind and circulation changes on the BoB SSS interannual variability, nor the one associated with interannual variations in rainfall over the Bay.

The goal of the present study is therefore to fill that gap by using an ocean model forced by interannual winds, precipitation and river runoffs from all major rivers that flow into the BoB. We will describe the BoB SSS variability in the model and compare it with available observations. We will further relate this variability to known climate modes. We will finally explore the main mechanisms controlling the BoB SSS interannual variations, in particular through sensitivity experiments isolating the respective impacts of wind stress, rain and runoff interannual variations onto SSS. In Section 5.2, we describe the reference simulation and sensitivity experiments, the validation datasets, as well as the statistical methods used to infer the respective influence of each process on the SSS interannual variability in the Bay. Section 5.3 provides a validation of the interannual variability of the SSS in our reference experiment. A detailed description of the main modes of interannual SSS variability in the Bay from the reference experiment is provided in Section 5.4. This section further assesses the mechanisms driving these variations through the analysis of sensitivity experiments forced either by interannual runoffs, oceanic precipitation or wind stress. The last section finally summarizes and discusses the outcome of the present study.

## 5.2. Data and Methods

### 5.2.1. Model configuration and forcing

The model configuration used in this study is based on the NEMO ocean general circulation modelling system [Madec, 2008], implemented in a regional IO configuration (27°E–142°E, 33°S–30°N) described in Vialard *et al.* [2013] and Akhil *et al.* [2014]. It solves the primitive equations on a 1/4° horizontal grid with 46 vertical levels (vertical resolution ranging from 6 m at the surface to 250 m at the bottom, with 7 levels in the upper 50 m). Vertical mixing is parameterized using a turbulent closure scheme that resolves a prognostic equation for the turbulent kinetic energy [Blanke and Delecluse, 1993]. The open boundaries are handled using a radiation-relaxation approach [Marchesiello *et al.*, 2001], where we use the radiation condition to determine whether a boundary is passive (outward propagation) or active (inward propagation). The boundaries are constrained with a 150-day time-scale relaxation to 5 day average velocities, temperature, and salinity from an interannual global 1/4° simulation that has been carried out as part of the Drakkar project [Drakkar Group, 2007] and has already been extensively validated over the tropical IO [Keerthi *et al.*, 2013; Nidheesh *et al.*, 2012; Vialard *et al.*, 2013].

The set of simulations analysed in the present paper uses a similar model configuration and forcing strategy to that of Akhil *et al.* [2014]. The only differences are the model forcing datasets and the length of the experiments. The model computes the latent heat, sensible heat, upward longwave radiation and shortwave radiation fluxes using bulk formulae. The simulations analyzed in the current paper use most necessary atmospheric variables (near surface wind, air temperature and specific humidity, downward longwave fluxes) from the DFS5.2 described in Brodeau *et al.* [2012] and Dussin *et al.* [2014]. DFS5.2 is derived from ERA 40 [Uppala *et al.*, 2005] until 2002 and ERA-Interim reanalysis [Dee *et al.*, 2011] afterward. All atmospheric fields are corrected to avoid temporal discontinuities and remove known biases. The Daily TropFlux 1°×1° gridded product [Praveen Kumar *et al.*, 2012] provides downward short wave radiation, derived from the (ISCCP)-FD surface radiations [Zhang *et al.*, 2004] with ad-hoc corrections derived from the tropical moored buoy array.

The model is forced with interannually varying precipitations from the GPCP [Huffman *et al.*, 1997], while evaporation is computed interactively using bulk formulae and the prescribed air relative humidity and winds from the DFS5.2 dataset. For the GB river system, just like in Chapter 4, we use the interannually varying monthly estimates of continental freshwater flux into the BoB described in Papa *et al.*, [2012]. This time-series is derived from a combination of *in-situ* level-discharge relationships (the so-called rating curve, [Papa *et al.*, 2010]) with river water level retrieved from multiple altimetry satellites (TOPEX/Poseidon, ERS-2, ENVISAT and Jason-2). For the IR River, *in-situ* discharge time series are unfortunately not available over the recent period. Furuichi *et al.* [2009] published monthly estimates derived from *in-situ* observations over the 1966-1996 period. Following a similar approach to that of Papa *et al.* [2012], we used these monthly *in-situ* discharge estimates, together with TOPEX/Poseidon river level time series over their common period of availability (1993-1996) to establish a rating curve. We then used this rating curve to derive a continuous, monthly estimate of the IR river discharge at the river mouths for 1993-2012 using TOPEX/Poseidon (1993-2002), ENVISAT (2002-2008) and Jason-2 (2008 onwards). For the peninsular rivers (MH, GD, KR), we used interannual gauge discharge data (<http://www.india-wris.nrsc.gov.in/>). The yearly average discharge from each of these rivers flowing into the Bay was scaled by a constant coefficient to constraint the long-term mean discharge to be identical to that of Dai and Trenberth, [2002]. All other rivers discharges are injected in the model based on the monthly climatology of Dai and Trenberth [2002]. No relaxation to observed SSS climatology is applied in any of the simulations used in this study.

### 5.2.2. Reference and sensitivity experiments

Using the aforementioned model configuration and forcing, a reference experiment initialized at rest from the World Ocean Atlas temperature and salinity climatologies [Locarnini *et al.*, 2010] is performed over the 1990–2012 period. This experiment is analysed over the 1993-2012 period to allow the ocean to spin-up over the first three years of the experiment. Experiments using this model configuration and a similar forcing strategy successfully reproduce the seasonal SSS variability in the BoB [Akhil *et al.*, 2014] but also intraseasonal [Nisha *et al.*, 2013; Vialard *et al.*, 2013] and interannual [Praveen Kumar *et al.*, 2014] SST fluctuations in the IO.

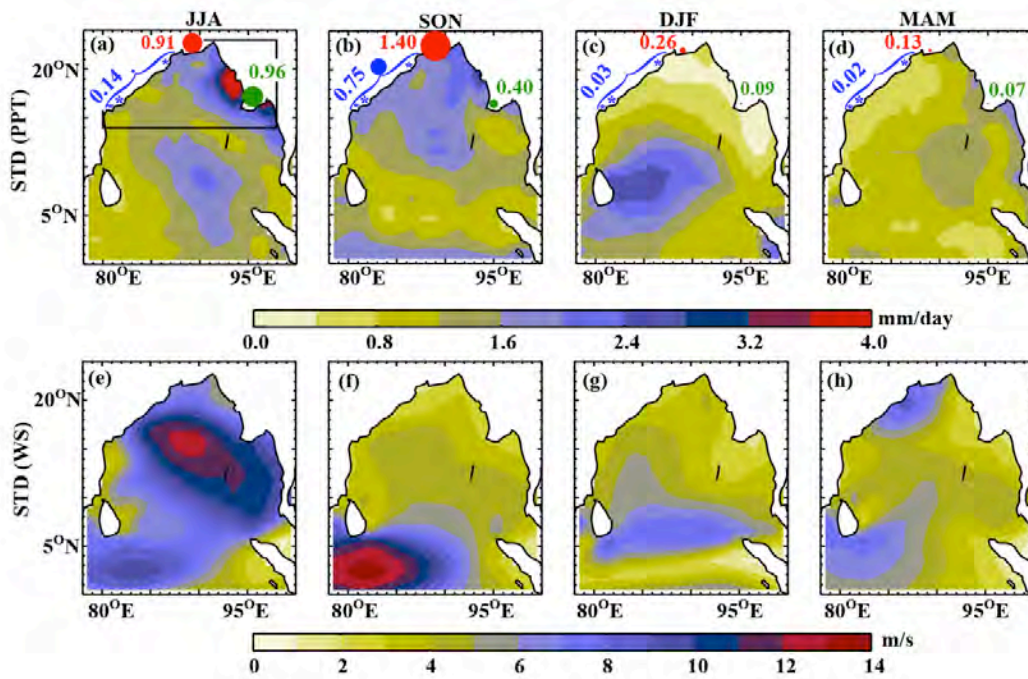


**Figure 5.1.** Maps of standard deviation of (**first row**) interannual precipitation anomalies and (**second row**) wind speed anomalies, for June-August (JJA), September-November (SON), December-February (DJF) and March-May (MAM). The dots on first row indicate the location of the mouth of all major rivers: the Ganga-Brahmaputra (GB; red), Irrawaddy (IR; green) and peninsular rivers (PNR: total of Mahanadi, Godavari, Krishna; blue). The radius of each dot is proportional to the standard deviation of the runoff interannual anomaly, with the value (in mm/day) indicated close to each dot. The river runoffs (volume per unit of time) were converted into an equivalent height per unit of time (mm/day) through a division by the oceanic area situated northward of 14°N (oceanic surface of the black box on panel (a)).

Figure 5.1 allows discussing the amplitude of interannual variability of the air-sea fluxes contributing to the modelled SSS interannual variability for each season, i.e. precipitation, river runoff and wind speed (that ultimately affects the salinity by modulating the oceanic circulation and vertical mixing). In the northern Bay, both freshwater forcing and winds exhibit a maximum interannual variability during and/or shortly after the monsoon (in JJA and SON). The GB river system (red dots on Figure 5.1) and the peninsular rivers (Mahanadi, Godavari, Krishna; blue stars) exhibit a maximum variability during the post-monsoon season (SON) with variations of 1.40 and 0.75 mm/day respectively. Interannual variations of the Irrawaddy river discharge (green dots) occur earlier, i.e. during the summer monsoon (0.96 mm/day in JJA), with the GB river discharge displaying a similar level of interannual variations during the same season (0.91 mm/day). During winter (DJF) and spring (MAM), interannual runoffs variations of these major rivers are about one order of magnitude weaker than

during the summer monsoon and post-monsoon seasons. Precipitation displays maximum interannual variability in the northeastern part of the basin during and shortly after the summer monsoon (Figure 5.1a, b). When averaged over the oceanic region north of 14°N, the amplitude of this interannual variability amounts to 1.05 mm/day in JJA and 1.1 mm/day in SON, an amplitude similar to that of major river runoffs. The precipitation interannual variability in the northern part of the Bay considerably weakens in winter and spring (Figure 5.1c, d), with a maximum of variability appearing in southern BoB east of Sri Lanka during the winter monsoon (Figure 5.1c). The amplitude of interannual wind variability is maximum in the central BoB during summer monsoon and south of Sri Lanka in the equatorial region during fall, a variability that is largely related to the IOD. To summarize, this figure clearly illustrates that both freshwater flux and wind forcing in the northern BoB exhibit a maximum variability during and shortly after the monsoon, with considerably less variations during the following seasons.

<b>Name</b>	<b>Description</b>
<b>REF</b>	Full forcing interannual
<b>Tau<sub>int</sub></b>	Interannual <b>Tau</b> and all other forcing are climatology
<b>P<sub>int</sub></b>	Interannual <b>P</b> and all other forcing are climatology
<b>R<sub>int</sub></b>	Interannual <b>R</b> and all other forcing are climatology

**Table 5.1:** List of experiments used in this study

In order to assess the mechanisms at stake in driving the interannual SSS variations in the reference experiment, a series of sensitivity experiments is also performed using interannually varying fluxes of either runoffs, precipitations or wind speed, but prescribing the seasonal climatology of the two remaining fluxes. Table 5.1 summarizes the experiments used in this study: the **Tau<sub>int</sub>** experiment is forced by interannual wind stress forcing, but uses a seasonal climatology of fresh water fluxes (precipitation and runoffs). The **P<sub>int</sub>** experiment is forced by interannual precipitation but uses a seasonal climatology of wind speed and river runoffs. Finally, the **R<sub>int</sub>** experiment uses interannual runoffs, keeping precipitation and wind speed forcing to climatological values. All sensitivity experiments are run over the 1990–2012 period, from the same initial condition as **REF** and are analysed over the 1993–2012 period. Interannual anomalies are calculated by removing the model mean seasonal cycle over the 1993-2012 periods.

The difference between SSS in the reference and sensitivity experiments allows an estimation of the SSS signals driven by interannual wind stresses, runoffs, precipitation fluctuations and the residual from others. We therefore decompose the interannual SSS variability in the reference experiment into contributions from interannual wind stress, interannual precipitation, interannual runoffs and a residual:

$$SSS'(\mathbf{REF})=SSS'(\mathbf{Tau}_{int}) + SSS'(\mathbf{P}_{int}) + SSS'(\mathbf{R}_{int}) + SSS'(\text{res}) \quad (5.1)$$

where the ' indicates interannual SSS variations. The first three terms on the r.h.s. of (5.1) are obtained from the interannual SSS variations from  $\mathbf{Tau}_{int}$ ,  $\mathbf{P}_{int}$  and  $\mathbf{R}_{int}$  respectively. They represent the contribution of wind stress  $SSS'(\mathbf{Tau}_{int})$ , oceanic precipitations  $SSS'(\mathbf{P}_{int})$  and continental runoffs  $SSS'(\mathbf{R}_{int})$  to the interannual SSS variability in the reference experiment. These three components do not add up exactly to the interannual SSS variability in the reference simulation because of the influence of internal ocean variability related with eddies and of nonlinearities. We obtain this last component as  $SSS'_{res} = SSS'(\mathbf{REF}) - SSS'(\mathbf{Tau}_{int}) - SSS'(\mathbf{P}_{int}) - SSS'(\mathbf{R}_{int})$ .

One of the objectives of this chapter is to provide a precise quantification of the contributions of various processes to the total interannual variability  $SSS'$ . Toward that end, we compute regression coefficients of the various contributions in (5.1) to the total SSS variability  $SSS'(\mathbf{REF})$ . These non-dimensional coefficients are computed for each season separately (JJA, SON, DJF and MAM) in order to quantitatively summarize the contribution of a specific process for each season. By construction, the coefficients for all the four processes in (5.1) add up to 1. We will provide these coefficients as percentages in the chapter: they always sum to 100% but can be negative for a process that has a negative correlation to the total variability.

We also investigate the relationship between the  $SSS'$  interannual variability and known interannual climate modes in the IO, i.e. the IOD and ENSO. To characterize these modes, we have used the standard indices already introduced in chapter 2: the Nino3.4 index for ENSO averaged during November-January and the DMI index for IOD averaged over September-November. The indices above have been normalized by their standard deviation to obtain dimensionless indices.

### 5.2.3. SSS validation datasets

The realism of the above simulation is assessed by comparing its SSS to a comprehensive SSS dataset detailed in *Chaitanya et al.* [2014b] and chapter 2, which compiles all *in-situ* SSS measurements available over the BoB during the 2006-2012 period. It consists of six different types of data: ARGO [*Roemmich et al.*, 2009] profilers, ship-of-opportunity XCTD profiles and bucket measurements, RAMA moorings [*McPhaden et al.*, 2009], OMNI moorings [*Venkatesan et al.*, 2013], ship-of-opportunity thermosalinograph transects and dedicated hydrographic cruises. These six datasets are gridded by computing the median of all available individual measurements on a  $1^\circ \times 1^\circ \times 3$  months grid. Data gaps in the resulting gridded dataset are not filled, in order to avoid any spurious pattern in the merged product. We will also use the  $1^\circ \times 1^\circ$  monthly Aquarius SSS dataset version 2.0 Level 3 provided by the NASA Jet Propulsion Laboratory (JPL) available from September 2011 to July 2013 (available from <ftp://podaac-ftp.jpl.nasa.gov/allData/aquarius/L3/mapped/CAPv3>) and detailed in chapter 2. Interannual anomalies derived from these *in-situ* and satellite SSS data are estimated by removing the NIOA SSS climatology assembled by *Chatterjee et al.* [2012], which includes all the data from the WOD09 [*Locarnini et al.*, 2010; *Antonov et al.*, 2010], complemented with CTD stations from Indian oceanographic cruises.

### 5.3. Validation of modelled interannual SSS variations

In this section, we first validate the modelled interannual SSS' variability from the reference experiment to the *in-situ* and remote sensing datasets described above.

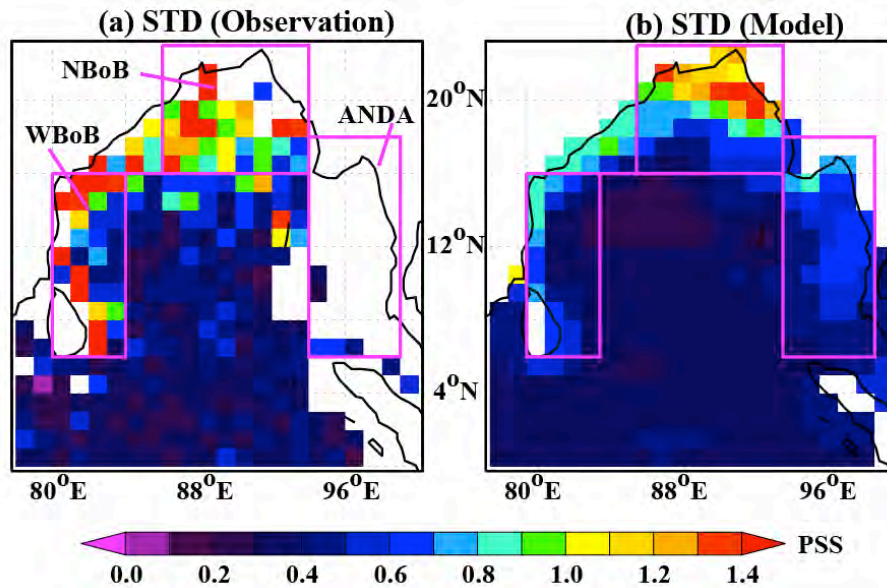


**Figure 5.2.** Standard Deviation of interannual SSS anomalies in the BoB for **(left)** observations and **(right)** model. In observations, The purple frames indicate three regions that will be analysed in more details: the western (WBoB, 80°E-84°E; 6°N-16°N) and northern (NBoB, 86°E-94°E; 16°N-23°N) and the Andaman Sea (ANDA, 94°E-99°E; 6°N-18°N).

Figure 5.2 displays the standard deviation (STD) of interannual SSS anomalies from the gridded *in-situ* dataset for 2006-2012 (Figure 5.2a) and from the model for 1993-2012 (Figure 5.2b). The regions of maximum variability agree qualitatively well between the model and observations. Both datasets indicate a maximum of SSS interannual variability (above 0.6) along the northern and western basin, and minimum variability in the central BoB. Some discrepancies can however be noted, such as an underestimation of the amplitude of the model SSS' signal along the east coast of India and an underestimation of the SSS' variability in the northern part of the domain between 16°N and 18°N. In addition, the model also displays a region of large interannual variability in the Andaman Sea, where the lack of *in-situ* observations prevents any model validation.

A more detailed analysis of the model ability to capture the large-scale SSS' temporal evolution is provided in Figure 5.3 for the three regions of maximum variability outlined on Figure 5.2. The first sub-region encompasses the northern part of the basin (NBoB, 86°E-94°E; 16°N-23°N) near the GB river mouth, where the largest SSS fluctuations are found in both model and *in-situ* observations. The second sub-region is located in the western part of the BoB (WBoB, 80°E-84°E; 6°N-16°N) and encompasses the coastal region through which the seasonal NBoB freshening is

transported southward during winter, as a fresh tongue that hugs the eastern Indian coastline (the so-called "river in the sea") [Akhil *et al.*, 2014; Chaitanya *et al.*, 2014a]. The third sub-domain is the Andaman Sea (ANDA, 94°E-99°E; 6°N-18°N), where the model output also suggests a marked variability (Figure 5.2b) but cannot be validated due to the lack of *in-situ* observations (Figure 5.2a). In the NBoB and WBoB regions, the model validation is performed by collocating model outputs with the *in-situ* gridded product (thereby avoiding observations-free areas), over the common period (2006-2012).

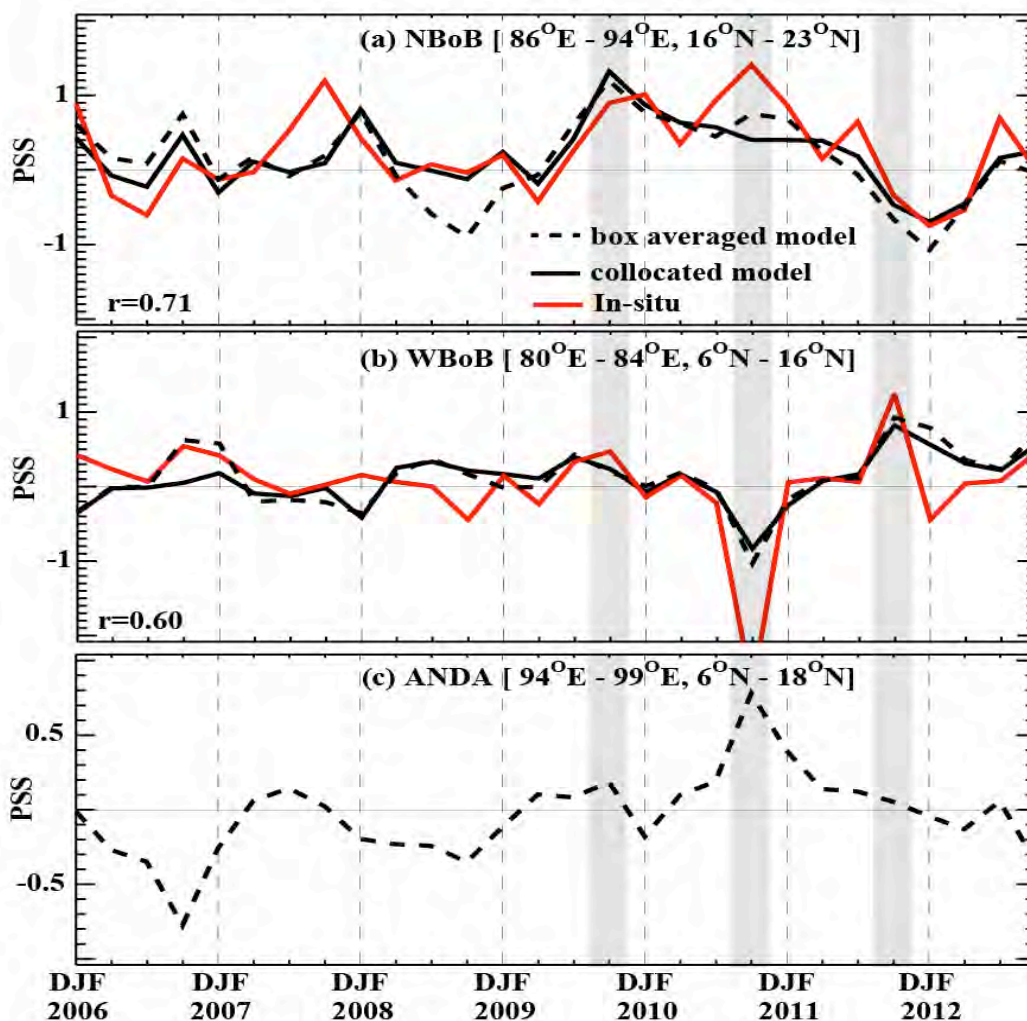


**Figure 5.3.** Time series of SSS interannual anomalies for observations (plain red), collocated model (plain black) and full model (dashed black) in the (top) NBoB, (middle) WBoB, and (bottom) ANDA boxes. Observed time series is not available for the ANDA box due to the scarcity of *in-situ* data. DJF2006 stands for December 2005 - January-February 2006, and so on. Shaded bands mark SON for the years 2009, 2010 and 2011.

Modelled and observed SSS' evolution agree generally well over the NBoB with a correlation coefficient of 0.71 (Figure 5.3a). The observed SSS' evolution in

this region exhibits successive periods of fresher-than-normal conditions and saltier-than-normal conditions, with anomalies ranging from -1 pss to 1.5 pss. The model is able to accurately capture the timing and amplitude of the fresher-than-normal period from SON 2011 to MAM 2012 (up to 0.7 pss of fresh anomaly), as well as the long-lasting salty period observed from JJA 2009 to DJF 2011. The shorter salty anomaly observed in SON 2007 is also captured by the model although it occurs three months later in the REF simulation (DJF 2008). In the western box (WBoB, Figure 5.3b) the model is also generally able to capture the timing of the anomalous strongest observed events (0.6 correlation), such as the anomalous freshening observed in SON 2010 and the anomalous saltening observed in SON 2011. As already suggested by Figure 5.2, the model however underestimates the amplitude of SSS' variability in the WBoB, for instance during the strong SON 2010 freshening. The model also exhibits strong anomalous events in the ANDA box, with fresh conditions in SON 2006 and salty conditions in SON 2010. We are however unable to validate the model SSS interannual variations in this region because of the absence of *in-situ* observation in this sub-basin.

Figure 5.3 suggests that fall is the season of largest SSS' in the WBoB and ANDA box and one of the strongest in the NBoB box. The amplitude of SSS' as a function of the season is further illustrated on Figure 5.4 for the model. The insufficient data coverage prevents us from providing an equivalent meaningful plot for observations. From this figure, it is evident that the largest interannual signals occur just after the monsoon in SON. In NBoB, significant interannual variations start appearing during summer monsoon (JJA) just offshore the mouth of the GB. These signals further strengthen (above 1.4 pss) and expand all over the box during SON, then weaken in winter and almost vanish in MAM. In WBoB, interannual signals are also largest in SON (above 1.4 pss) and still significant in DJF (~0.8 pss) but are totally absent during JJA and MAM. Finally, the ANDA box exhibits strong interannual variations off the mouth of the Irrawaddy river in JJA (~0.8 pss) and over the eastern half of the basin in SON (~0.8 pss). Anomalies during the other two seasons are weaker.

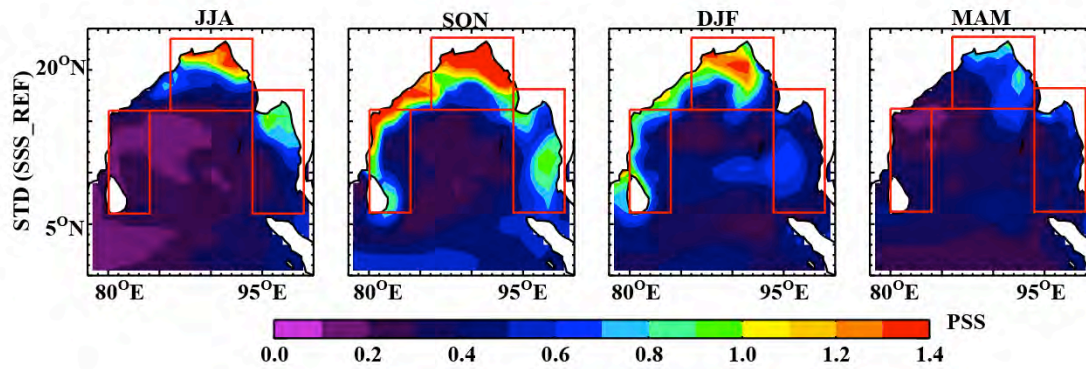


**Figure 5.4.** Maps of standard deviation of REF SSS interannual anomaly for each season.

From Figure 5.4, it is obvious that largest interannual SSS signals occur in SON. Figure 5.5 therefore provides a detailed validation of the modelled SSS' spatial patterns to the *in-situ* product for three successive fall seasons (i.e. SON 2009, 2010 and 2011) that are reasonably well sampled by the *in-situ* dataset. For SON 2011, the availability of Aquarius data also allows to compare the model results with these satellite data. As already seen in Figure 5.3, SON 2009 exhibits large salty anomalies in the northern and western box along with weaker salty anomalies in the central part of the Bay (Figure 5.5a). Collocated model data generally agree with this pattern, although the amplitude of the salty signal along the eastern coast of India is underestimated (Figure 5.5b). In SON 2010, both model and observations display a strong salty pattern in the northern part of the Bay while the western part of the Bay exhibits an opposite signal, with fresh anomalies north and east of Sri Lanka (Figure 5.5d). The central part of the Bay displays fresh anomalies west of 88°E and salty anomalies east of it. Finally the southern part of the Bay exhibits salty anomalies south of 4°N. The model generally captures very accurately all these features (Figure 5.5e). A large salty anomaly can also be noticed in the Andaman Sea (Figure 5.5f), a region that is not sampled by the *in-situ* dataset. Finally, SON 2011 is period of general freshening in the northern part the Bay (Figure 5.5g), although available *in-situ* observations in the NBoB show more patchy patterns than during other periods (Figure 5.5a, d) with both positive and negative pixels. A large salty anomaly is also observed on the western side of the WBoB. Salinity anomalies in the central part of the Bay are quite patchy. The model reproduces very well the salty anomaly in the WBoB (Figure 5.5h) but does not very accurately capture the more complex SSS structure seen in the central and northern part of the Bay, although box-averaged SSS

in NBoB is fresher than normal for both model and observations (Figure 5.3a). The availability of Aquarius from 2011 allows us to compare the model SSS' pattern everywhere in the Bay with this satellite product (Figure 5.5i, j). These two datasets agree quite well. There are however two obvious flaws: first, the salty signal along the east coast of India expands as far north as 20°N in the model while it is restricted to the south of 16°N in the satellite data. Second, the model exhibits a salty signal throughout the Andaman Sea, although Aquarius indicates a fresh signal over the northeastern half of it. While the first flaw is most probably related to a model deficiency, the second one is harder to interpret, in the absence of *in-situ* ground truth over the Andaman Sea.

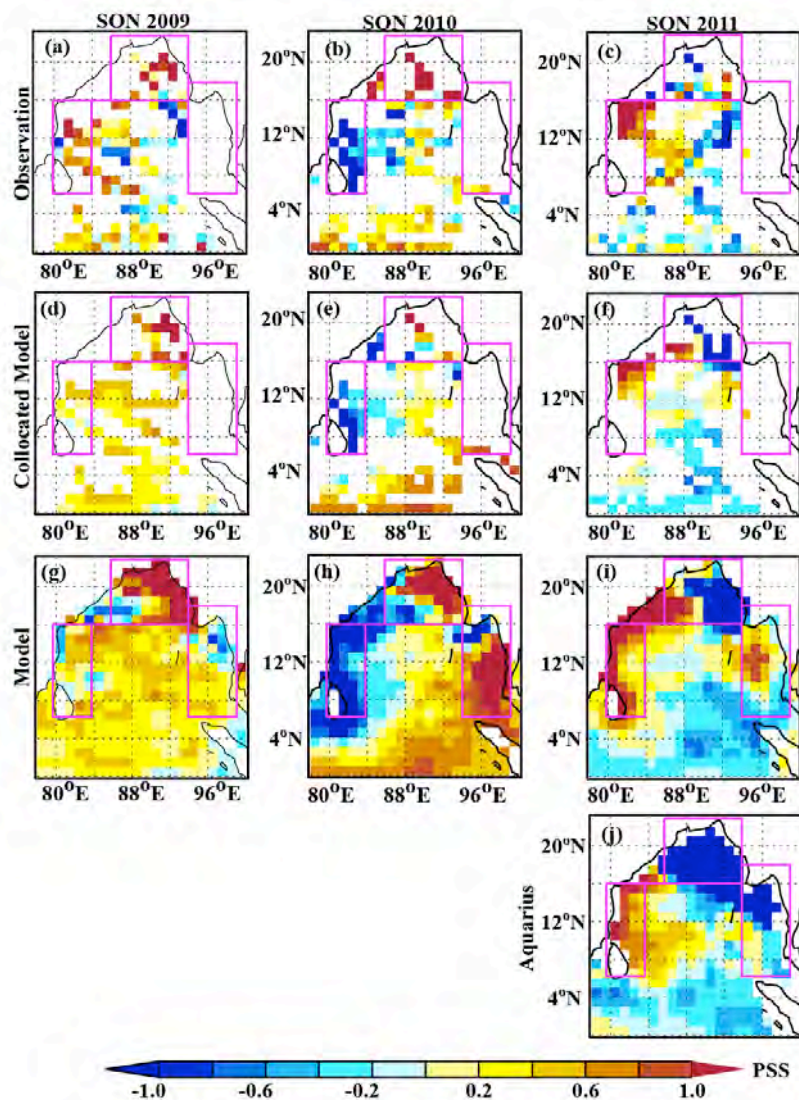


**Figure 5.5.** Map of SON SSS interannual anomalies for **(top)** observations, **(middle top)** collocated model and **(middle bottom)** full model and **(bottom)** Aquarius in 2009, 2010 and 2011. Aquarius data is only available from 2011 onwards.

The above diagnostics therefore demonstrate that the model accurately captures the main patterns of SSS' variability in the BoB: maximum interannual variability in the model and observations are indeed found in the same regions; modelled and observed year-to-year SSS variations over the regions of maximum interannual SSS variability are in good agreement, both in magnitude and in timing. The data coverage is too sparse to allow a detailed description of SSS interannual variability from observations everywhere in the Bay. The good agreement between model and observed interannual variability however gives us confidence in analysing the model outputs to decipher the mechanisms of interannual SSS variability in the BoB in more details.

## **5.4. Processes driving the SSS interannual variability in the BoB**

In Section 5.4.1, we describe the main patterns of SSS' variability using an empirical orthogonal function (EOF) analysis and relate this variability to known climate modes. Section 5.4.2 then provides a quantitative estimate of the relative importance of each forcing term (wind stress, precipitation and runoff) in driving interannual SSS variations in different regions, through the analysis of the sensitivity experiments described in Section 5.2.2.

### **5.4.1. Main patterns of SSS variability**

The SSS interannual variability in the BoB being maximum in SON, the main patterns of SSS' variability in this season are extracted by applying an EOF analysis to the SON SSS in the BoB (78°E-100°E, 0°N-23°N). The first EOF mode in SON (EOF1), its corresponding principal component (PC1) as well interannual anomalies of SSS, currents, SLA and wind stress regressed on this principal component are displayed for JJA, SON and DJF in Figure 5.6. These regressions onto PC1 allow describing the relationship between the SSS variability described by EOF1 in SON with the variability of SSS, sea level, surface currents and wind stress before, during and after the season of maximum SSS variability in this region (SON). Similar diagnostics are provided for EOF2 and EOF3 on Figures 5.7 and 5.8.

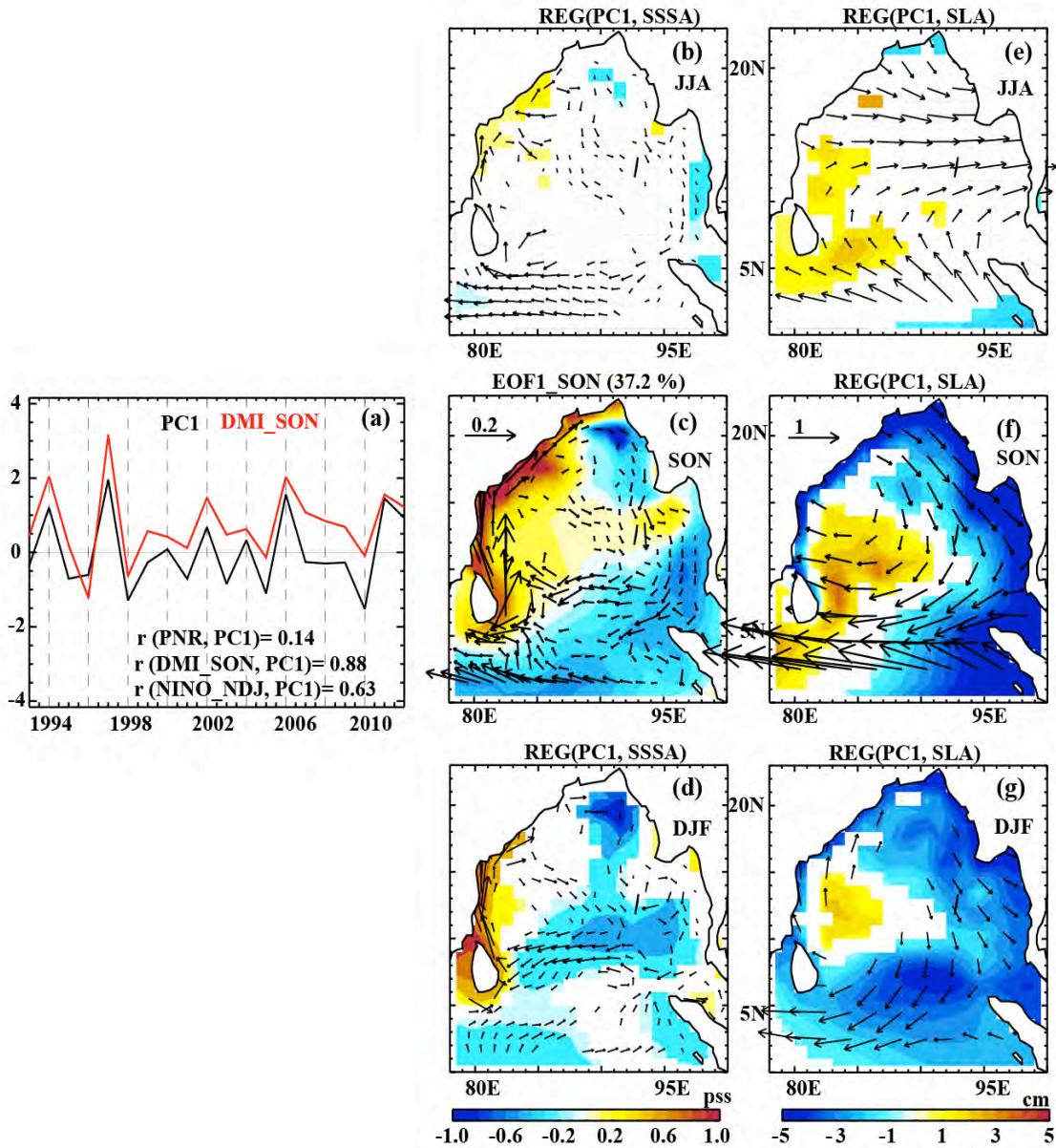


**Figure 5.6.** (a) PC1 time series of SON SSS interannual anomalies in REF experiment and (c) corresponding EOF1 pattern (color) along with regression currents anomalies onto PC1 (vectors). EOF analysis is made on the basis of trimesters (SON) and the associated PCs hence display one value per year. Correlation of NDJ Nino3.4, SON DMI and peninsular rivers discharge (PNR) with PC1 is indicated on panel (a). Percentage of variance explained by EOF1 is indicated on panel (c). Regression of SSS (color) and currents (vectors) interannual anomalies in (b) JJA and (d) DJF onto PC1. Regression of SLA (color) and wind stress (vectors) anomalies in (e) JJA, (f) SON and (g) DJF onto PC1. Regression coefficients for wind, current and sea level anomalies are only plotted when significant at 90% confidence level.

The first mode represents 37.2% of the SSS variance in SON. It is characterized by a saltening signal along the eastern coast of India and Sri Lanka and a weaker freshening signal in southern, southeastern and northeastern BoB (Figure 5.6c). This variability along the eastern coast of India is only related with modest

positive SSS' anomalies in the northern part of the Bay near the GB river mouth (Figure 5.6c). These SSS' anomalies along the east coast of India seem to appear suddenly in SON, with very weak related SSS' signals during the preceding monsoon season (Figure 5.6b). They however persist until the following winter south of 15°N, along the western boundary of the Bay (Figure 5.6d). This variability in SON is also related with negative SLA all along the rim of the BoB in SON (Figure 5.6f) and DJF (Figure 5.6g). This sea level signal is consistent with an upwelling coastal Kelvin wave propagating into the BoB coastal waveguide. This upwelling coastal Kelvin wave originates from the equatorial waveguide, where it is forced by equatorial easterlies in SON (Figure 5.6f) [McCreary *et al.*, 1993], but is probably also reinforced by southward alongshore wind stresses in the eastern BoB. The resulting negative SLA anomalies along the east coast of India are associated with the northward currents anomalies there in SON (Figure 5.6c) and DJF (Figure 5.6d), suggesting the importance of anomalous advection in driving the SSS' variations there. The western boundary of the BoB is indeed characterized by a marked meridional gradient of SSS at the end of the monsoon season, with decreasing salinity from South to North [e.g. Chaitanya *et al.*, 2014b]. The boreal summer and winter wind and SLA patterns in Figure 5.6e, g are reminiscent of the signature of a positive IOD event in the BoB, as discussed in Aparna *et al.* [2012]. This relationship between the first mode of SSS' variability and IOD events is further assessed by comparing PC1 to the value of the DMI index averaged over SON (Figure 5.6a). The two time series closely match, with a 0.88 correlation, suggesting that IOD events are responsible for most of the SSS' variations along the eastern coast of India, through their remote impact on SLA and currents. Consistent with this result, the positive IOD that matured in SON 2011 is associated with a strong salty anomaly along the eastern coast of India and fresh anomaly in the northeastern and southern BoB, evident in all the datasets (Figure 5.3 and 5.5). Similarly, the negative IOD of 2010 is associated with a fresh anomaly along the eastern coast of India and saltening in the northeastern and southern BoB (Figure 5.3 and 5.5). The PC1 also displays a significant although weaker correlation with ENSO (0.51), presumably because of the tendency of ENSO and IOD events to co-occur. On the other hand, this PC is poorly correlated (0.14) with peninsular rivers runoffs along the eastern coast of India, suggesting that local continental freshwater fluxes marginally influence the SSS' variability there.

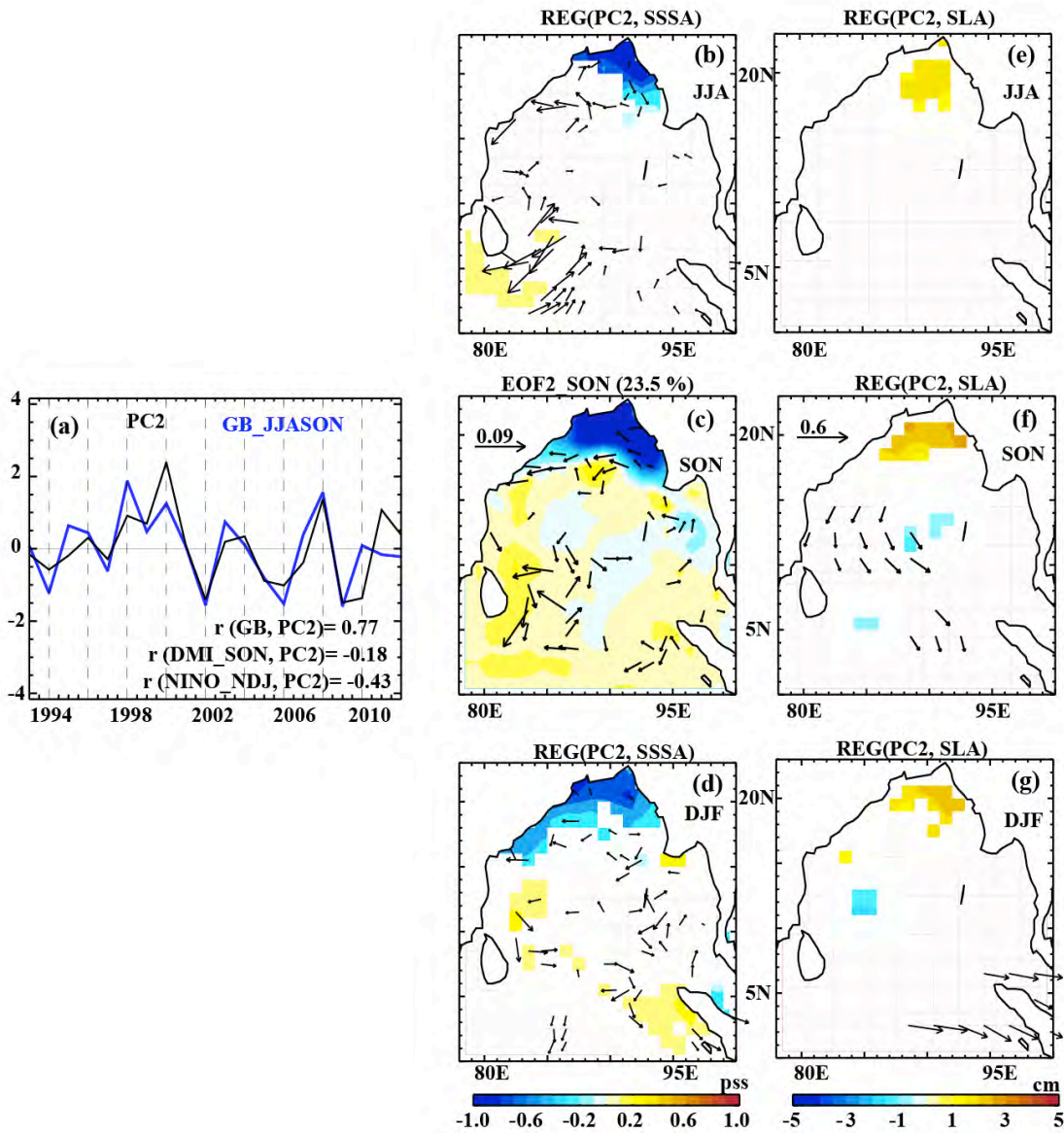


**Figure 5.7.** Same as Figure 5.6 but for EOF2.

The second EOF in SON represents 23.5% of the SSS variance and is characterized by a strong freshening confined to the northern part of the BoB, north of 18°N (NBoB region; Figure 5.7c). As suggested by the EOF analysis, this variability in the northern part of the Bay is not related to any significant SSS anomalies elsewhere (Figure 5.7c). This signal in NBoB generally appears during the summer monsoon close to the GB river mouth (Figure 5.7b) and persists but weakens through the following winter (Figure 5.7d) and spring (not shown). These SSS' variations in SON are related to modest positive SLA signals in the NBoB in summer, fall and winter (Figure 5.7e-g) but not related to any remote and large-scale SLA, wind nor currents signal in the NBoB (Figure 5.7b, g). This strongly suggests that this

variability is not remotely but rather locally driven. An obvious candidate for driving these SSS' variations is the local influence of the interannual fluctuations of the neighbouring GB river discharge. The time series associated with EOF2 (PC2) and the GB river runoff averaged over JJASON are indeed strongly related with each other, with a 0.77 correlation. The PC2 is not correlated with the IOD index, but weakly correlated with ENSO (0.43) presumably because of the influence of ENSO on the GB river runoff through its impact on northeastern Indian summer monsoon rainfall [e.g. Vecchi and Harrison, 2004]. While most of the years exhibiting positive (resp. negative) SSS' anomalies are closely related to negative (resp. positive) GB discharge anomalies (2000, 2002, 2006, 2008, 2009), a few years of anomalous SSS in this region are not related with consistent discharge anomalies as in 2010 or 2011, suggesting that other processes could be at stake in driving these variations during these periods (this will be further discussed in Section 5.4.2).

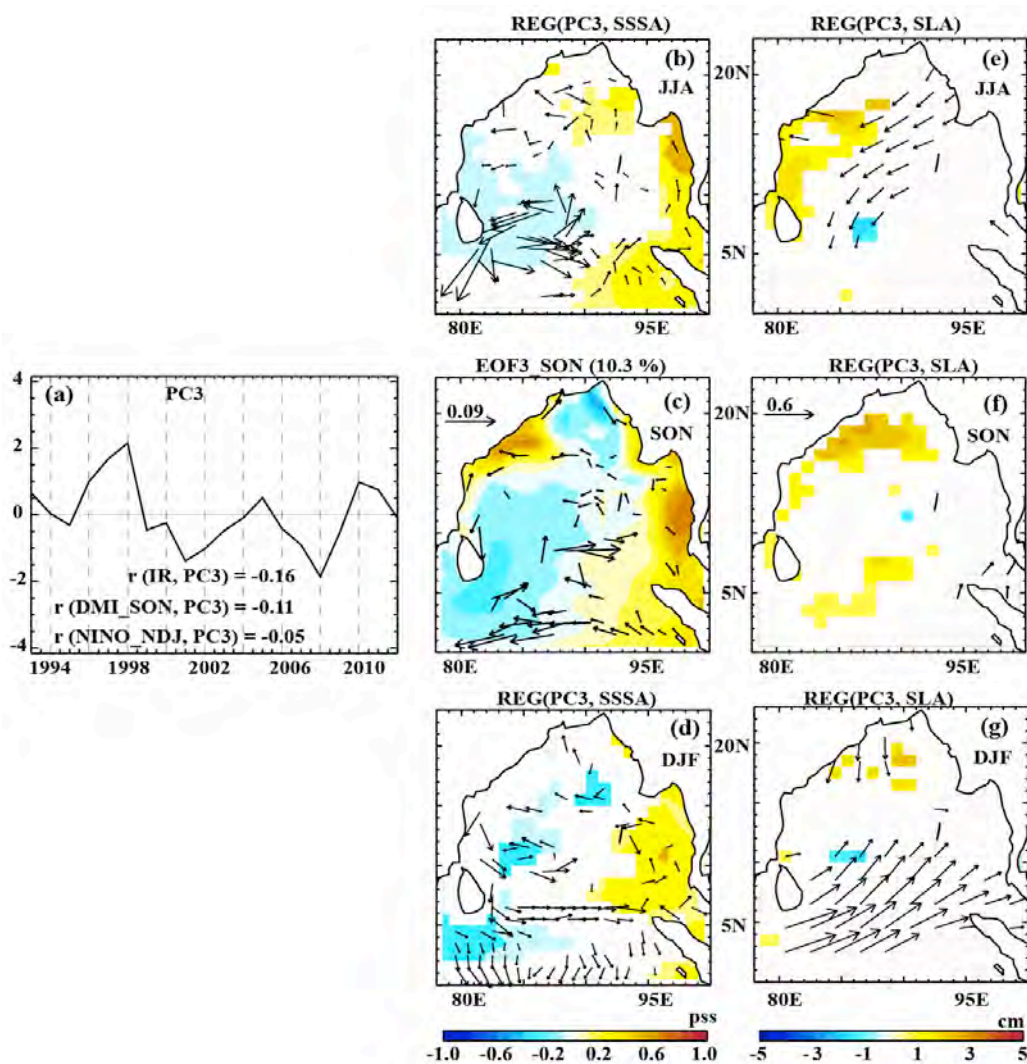
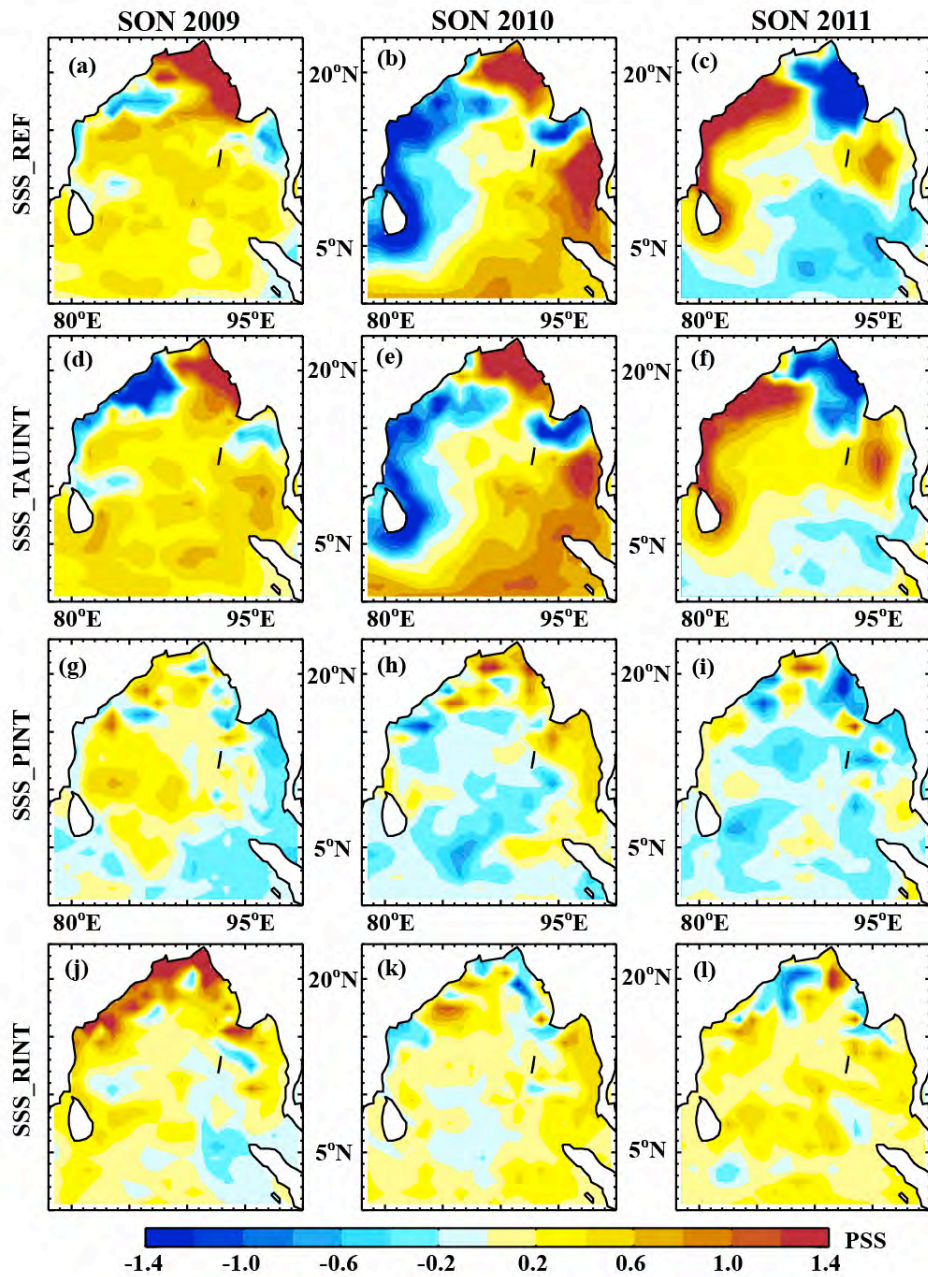


Figure 5.8. Same as Figure 5.6 but for EOF3.

Finally, the third EOF explains 10.3% of the SSS' variance in SON and is characterized by a saltening signal in the Andaman Sea, maximum off the coast of Thailand around 12°N (Figure 5.8c). This SSS' signal in SON is related to a SSS signal off the Irrawaddy river mouth that develops during the preceding summer (Figure 5.8b) and weakens during the following winter (Figure 5.8d). This signal in the Andaman Sea is not related to IOD, ENSO, nor to the Irrawaddy river discharge fluctuations (Figure 5.8a, correlations of -0.11, -0.05 and -0.16, respectively). There are in addition neither strong nor recognizable large-scale wind, current or SLA signal (Figure 5.8b-g) associated with this SSS signal in the Andaman Sea. Finally, the time series related to EOF3 exhibits fluctuations at a lower frequency than the one depicted by PC1 and PC2 (Figure 5.6c).

The simple analysis provided on Figures 5.6, 5.7 and 5.8 suggests that interannual SSS variability in the BoB in SON can be described by three modes of variability with largest SSS signals in the Northern BoB (NBoB box), along the eastern coast of India (WBoB box) and in the Andaman Sea (ANDA box), respectively. SSS' variability in the WBoB appears to be primarily driven by IOD events, through their remote impact on surface currents and anomalous advection along the east coast of India. The SSS' variability in the NBoB is more locally driven by interannual anomalies of the GB river runoff (which are weakly correlated to ENSO through its effect on northeastern India rainfall). SSS interannual anomalies in the ANDA region also appear to be more local, with no clearly identified driving process so far. The orthogonality properties of EOFs implies that the SSS' variabilities in those three regions are largely independent from each other (PC1, PC2 and PC3 are uncorrelated by construction). /The following subsection will clarify the processes responsible for SSS' variations in those three regions, by evaluating the respective contributions of runoffs, precipitations and wind stress interannual variations to SSS', through the analysis of the sensitivity experiments described in Section 5.2.2.

### 5.4.2. Relative importance of each forcing



**Figure 5.9.** Maps of interannual SSS anomaly from (1<sup>st</sup> line) REF, (2<sup>nd</sup> line)  $Tau_{int}$ , (3<sup>rd</sup> line)  $P_{int}$  and (4<sup>th</sup> line)  $R_{int}$  in (1<sup>st</sup> column) SON 2009, (2<sup>nd</sup> column) SON 2010 and (3<sup>rd</sup> column) SON 2011.

Figure 5.9 provides a first illustration of the SSS' anomalies simulated by each sensitivity experiment for the three consecutive fall seasons from 2009 to 2011 depicted in Figure 5.5. For those three years, SSS' patterns are generally similar in the reference simulation and in the  $Tau_{int}$  sensitivity experiment (Figure 5.9a-f). This suggests that interannual wind stress variations play an important role in controlling interannual SSS variability everywhere in the Bay for the 2009-2011 period. The SSS

interannual anomalies of  $P_{int}$  experiments are very modest (Figure 5.9g-i), suggesting that interannual precipitations do not play a strong role in shaping interannual SSS anomalies, at least for these three years. Results from  $R_{int}$  are more contrasted (Figure 5.9j-l), with a weak response to runoff interannual anomalies in SON 2010 and 2011, but a larger signal along the eastern coast of India north of  $15^{\circ}N$  in SON 2009. For this year and location,  $R_{int}$  favours a salty signal that opposes the fresh signal generated promoted by  $Tau_{int}$ , resulting in rather weak SSS' anomalies in the reference simulation. In the northeastern BoB on the other hand,  $R_{int}$  and  $Tau_{int}$  both induce positive SSS' anomalies (with comparable contribution of each of the two).

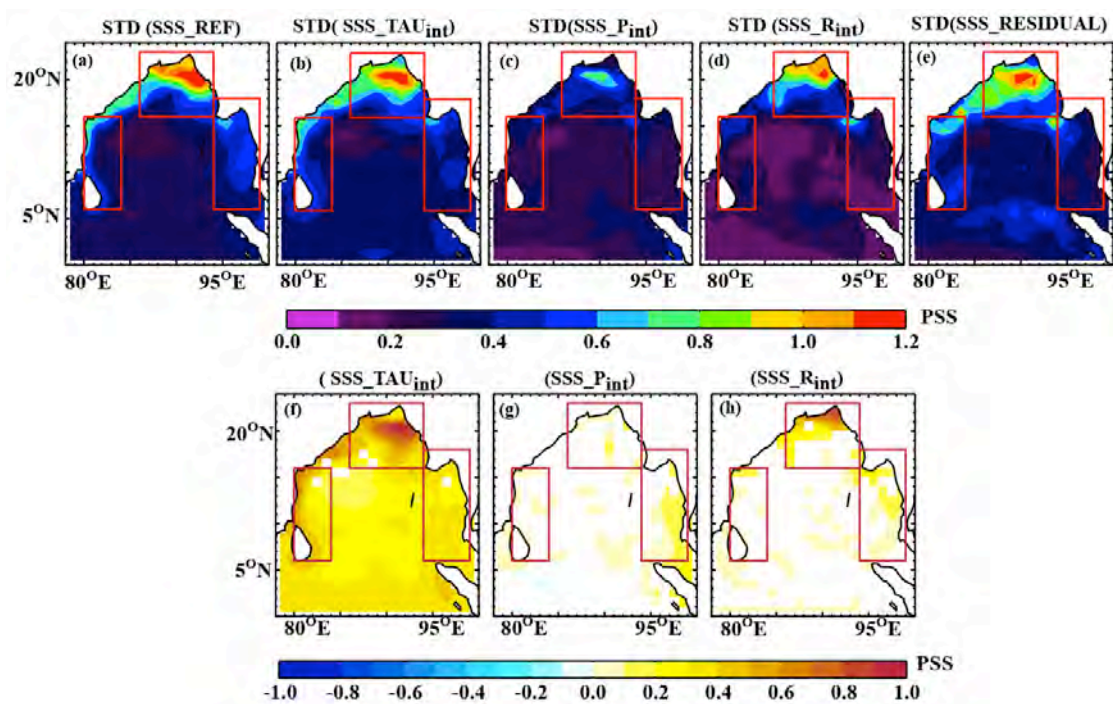


**Figure 5.10. (First line)** STD Maps of SSS interannual anomaly for (a) REF, (b)  $Tau_{int}$ , (c)  $P_{int}$ , (d)  $R_{int}$  and (e) Residual ( $REF - (Tau_{int} + P_{int} + R_{int})$ ), **(second line)** Contribution of each term ( $Tau_{int}$ ,  $P_{int}$  and  $R_{int}$ ) to the SSS' variability in REF. The contributions in the (f-h) are computed as the correlation to the SSS' variability in REF, multiplied by its standard deviation. The regions where the contribution by the residual terms is larger is stipulated.

A more quantitative assessment of the influence of oceanic precipitations, continental runoffs and wind stress variations on the interannual SSS evolution in the Bay is further provided on Figure 5.10. The amplitude of the interannual SSS anomalies driven by rainfall are rather weak in all regions (Figure 5.10c) compared to the other components (Figure 5.10b, d, e). The interannual variations of wind stress only contribute to large interannual SSS variations along the east coast of India (Figure 5.10b), demonstrating that interannual variations of river runoffs and

precipitations do not play any significant role in driving SSS' variations there.  $Tau_{int}$ ,  $R_{int}$  and the residual all display large interannual SSS variations in the northern BoB (Figure 5.10b, d, e).  $SSS'(R_{int})$  (see equation 5.1) are largest very close to the coast near the GB river mouth while  $SSS'(Tau_{int})$  and  $SSS'(Res)$  are largest further offshore, near 20°N at the location of the climatological SSS front.

The contributions of each of the terms  $Tau_{int}$ ,  $P_{int}$  and  $R_{int}$  on panels f-h are computed as the correlation to the total SSS variability, multiplied by its standard deviation. With such a normalization f, g, h and the contribution from the residual add up to a. As expected, the SSS variability in the northern BoB is controlled by river runoffs (up to 80%) near the Ganga-Bramaputra river mouth and by the wind forcing further offshore. Along the eastern coast of India and through out the central and southern BoB, the wind forcing controls most of the SSS interannual variability (more than 80%). Interannual precipitations variability does not explain much of the SSS' variability anywhere, except in the Andaman Sea where it explains up to 50% of the SSS' variations along the coast of Thailand. In this region, the three sensitivity experiments appear to play a role. Finally, although it has large amplitude in the NBoB (Figure 5.10e), the residual term does not explain much of the SSS variability in REF most likely because this residual term is a signature of mesoscale eddies that do not exhibit any large-scale signature.

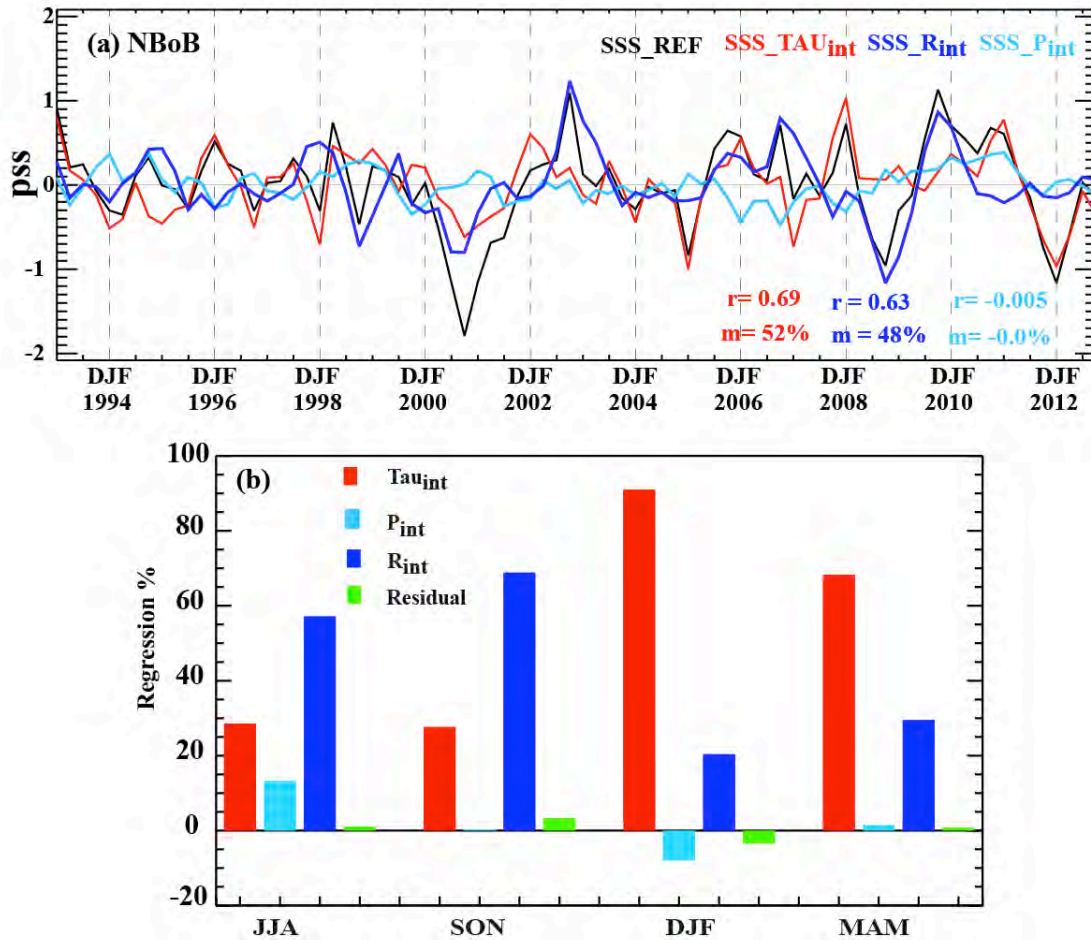


**Figure 5.11:** (a) Time series of interannual SSS anomaly in NBoB from REF (black), Tau<sub>int</sub> (red), P<sub>int</sub> (light blue) and R<sub>int</sub> (deep blue) experiments. Correlation( $r$ ) and regression ( $m$ ) values of each sensitivity experiments on to the REF are added in each panel. (b) Bar plot showing the respective contribution in % of SSS'(Tau<sub>int</sub>), SSS'(R<sub>int</sub>), SSS'(P<sub>int</sub>) and SSS'(Res) to the SSS' variability in REF in NBoB calculated as explained in Section 5.2.2

Figure 5.11 provides a more detailed description of the relative contributions from the wind stress, rainfall and river runoffs interannual variations in the NBoB region. Both SSS'(Tau<sub>int</sub>) and SSS'(R<sub>int</sub>) correlates well with REF (0.69 and 0.63 correlation respectively), with SSS'(Tau<sub>int</sub>) and SSS'(R<sub>int</sub>) explaining respectively 52% and 48% of SSS variability in the reference experiment. Some periods of strong interannual anomalies are mainly explained by runoffs variations (e.g. 2008 freshening) while wind variations play a dominant role during other epochs (2010-2012). In other instances, the influence of wind and runoff forcing add up (e.g. 2000, 2009) or oppose each other (e.g. 2007). Precipitation does not generally play a significant role, except during some peculiar periods (e.g. 1998, 2006, 2010) where its contribution is not negligible. The contribution of each process to the reference experiment standard deviation strongly varies from one season to another (Figure

5.11b). The SSS variability in summer and fall is dominated by runoffs interannual variations (50 to 80%), with GB runoffs being significantly correlated (-0.55 and -0.77, respectively) with SSS' anomalies during these seasons. During winter and spring, wind variability contributes most to SSS' variability (Figure 5.11b). While it is relatively straightforward to understand how the strong interannual runoffs variations during and shortly after the monsoon season may affect the interannual SSS variability in the northern part of the Bay, the way interannual winds control SSS interannual variations in DJF and MAM (lateral advection, vertical mixing) remains unclear.

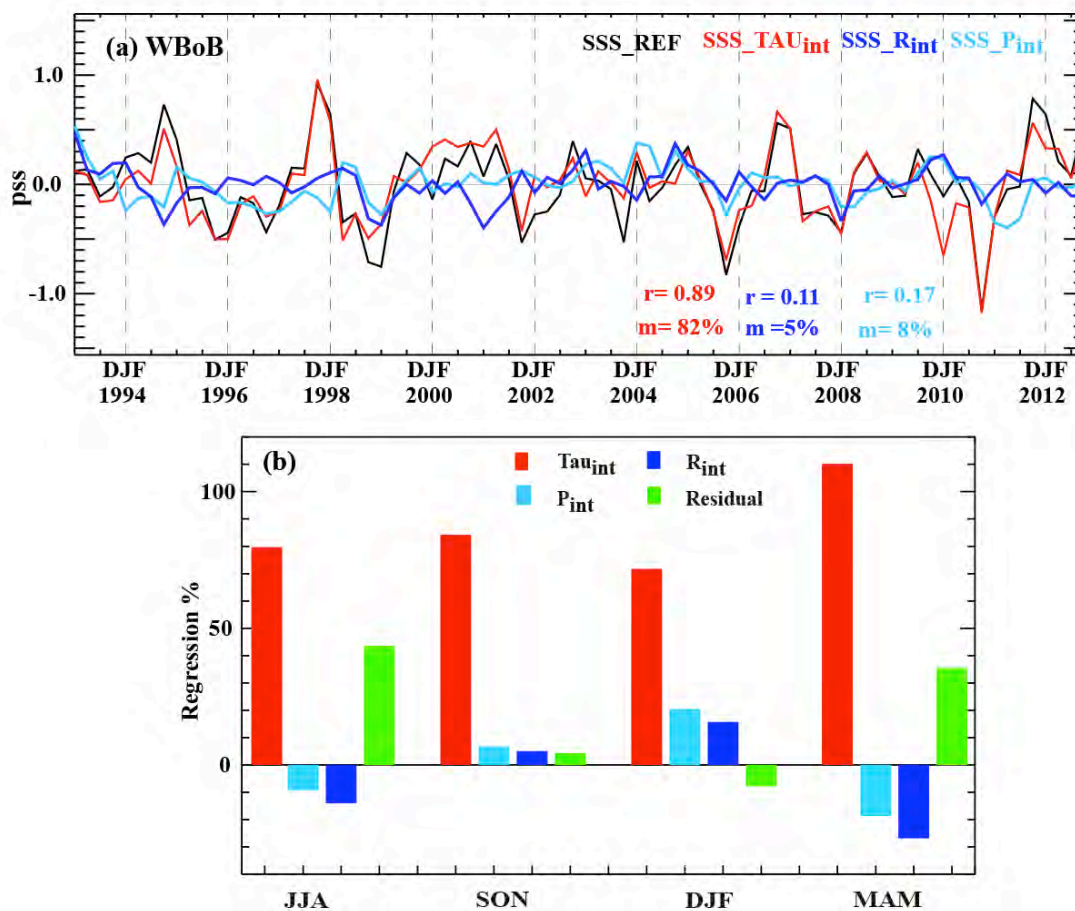


**Figure 5.12:** (a) Time series of interannual SSS anomaly in WBoB from REF (black), Tau<sub>int</sub> (red), P<sub>int</sub> (light blue) and R<sub>int</sub> (deep blue) experiments. Correlation( $r$ ) and regression( $m$ ) values of each sensitivity experiments on to the REF are added in each panel. (b) Bar plot showing the respective contribution in % of SSS'(Tau<sub>int</sub>), SSS'(R<sub>int</sub>), SSS'(P<sub>int</sub>) and SSS'(Res) to the SSS' variability in REF in NBoB calculated as explained in Section 5.2.2. The value of the correlation of SSS'(REF) with meridional currents anomalies in WBOB is indicated above the corresponding bars in panel b.

Figure 5.12 provides a similar analysis but for the WBoB box. Here, interannual wind stress fluctuations explain 82% of the total SSS interannual

variability (0.89 correlation between  $\text{Tau}_{\text{int}}$  and REF), with precipitation, runoffs and eddies/nonlinearities having a weaker impact (Figure 5.12a). Wind variability remains the main contributor to SSS' in WBoB for every season (Figure 5.12b). The high correlation of SSS'(REF) with REF meridional currents interannual anomalies in SON (0.92) and to a lesser extent in JJA (0.6) and DJF (0.7) strongly suggests that interannual modulation of the EICC intensity drives SSS' variability through horizontal advection changes in this region. Combining these results with those derived from Figure 5.6 allow us to conclude that the IOD-related winds variations drive equatorial and coastal Kelvin waves that propagate along the rim of the Bay. The resulting sea level variations along the east coast of India modulate the intensity of the EICC and SSS' variability in this region. On some occasions, interannual runoff anomalies (e.g. in late 1998 and 2000) and precipitations during the winter monsoon (e.g. late 1998) can also play a significant role (Figure 5.12a), although it is less systematic than the IOD-driven signal.

Results for the ANDA box are finally provided on Figure 5.13. In this region, the three processes (wind stress, precipitations and runoffs variations) all significantly contribute to SSS' variations.  $\text{SSS}'(\text{Tau}_{\text{int}})$ ,  $\text{SSS}'(\text{P}_{\text{int}})$  and  $\text{SSS}'(\text{R}_{\text{int}})$  indeed display positive correlations with REF (0.68, 0.51 and 0.51 respectively) and  $\text{Tau}_{\text{int}}$ ,  $\text{R}_{\text{int}}$  and  $\text{P}_{\text{int}}$  respectively explain 45%, 33% and 18% of SSS variability. As for the NBoB, the wind stress variability dominates the SSS' variability during fall, winter and spring, with precipitation contributing almost equally during and shortly after the monsoon. The dominant process driving SSS' fluctuations there however strongly varies from year to year: the strong salty anomaly simulated in 1998-1999 is largely driven by wind fluctuations while the 2005 and 2010 salty events are prominently driven by runoffs and precipitation, respectively. It must be underlined that the Andaman Sea is the only region where precipitation plays a major role in driving SSS interannual variability. The process by which the wind influences the SSS in this region (lateral advection, vertical mixing) has yet to be further investigated.

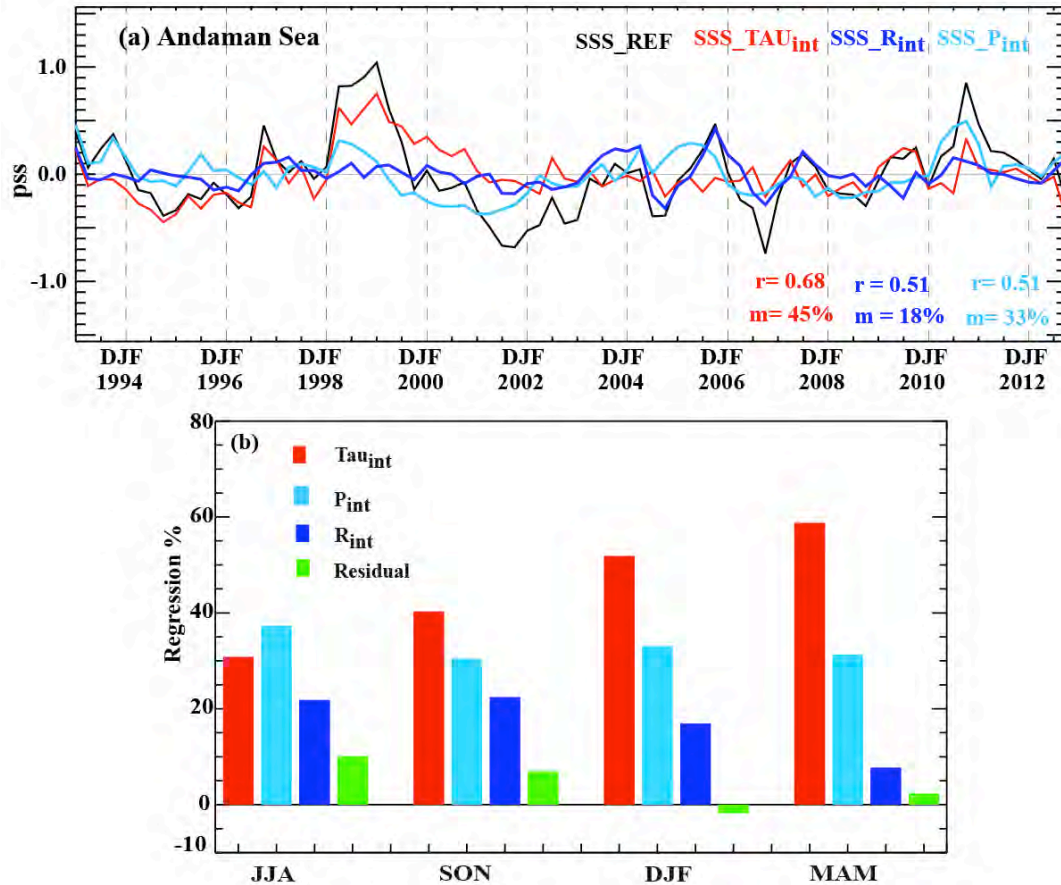


**Figure 5.13:** (a) Time series of interannual SSS anomaly in Andaman Sea box from REF (black), Tau<sub>int</sub> (red), P<sub>int</sub> (light blue) and R<sub>int</sub> (deep blue) experiments. Correlation and regression values of each sensitivity experiments on to the REF are added in each panel. (b) Bar plot showing the respective contribution in % of SSS'(Tau<sub>int</sub>), SSS'(R<sub>int</sub>), SSS'(P<sub>int</sub>) and SSS'(Res) to the SSS' variability in REF in NBoB calculated as explained in Section 5.2.2.

## 5.5. Summary and Discussion

### 5.5.1. Summary

The intense near-surface haline stratification in the BoB is believed to exert a strong control on upper ocean mixing and surface temperature, and thus on the climate of the neighbouring countries [Shenoi *et al.*, 2002]. Several studies have already investigated the seasonal SSS variations in the BoB and their driving mechanisms, using both observations and models [Rao and Sivakumar, 2003; Shetye *et al.*, 1991, 1993, 1996; Vinayachandran *et al.*, 2002b; Vinayachandran and Kurian, 2007; Benshila *et al.*, 2014; Akhil *et al.*, 2014; Chaitanya *et al.*, 2014a]. Due to the scarcity of available *in-situ* observations, little is known about the BoB SSS variability at

interannual timescales. Over the past few years, the SSS observing system and modelling platforms over the BoB have improved, so that it is now possible to monitor and understand SSS year-to-year variations in this region. The aim of the current study is to use a simulation, validated with available observations, to describe the SSS interannual variability in the BoB and understand its driving mechanisms.

The observational dataset consists of a blended product of all available *in-situ* SSS observations over the BoB during the 2006-2012 period. We also use an eddy-permitting ( $1/4^\circ$ ) ocean general circulation model regional simulation forced with interannually varying wind stress, precipitation and river runoffs, and no relaxation towards climatological observed SSS. The model SSS agrees qualitatively well with observations at interannual timescales. Maximum interannual SSS variability occurs around the rim of the Bay right after the monsoon, with a minimum variability in the central part of the basin, in both the model and observations. The modelled and observed interannual SSS evolution are in good agreement in the two regions of maximum variability, i.e. the northern BoB and along the east coast of India (correlations between 0.6 and 0.7). SSS signals in the third region of strong variability, i.e. the Andaman Sea, cannot be validated due to the lack of *in-situ* data. The SSS variability in these three regions is largely independent from one region to another.

In the northern BoB, interannual variations of precipitations play a minor role: the interannual SSS variability during and right after the summer monsoon (around 1 pss amplitude) is indeed largely driven by interannual variations of the GB river runoffs (0.77 correlation), while wind stress variations drive most of the SSS changes from winter to spring. This SSS variability in the northern BoB is modestly ( $\sim 0.4$ ) correlated with ENSO, probably due to the influence of this climate mode on the rainfall over the encatchment basin of the GB. The SSS variability along the western boundary is largest right after the monsoon during SON and remotely controlled by the IOD. Wind stress variations associated with positive IOD events in the equatorial region and along the eastern rim of the Bay both drive coastal upwelling Kelvin waves that propagate to the east coast of India. The related negative sea level variations act to weaken the intensity of EICC, hence limiting the seasonal southward advection of fresh water from the northern part of the Bay [Chaitanya *et al.*, 2014b; Akhil *et al.*, 2014] and resulting in a positive SSS anomaly of the order of 1 pss there. Conversely,

during a negative IOD event, downwelling Kelvin waves induce an acceleration of EICC, favouring the southward advection of the fresh plume. Finally, the variability of precipitation, Irrawaddy river runoffs and wind stress all combine together to drive SSS interannual variability in the Andaman Sea, with winds playing the largest role from fall to spring, but precipitation almost as important in fall and dominant during summer.

### 5.5.2. Discussion

Several studies already discussed the impact of IOD on the SSS evolution in the IO [Thompson *et al.*, 2006; Vinayachandran and Nanjudiah, 2009; Grunseich *et al.*, 2011; Durand *et al.*, 2013]. All these authors reported salty (fresh) anomalies in the central IO south of the equator and fresh (salty) anomalies just north of the equator during positive (negative) IOD years. They attributed these SSS variations to variations in horizontal advection process associated with IOD-related surface currents changes in this tropical region. The present study is also in line with these previous studies with an overall freshening of the southern part of the Bay during positive IOD events (Figure 5.6). In addition to this, our study reveals that IOD events also impact the SSS variability along the east coast of India, with a strong anomalous saltening (freshening) in this region during positive (negative) IOD events. As for the southern part of the Bay, anomalous alongshore currents are responsible for these SSS fluctuations in this region through a modulation of the horizontal advection.

Two other studies [Durand *et al.*, 2011; Chaitanya *et al.*, 2014b] specifically addressed the SSS interannual variability in the northern part of the Bay and the related impact of the GB river runoff fluctuations. Using an ocean model forced by the altimetry-derived GB runoff similar to our study, Durand *et al.* [2011] demonstrated that these runoffs strongly influence the SSS variability north of 15°N but that their impact does not extend south of 10°N. They attributed this behaviour to the coarse resolution of their model (1/2°) that may not be able to export SSS anomalies beyond the southern tip of India. While our model has a twice higher horizontal resolution (1/4°), our conclusions are in line with their results, with a limited impact of the interannual GB river runoff south of 15°N. Our results however suggest that the limited impact of GB runoffs south of 15°N may not result from a model caveat: our

modelling analysis indeed shows that the SSS variability in the northern and western part of the Bay are independent from each other, the later being largely driven by IOD-related surface currents variations rather than advection of SSS anomalies from the northern part of the basin. Our results additionally demonstrate a strong influence of the wind stress variability on SSS variations during winter and spring, the impact of GB runoffs being dominant during and shortly after the summer monsoon. Our results further indicate that rainfall only weakly contributes to SSS interannual variability in the northern BoB.

Using *in-situ* SSS observations and a simple mixed layer salt budget, *Chaitanya et al.* [2014b] also suggested that the year-to-year large-scale SSS variability in the northern BoB over the 2009-2012 period is primarily driven by freshwater flux variability, with a significant contribution from both oceanic precipitation and GB runoff. They also acknowledge that the oceanic surface circulation can occasionally contribute to the SSS variations there. In contrast to their conclusion, our results suggest that the freshwater fluxes in this region are primarily driven by the GB runoff fluctuations, the impact of precipitations being nearly negligible over the 1993-2012 period. A careful examination however largely reconcile the apparent contradiction between these two results: they indeed show that the strong saltening event from summer 2009 to fall 2010 can be almost entirely attributed to GB fluctuations (their Figures 5.7 and 5.8), in line with our results (Figure 5.11). In contrast, they attributed the freshening from fall 2010 to winter 2012 to a combination of anomalous precipitations, runoffs and horizontal advection: during this period, our model results also show that, in addition to the influence GB fluctuations, both precipitation and wind stress variations significantly contribute to SSS variations during this specific period (Figure 5.11). Aside from their rather crude simple model assumption that neglects vertical exchanges and does not account for MLD changes, the significant influence of precipitation on NBoB SSS variations in their study may come from their limited temporal coverage (2009-2012) compared to the present study that almost covers two decades.

The rather good agreement between the model and observed SSS interannual variations in the NBoB and WBoB gives us confidence in the mechanisms responsible for the SSS variations in these regions in our model. However, an obvious caveat of

the present model configuration is to underestimate the amplitude of the SSS variations in the WBoB (Figure 5.3b). There are several possible reasons for that. First, the comparisons between model and observations in *Akhil et al.* [2014] (their Figures 4.3 and 4.4) suggest that the model post-monsoon SSS may be overestimated in the northern BoB, hence resulting in an underestimated meridional advection along the east coast of India. A first way to improve the SSS interannual variations in the model would hence be to improve the SSS mean state, for example through a flux correction approach. As shown by *Benshila et al.* [2014], the ~25 km resolution of our model does not allow to fully simulate the intense and narrow structure of the EICC, which would also tend to result in underestimated meridional advection there. The western rim of the BoB is an area of intense eddy activity [*Durand et al.*, 2009]. Our model is eddy-permitting, but not really eddy-resolving, and does not permit assessing the effect of the oceanic mesoscale circulation on the coastal freshwater strip. Refining the model resolution may therefore also be a way to further improve the realism of our simulation. Increasing the horizontal resolution may improve the representation of the EICC and offshore freshwater export from this coastal freshwater strip while increasing the vertical resolution in the upper layers (from 6 m to 1 m) may also improve the representation of vertical mixing in occasionally very sharp near-surface salinity stratification in the BoB [*Vinayachandran and Kurian*, 2007].

Although our simulation indicates that the Andaman Sea is the third largest region of SSS interannual variations in the BoB, it is difficult to assess the realism of our simulation in this region due to the dearth of *in-situ* observations. The shallow bathymetry in this region has prevented so far the deployment of Argo profilers. Argo profilers with shallower than usual parking depth, moorings, dedicated oceanic cruises but also remotely-sensed SSS estimation from Aquarius, SMOS and SMAP (Soil Moisture Active and Passive, NASA's latest satellite successfully launched on 29th January 2015, see <http://smap.jpl.nasa.gov/>) may however provide valuable information on interannual SSS fluctuations in this region in the near future. In this paper, we did not discuss the interannual SSS variations in the central part of the Bay, because these signals are far weaker than along the rim of the Bay (Figure 5.3) and because our model does not perform well in reproducing the SSS variations there (not shown). An improved simulation of modelled SSS in this region is therefore a prerequisite before studying the mechanisms at stake in driving the (weak) SSS

interannual variations in the central BoB.

Finally, the most obvious limitation of the present study lies in the detailed identification of the oceanic processes responsible for the SSS variations. While SSS variations are quite easily linked with changes in neighbouring precipitation or rainfall, the wind can indeed affect SSS through several distinct processes (lateral advection, vertical processes including both advection and mixing). Analyses in this chapter demonstrate pretty convincingly that wind stress impacts SSS interannual variations along the eastern coast of India occurs through of a IOD-related modulation of horizontal advection driven by the EICC. On the other hand, the detailed mechanisms by which wind stress interannual variations impact SSS interannual anomalies in the NBoB and ANDA boxes remain elusive. From the tools used so far, it is difficult to separate out the different oceanic processes that may affect SSS variations through wind changes: changes in surface currents driving horizontal advection changes, change in halocline depth driving changes in vertical exchange between the fresh waters at the surface and saltier waters at depth or change in the amplitude of vertical mixing through changes in local wind stirring. An obvious solution to address this question will be to look into the online tendency term of the salt budget equation of the model, in order to separate out the influence of horizontal and vertical oceanic processes in driving the SSS variations in the BoB.

## Chapter 6

### Summary and Perspectives

---

#### 6.1 Summary

*Why is it important to study salinity variability in the Bay of Bengal?* Along with temperature, salinity exerts an important control on seawater density, with important consequences on ocean dynamics and thermodynamics. Salinity influences oceanic stratification and hence plays an important role in controlling mixed layer depth variations and near-surface mixing, especially at low latitudes where the fresh water influx is higher. The BoB stands out as a very peculiar region for salinity distribution in the tropical belt. Heavy rainfall and strong river runoffs associated with the southwest monsoon make the bay one of the freshest regions in the tropical oceans. This surface fresh water flux results in a strong near-surface stratification, which reduces vertical mixing between the surface and subsurface colder water. As a result, SST remains above 28°C, a necessary condition to maintain deep atmospheric convection and rainfall over the BoB. The BoB salinity stratification may also influence the intensity of the devastating tropical cyclones in this region, by inhibiting oceanic cooling below those cyclones, and hence favouring cyclone intensification. These strong impacts of haline stratification on SST, and potentially on the atmosphere and regional climate, call for a precise description of the SSS spatial structure and temporal variability within the Bay, and an improved understanding of the processes controlling this variability.

*Previous knowledge of the processes of SSS variability.* Despite the potentially important role of salinity in the climate dynamics of this region, the knowledge of SSS variability in the BoB is far from complete. Several observational studies have already depicted the SSS large-scale seasonal variations in the BoB, based on either hydrographic measurements along specific shipping lanes and dedicated cruises or SSS climatologies built from the available in-situ observations in the Bay. These studies depicted a marked seasonal cycle, with an intense freshening of the northern part of the basin from summer to fall that subsequently spreads along the

western boundary. This fresh pool finally erodes during winter, to reach its minimal extent in spring. Beyond this seasonal picture, much less is known about SSS variations at other timescales. The monitoring of SSS interannual variability is indeed very challenging due to the insufficient spatio-temporal sampling of the *in-situ* network.

*An improved description of SSS interannual variations in the BoB.* The launch of the Argo program allowed to considerably increase the number of salinity measurements in the Bay. Compiling all *in-situ* SSS measurements available over the BoB (ARGO profilers, ship-of-opportunity XCTD profiles and bucket measurements, RAMA and OMNI moorings, ship-of-opportunity thermosalinograph transects and dedicated hydrographic cruises), *Chaitanya et al.*, [2014b] built a comprehensive SSS dataset, for the 2006-2012 period. This dataset allowed them to describe the main features of interannual SSS variability over the Bay. They found that the maximum interannual variability occurs along the northern rim of the Bay with a minimum variability in the central part of the basin. The largest interannual SSS fluctuations occur at the head of the Bay near the Ganga-Brahmaputra river mouth with successive periods of fresher than normal conditions and saltier than normal conditions of about 1 pss lasting one to two years. The second region of largest interannual SSS variability is found along the eastern coast of India, with anomalously fresh or salty spells shortly after the summer monsoon.

*An evaluation of SMOS and Aquarius SSS retrievals in the BoB.* Although this *in-situ* product provided precious information on the SSS variability in the BoB, the spatio-temporal sampling of the *in-situ* network is still insufficient to achieve a complete description of the SSS variations in every region of the BoB. The recent development of SSS remote-sensing capabilities (SMOS and AQUARIUS) provides a unique opportunity to improve the monitoring of SSS. This semi-enclosed basin surrounded by land is however particularly challenging for the retrieval of satellite-derived SSS measurements because of the potential contamination of the SSS signal by radio frequency interferences and land-induced contamination in this near coastal environment. During the course of my PhD, I therefore performed an in-depth assessment of the ability of both satellites to monitor the seasonal and interannual SSS signals in the BoB by comparing their retrieval to the above *in-situ* dataset. This

comparison allowed me to demonstrate that Aquarius reasonably captures observed seasonal and interannual large-scale SSS evolution everywhere in the BoB, including the northern and western part of the Bay where the largest SSS variations occur. In contrast, SMOS does not perform better than existing climatologies in this region, possibly because of a heavier contamination by radio-frequency interferences and land effects. This analysis also reveals that both satellites exhibit large seasonal and interannual SSS signals in the Andaman Sea, which is completely devoid of *in-situ* observations. Overall, my PhD work demonstrated that Aquarius provides a promising avenue to study the SSS variability in the BoB, while the serious issues encountered by SMOS advocate for improvements of its SSS retrieval algorithm there.

***Using modelling to further study the BoB SSS variability.*** While the recently improved *in-situ* salinity observing network allowed to improve the description of the SSS variability within the Bay, it is, however, not yet sufficient to quantitatively assess the mechanisms that govern the seasonal and interannual SSS evolution. An interesting alternative relies in the use of oceanic simulations to investigate such mechanisms. The investigation of the processes governing the seasonal SSS variations using such tools have long been hampered by the use of a relaxation toward observed surface salinity climatology in models which artificially compensate any error in the forcing or in the model physics. At interannual timescales, the major limitation for representing interannual salinity variability by models was the lack of reliable continental freshwater forcing. The new dataset of satellite altimetry-derived monthly discharges of major river runoff [*Papa et al.*, 2010, 2012] represents an unprecedented source of information to quantify continental freshwater forcing flux into Indian Ocean circulation models. In a second stage of my PhD, I therefore used an eddy-permitting regional simulation forced with these altimeter-derived estimates of the river runoffs and precipitations and no relaxation toward climatological SSS to study the seasonal and interannual evolution of SSS in the BoB, and to quantify the processes driving this variability.

***Mechanisms of SSS seasonal variability.*** I first demonstrated that this modelling strategy allows to accurately capture the seasonal SSS variations. In particular, comparison to *in-situ* data along shipping lines shows that the model is able to capture the very narrow structure and intense freshening associated with the post-

monsoon “river in the sea” [Chaitanya *et al.*, 2014a] along the east coast of India. The analysis of the mixed layer salt tendency terms further allowed me to show, in agreement with previous studies, that the strong seasonal freshening that occurs shortly after the monsoon in the northern part of the Bay results from the Ganges-Brahmaputra river discharge. The seasonal southward expansion of this fresh pool from the northern BoB to the east coast of India is driven by horizontal advection of these fresh waters by the southward flowing coastal current. While this had been suggested by some studies before, it is the first time that this result is quantitatively demonstrated, furthermore in a forced ocean model simulation that resolves the post-monsoon “river in the sea”. Contrary to what was thought before, I showed that SSS is restored to its pre-monsoon values through turbulent vertical exchanges with underlying saltier waters, rather than by horizontal transport. Beneath the coastal plume of freshwater lies a thick salinity-stratified barrier layer. I showed that this barrier layer only acts as a “barrier” for vertical heat fluxes, but is associated with intense vertical salt fluxes. I showed that this is a generic result, that is valid beyond the specific case of the BoB.

***Mechanisms of SSS interannual variability.*** I further demonstrated that my modelling setup accurately captures interannual SSS variations depicted by the blended *in-situ* product. The SSS displays three poles of relatively independent interannual variability near the Ganges-Brahmaputra estuary, along the east coast of India and in the Andaman Sea. Sensitivity experiments forced by interannual variations of wind stress, runoffs or rainfall (with the other fluxes held to their climatological values) allow studying the dominant processes in each of those regions. SSS fluctuations in the Northern BoB are driven by interannual variations of the Ganga-Brahmaputra river runoffs after the monsoon and by wind stress fluctuations from winter to spring. Interannual SSS variability along the east coast of India is maximum right after the monsoon, and remotely driven by the IOD variability that drives coastal Kelvin waves propagating from the equator to the eastern coast of India. These waves modulate the intensity of the coastal current and the related advection of fresh water from the northern part of the Bay. Although I was unable to validate the SSS variability in the Andaman Sea due to the lack of *in-situ* data, my model results suggest that the SSS interannual variability in this region is driven by the combined influence of precipitation, Irrawaddy runoffs and wind stress fluctuations, with winds

playing a greater role during winter and spring. Apart from this localized feature, the overall impact of interannual variability of precipitation on the BoB SSS variability thus appears very minor.

*Overall*, this thesis allowed to substantially improve the description and understanding of SSS seasonal and interannual variability in the BoB. Yet, our approach presents obvious caveats and interesting perspectives, which are described in the following section.

## 6.2 Perspectives

*Wind-related processes controlling SSS interannual variability.* The first immediate limitation of the present PhD work lies in the detailed identification of the oceanic processes responsible for the interannual SSS variations in the BoB. While it is easy to understand how changes in precipitation or rainfall can affect locally SSS variations, it is not so easy for the wind forcing because several distinct processes related to wind variations can affect the SSS variations, including (i) changes in surface currents driving horizontal advection changes, (ii) changes in halocline depth driving changes in vertical exchange between the fresh waters at the surface and saltier waters at depth or (iii) changes in the amplitude of vertical mixing through changes in local wind stirring. The sensitivity experiments performed during my PhD work clearly demonstrated that wind stress impacts SSS interannual variations along the eastern coast of India through of a modulation of horizontal advection driven by IOD-related anomalous surface currents. But the experiments performed so far did not to allow to separate out the different oceanic processes related to wind changes that may affect the interannual SSS variations in the northern Bay of Bengal and in the Andaman Sea. Although I did not have the time to do it within my PhD deadlines, the first short-term perspective of my work is therefore to address this question by analysing the tendency term of the model salt budget equation, in order to separate out the influence of horizontal and vertical oceanic processes in driving the SSS variations in the BoB.

*Improved SSS monitoring in the BoB.* On the observational front, the most obvious limitation of my PhD work lies in the scarcity of the spatial and temporal

sampling of the *in-situ* SSS network. The eastern half of the Bay is in particular under-sampled compared to the western half, making it hard to study SSS variations there. For example, our model, SMOS and Aquarius all display a remarkable region of high SSS variability in the Andaman Sea, with a comparable magnitude to that observed in the northern part of the BoB. The development of an *in-situ* observing system in this region would allow to assess the quality of the space-borne and model SSS datasets there, in order to judge if they can be used for monitoring SSS and understand mechanisms of SSS variability there. The shallow bathymetry in this region has so far prevented satisfactory coverage of Argo profilers in this region (at the time of writing, only one such float is present over the whole Andaman Sea). Argo profilers with shallower-than-usual parking depth, dedicated oceanic cruises and remotely-sensed SSS from Aquarius may provide valuable information about interannual SSS fluctuations in this region. An improved monitoring of near-coastal SSS in the western BoB would also be a great improvement of the *in-situ* observing system, as it would allow better describing the offshore structure of the seasonal post-monsoon freshening, and how this freshening weakens as it progresses southward. In addition to the extension of the observational SSS observing system, dedicated measurements of mixed layer processes, with microstructure measurements would allow to confirm one the major modelling results of this PhD, i.e. the identification of the vertical exchanges of salt as the key process restoring SSS to its pre-monsoon values in the western and northern BoB.

***Mixed layer salinity budget from Aquarius data.*** Given the ability of Aquarius to capture SSS variations in the BoB, another promising avenue of the present PhD would be to perform a salt budget similar to *Chaitanya et al.* [2014b] but using Aquarius SSS retrieval in place of *in-situ* dataset in order to better understand the processes driving the SSS variability in different regions of the Bay. A first difficulty of this exercise would of course be to estimate the mixed layer depth over which to compute the budget, a critical element for such studies. This mixed layer depth variability can hopefully be estimated from Argo data. A meaningful investigation of the mixed-layer salt budget in the Bay is in addition not possible yet, because Aquarius data are only available from 2011 onward and interannual altimetry-derived runoffs data only available until the end of 2012. An update of these interannual runoffs data over the past three years would allow to assess the main processes

controlling the SSS in the different regions of the BoB and compare these results with our model analysis.

***Towards increased model resolution.*** The western rim of the BoB is one of the regions of largest SSS variability, with a very narrow offshore structure (~50 to 100 km), due to the coastally trapped nature of the East India Coastal Current [*Chaitanya et al.*, 2014a]. However, the ~25 km resolution of our model did not allow to accurately simulate the amplitude of these coastal SSS signal and the related amplitude of the EICC. In addition, the western rim of the BoB is an area of intense eddy activity, which efficiently mixes the coastal freshwater with offshore saltier water after the monsoon [e.g. *Hareesh Kumar et al.*, 2013]. Increasing the model horizontal resolution would have two advantages. It would allow to better resolve the first radius of deformation in the BoB (typically 50 to 125 km, [*Chelton et al.*, 1998]), which is both the theoretical typical spatial scale of the EICC and the scale of mesoscale features. Refining the model resolution to  $1/12^\circ$  may improve the realism of our EICC simulation [*Benshila et al.*, 2014]. It would also allow the model to be eddy-resolving and hence to be able to assess the effect of the oceanic mesoscale circulation on the coastal freshwater strip. Finally, increasing the vertical resolution in the upper layers (from 6 m to 1 m) may improve the representation of the very sharp near-surface salinity stratification that is occasionally observed in the BoB. It would also allow testing the impact of the diurnal cycle of the buoyancy forcing fluxes on salinity stratification. The modelling of the BoB (and in particular of its salinity structure) will undoubtedly benefit from higher resolution simulations in the future.

***Exploring other timescales.*** This PhD focussed on the SSS evolution at two important timescales: the seasonal and interannual ones. The IO is however also home to strong intraseasonal modes of variability, such as active-break phases of monsoon in summer and the Madden Julian oscillation in winter [e.g. *Zhang*, 2005]. SSS can exhibit rather large intraseasonal signals in the BoB [*Drushka et al.*, 2014; *Rao et al.*, 2011]. The intraseasonal SSS variability in the BoB and the processes driving this variability remain poorly documented and not understood. Combining *in-situ* and satellite observation data with an eddy-resolving regional simulation may allow to give further insights on the SSS variability in the BoB.

***Salinity effects on the BoB mean climate.*** Finally, The main motivation to better monitor and understand the salinity evolution in the Bay is its potential impact on the SST and therefore on atmospheric convection [Shenoi et al., 2002]. The ocean forced modelling study by *de Boyer Montégut et al.* [2007] quite convincingly demonstrated that the salinity stratification plays a significant role in maintaining high SSTs in the BoB. A comprehensive assessment of the role of salinity in the BoB on the regional climate however further requires the use of coupled models, with a sufficiently high oceanic and atmospheric resolution to properly capture the horizontal and vertical salinity structure in the Bay along with the atmospheric circulation and precipitation patterns. To our knowledge, *Seo et al.* [2009] is to date the only attempt to examine this climatic impact in a coupled framework. They concluded that the salinity stratification has a non-negligible effect on the mean climate, but mostly in winter, when a better salinity structure in the BoB resulted in a strong (up to 1°C) cooling in the BoB. The strategy used in that study (applying a strong relaxation to salinity to model the effect of rivers) is however debatable and more studies are probably needed in order to ascertain the influence of BoB haline stratification on the mean climate. In addition to that, recent studies [*Durack and Wiffels, 2010; Terray et al., 2012*] suggest that long-term changes in the hydrological cycle associated with global warming will tend to reinforce the current SSS contrasts, i.e. should decrease SSS in already fresh regions. This effect may be particularly strong in the BoB, a relatively small, semi enclosed basin with heavy rainfall, which collects freshwater over large catchment basins through three major rivers (Ganges, Brahmaputra and Irrawaddy). Little is known about the long-term variability of salinity in the BoB and its influence on regional climate. Another interesting perspective to this PhD work would be to use a newly developed high-resolution coupled model that realistically simulates both the Bay of Bengal stratification and northern Indian Ocean climate [*Samson et al., 2014*] to study the air-sea interactions associated with the mean salinity structure (or projected change in this structure) in the BoB.

## References

- Adler RF, et al. (2003) The Version 2 Global Precipitation Climatology Project (GPCP) monthly precipitation analysis 1979-present, *J. Hydrometeorol.*, 4(6), 1147–1167.
- Agarwal N, R Sharma, A Parekh, S Basu, A Sarkar and V Agarwal (2012) Argo observations of barrier layer in the tropical Indian Ocean, *J. Adv. Space Res.*, <http://dx.doi.org/10.1016/j.asr.2012.05.021>
- Akhil VP, F Durand, M Lengaigne, J Vialard, MG Keethi, VV Gopalakrishna, C Deltel, F Papa, C de Boyer Montégut (2014) A modeling study of the processes of surface salinity seasonal cycle in the Bay of Bengal, *J. Geophys. Res.*, 116, 3926–3947, doi: 10.1002/2013JC009632
- Alam MM, MA Hossain and S Shafee (2003) Frequency of Bay of Bengal cyclonic storms and depressions crossing different coastal zones, *Int. J. Climatol.*, 23, 1119–1125, doi:10.1002/joc.927.
- Alory G, T Delcroix, P Téchiné, S Cravatte, G Reverdin, D Varillon, E Kestenare, C Maes, R. Morrow, D Diverrès, J Grelet, Y Gouriou, J Perrier and S Jacquin (2015) The French global Voluntary Observing Ships network of Sea Surface Salinity, in preparation for Deep Sea Research.
- Antonov JI, D Seidov, TP Boyer, RA Locarnini, AV Mishonov, HE Garcia, OK Baranova, MM Zweng and DR Johnson (2010) World Ocean Atlas 2009, Volume 2: Salinity, edited by S. Levitus, 184 pp., U.S. Govt. Print. Off., Washington, D.C. Aquarius User Guide, Document # JPL D-70012, National Aeronautics and Space Administration, Physical Oceanography Distributed Active Archive Center (PO.DAAC), Jet Propulsion Laboratory, 41 pp., 2011.
- Aparna SG, JP McCreary, D Shankar and PN Vinayachandran (2012) Signatures of Indian Ocean Dipole and El Niño–Southern Oscillation events in sea level variations in the Bay of Bengal, *J. Geophys. Res.*, 117,10012,doi: 10.1029/2012JC008055.
- Aretxabaleta AL, J Gourrion, Joaquim Ballabrera-Poy et al. (2010) Bridging the gap between surface salinity satellites: SMOS and Aquarius. In ESA Living Planet Symposium.
- Babu MT, YVB Sarma, VSN Murty and P Vethamony (2003) On the circulation in the Bay of Bengal during northern spring inter-monsoon (March-April 1987), *Deep-Sea Res. II*, 50(5); 855-865.
- Barnier B, et al. (2006) Impact of partial steps and momentum advection schemes in a global ocean circulation model at eddy permitting resolution. *Ocean Dyn.*, 56, 543–567. Doi: 10.1007/s10236-006-0082-1
- Benshila R, F Durand, S Masson, R Bourdalle-Badie, C de Boyer Montégut, F Papa and G Madec (2014) The upper Bay of Bengal salinity structure in a high-resolution model, *Ocean Modelling* 74, 36-52.

- Bjerknes J (1969) Atmospheric teleconnections from the equatorial Pacific, *Mon. Weather Rev.*, 97, 163–172
- Blanke B and P Delecluse (1993) Low frequency variability of the tropical atlantic ocean simulated by a general circulation model with mixed layer physics. *J. Phys. Oceanogr.*, 23, 1363–1388.
- Blanford HF (1884) On the connexion of the Himalaya snowfall with dry winds and seasons of drought in India, *Proc. Roy. Soc. London*, 37, 1-23
- Brodeau L, B Barnier, AM Treguier, T Penduff and S Gulev (2010) An ERA40-based atmospheric forcing for global ocean circulation models. *Ocean Model.*, 31, 3-4, 88- 104, doi:10.1016/j.ocemod.2009.10.005.
- Brodeau et al., (2012) An ERA40-based atmospheric forcing for global ocean circulation models. *Ocean Modelling*, Volume 31, Issues 34, 2010, Pages 88 - 104, ISSN 1463-5003
- Boutin J, N Martin, X Yin, J Font, N Reul and P Spurgeon (2012) “First assessment of SMOS data over open ocean: part II Sea Surface Salinity,” *IEEE Transactions on Geoscience and Remote Sensing.*, doi: 10.1109/TGRS.2012.2184546.
- Boutin J, N Martin, G Reverdin, X Yin and F Gaillard (2013) Sea surface freshening inferred from SMOS and ARGO salinity: Impact of rain, *Ocean Sci.*, 9, 183-192, doi: 10.5194/os-9-183-2013.
- Boyer TP, JI Antonov , OK Baranova, HE Garcia, DR Johnson, RA Locarnini, AV Mishonov, TD O’Brien, D Seidov, IV Smolyar, MM Zweng (2009) *World Ocean Database 2009*. S. Levitus, Ed., NOAA Atlas NESDIS 66, U.S. Gov. Printing Office, Wash., D.C., 216 pp., DVDs.
- Chaitanya AVS, M Lengaigne, J Vialard, VV Gopalakrishna, F Durand, C KranthiKumar, S Amrithash, V Suneel, F Papa, M Ravichandran (2014a) Fishermen-operated salinity measurements reveal a "river in the sea" flowing along the east coast of India, *BAMS*, online first, doi: <http://dx.doi.org/10.1175/BAMS-D-12-00243.1>
- Chaitanya AVS, F Durand, S Mathew, VV Gopalakrishna, F Papa, M Lengaigne, J Vialard, C Krantikumar and R Venkatesan (2014b) Observed year-to-year sea surface salinity variability in the Bay of Bengal during the period 2009-2014, *Oc. Dyn.*, accepted
- Chatterjee A, D Shankar, SSC Shenoi, GV Reddy, GS Michael, M Ravichandran, VV Gopalkrishna, EP Rama Rao, TVS Udaya Bhaskar and VN Sanjeevan (2012) A new atlas of temperature and salinity for the north Indian Ocean, *J. Earth Syst. Sci.*, 121(3), 559–593, doi: 10.1007/s12040-012-0191-9.
- Chelton DB, Deszoeke RA, Schlax MG, El Naggar K and Siwertz N (1998) Geographical variability of the first baroclinic Rossby radius of deformation. *Journal of Physical Oceanography*, 28(3), 433-460.
- Chelton DB, MG Schlax and RM Samelson (2011) Global observations of nonlinear mesoscale eddies, *Prog. Oceanogr.*, 91, 167-216.
- Chen G, D Wang and Y Hou (2012) The features and interannual variability mechanism of mesoscale eddies in the Bay of Bengal, *Cont. Shelf Res.*, 47, 178-185.

- Cheng X, SP Xie, JP McCreary, Y Qi and Y Du (2013) Intraseasonal variability of sea surface height over the Bay of Bengal. *J. Geophys. Res.*, 118,816-830, doi: 10.1002/jgrc.20075.
- Cherchi A and A Navarra (2012) Influence of ENSO and of the Indian Ocean Dipole on the Indian summer monsoon variability, *Clim. Dyn.*, 2013,41,81-103.
- Cione JJ and EW Uhlhorn (2003) Sea surface temperature variability in hurricanes: Implications with respect to intensity change, *Mon. Weather Rev.*, 131, 1783–1796, doi: 10.1175//2562.1.
- Currie JC, Lengaigne M, Vialard J, Kaplan DM, Aumont O, Naqvi SWA and Maury O (2013) Indian Ocean Dipole and El Niño/Southern Oscillation impacts on regional chlorophyll anomalies in the Indian Ocean, *Biogeosciences*, 10, 6677-6698, doi: 10.5194/bg-10-6677-2013
- Cuypers Y, X Le Vaillant, P Bouruet-Aubertot, J Vialard and M McPhaden (2013) Tropical storm-induced near inertial internal waves during the Cirene experiment: energy fluxes and impact on vertical mixing, *J. Geophys. Res.*, 118, 358-380, doi: 10.1029/2012JC07881.
- Dai A and KE Trenberth (2002) Estimates of freshwater discharge from continents: Latitudinal and seasonal variations, *J. Hydrometeorol.*,3(6), 660–687
- de Boyer Montégut C, G Madec, AS Fischer, A Lazar and D Iudicone (2004) Mixed layer depth over the global ocean: an examination of profile data and a profile-based climatology, *J. Geophys. Res.*, 109, C12003, doi: 10.1029/2004JC002378.
- de Boyer Montégut C (2005) Couche mélangée océanique et bilan thermohalin de surface dans l’Océan Indien Nord. PhD thesis, University of Paris VI, 181
- de Boyer Montégut C, J Mignot, A Lazar and S Cravatte (2007) Control of salinity on the mixed layer depth in the world ocean. Part I: general description, *J. Geophys. Res.*, 112, C06011, doi: 10.1029/2006JC003953.
- Dee DP, et al. (2011) The ERA-interim reanalysis: configuration and performance of the data assimilation system. *Q J R Meteorol Soc* 137:553–597. doi:10.1002/qj.828
- Delcroix T, MJ McPhaden, A Dessier and Y Gouriou (2005) Time and space scales for sea surface salinity in the tropical oceans, *Deep Sea Research Part I: Oceanographic Research Papers.*, 52(5), 787-813.
- Diansky NA, VB Zalesny, SN Moshonkin and AS Rusakov (2006) High resolution modeling of the monsoon circulation in the Indian Ocean, *Oceanology*, Engl. Transl., 46, 608–628.
- Drakkar Group (2007) Eddy-permitting ocean circulation hindcasts of past decades. *CLIVAR Exchanges*, 42 12(3), 8–10.
- Drushka K, J Sprintall and ST Gille (2014). Subseasonal variations in salinity and barrier-layer thickness in the eastern equatorial Indian Ocean. *J. Geophys. Res.* 119,805–823, doi: 10.1002/2013JC009422
- Du Y, Xie SP, Huang G and Hu K. (2009) Role of air–sea interaction in the long persistence of El Niño–induced north Indian Ocean warming, *J. Climate*, 22(8), 2023-2038, doi:10.1175/2008JCLI2590.1

- Durack PJ and Wijffels SE (2010) Fifty-year trends in global ocean salinities and their relationship to broad-scale warming. *Journal of Climate*, 23(16), 4342-4362.
- Durand F, D Shankar, C de Boyer Montegut, SSC Shenoi, B Blanke and G Madec (2007) Modeling the barrier-layer formation in the Southeastern Arabian Sea, *J. Clim.*, 20, 2109– 2120, doi:10.1175/JCLI4112.1.
- Durand F, D Shankar, F Birol and SSC Shenoi (2009) Spatiotemporal structure of the East India Coastal Current from satellite altimetry, *J. Geophys. Res.*, 114, C02013, doi: 10.1029/2008JC004807.
- Durand F, F Papa, A Rahman and SK Bala (2011) Impact of Ganges- Brahmaputra interannual discharge variations on Bay of Bengal salinity, *J. Earth Syst. Sci.*, 120(5), 859–872, doi: 10.1007/s12040-011-0118-x.
- Durand F, G Alory, R Dussin and N Reul (2013) SMOS reveals the signature of Indian Ocean Dipole events, *Ocean Dynamics*, 63(11-12), 1203-1212.
- Dussin R, Treguier AM, Molines JM, Barnier B, Penduff T, Brodeau L and Madec G (2009) Definition of the interannual experiment ORCA025-B83, 1958-2007. LPO Report, 902.
- Dussin R, B Barnier and L Brodeau (2014) Atmospheric forcing data sets to drive eddy-resolving global ocean general circulation models, EGU General Assembly Conference Abstracts
- Fasullo J (2004) Biennial characteristics of All India rainfall. *J. Clim*, 17, 2972-2982.
- Feng M and Meyers G (2003) Interannual variability in the tropical Indian Ocean: a two-year time-scale of Indian Ocean Dipole, *Deep-Sea Res. Pt. II*, 50(12-13), 2263–2284, doi:10.1016/S0967-0645(03)00056-0.
- Findlater J (1971) Mean monthly airflow at low levels over the western Indian Ocean. *Geophysical Memoirs*, 115, 55.
- Flagg CA and Kim HS (1998) Upper ocean currents in the northern Arabian Sea from shipboard ADCP measurements collected during the 1994–1996 U.S. JGOFS and ONR Programs. *Deep-Sea Research II*, 45, 1917–1959.
- Furuichi T, Win Z and Wasson RJ (2009) Discharge and suspended sediment transport in the Ayeyarwady River, Myanmar: centennial and decadal changes. *Hydrological Process* 23:1631–1641. doi: 10.1002/hyp.7295
- Gadgil S, PV Joseph and NV Joshi (1984) Ocean–atmosphere coupling over monsoon regions; *Nature*, 312, 141–143.
- Gadgil S (2003) The Indian Monsoon and its variability. *Annual Review of Earth and Planetary Sciences* 31:429-467
- Gadgil S and KR Kumar (2006) The Asian Monsoon, Agriculture and Economy in The Asian Monsoon ed. B Wang Springer, Praxis UK, p 651-683.
- Gershunov A, Schneider N and Barnett T (2001) Low frequency modulation of the ENSO-monsoon rainfall relationship: signal or noise? *J Climate* 14:2486–2492
- Nat Hazards (2007) 42:273–285
- Gierach MM, Vazquez-Cuervo J, Lee T and Tsonos VM (2013) Aquarius and SMOS detect effects of an extreme Mississippi River flooding event in the Gulf of Mexico. *Geophysical Research Letters*, 40(19), 5188-5193.

- Girishkumar MS, M Ravichandran and MJ McPhaden (2013) Temperature inversions and their influence on the mixed layer heat budget during the winters of 2006–2007 and 2007–2008 in the Bay of Bengal, *J. Geophys. Res. Oceans.*, 118, 2426–2437, doi: 10.1002/jgrc.20192.
- Graham NE and TP Barnett (1987) Sea surface temperature, surface wind divergence, and convection over tropical oceans, *Science*, 238,4827, 657-659.
- Grunseich G, B Subrahmanyam, VSN Murty, and BS Giese (2011) Sea surface salinity variability during the Indian Ocean Dipole and ENSO events in the tropical Indian Ocean, *J. Geophys. Res.*, 116, C11013, doi: 10.1029/2011JC007456.
- Hahn D and J Shukla (1976) An apparent relationship between Eurasia snow cover and Indian monsoon rainfall. *J. Atmos. Sci.*, 33, 2461-2463.
- Han W and JP McCreary (2001) Modeling salinity distribution in the Indian Ocean, *J. Geophys. Res.*, 106, 859– 877
- Han W, JP McCreary and KE Kohler (2001) Influence of precipitation minus evaporation and Bay of Bengal rivers on dynamics, thermodynamics, and mixed layer physics in the upper Indian Ocean, *J. Geophys. Res.*, 106, 6895– 6916.
- Han W and PJ Webster (2002) Forcing mechanisms of sea-level interannual variability in the Bay of Bengal. *J. Phys. Oceanogr.* 32, 216-239
- Hareesh Kumar PV, B Matthew, MR Ramesh Kumar, AR Rao, PSV Jagadesh, KG Radhakrishnan and TN Shyni (2013) ‘Thermohaline front’ off the east coast of India and its generating mechanism, *Oc. Dyn.*, DOI 10.1007/s10236-013-0652-y
- Hasson A, T Delcroix, J Boutin, R Dussin and J Ballabrera-Poy (2014) Analyzing the 2010–2011 La Niña signature in the tropical Pacific sea surface salinity using in situ data, SMOS observations, and a numerical simulation, *J. Geophys. Res. Oceans*, 119, 3855–3867, doi: 10.1002/2013JC009388.
- Hernande O, J Boutin, N Kolodziejczyk, G Reverdin, N Martin, F Gaillard, N Reul and JL Vergely (2014) SMOS salinity in the subtropical North Atlantic salinity maximum: 1. Comparison with Aquarius and in situ salinity, *J. Geophys. Res. Oceans*, 119, 8878–8896
- Hood RR, JD Wiggert and SWA Naqvi (2009) "Indian Ocean research: Opportunities and challenges." *Indian Ocean Biogeochemical Processes and Ecological Variability*, 409-429.
- Hood RR, SWA Naqvi, JD Wiggert, T Landry, LE Rixen, LE Beckley, C Goyet, and GL Cowie (2011), "SIBER Sustained Indian Ocean Biogeochemistry and Ecosystem Research: Science plan and implementation strategy."
- Horii T, Hase H, Ueki I and Masumoto Y (2008) Oceanic precondition and evolution of the 2006 Indian Ocean dipole, *Geophys. Res. Lett.*, 35(3), L03607, doi:10.1029/2007GL032464.
- Howden SD and R Murtugudde (2001) Effects of river inputs into the Bay of Bengal. *J Geophys Res.*, 106:19825–19843.
- Hoyos CD and PJ Webster (2007) The role of intraseasonal variability in the nature of Asian monsoon precipitation, *J. Clim.*, 20, 4402–4424.

- Huffman G, R Adler, P Arkin, A Chang, R Ferraro, R Gruber, J Janowiak, A McNab, Rudolf B and Schneider U (1997) The global precipitation climatology project (GPCP) combined precipitation data set, *Bull. Amer. Meteor. Soc.* 78, 5-20.
- Izumo, Takeshi, Jérôme Vialard, Matthieu Lengaigne, Clément de Boyer Montégut, Swadhin K. Behera, Jing-Jia Luo, Sophie Cravatte, Sébastien Masson, and Toshio Yamagata. "Influence of the state of the Indian Ocean Dipole on the following year's El Niño." *Nature Geoscience* 3, no. 3 (2010): 168-172.
- Jackett DR and TJ McDougall (1995) Minimal adjustment of hydrographic profiles to achieve static stability, *J. Atmos. Oceanic Technol.*, 12, 381–389.
- Jensen TG (2001) Arabian Sea and Bay of Bengal exchange of salt and tracers in an ocean model, *Geophys. Res. Lett.*, 28, 3967– 3970.
- Jensen TG (2003) Cross-equatorial pathways of salt and tracers from the northern Indian Ocean: Modelling results, *DSR Part II*, 50, 2111-2127
- Jian J, Webster PJ and Hoyos CD (2009) Large-scale controls on Ganges and Brahmaputra river discharge on intraseasonal and seasonal time-scales. *Q J R Meteorol Soc*, 135, 353–370. doi: 10.1002/qj.384
- Joseph PV (1990) Warm pool over the Indian Ocean and monsoon onset, *Trop. Ocean Atmos. Newsl.*, Winter, (53), 1–5.
- Jourdain N, M Lengaigne, J Vialard, G Madec, C Menkes, E Vincent, S Jullien and B Barnier (2013) Observation based estimates of surface cooling inhibition by heavy rainfall under tropical cyclones, *J. Phys. Oceanogr.*, doi:10.1175/JPO-D-12-085.1.
- Kerr YH, et al. (2010) The SMOS Mission: New Tool for Monitoring Key Elements of the Global Water Cycle, *Proceedings of the IEEE.*, 98(5), 666-687.
- Keerthi MG, M Lengaigne, J Vialard, C de Boyer Montégut and PM Muraleedharan, (2013) Interannual variability of the Tropical Indian Ocean mixed layer depth, *Clim. Dyn.*, 40,743-759.
- Klein SA, BJ Soden and NC Lau (1999) Remote sea surface temperature variations during ENSO: Evidence for a tropical atmospheric bridge. *J. Climate*, 12, 917–932.
- Kumar KK, Rajagopalan KB and Cane MA (1999) On the weakening relationship between the Indian monsoon and ENSO. *Science* 284:2156–2159
- Lagerloef G, et al. (2008) The Aquarius/SAC-D mission: Designed to meet the salinity remote sensing challenge *Oceanography* 21(1), 68–81 doi: 10.5670/oceanog.2008.68.
- Lagerloef G, HY Kao, O Melnichenko, P Hacker, Eric Hackert, Y Chao, K Hilburn, T Meissner, S Yueh, L Hong and T Lee (2013) Aquarius salinity Validation Analysis, Aquarius project document AQ-014-PS-0016, JPL, 18 February 201
- Lagerloef G, FR Colomb, D Le Vine, F Wentz, S Yueh, C Ruf, J Lilly, J Gunn, Y Chao, A deCharon, G Feldman and C Swift (2008) The Aquarius/SAC-D Mission: Designed to meet the salinity remote-sensing challenge. *Oceanography* 21(1):68–81.
- Large WG and Danabasoglu G (2006) Attribution and impacts of upper-ocean biases in CCSM3. *Journal of Climate* 19: 2325-2346.

- Large WG and SG Yeager (2004) Diurnal to decadal global forcing for ocean and sea-ice models, NCAR technical note. 22 pp.
- Large WG and G Danabasoglu (2006) Attribution and impacts of upper ocean biases in CCSM3. *J. Climate.*, 19, 2325-2346.
- Lee CM, Jone BH, Brink KH and Fischer AS (2000) The upper ocean response to monsoonal forcing in the Arabian Sea: seasonal and spatial variability. *Deep-Sea Research II*, 47, 1177–1226.
- Lengaigne M, G Madec, G Alory and C Menkes (2003) Sensitivity of the tropical pacific ocean to isopycnal diffusion on tracer and dynamics. *J. Geophys. Res.*, 108 (C11), 3345, doi :10.1029/2002JC001704
- Levy M, A Estubier and G Madec (2001) Choice of an advection scheme for biogeochemical models. *Geophys. Res. Let.*, 28.
- Locarnini RA, AV Mishonov, JI Antonov, TP Boyer, Garcia HE, Baranova OK, Zweng MM and DR Johnson (2010) World Ocean Atlas, 2009, vol 1. In: Levitus TS (ed) NOAA Atlas NESDIS 68. U.S. Government Printing Office, Washington, DC.
- Lukas RB and EJ Lindstrom (1991) The mixed layer of the western equatorial Pacific Ocean, *J. Geophys. Res.*, 96, 3343– 3357
- Madec G (2008) NEMO ocean engine, Note Pôle Modél. 27, Inst. Pierre- Simon Laplace, Paris.
- Marchesiello P, JC McWilliams and AF Shchepetkin (2001) Open boundary conditions for long-term integration of regional ocean models. *Ocean Modell.* 3, 1–20.
- McCreary JP, PJ Kundu and RL Molinari (1993) A numerical investigation of dynamics, thermodynamics and mixed layer processes in the Indian Ocean, *Prog. Oceanogr.*, 31, 181– 244.
- McCreary JP, W Han, D Shankar and SR Shetye (1996) Dynamics of the East India Coastal Current: 2. Numerical solutions, *J Geophys Res.*, 101(C6), 13993–14010, doi: 10.1029/96JC00560.
- McMullan KD, MA Brown, M Martin-Neira, W Rits, S Ekholm, J Marti and J Lemanczyk (2008) SMOS: The Payload, *IEEE Transactions on Geoscience and Remote Sensing*, 46(3), 594-605.
- McPhaden MJ (2004) Evolution of the 2002/03 El Niño. *Bull. Amer. Meteor. Soc.*, 85, 677–69
- McPhaden MJ, G Meyers, K Ando, Y Masumoto, VSN Murty, M Ravichandran, F Syamsudin, J Vialard, L Yu and W Yu (2009) RAMA: The Research Moored Array for African-Asian-Australian Monsoon Analysis and Prediction, *Bull. Am. Meteorol Soc.*, 90:459-480.
- Mecklenburg S, Y Kerr, J Font and A Hahne (2008) The Soil Moisture and Ocean Salinity (SMOS) Mission - An overview, *Geophysical Research Abstracts.*, Vol. 10.
- Mecklenburg S, M Drusch, YH Kerr, J Font, M Martin-Neira, S Delwart, G Buenadicha, N Reul, E Daganzo-Eusebio, R Oliva and R Crapolicchio (2012) ESA's Soil Moisture and Ocean Salinity Mission: Mission Performance and

- Operations. *IEEE Transactions on Geoscience and Remote Sensing* 50(5)., Part 1:1354-1366.
- Meehl GA (1987) The annual cycle and interannual variability in the tropical Indian and Pacific Ocean regions. *Mon. Wea. Rev.*, 115, 27–50
- Meehl GA (1994) Coupled land–ocean–atmosphere processes and south Asian monsoon variability. *Science*, 266: 263 – 267.
- Menezes VV, ML Vianna and HE Phillips (2014) Aquarius sea surface salinity in the South Indian Ocean: Revealing annual-period planetary waves, *J. Geophys. Res. Oceans*, 119, 3883–3908, doi:10.1002/2014JC009935.
- Mesinger F and A Arakawa (1976) Numerical methods used in Atmospheric models. GARP Publication Series No 17.
- Meyers GA, PC McIntosh, L Pigot and MJ Pook (2007) The years of El Niño, La Niña and interactions with the tropical Indian Ocean. *J Climate*, 20, 2872-2880.
- Mignot J, C de Boyer Montégut, A Lazar and S Cravatte (2007) Control of salinity on the mixed layer depth in the world ocean: 2. Tropical areas, *J. Geophys. Res.*, 112, C10010, doi: 10.1029/2006JC003954.
- Molinari RL, D Olson and G Reverdin (1990) Surface current distributions in the tropical Indian Ocean derived from compilations of surface buoy trajectories, *J. Geophys. Res.*, 95, 7217-7238,
- Morrison JM, Codispoti LA, Smith SL, Wishner K, Flagg C, Gardner WD, Gaurin S, Naqvi SWA, Manghnani V, Prosperie L and Gundersen JS (1999) The oxygen minimum zone in the Arabian Sea during 1995 - overall seasonal and geographic patterns, and relationship to oxygen gradients, *Deep-Sea Res. Pt. II*, 46, 1903–1931, doi:10.1016/S09670645(99)00048-X
- Moum JN, A Perlin, JD Nash and MJ McPhaden (2013) Seasonal sea surface cooling in the equatorial Pacific cold tongue controlled by ocean mixing. *Nature*, 500, 64-67, doi: 10.1038/nature12363.
- Mujumdar M, Preethi B, Sabin TP, Ashok K, Saeed S, Pai DS and Krishnan R (2012) The Asian summer monsoon response to the LaNiña event of 2010. *Meteorol Appl* 19:216–225
- Murtugudde R, JP McCreary Jr. and AJ Busalacchi (2000) Oceanic processes associated with anomalous events in the Indian Ocean with relevance to 1997–1998. *J. Geophys. Res.*, 105, 3295–3306
- Murtugudde R, Wang L, Hackert E, Beauchamp J, Christian J and Busalacchi AJ (2004) Remote sensing of the Indo-Pacific region: ocean colour, sea level, winds and sea surface temperatures, *Int. J. Remote. Sens.*, 25(7-8), 1423–1435, doi:10.1080/01431160310001592391.
- Murthy VSN, YVB Sarma, DP Rao and CS Murthy (1992) Water characteristics, mixing and circulation in the Bay of Bengal during southwest monsoon. *J. Mar. Res.*, 50, 207–228.
- Neetu S, M Lengaigne, EM Vincent, J Vialard, G Madec, G Samson, MR Ramesh Kumar and F Durand (2012) Influence of upper-ocean stratification on tropical cyclone-induced surface cooling in the Bay of Bengal, *J. Geophys. Res.*, 117, C12020, doi: 10.1029/2012JC008433.

- Nidheesh AG, M Lengaigne, J Vialard, AS Unnikrishnan and H Dayan (2012) Decadal and long-term sea level variability in the tropical Indo-Pacific Ocean, *Clim. Dyn.*, 41,381-402.
- Niiler PP and EB Kraus (1977) One-dimensional models of the upper ocean. *Modelling and Prediction of the Upper Layer of the Ocean*, E. B. Kraus, Ed. Pergamon press, Oxford, 143-172.
- Nisha K, M Lengaigne, VV Gopalakrishna, J Vialard, S Pous, AC Peter, F Durand and S Naik (2013) Processes of summer intraseasonal sea surface temperature variability along the coasts of India, *Ocean Dynamics*, 63, 329-346.
- Nyadjro ES, B Subrahmanyam and JF Shriver (2011) Seasonal variability of salt transport during the Indian Ocean monsoons, *J. Geophys. Res.*, 116, doi: 10.1029/2011JC006993.
- Ohba M and Ueda H (2005) Basin wide warming in the equatorial Indian Ocean associated with El Nino. *Scientific Online Letters on the Atmosphere*,1, 089-092, doi:10.2151/sola.
- Pant GB and B Parthasarathy (1981) Some aspects of an association between the southern oscillation and Indian summer monsoon, *Arch. Meteorol. Geophys. Bioklimatol., Ser. B* , 29, 245–251.
- Papa F, F Durand, A Rahman, SK Bala and WB Rossow (2010) Satellite altimeter-derived monthly discharge of the Ganga-Brahmaputra River and its seasonal to interannual variations from 1993 to 2008, *J. Geophys. Res.* 115 C12013 doi: 10.1029/2009JC006075.
- Papa F, Bala SK, Pandey RK, Durand F, Gopalakrishna VV, Rahman A and Rossow WB (2012) Ganga–Brahmaputra river discharge from Jason-2 radar altimetry: an update to the long-term satellite-derived estimates of continental freshwater forcing flux into the Bay of Bengal. *J. Geophys. Res.* 117, C11021.<http://dx.doi.org/10.1029/2012JC008158>.
- Parampil SR, A Gera, M Ravichandran and D Sengupta (2010) Intraseasonal response of mixed layer temperature and salinity in the Bay of Bengal to heat and freshwater flux, *J. Geophys. Res.*, 115, C05002, doi: 10.1029/2009JC005790.
- Paulson CA and JJ Simpson (1977) Irradiance measurements in the upper ocean. *J. Phys. Oceanogr.*, 7 (6), 952–956.
- Périgaud C and P Delecluse (1992) Annual sea level variations in the southern tropical Indian Ocean from Geosat and shallow-water simulations, *J. Geophys. Res.*, 97(C12), 20169–20178, doi:10.1029/92JC01961.
- Prasad TG (1997) Annual and seasonal mean buoyancy fluxes for the tropical Indian Ocean, *Current Science*, 73, 667-674.
- Prasanna Kumar S, PM Muraleedharan, TG Prasad, M Gauns, N Ramaiah, SN de Souza, S Sardesai and M Madhupratap (2002) Why is the Bay of Bengal less productive during summer monsoon compared to the Arabian Sea?, *Geophys. Res. Lett.*, 29(24), 2235, doi:10.1029/2002GL016013.
- Praveen Kumar B, Vialard J, Lengaigne M, Murty VSN and McPhaden MJ (2012) TropFlux: air-sea fluxes for the global tropical oceans—description and evaluation against observations. *Clim Dyn* 38:1521–1543

- Praveen Kumar B, Vialard J, M Lengaigne, VSN Murty, GR Foltz, MJ McPhaden, S Pous, and de Boyer Montégut (2014) Processes of interannual mixed layer temperature variability in the thermocline ridge of the Indian Ocean. *Climate Dynamics*, 43, 9-10, 2377-2397.
- Rahman SH, D Sengupta and M Ravichandran (2009) Variability of Indian summer monsoon rainfall in daily data from gauge and satellite, *J. Geophys. Res.*, 114, D17113, doi: 10.1029/2008JD011694.
- Rao LVG and PS Ram (2005), "Upper ocean physical processes in the Tropical Indian Ocean".
- Rao RR and R Sivakumar (2000) Seasonal variability of nearsurface thermal structure and heat budget of the mixed layer of the tropical Indian Ocean from a new global ocean temperature climatology. *J. Geophys. Res.*, 105, 995–1015.
- Rao RR and R Sivakumar (2003) Seasonal variability of sea surface salinity and salt budget of the mixed layer of the north Indian Ocean, *J. Geophys. Res.*, 108(C1), 3009, doi: 10.1029/2001JC00907.
- Rao SA, Behera SK, Masumoto Y and Yamagata T (2002) Interannual subsurface variability in the tropical Indian Ocean with a special emphasis on the Indian Ocean Dipole, *Deep-Sea Res. Pt. II*, 49(7-8), 1549–1572, doi:10.1016/S0967-0645(01)00158-8
- Rao SA, Saha SK, Pokhrel S, Sundar D, Dhakate AR, Mahapatra S, Ali S, Chaudhari HS, Shreeram P, Vasimalla S, Srikanth AS, Suresh RRV (2011) Modulation of SST, SSS over northern Bay of Bengal on ISO time scale, *Journal of Geophysical Research*, 116, doi:10.1029/2010JC006804, C09026, 1-11
- Rasmusson EM and TH Carpenter (1982) Variations in the tropical sea-surface temperature and surface wind fields associated with the southern oscillation El Nino. *Monthly Weather Review*, 110, 354-384
- Ratheesh S, R Sharma and S Basu (2012) Projection-Based Assimilation of Satellite-Derived Surface data in an Indian ocean circulation model, *Marine Geodesy*, 35 (2), 175 -187
- Ratheesh S, B Mankad, S Basu, R Kumar and R Sharma (2013) Assessment of Satellite-Derived Sea Surface Salinity in the Indian Ocean, *IEEE Geoscience and Remote Sensing Letters* 10(3)., 428-431, doi 10.1109/LGRS.2012.2207943.
- Ratheesh S, R Sharma, R Sikhakolli, R Kumar and S Basu (2014) Assessing Sea Surface Salinity Derived by Aquarius in the Indian Ocean, *IEEE Geoscience and Remote Sensing Letters*, vol.11, no.4, pp.719, 722.
- Reul N, J Tenerelli, J Boutin, B Chapron, F Paul, E Brion, F Gaillard and O Archer (2012) Overview of the First SMOS Sea Surface Salinity Products. Part I: Quality Assessment for the Second Half of 2010, *IEEE Transactions on Geoscience and Remote Sensing* 50(5)., Part 1:1636-1647.
- Reul N, S Fournier, J Boutin, O Hernandez, C Maes, B Chapron, G Alory, Y Quilfen, J Tenerelli, S Morisset, Y Kerr, S Mecklenburg and S Delwart (2013) Sea Surface Salinity Observations from Space with the SMOS Satellite: A New Means to Monitor the Marine Branch of the Water Cycle. *Surv Geophys.*, doi 10.1007/s10712-013-9244-0.

- Reul N, B Chapron, T Lee, C Donlon, J Boutin and G Alory (2014) Sea surface salinity structure of the meandering Gulf Stream revealed by SMOS sensor, *Geophys. Res. Lett.*, 41, 3141–3148, doi:10.1002/2014GL059215.
- Reverdin G, Cadet DL and Gutzler D (1986) Interannual displacements of convection and surface circulation over the equatorial Indian Ocean, *Q. J. Roy. Meteor. Soc.*, 112(471), 43–67, doi:10.1002/qj.49711247104
- Roemmich D, et al. (1999) On the design and implementation of Argo: An initial plan for a global array of profiling floats. International CLIVAR Project Office Report 21, GODAE Report 5. GODAE International Project Office, Melbourne, Australia, 32 pp.
- Roemmich D, Johnson GC, Riser S, Davis R, Gilson J, Owens WB, Garzoli SL, Schmid C, Ignaszewski M (2009) The Argo Program: Observing the global ocean with profiling floats. *Oceanography* 22(2):34–43. doi:10.5670/oceanog.2009.36
- Roulet G and Madec G (2000) Salt conservation, free surface and varying volume : a new formulation for Ocean GCMs, *J. Geophys. Res.*, 105, 23,927–23,942.
- Saji NH, Goswami BN, Vinayachandran PN and Yamagata T (1999) A dipole mode in the tropical Indian Ocean, *Nature*, 401(6751), 360–363
- Samson G, S Masson, M Lengaigne, MG Keerthi, J Vialard, S Pous, G Madec, NC Jourdain, S Jullien, C Menkes and P Marchesiello (2014) The NOW regional coupled model: Application to the tropical Indian Ocean climate and tropical cyclone activity, *J. Adv. Model. Earth Syst.*, 6, 700–722, doi:10.1002/2014MS000324.
- Schott F, Fieux M, Kindle J, Swallow J and Zantopp R (1988) The boundary currents east and north of Madagascar. Part II: Direct measurements and model comparisons. *Journal of Geophysical Research*, 93, 4963–4974.
- Schott F and JP McCreary (2001) The monsoon circulation of the Indian Ocean, *Prog. Oceanogr.*, 51, 1–123, doi: 10.1016/S0079-6611(01)00083-0.
- Schott F, M Dengler and R Schoenefeldt (2002) The shallow thermohaline circulation of the Indian Ocean, *Prog. Oceanogr.*, 53, 57–103.
- Schott FA, Xie SP and McCreary JP (2009) Indian Ocean circulation and climate variability, *Rev. Geophys.*, 47, RG1002, doi:10.1029/2007RG000245
- Sengupta D, GN Bharath Raj and SSC. Shenoi (2006) Surface freshwater from Bay of Bengal runoff and Indonesian throughflow in the tropical Indian Ocean, *Geophys. Res. Lett.*, 33, L22609, doi: 10.1029/2006GL027573.
- Sengupta D, RG Bharath and DS Anitha (2008) Cyclone-induced mixing does not cool SST in the post-monsoon north Bay of Bengal, *Atmos. Sci. Lett.*, 9, 1-6, doi:10.1002/asl.162.
- Seo H, SP Xie, R Murtugudde, M Jochum and AJ Miller (2009) Seasonal effects of Indian Ocean freshwater forcing in a regional coupled model, *J. Clim.*, 22, 6577–6596.
- Shankar D, JP McCreary, W Han and SR Shetye (1996) Dynamics of the East India Coastal Current 1. Analytic solutions forced by interior Ekman pumping and

- local alongshore winds, *J. Geophys. Res.*, 101, 13, 975–13,991, doi: 10.1029/96JC00559.
- Shankar D (1998) Low-frequency variability of sea level along the coast of India. Ph.D. Thesis, Goa University, Goa, India, 207 pp. (<http://hdl.handle.net/2264/24>).
- Shankar D, PN Vinayachandran and AS Unnikrishnan (2002) The monsoon currents in the north Indian Ocean, *Prog. Oceanogr.* 52,63–120, doi: 10.1016/S0079-6611(02)00024-1.
- Sharma R, N Agarwal, IM Momin, S Basu and VK Agarwal (2010) Simulated Sea Surface Salinity Variability in the Tropical Indian Ocean, *J. Climate*, 23, 6542–6554. doi: 10.1175/2010JCLI3721.1
- Shenoi SSC (2010) Intra-seasonal variability of the coastal currents around India: A review of the evidences from new observations, *Indian Journal of Marine Sciences*, 39 (4), pp. 489-496.
- Shenoi SSC, D Shankar and SR Shetye (1999) On the sea surface temperature high in the Lakshadweep Sea before the onset of the southwest monsoon, *J. Geophys. Res.*, 104, 15 703–15 712.
- Shenoi SSC, D Shankar and SR Shetye (2002) Difference in heat budgets of the near-surface Arabian Sea and Bay of Bengal: Implications for the summer monsoon, *J. Geophys. Res.*, 107(C6), 3052, doi: 10.1029/2000JC000679.
- Shesu RV, UdayaBhaskar TVS, Pattabhi Rama Rao E, Devender R and HemasundarRao T (2013) Open source architecture for web-based oceanographic data services. *Data Sci J* 12:47-55
- Shetye SR, SSC Shenoi, AD Gouveia, GS Michael, D Sundar and G Nampoothiri (1991a) Wind-driven coastal upwelling along the western boundary of the Bay of Bengal during the southwest monsoon, *Cont. Shelf Res.*, 11, 1397–1408.
- Shetye SR, Gouveia AD, Shenoi SSC, Sundar D, Michael GS and Nampoothiri G (1991b) The western boundary current of the seasonal subtropical gyre in the Bay of Bengal. *Journal of Geophysical Research*, 98, 945–954.
- Shetye SR (1993) The movement and implications of the Ganges–Brahmaputra runoff on entering the Bay of Bengal, *Curr. Sci.* 64 (1), 32–38.
- Shetye SR, AD Gouveia, D Shankar, GS Michael and G Nampoothiri (1996) Hydrography and circulation of the western Bay of Bengal during the Northeast Monsoon, *J. Geophys. Res.*, 101, 14,011 – 14,025.
- Shi W, Morrison JM, Böhm E and Manghnani V (2000) The Oman upwelling zone during 1993, 1994 and 1995. *Deep-Sea Research II*, 47, 1227–1247.
- Shuen X, M Kimoto and A Sumi (1998) Role of Land Surface Processes Associated with Interannual Variability of Broad-scale Asian Summer Monsoon as Simulated by the CCSR/NIES AGCM. *J. Meteorol. Soc. Japan*, 76 (2), 217–236
- Singh OP (2002) Interannual variability and predictability of sea level along the Indian Coast, *Theor. Appl. Climatol.*, 72, 11–28.
- Smith RL, Huyer A, Godfrey JS and Church JA (1991) The Leeuwin Current off western Australia, 1986–1987. *Journal of Physical Oceanography*, 21, 322–345.

- Smith SL and Codispoti LA (1980) Southwest monsoon of 1979: chemical and biological response of Somali coastal waters. *Science*, 209, 597-600.
- Srinivas K, PKD Kumar and C Revichandran (2005) ENSO signature in the sea level along the coastline of the Indian subcontinent, *Indian J. Mar. Sci.*, 34, 225–236.
- Subramanian V (1993) Sediment load of Indian rivers; *Curr. Sci.* 64 928–930.
- Subrahmanyam B, G Grunseich and ES Nyadjro (2013) Preliminary SMOS salinity measurements and validation in the Indian Ocean, *IEEE Transactions Geoscience and Remote Sensing*, 50, 12, doi: 10.1109/TGRS.2012.2199122.
- Sudre J, C Maes and V Garçon (2013) On the global estimates of geostrophic and Ekman surface currents, *Limnology and Oceanography: Fluids and Environments*, 3, 1–20, doi: 10.1215/21573689-2071927.
- Swallow JC and Bruce JC (1966) Current measurements off the Somali coast during the southwest monsoon of 1964. *Deepsea Research*, 13, 861–888.
- Swallow JC, Molinari RL, Bruce JG, Brown OB and Evans RH (1983) Development of near-surface flow pattern and water mass distribution in the Somali Basin in response to the southwest monsoon of 1979. *Journal of Physical Oceanography*, 13, 1398–1415.
- Swallow JC, Fieux M and Schott F (1988) The boundary currents east and north of Madagascar, Part I: Geostrophic currents and transports. *Journal of Geophysical Research*, 93, 4951–4962.
- Swallow JC, Schott F and Fieux M (1991) Structure and transport of the East African Coastal Current. *Journal of Geophysical Research*, 96, 22254–22267.
- Terray L, L Corre, S Cravatte, T Delcroix, G Reverdin and A Ribes (2012) Near-surface salinity as nature's rain gauge to detect human influence on the tropical water cycle, *J. Clim.*, 25, 958–977, doi:10.1175/JCLI-D-10-05025.1.
- Thadathil P, VV Gopalakrishna, PM Muraleedharan, GV Reddy, N Araligidat and SSC Shenoy (2002) Surface layer temperature inversion in the Bay of Bengal, *Deep Sea Res., Part I*, 49, 1801–1818.
- Thadathil P, PM Muraleedharan, RR Rao, YK Somayajulu, GV Reddy and C Revichandran (2007) Observed seasonal variability of barrier layer in the Bay of Bengal, *J. Geophys. Res.*, 112, C02009, doi: 10.1029/2006JC003651.
- Thompson B, Gnanaseelan C and Salvekar PS (2006) Variability in the Indian Ocean circulation and salinity and its impact on SST anomalies during dipole events. *J Mar Res* 64:853-880
- Trenberth KE, Branstator GW, Karoly D, Kumar A, Lau NC and Ropelewski C (1998) Progress during TOGA in understanding and modeling global teleconnections associated with tropical sea surface temperatures. *J. Geophys. Res.* 103, 14291-14324
- Uppala SM and co-authors (2005) The ERA-40 re-analysis. *Q.J.R. Meteorol. Soc.*, 131: 2961–3012. doi: 10.1256/qj.04.176.
- Varkey MJ (1986) Salt balance and mixing in the Bay of Bengal, Ph.D thesis, 109 pp., Kerala Univ., Kerala, India,

- Varkey MJ, Murty VSN and Suryanarayana A (1996) Physical oceanography of the Bay of Bengal and Andaman Sea. *Oceanography and Marine Biology (an annual Review)*34, 1–70
- Vecchi GA and DE Harrison (2004) Interannual Indian rainfall variability and Indian Ocean sea surface temperature anomalies. *Earth Climate: The Ocean Atmosphere Interaction*. American Geophysical Union, *Geophys. Mono.* 147, (Eds.) C. Wang, 247-260.
- Venkatesan R, Arul Muthiah M, Ramesh K, Ramasundaram S, Sundar R and Atmanand MA (2013) Satellite communication systems for ocean observational platforms: Societal importance and challenges. *The Journal of Ocean Technology* 8(3): 47-73.
- Vialard J, P Delecluse and C Menkes (2002) A modeling study of salinity variability and its effects in the tropical Pacific Ocean during the 1993–1999 period, *J. Geophys. Res.*, 107(C12), 8005, doi:10.1029/2000JC000758.
- Vialard J, K Drushka, H Bellenger, M Lengaigne, S Pous and JP Duvel (2013) Understanding Madden-Julian-Induced sea surface temperature variations in the North Western Australian Basin, *Clim. Dyn.*, doi:10.1007/s00382-012-1541-7.
- Vialard J, P Delecluse and C Menkes (2002) A modeling study of salinity variability and its effects in the tropical Pacific Ocean during the 1993–1999 period, *J. Geophys. Res.*, 107(C12), 8005, doi: 10.1029/2000JC000758.
- Vinayachandran PN, S Iizuka and T Yamagata (2002a) Indian Ocean dipole mode event in an ocean general circulation model, *Deep Sea Res. II.* 49, 1573–1596.
- Vinayachandran PN, VSN Murty and V Ramesh Babu (2002b) Observations of barrier layer formation in the Bay of Bengal during summer monsoon, *J. Geophysical Research*, 107(C12), doi:10.1029/2001JC000831.
- Vinayachandran PN, T Kagimoto, Y Masumoto, P Chauhan, SR Nayak and T Yamagata (2005) Bifurcation of the East India Coastal Current east of Sri Lanka, *Geophys. Res. Lett.*, 32, L15606, doi:10.1029/2005GL022864.
- Vinayachandran PN and J Kurian (2007) Hydrographic observations and model simulation of the Bay of Bengal freshwater plume, *Deep Sea Res Part I*, 54, 471–486.
- Vinayachandran PN and RS Nanjundiah (2009) Indian Ocean sea surface salinity variations in a coupled model, *Clim Dyn.*, doi: 10.1007/s00382–008–0511–6.
- Vinayachandran PN, CP Neema, S Mathew and R Remya (2012) Mechanisms of summer intraseasonal sea surface temperature oscillations in the Bay of Bengal, *J. Geophys. Res.*, 117, C01005, doi:10.1029/2011JC007433.
- Vinayachandran PN, D Shankar, S Vernekar, KK Sandeep, P Amol, CP Neema and A Chatterjee (2013) A summer monsoon pump to keep the Bay of Bengal salty, *Geophys. Res. Lett.*, 40, 1777–1782, doi:10.1002/grl.50274.
- Vinayachandran PN, Shankar D, Vernekar S, Sandeep KK, Amol P, Neema CP and Chatterjee A (2013). A summer monsoon pump to keep the Bay of Bengal salty. *Geophysical Research Letters*, 40(9), 1777-1782.
- Vincent EM, M Lengaigne, J Vialard, G Madec, N Jourdain and S Masson (2012) Assessing the Oceanic Control on the Amplitude of sea Surface Cooling induced

- by Tropical Cyclones, *J. Geophys. Res.*, 117, C05023, doi: 10.1029/2011JC007705.
- Walker GT (1924) Correlations in seasonal variations of weather. I. A further study of world weather. *Mem. Indian Meteorol. Dep.* 24, 275-332.
- Wang C and J Picaut (2004) Understanding ENSO physics -A review. In: *Earth's Climate: The Ocean-Atmosphere Interaction*. C. Wang, S.P. Xie, and J. A. Carton, Eds., AGU Geophysical Monograph Series, 147:21-48.
- Webster PJ and S Yang (1992) Monsoon and ENSO: Selectively Interactive Systems. *Quart. J. Roy. Meteor. Soc.*, 118 (507), 877-926, doi:10.1002/qj.49711850705.
- Webster PJ, Moore AM, Loschnigg JP and Leben RR (1999) Coupled ocean-atmosphere dynamics in the Indian Ocean during 1997-98, *Nature*, 401(6751), 356-60, doi:10.1038/43848
- Webster PJ, et al. (2002) The JASMINE pilot study, *Bull. Am. Meteorol. Soc.*, 83, 1603-1630, doi: 10.1175/BAMS-83-11-1603.
- Weller RA, Baumgartner, MA, Josey SA, Fischer AS and Kindle JC (1998) Atmospheric forcing in the Arabian Sea during 1994-1995: observations and comparisons with climatology and models. *Deep-Sea Research*, 45, 1961-1999.
- Wu R and BP Kirtman (2003) On the impacts of the Indian summer monsoon on ENSO in a coupled GCM. *Quart. J. Roy. Meteor. Soc.*, 129 (595), 3439-3468, doi:10.1256/qj.02.214.
- Wu L, F Wang, D Yuan and M Cui (2007) Evolution of freshwater plumes and salinity fronts in the northern Bay of Bengal, *J. Geophys. Res.*, 112, C08017, doi: 10.1029/2005JC003308.
- Wyrtki K (1971) *Oceanographic atlas of the International Indian Ocean Expedition*. 531 pp. Washington, DC: National Science Foundation.
- Xavier PK, Marzin C and Goswami BN (2007) An objective definition of the Indian summer monsoon season and a new perspective on the ENSO-monsoon relationship, *Q. J. Roy. Meteor. Soc.*, 133(624), 749-764, doi:10.1002/qj.45
- Xie P, and PA Arkin (1997) Analyses of Global Monthly Precipitation Using Gauge Observations, Satellite Estimates, and Numerical Model Predictions, *J. of Climate.*, 9, 840-858.
- Xie SP, Hafner J, Tokinaga H, Du Y, Sampe T and Hu KaiMing HG (2009) Indian Ocean capacitor effect on Indo-western Pacific climate during the summer following El Niño, *J. Climate*, 22(3), 730-747, doi: <http://dx.doi.org/10.1175/2008JCLI2544.1>
- Yu L, JJ O'Brien and J Yang (1991) On the remote forcing of the circulation in the Bay of Bengal. *J. Geophys. Res.*, 96, 20 449-20 454.
- Yu Z and JP McCreary (2004) Assessing precipitation products in the Indian Ocean using an ocean model. *J. Geophys. Res.*, 109, C05013, doi: 10.1029/2003JC002106.
- Yueh S, W Tang, A Fore, A Hayashi, YT Song and G Lagerloef (2014) Aquarius geophysical model function and combined active passive algorithm for ocean

- surface salinity and wind retrieval, *J. Geophys. Res. Oceans*, 119, 5360–5379, doi: 10.1002/2014JC009939.
- Zhang YC, WB Rossow, AA Lacis, V Oinas and MI Mishchenko (2004) Calculation of radiative flux profiles from the surface to top-of-atmosphere based on ISCCP and other global datasets: Refinements of the radiative transfer model and the input data, *J. Geophys. Res.*, 27.
- Zhang C (2005) Madden-Julian oscillation, *Reviews of Geophysics*, 43(2).
- Zhang H, Ge Chen, Chengcheng Qian and Haoyu Jiang (2013) Assessment of Two SMOS Sea Surface Salinity Level 3 Products Against Argo Upper Salinity Measurements, *Geoscience and Remote Sensing Letters, IEEE*, vol.10, no.6, 1434,1438
- Zweng MM, JR Reagan, JI Antonov, RA Locarnini, AV Mishonov, TP Boyer, HE Garcia, OK Baranova, DR Johnson, D Seidov and MM Biddle (2013) *World Ocean Atlas 2013, Volume 2: Salinity*. S. Levitus, Ed., A. Mishonov Technical Ed.; NOAA Atlas NESDIS 74, 39 pp.